MEASUREMENT OF THE NEUTRAL D MESON MIXING PARAMETERS AT THE BABAR EXPERIMENT

Memòria presentada per optar al títol de doctor en física

per

Jordi Garra Ticó

Juny - 2010

Director: Eugeni Graugés Pous.

Programa de doctorat: Física avançada
Bienni 2003-2005

Departament d'estructura i constituents de la matèria

UNIVERSITAT DE BARCELONA

Eugeni Graugés Pous, professor agregat del departament d'estructura i constituents de la matèria de la Universitat de Barcelona, certifica:

que la present memòria, *Measurement of the neutral D meson mixing parameters at the BaBar experiment*, s'ha realitzat sota la seva direcció al departament d'estructura i constituents de la matèria de la Universitat de Barcelona per part de Jordi Garra Ticó, i constitueix la seva tesi doctoral.

Barcelona, 15 de juny de 2010.

Eugeni Graugés Pous

Al meu padrí Eugeni

Contents

Agraïments

L'anàlisi que presento en aquest document és el resultat d'una feina que ha durat anys. En primer lloc vull donar les gràcies al meu director, l'Eugeni Graugés Pous, i també al Fernando Martínez Vidal. Tots dos m'han encaminat en aquesta recerca i gràcies a ells he pogut posar les mans en un gran experiment com ha estat BaBar, alhora que he après a treballar amb el rigor científic necessari per a escriure aquesta tesi.

Si digués que el Lluís Garrido Beltran m'ha resolt els meus dubtes d'estadística no estaria essent del tot sincer. En realitat m'ha orientat a resoldre-me'ls jo mateix, amb la qual cosa n'he après molt més. Moltes gràcies, i moltes gràcies també al Ricardo Graciani, al Xavi Vilasís i a l'Hugo Ruiz.

La mesura dels paràmetres d'oscil·lació de mesons D neutres l'he feta juntament amb el Fernando Martínez Vidal i el Diego Milanés, a València, el Nicola Neri i la Giulia Casarosa, a Pisa, i el Brian Meadows i el Rolf Andreassen, a Cincinnati. Gràcies a tots ells.

Durant els meus anys d'estudiant de doctorat he picat milers de línies de codi. Els entrebancs que m'he trobat al llarg del camí els he resolt amb l'ajuda de l'Adri Casajús i de l'Albert Puig, i els agraeixo tot allò que he après amb ells.

També m'han ajudat molt les discussions i les bones estones passades amb els meus companys de feina: el Jorge Mondéjar, l'Alberto Hernández, la Majo Rodríguez, l'Elies López, el Carlos González, el Miguel Escobedo, el Sandro Camboni, el Raül Sànchez, l'Antonio Pérez-Calero, el Clemens Bauer, el Ricci Vázquez, el Marc Grabalosa, l'Ernest Aguiló, la Míriam Calvo, l'Arianna Carbone, l'Edu Picatoste, el David Gascón, l'Albert Comerma i el Blai Pié.

Del temps que vaig estar treballant a SLAC vull destacar la Neus López March i el Riccardo Cenci, que em van ensenyar els secrets del subdetector SVT. No m'oblido de totes les persones, majoritàriament italians, de l'experiment BaBar, que van fer les meves estades allà molt més agradables. Gràcies pels bons moments al Rose & Crown de Palo Alto i a l'Oasis de Menlo Park, per acompanyar-me a l'aeroport de San Francisco, per les excursions a les ciutats i fantàstics parcs naturals de Califòrnia, per haver-me ensenyat la llengua i la cuina italianes i, en definitiva, per haver-me donat un cop de mà sempre que ho he necessitat.

Els més importants els deixo pel final: els meus pares i la meva família, a qui agraeixo el seu suport incondicional. Sense ells no ho hauria aconseguit mai.

Resum

El fenomen de les oscil·lacions és un procés en què un mesó elèctricament neutre es produeix com a partícula, però es desintegra com si fos la seva antipartícula.

Les oscil·lacions i la violació de la simetria CP al sector dels mesons D neutres es va començar a discutir als anys 70 del segle 20 [1]. Tanmateix, no ha estat fins els darrers anys, quan hi ha hagut mostres prou grans i ben identificades de desintegracions de mesons D neutres, que s'ha pogut observar evidència del fenomen de les oscil·lacions en diferents tipus de mesures dependents del temps. El fenomen de la violació de CP encara no s'ha observat, i els límits superiors se'n situen al voltant de 0.01.

En els últims tres anys, les col·laboracions BaBar i Belle han establert evidència d'oscil·lacions en mesons D neutres, que també la col·laboració CDF ha confirmat.

Al §1.5 s'hi presenten totes les cerques fins avui en dia d'oscil·lacions i violació de CP al sector dels mesons D neutres. La primera evidència d'oscil·lacions, en desintegracions $D^0 \to K^+\pi^-$ [2], és d'especial interès, amb una significança al nivell de $3.9\,\sigma$. Aquesta observació es va confirmar en una mesura similar de la col·laboració CDF [3].

La col·laboració Belle ha mostrat evidència d'oscil·lacions de mesons D neutres, amb una significança al nivell de $3.2\,\sigma$, en l'observació de diferències en temps de vida en desintegracions a estats finals amb CP parell $D^0 \to K^+K^-$ i $D^0 \to \pi^+\pi^-$, en comparació amb desintegracions a l'estat propi de gust $D^0 \to K^-\pi^+$ [4]. Aquesta observació es va confirmar a BaBar, en una anàlisi amb els gust etiquetat dels mesons [5], i també en un conjunt combinat d'esdeveniments disjunts etiquetats i sense etiquetar [6], que presenta la significança més gran d'oscil·lacions de mesons D fins avui en dia, al nivell de $4.1\,\sigma$. La col·laboració BaBar també ha mostrat evidència d'oscil·lacions en desintegracions $D^0 \to K^+\pi^-\pi^0$ [7].

Aquest document presenta la cerca d'oscil·lacions en desintegracions $D^0 \to K_s\pi^+\pi^-$ i $D^0 \to K_sK^+K^-$ i els seus conjugats CP. Aquesta anàlisi segueix el mètode suggerit a [8]. Un resultat anterior de la col·laboració Belle [9], només amb esdeveniments amb $K_s\pi^+\pi^-$, suggereix fortament la presència d'oscil·lacions en aquestes desintegracions, i presenta una observació amb una significança de $2.2\,\sigma$.

Introducció a les oscil·lacions de mesons D neutres

En un sistema d'un parell de mesons D neutres, hi ha diferents estats que són rellevants de cara a la discussió de diversos processos:

- Els dos estats propis de gust, $|D^0\rangle$ i $|\bar{D}^0\rangle$, tenen un contingut en quarks ben definit i són els estats rellevants en els processos de producció i desintegració. Quan es propaguen per l'espai i el temps, estan mesclats l'un amb l'altre.
- Els dos estats propis de l'hamiltonià, $|D_1\rangle$ i $|D_2\rangle$, tenen una massa i un temps de vida mitjana ben definits, i es propaguen per l'espai i el temps d'una manera ben definida. En la base pròpia dels estats de gust, s'expressen com

$$|D_{1,2}\rangle = p\left|D^0\right\rangle \pm q\left|\bar{D}^0\right\rangle . \tag{1}$$

- Si hi ha conservació de la simetria CP, els estats propis de l'hamiltonià també serien estats propis de CP, $|D_+\rangle$ i $|D_-\rangle$.

Al sistema de dos kaons neutres, és rellevant observar que els seus estats propis de massa tenen temps de vida diferents, tot i que masses similars, per la qual cosa convé definir els seus estats K_l i K_s com els seus estats de temps de vida llarg i curt, respectivament. Tanmateix, en mesons D neutres, el temps característic d'oscil·lació és més llarg que el temps mig de desintegració, per la qual cosa hi és més convenient fer servir la base dels estats de gust.

Com que gairebé totes les expressions i discussions vàlides pel D^0 són també vàlides pel $\bar{D}^0$, i amb la intenció de simplificar la notació, en aquest document es fa servir $\tilde{D}^0$ per referir-se a ambdós estats de gust del mesó D. Quan una expressió és diferent pel D^0 i pel $\bar{D}^0$, s'escriu separadament per ambdós.

Una combinació lineal arbitrària d'estats propis de gust del mesó neutre D, $a|D^0\rangle + b|\bar{D}^0\rangle$, evoluciona amb el temps segons l'equació d'Schrödinger dependent del temps,

$$i\frac{d}{dt}\begin{pmatrix} a \\ b \end{pmatrix} = \mathcal{H}\begin{pmatrix} a \\ b \end{pmatrix} \equiv \left(M - \frac{i}{2}\Gamma\right)\begin{pmatrix} a \\ b \end{pmatrix}, \tag{2}$$

on M i Γ són matrius hermítiques 2×2, però l'hamiltonià efectiu $\mathcal{H}$ no ho és. $|D_1\rangle$ i $|D_2\rangle$ són els estats propis d'$\mathcal{H}$, amb valors propis $\left(m_1 + \frac{i}{2}\Gamma_1\right)$ i $\left(m_2 + \frac{i}{2}\Gamma_2\right)$, respectivament.

Definint

$$\Gamma = \frac{\Gamma_1+\Gamma_2}{2}, \qquad x = \frac{m_1 - m_2}{\Gamma}, \qquad y = \frac{\Gamma_1-\Gamma_2}{2\Gamma}, \tag{3}$$

l'evolució temporal dels estats propis de l'hamiltonià es pot escriure com

$$|D_{1,2}(t)\rangle = e^{-\frac{\Gamma t}{2}} h_{1,2}(t)\, |D_{1,2}\rangle , \tag{4}$$

on

$$h_{1,2}(t) = e^{\mp\frac{(y+ix)\Gamma t}{2}}. \tag{5}$$

Els estats propis de l'hamiltonià s'expressen en termes dels estats propis de gust com

$$|D_{1,2}\rangle = p\left|D^0\right\rangle \pm q\left|\bar{D}^0\right\rangle, \tag{6}$$

on els paràmetres p i q es poden escollir de manera que verifiquin $|p|^2 + |q|^2 = 1$.

Les amplades d'un estat inicial $|D^0\rangle$ o $|\bar{D}^0\rangle$ a l'instant de producció a un estat final $\langle f|$ s'expressen com

$$\begin{aligned} A_f &= \langle f|\mathcal{H}|D^0\rangle, \\ \bar{A}_f &= \langle f|\mathcal{H}|\bar{D}^0\rangle, \\ \chi &= \frac{q}{p}\frac{\bar{A}_f}{A_f}, \end{aligned} \tag{7}$$

de manera que l'amplada de desintegració dels estats de gust evoluciona amb el temps com

$$\langle f|\mathcal{H}|\tilde{D}^0(t)\rangle = e^{-\frac{\Gamma t}{2}}\tilde{A}_f\left(\frac{1+\chi^{\pm 1}}{2}h_1(t) + \frac{1-\chi^{\pm 1}}{2}h_2(t)\right), \tag{8}$$

on ± 1 a l'exponent de χ és $+1$ per l'estat $|D^0\rangle$ i -1 per l'estat $|\bar{D}^0\rangle$, i es fa servir la notació $\tilde{A}_f$ per referir-se tant a l'amplada A_f com $\bar{A}_f$, de manera similar a la notació $\tilde{D}^0$ pels estats D^0 i $\bar{D}^0$.

Les anteriors expressions matemàtiques s'han presentat sense demostració amb la intenció d'introduir l'anàlisi. La seva derivació i la definició dels paràmetres d'oscil·lació x i y en termes dels valors propis de l'hamiltonià s'ha descrit en detall a §1.1.

Des d'un punt de vista teòricament estricte, els estats propis de gust $\tilde{D}^0$ no tenen un temps de vida ben definit, ja que l'expressió (8) mostra que evolucionen al llarg del temps com una barreja d'ambdós estats D^0 i $\bar{D}^0$. Tanmateix, és molt habitual referir-se al temps de vida del $\tilde{D}^0$ com la diferència de temps entre els instants de producció i de desintegració d'un estat del mesó D neutre, tot i que el seu gust a l'instant de producció pugui ser diferent a l'instant de desintegració.

Introducció a la violació de CP en desintegracions de mesons D

Les possibles manifestacions de violació de CP es poden classificar de manera independent de models:

- La violació de CP en la desintegració té lloc en desintegracions de mesons, tant carregats com neutres. Es dóna quan l'amplada de desintegració d'una partícula és diferent de la de la seva partícula amb CP conjugada. Es pot mesurar en desintegracions de partícules a estats finals que no siguin propis de CP, tals com

$$a_f = \frac{\Gamma\left(B^+ \to f\right) - \Gamma\left(B^- \to \bar{f}\right)}{\Gamma\left(B^+ \to f\right) + \Gamma\left(B^- \to \bar{f}\right)} = \frac{1 - \left|\bar{A}_{\bar{f}}/A_f\right|^2}{1 + \left|\bar{A}_{\bar{f}}/A_f\right|^2}. \tag{9}$$

- La violació de CP en l'oscil·lació té lloc en desintegracions de mesons neutres, quan els estats propis de l'hamiltonià no són al mateix temps propis de CP. Es pot mesurar a traves d'asimetries en desintegracions semilèptòniques, tals com

$$a_{sl} = \frac{\Gamma\left(\bar{D}^0 \to \ell^+ \nu X\right) - \Gamma\left(D^0 \to \ell^- \bar{\nu} X\right)}{\Gamma\left(\bar{D}^0 \to \ell^+ \nu X\right) + \Gamma\left(D^0 \to \ell^- \bar{\nu} X\right)} = \frac{1 - |q/p|^4}{1 + |q/p|^4}. \tag{10}$$

- La violació de CP en la interferència entre desintegracions amb i sense oscil·lació té lloc en desintegracions a estats finals comuns a $|D^0\rangle$ i $|\bar{D}^0\rangle$. Es pot mesurar a través de la comparació de desintegracions d'un estat neutre que evoluciona amb el temps, creat ja sigui com a D^0 o $\bar{D}^0$, a estats finals propis de CP.

Prediccions del model estàndard d'oscil·lacions i violació de CP

Al model estàndard, les oscil·lacions tenen el seu origen en contribucions a curtes i a llargues distàncies. Les contribucions a curtes distàncies vénen de diagrames de caixa amb quarks i bosons $W^{\pm}$. El model estàndard prediu efectes d'oscil·lació petits, perquè els quarks b tenen una supressió CKM en aquestos diagrames, i els quarks d i s hi tenen una supressió GIM [10]. La contribució principal a curtes distàncies és al paràmetre x. Les contribucions a llargues distàncies vénen de diagrames amb bucles amb estats hadrònics intermedis. S'espera que aquestes contribucions siguin dominants, però petites, tanmateix. Com que aquestes contribucions no són pertorbatives, són difícils d'estimar, però hi ha prediccions [11,12] que fiten x i y al rang $[0.001, 0.01]$, amb $|x| < |y|$.

Si hi hagués efectes de nova física, es podrien trobar en contribucions de noves partícules als bucles dels diagrames. Per exemple, si es trobés $|x|$ molt més gran que $|y|$, això podria indicar efectes de nova física.

El model estàndard prediu que la violació de CP al sector dels mesons D és de l'ordre de $\sim 10^{-3}$. Si es trobés violació de CP amb la sensibilitat de què es disposa actualment, ($\sim 10^{-2}$), això també seria un indici de nova física [12].

Cerques d'oscil·lacions i violació de CP

El fenomen de les oscil·lacions s'ha estudiat en diverses desintegracions hadròniques suprimides: en la dependència temporal dels esdeveniments amb càrrega de signe oposat en $D^0 \to K^+\pi^-$ [2,13,3], en la raó de temps de vida mesurats en $D^0 \to K^+K^-$ i $D^0 \to \pi^+\pi^-$ respecte a esdeveniments $D^0 \to K^-\pi^+$ [5,4,6], i en una anàlisi d'amplada de desintegració dependent del temps en esdeveniments $D^0 \to K^+\pi^-\pi^0$ [7]. Les col·laboracions BaBar i Belle també han estudiat el fenomen de les oscil·lacions en desintegracions semileptòniques [14,15,16], així com també en una anàlisi d'amplada de desintegració dependent del temps en desintegracions $D^0 \to K_s\pi^+\pi^-$ [8,9].

El gust dels mesons D s'etiqueta a l'instant de producció a través de les desintegracions $D^{\star +} \to D^0\pi_s^+$ i la seva conjugada, on la càrrega del pió de baix moment $\pi_s^{\pm}$ etiqueta el gust dels mesons D produïts.

La violació de CP s'ha estudiat en desintegracions simplement suprimides per Cabibbo en estats finals de CP parell $D^0 \to \pi^+\pi^-$ i $D^0 \to K^+K^-$ [17,18], i $D^0 \to \pi^+\pi^-\pi^0$ [19,20] i $D^0 \to K^+K^-\pi^0$

[19]. El model estàndard prediu que la violació de CP en aquests modes de desintegració és $\sim 10^{-4} - 10^{-5}$, per la qual cosa, si s'hi trobés evidència d'aquesta violació seria un senyal de nova física més enllà del model estàndard. [12]. La violació de CP també s'ha estudiat en desintegracions $D^0 \to K^+\pi^-\pi^0$ [7, 21] i $D^0 \to K^+K^-\pi^+\pi^-$.

Oscil·lacions en l'anàlisi de Dalitz dependent del temps en desintegracions $D^0 \to K_s h^+ h^-$ $(h = \pi, K)$

L'anàlisi que es presenta en aquest document està dedicada a la mesura dels paràmetres d'oscil·lació x i y, definits a (3) a través d'un estudi de l'espai de fases dependent del temps en desintegracions $D^0 \to K_s h^+ h^-$ $(h = \pi, K)$.

El quadrat del mòdul de l'amplada expressada a l'equació (5) és proporcional a la funció de distribució de probabilitat (PDF) del temps de vida del $\tilde{D}^0$, que depèn del punt en l'espai de fases i el temps de vida del $\tilde{D}^0$,

$$\left|\langle f|\mathcal{H}|\tilde{D}^0(t)\rangle\right|^2 = \left|\tilde{A}_f\right|^2 e^{-\Gamma t}\left|\frac{1+\chi^{\pm 1}}{2}h_1(t) + \frac{1-\chi^{\pm 1}}{2}h_2(t)\right|^2 \tag{11}$$

$$= \left|\tilde{A}_f\right|^2 e^{-\Gamma t}\left[\frac{1+|\chi|^{\pm 2}}{2}\cosh(y\Gamma t) + \frac{1-|\chi|^{\pm 2}}{2}\cos(x\Gamma t) - \mathrm{Re}\left(\chi^{\pm 1}\right)\sinh(y\Gamma t) + \mathrm{Im}\left(\chi^{\pm 1}\right)\sin(x\Gamma t)\right], \tag{12}$$

on els signes $\pm$ als exponents de χ són $+1$ per l'estat D^0 i -1 per l'estat $\bar{D}^0$.

Com en la majoria de cerques d'oscil·lació en mesons D neutres, se selecciona una mostra pura d'esdeveniments de senyal a partir del signe de la càrrega del pió de baix moment en desintegracions $D^{\star\pm} \to \tilde{D}^0\pi^\pm$, on un $\tilde{D}^0$ és un D^0 si aquest pió té càrrega positiva i un $\bar{D}^0$ si la té negativa. S'estudien els mesons $\tilde{D}^0$ als canals de desintegració $\tilde{D}^0 \to K_s\pi^+\pi^-$ i $\tilde{D}^0 \to K_s K^+K^-$, on el K_s es reconstrueix al canal $K_s \to \pi^+\pi^-$.

És molt important adonar-se que l'expressió (11) mostra que els termes que descriuen el temps de vida del $\tilde{D}^0$ no són independents d'aquells que en descriuen l'espai de fases i, per aquest motiu, la sensibilitat als paràmetres d'oscil·lació es perdria en un ajust en què s'haguessin integrat el temps de vida o l'espai de fases. Per tant, aquesta anàlisi pretén obtenir els paràmetres d'oscil·lació x i y en un ajust combinat a l'espai de fases $\tilde{A}_f$ i la distribució de temps de vida del $\tilde{D}^0$ en una mostra de mesons $\tilde{D}^0$ amb el gust etiquetat.

Un altre punt clau d'aquesta anàlisi és el fet que la regió cinemàticament permesa de l'espai de fases pels canals de desintegració que s'han considerat és la mateixa per ambdós mesons D^0 i $\bar{D}^0$. Sense aquesta propietat, seria impossible eliminar una fase forta relativa addicional δ entre les amplades de desintegració del D^0 i $\bar{D}^0$ al mateix estat final. Altres cerques d'oscil·lacions són sensibles als paràmetres x' and y', relacionats amb els paràmetres d'oscil·lació a partir de

$$\begin{pmatrix} x' \\ y' \end{pmatrix} = \begin{pmatrix} \cos\delta & \sin\delta \\ -\sin\delta & \cos\delta \end{pmatrix}\begin{pmatrix} x \\ y \end{pmatrix}. \tag{13}$$

L'extracció directa dels paràmetres d'oscil·lació x i y, sense ambigüitats de fase forta, només és possible amb estats finals tals com $K_s\pi^+\pi^-$, $K_sK^+K^-$, $\pi^+\pi^-\pi^0$, però no $K^+\pi^-\pi^0$, per exemple.

L'expressió (11) es fa servir per estudiar la dependència en el temps de vida del $\tilde{D}^0$ com a funció de la posició de l'esdeveniment al gràfic de Dalitz. Això dóna sensibilitat als paràmetres d'oscil·lació x i y directament, si s'assumeix conservació de CP en la desintegració. Per aconseguir sensibilitat a aquestos paràmetres, es necessita un model fenomenològic acurat de la variació de l'amplada sobre el gràfic de Dalitz.

L'escala de temps dels efectes d'oscil·lació en mesons D neutres és dos ordres de magnitud més llarga que el temps de vida mitjana del propi mesó. En altres paraules, aquesta partícula es desintegra més ràpidament que no pas té temps d'oscil·lar. Per aquest motiu, és necessari seleccionar els esdeveniments de manera que la puresa de la mostra sigui tan alta com sigui possible, tot i mantenint, quan es pugui, una eficiència elevada d'esdeveniments de senyal.

Els esdeveniments que passen els criteris de selecció s'han caracteritzat, és a dir, s'han trobat funcions que descriuen les distribucions de les variables rellevants en aquestos esdeveniments. Aquestes variables són m_D, definida com la massa del $\tilde{D}^0$, reconstruïda a partir dels 4-moments de totes les seves filles, Δm, definida com la diferència entre les masses reconstruïdes del $D^{\star\pm}$ i el $\tilde{D}^0$, el temps de vida reconstruït t del $\tilde{D}^0$, obtingut a partir de la seva distància de vol, i l'error σ_t en la mesura del temps de vida del $\tilde{D}^0$. S'han introduït diverses categories de senyal i fons per simplificar la descripció dels diferents components que contribueixen als esdeveniments de senyal i fons. A més, les variables que identifiquen un esdeveniment a l'espai de fases, normalment anomenades variables de Dalitz, s'introdueixen a §2, així com el model de desintegració que les descriu.

Es considera que un mesó D és verdader si les quatre partícules carregades del canal de senyal s'han reconstruït i vinculat correctament a les seves corresponents partícules generades. Un pió de baix moment es considera verdader si la seva mare és un $D^{\star}$. Les categories s'han definit d'acord amb aquestes consideracions, i es mostren a la taula 1.

Categoria	D	$\pi_s^{\pm}$	Descripció	Comportament picat
1	verdader	verdader	Senyal	m_D i Δm
2	verdader	fals		m_D
3	fals	verdader		Δm
4	fals	fals	Fons combinatori	No n'hi ha
5			$D^0 \to 4\pi/2\pi 2K$	m_D i Δm
6			$D^0 \to K_S^0 K_S^0$	m_D i Δm

Table 1: Categories de senyal i fons.

Per cada categoria, les variables genèriques s'han caracteritzat separadament. La figura 1 mostra les distribucions d'm_D i Δm per esdeveniments de dades a BaBar.

A l'anàlisi de BaBar s'ha fet servir el model de desintegració d'una publicació de BaBar [23]

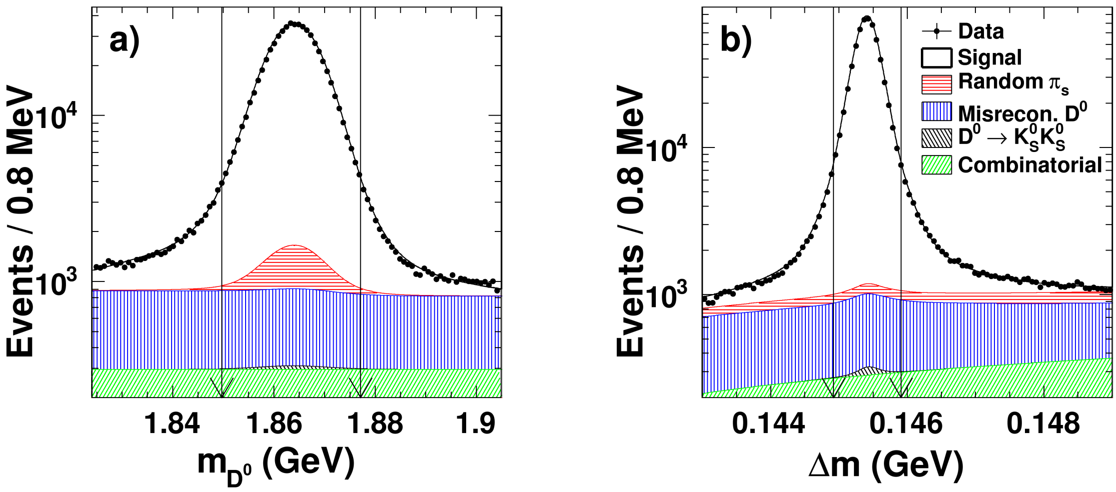

Figure 1: Distribucions d'm_D i Δm per esdeveniments de dades de $K_s\pi^+\pi^-$.

sobre la mesura de l'angle γ de la matriu CKM. En aquest model, l'amplada s'expressa com

$$\mathcal{M}_r = Z_l(m_{ab}^2, m_{ac}^2) B_l^{D^0 c}(p, p_r) B_l^{ab}(q, q_r) \Delta_r(m_{ab}), \tag{14}$$

$$\mathcal{M} = \sum_r a_r e^{i\phi_r} \mathcal{M}_r, \tag{15}$$

on Z_λ descriu la distribució angular dels productes de desintegració, $B_{\lambda,r}$ són els factors de penetració de Blatt-Weisskopf [24], i G_r és un propagador que descriu la ressonància. La majoria de propagadors són funcions de Breit-Wigner relativistes, excepte la funció de Gounaris-Sakurai [25] que s'ha fet servir per per descriure el component ρ^0 i una combinació de les formulacions de la matriu K i LASS [26] per descriure correctament les ones S de $\pi\pi$ i $K\pi$, amb una forta superposició. La figura 2 mostra els gràfics de Dalitz d'esdeveniments de dades als canals $K_s\pi^+\pi^-$ i $K_sK^+K^-$.

Per extreure els paràmetres d'oscil·lació x i y s'ha fet un ajust de màxima versemblança. Aquest ajust s'ha fragmentat en tres passos per facilitar-ne la convergència i reduir el temps de computació, tant en dades reals com en esdeveniments Monte Carlo simulats.

El resultat de BaBar per x i y és

$$x = (0.16 \pm 0.23 \text{ (stat)} \pm 0.12 \text{ (exp)} \pm 0.08 \text{ (mod)}) \cdot 10^{-2}, \tag{16}$$

$$y = (0.57 \pm 0.20 \text{ (stat)} \pm 0.13 \text{ (exp)} \pm 0.07 \text{ (mod)}) \cdot 10^{-2}, \tag{17}$$

on la primera incertesa és estadística, la segona és la incertesa sistemàtica experimental, i la tercera és la incertesa sistemàtica associada al model de desintegració.

L'anàlisi que s'ha fet a BaBar és la primera mesura combinada amb esdeveniments $K_s\pi^+\pi^-$ i $K_sK^+K^-$, i la mesura més precisa dels paràmetres x i y que s'ha fet fins ara. Exclou la hipòtesi d'absència d'oscil·lacions amb una significança d'$1.9\,\sigma$, similar a la de Belle [9], que l'exclou amb

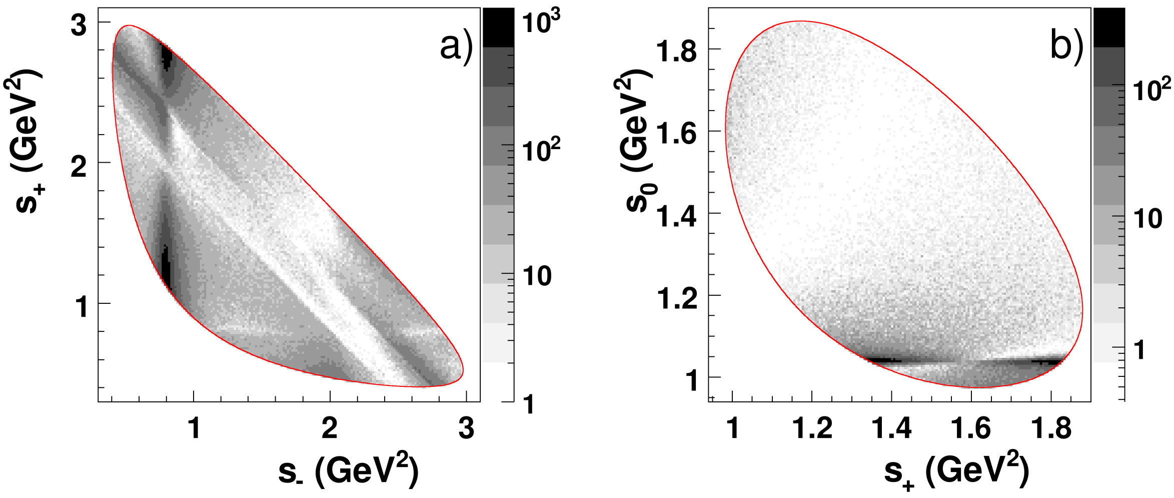

Figure 2: Gràfics de Dalitz dels modes $K_s\pi^+\pi^-$ i $K_sK^+K^-$ per esdeveniments de dades.

una significança de $2.2\,\sigma$,

$$x = (0.80 \pm 0.29 \ {}^{+0.09}_{-0.07} \ {}^{+0.10}_{-0.14}) \cdot 10^{-2}, \tag{18}$$

$$y = (0.33 \pm 0.24 \ {}^{+0.08}_{-0.12} \ {}^{+0.06}_{-0.08}) \cdot 10^{-2}. \tag{19}$$

L'anàlisi de Belle també conté una mesura de violació de CP,

$$\left|\frac{q}{p}\right| = (0.86 \ {}^{+0.30}_{-0.29} \ {}^{+0.06}_{-0.08} \pm 0.08) \cdot 10^{-2}, \tag{20}$$

$$\phi_f = (-14 \ {}^{+16}_{-18} \ {}^{+6}_{-3} \ {}^{+2}_{-4})^\circ. \tag{21}$$

El resultat de BaBar afavoreix un valor més petit per x que per y, cosa que fa que el valor central es desplaci cap a la predicció del model estàndard. Això es pot observar a la figura 3, que mostra els nivells de significança a les cinc primeres desviacions estàndard [22], obtingudes a partir de totes les mesures disponibles abans i després de l'última mesura de BaBar. En aquests gràfics, s'observa una millora significativa en el coneixement actual dels paràmetres d'oscil·lació.

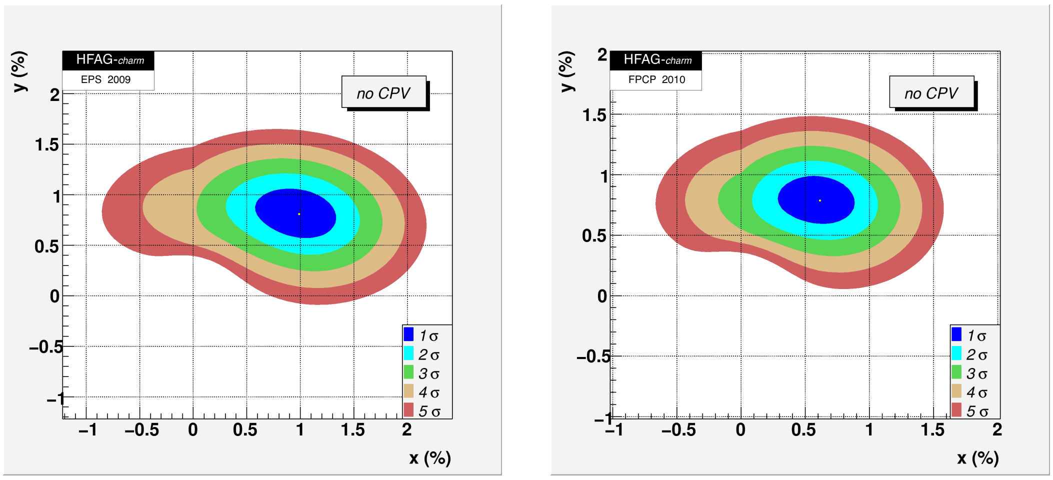

Figure 3: Mitjanes dels paràmetres x i y del Heavy Flavor Averaging Group, abans (esquerra) i després (dreta) de l'última mesura de BaBar.

Descripció del document

Els conceptes teòrics de les oscil·lacions i la violació de CP s'expliquen a §1. El model de desintegració que s'ha fet servir per descriure les amplades $\tilde{A}_f$ s'ha descrit a §2. Des de la vessant experimental, §3 descriu les diferents parts del detector BaBar. Els criteris de selecció dels esdeveniments es discuteixen a §4, i §5 discuteix la caracterització del senyal i el fons. L'estratègia de l'ajust s'explica a §6, així com els testos realitzats amb esdeveniments Monte Carlo simulats, incloent-hi components de senyal i fons. Finalment, a §7, s'hi expliquen les diferents fonts d'error sistemàtic, i les regions de nivell de confiança i significança dels resultats de la mesura d'oscil·lació s'avaluen a §8.

Summary

Mixing is a process in which an electrically-neutral meson is produced as a particle but decays as its anti-particle partner.

Mixing and CP violation in the neutral D meson sector were first discussed in the nineteen seventies [1]. However, it has not been until the last years, when sufficiently large and well identified samples of neutral D meson decays have become available, that clear evidence of mixing has been seen in several kinds of time-dependent measurements. CP violation has not yet been observed, and upper limits are currently at about the 0.01 level.

In the past three years, both BaBar and Belle collaborations have established evidence of mixing in neutral D mesons, which has also been confirmed by the CDF collaboration.

All the searches for mixing and CP violation in the neutral D meson sector up to date are presented in §1.5. Of special interest is the first evidence of neutral D meson mixing in wrong-sign $D^0 \to K^+\pi^-$ decays [2], with a significance at the level of $3.9\,\sigma$. This observation has been confirmed in a similar measurement by the CDF collaboration [3].

The Belle collaboration has reported neutral D meson mixing evidence, with a significance at the level of $3.2\,\sigma$, in the observation of lifetime differences in decays to CP-even final states $D^0 \to K^+K^-$ and $D^0 \to \pi^+\pi^-$, compared with decays to the flavor eigenstate $D^0 \to K^-\pi^+$ [4]. This observation has been confirmed in a tagged analysis by the BaBar collaboration [5], and also in a combined set of disjoint tagged and untagged events [6], which shows the largest significant evidence up to date of D meson mixing, at the level of $4.1\,\sigma$. The BaBar collaboration also reports further evidence for mixing in $D^0 \to K^+\pi^-\pi^0$ decays [7].

This document presents a search for mixing in $D^0 \to K_s\pi^+\pi^-$ and $D^0 \to K_sK^+K^-$ decays and their CP conjugates. This analysis follows the method suggested in [8]. An earlier result from the Belle collaboration [9], only in $K_s\pi^+\pi^-$ events, is strongly suggestive of mixing, and reports an observation with a significance at the level of $2.2\,\sigma$.

Introduction to mixing of neutral D mesons

For a system of a pair of neutral D mesons, different neutral states are relevant to the discussion of different processes:

- The two flavor eigenstates, $|D^0\rangle$ and $|\bar{D}^0\rangle$, have a definite quark content and are those relevant to particle production and decay processes. They are mixed with each other as they propagate through space and time, since they are not Hamiltonian eigenstates.

- The two Hamiltonian eigenstates, $|D_1\rangle$ and $|D_2\rangle$, have definite mass and lifetime, and they propagate through space and time in a definite way.

- If CP were preserved, the Hamiltonian eigenstates would also be CP eigenstates, namely $|D_+\rangle$ and $|D_-\rangle$.

For the system of the two neutral kaons, it is relevant to observe that their mass eigenstates have different average lifetimes, although similar masses, so it is convenient to define their states as K_l and K_s for the long-lived and short-lived states, respectively. However, for neutral D mesons, the mixing rate is slower than the decay rate, so the flavor eigenstates are the most convenient basis for them.

Since almost all the expressions and discussions valid for the D^0 are also valid for the $\bar{D}^0$, and with the purpose of simplifying the notation, $\tilde{D}^0$ is used throughout this document to refer to both the D^0 and the $\bar{D}^0$ flavor eigenstates of the D meson. Whenever an expression is different for the D^0 and the $\bar{D}^0$, it is written explicitly for both of them.

An arbitrary linear combination of the neutral D flavor eigenstates, $a|D^0\rangle + b|\bar{D}^0\rangle$, evolves in time according to the time-dependent Schrödinger equation

$$i\frac{d}{dt}\begin{pmatrix} a \\ b \end{pmatrix} = \mathcal{H}\begin{pmatrix} a \\ b \end{pmatrix} \equiv \left(M - \frac{i}{2}\Gamma\right)\begin{pmatrix} a \\ b \end{pmatrix}, \tag{22}$$

where M and Γ are 2×2 Hermitian matrices, but the effective Hamiltonian $\mathcal{H}$ is not. $|D_1\rangle$ and $|D_2\rangle$ are the eigenstates of $\mathcal{H}$, with eigenvalues $\left(m_1 + \frac{i}{2}\Gamma_1\right)$ and $\left(m_2 + \frac{i}{2}\Gamma_2\right)$, respectively.

Defining

$$\Gamma = \frac{\Gamma_1 + \Gamma_2}{2}, \qquad x = \frac{m_1 - m_2}{\Gamma}, \qquad y = \frac{\Gamma_1 - \Gamma_2}{2\Gamma}, \tag{23}$$

the time evolution of the Hamiltonian eigenstates can be written as

$$|D_{1,2}(t)\rangle = e^{-\frac{\Gamma t}{2}} h_{1,2}(t)\,|D_{1,2}\rangle\,, \tag{24}$$

with

$$h_{1,2}(t) = e^{\mp\frac{(y+ix)\Gamma t}{2}}. \tag{25}$$

The Hamiltonian eigenstates are expressed in terms of the flavor eigenstates as

$$|D_{1,2}\rangle = p\left|D^0\right\rangle \pm q\left|\bar{D}^0\right\rangle, \tag{26}$$

where the p and q parameters can be chosen to verify $|p|^2 + |q|^2 = 1$.

The amplitudes of an initial $|D^0\rangle$ or $|\bar{D}^0\rangle$ flavor eigenstate at production time into a final state $\langle f|$ are expressed as

$$\begin{aligned} A_f &= \langle f|\mathcal{H}|D^0\rangle, \\ \bar{A}_f &= \langle f|\mathcal{H}|\bar{D}^0\rangle, \\ \chi &= \frac{q}{p}\frac{\bar{A}_f}{A_f}, \end{aligned} \tag{27}$$

so the amplitude of the flavor eigenstates evolves in time as

$$\langle f|\mathcal{H}|\tilde{D}^0(t)\rangle = e^{-\frac{\Gamma t}{2}}\tilde{A}_f\left(\frac{1+\chi^{\pm 1}}{2}h_1(t) + \frac{1-\chi^{\pm 1}}{2}h_2(t)\right), \tag{28}$$

where ± 1 in the exponent of χ is $+1$ for the $|D^0\rangle$ and -1 for the $|\bar{D}^0\rangle$ states, and the notation $\tilde{A}_f$ is used to refer to both the A_f and $\bar{A}_f$ amplitudes, similarly to the $\tilde{D}^0$ notation for both D^0 and $\bar{D}^0$ states.

The previous mathematical expressions are shown here without proof with the purpose of presenting an introduction and overview of the analysis. The derivation of these expressions, as well as the definition of the mixing parameters x and y in terms of the Hamiltonian eigenvalues, is described in detail in §1.1.

From a strict theoretical point of view, the flavor eigenstates $\tilde{D}^0$ do not have a well definite lifetime, since expression (28) shows that they evolve in time as an entanglement of both D^0 and $\bar{D}^0$ states. However, it is very common to refer to the $\tilde{D}^0$ lifetime as the time difference between the production and decay of a neutral D meson state, although the flavor at production may be different from that at decay.

Introduction to CP violation in neutral D meson decays

The possible manifestations of CP violation can be classified in a model-independent way:

- CP violation in the decay occurs in decays of both charged and neutral mesons. It occurs when the amplitude of a decay is different from that of the decay of its CP conjugate. It can be measured in decays of particles into final states that are not CP eigenstates, such as

$$a_f = \frac{\Gamma\left(B^+ \to f\right) - \Gamma\left(B^- \to \bar{f}\right)}{\Gamma\left(B^+ \to f\right) + \Gamma\left(B^- \to \bar{f}\right)} = \frac{1 - \left|\bar{A}_{\bar{f}}/A_f\right|^2}{1 + \left|\bar{A}_{\bar{f}}/A_f\right|^2}. \tag{29}$$

- CP violation in the mixing occurs in neutral meson decays, when the Hamiltonian eigenstates cannot be chosen to be CP eigenstates as well. It can be measured through asymmetries in semileptonic decays, such as

$$a_{sl} = \frac{\Gamma\left(\bar{D}^0 \to \ell^+\nu X\right) - \Gamma\left(D^0 \to \ell^-\bar{\nu}X\right)}{\Gamma\left(\bar{D}^0 \to \ell^+\nu X\right) + \Gamma\left(D^0 \to \ell^-\bar{\nu}X\right)} = \frac{1 - |q/p|^4}{1 + |q/p|^4}. \tag{30}$$

- CP violation in the interference between decays with and without mixing occurs in decays into final states that are common to $|D^0\rangle$ and $|\bar{D}^0\rangle$. It can be measured through the comparison of decays of a neutral state that evolves in time, produced either as a D^0 or as a $\bar{D}^0$, into final CP eigenstates.

Standard model predictions of D meson mixing and CPV

Mixing in the standard model originates from short and long distance contributions. Short distance contributions come from box diagrams with quarks and $W^{\pm}$ bosons. The standard model predicts small mixing effects because b quarks are CKM suppressed and s and d quarks are GIM suppressed [10]. The main short distance contribution is to the x mixing parameter. Long distance contributions come from loop diagrams with hadronic intermediate states. These contributions are expected to be dominant, but still small. Since they are not perturbative, they are difficult to estimate, but predictions exist [11,12] that bound x and y in the range $[0.001, 0.01]$, with $|x| < |y|$.

New physics could arise through new particles in loops. For example, if $|x|$ was found to be much larger than $|y|$, this could be a hint of new physics.

The standard model predicts CPV in the D sector to be $\sim 10^{-3}$. If CPV was to be found with the current sensitivity ($\sim 10^{-2}$), this would also be a hint of new physics [12].

Mixing and CP violation searches

Mixing has been studied using a variety of suppressed hadronic decays: in the time dependence of the wrong sign events in $D^0 \to K^+\pi^-$ [2,13,3], in the ratio of lifetimes of $D^0 \to K^+K^-$ and $D^0 \to \pi^+\pi^-$ events with respect to $D^0 \to K^-\pi^+$ events [5,4,6], and in a D^0 time-dependent amplitude analysis of $D^0 \to K^+\pi^-\pi^0$ events [7]. Mixing has also been studied in semileptonic events [14,15,16] by the BaBar and Belle collaborations, and in a time-dependent amplitude analysis of $K_s\pi^+\pi^-$ events [8,9].

D mesons are tagged at production by means of $D^{\star+} \to D^0\pi_s^+$ and its conjugate, where the charge of the low momentum pion $\pi_s^{\pm}$ tags the flavor of the produced D meson.

CP violation has been studied in single Cabibbo-suppressed decays with CP even final states $D^0 \to \pi^+\pi^-$ and $D^0 \to K^+K^-$ [17,18] and $D^0 \to \pi^+\pi^-\pi^0$ [19,20] and $D^0 \to K^+K^-\pi^0$ [19]. The standard model predicts CP violation in these modes to be $\sim 10^{-4} - 10^{-5}$, so evidence of CP violation in them would be a sign of physics beyond the standard model [12]. CP violation has also been studied in $D^0 \to K^+\pi^-\pi^0$ events [7,21] and in $D^0 \to K^+K^-\pi^+\pi^-$ decays.

Mixing in time-dependent Dalitz plot analyses of $D^0 \to K_S^0 h^+h^-$ $(h = \pi, K)$ events

The analysis presented in this document is devoted to measure the mixing parameters x and y defined in (23) by means of a study of the $\tilde{D}^0$ lifetime dependence on the region of the phase space in decays $D^0 \to K_S^0 h^+h^-$ $(h = \pi, K)$.

The squared amplitude expressed in equation (25) is proportional to the $\tilde{D}^0$ lifetime probability distribution function (PDF), which depends on the point in the phase space and the $\tilde{D}^0$ lifetime,

$$\left|\langle f|\mathcal{H}|\tilde{D}^0(t)\rangle\right|^2 = \left|\tilde{A}_f\right|^2 e^{-\Gamma t}\left|\frac{1+\chi^{\pm 1}}{2}h_1(t) + \frac{1-\chi^{\pm 1}}{2}h_2(t)\right|^2 \tag{31}$$

$$\begin{aligned} &= \left|\tilde{A}_f\right|^2 e^{-\Gamma t}\left[\frac{1+|\chi|^{\pm 2}}{2}\cosh(y\Gamma t) + \frac{1-|\chi|^{\pm 2}}{2}\cos(x\Gamma t)\right. \\ &\qquad \left. - \operatorname{Re}\left(\chi^{\pm 1}\right)\sinh(y\Gamma t) + \operatorname{Im}\left(\chi^{\pm 1}\right)\sin(x\Gamma t)\right], \end{aligned} \tag{32}$$

where the $\pm$ signs in the exponents of χ are $+1$ for D^0 and -1 for $\bar{D}^0$ states.

As in most of the neutral D meson mixing searches, a pure sample of signal events is selected by tagging the $\tilde{D}^0$ flavor at production by means of the sign of the charge of the slow pion in $D^{\star\pm} \to \tilde{D}^0\pi^\pm$ decays, where $\tilde{D}^0$ is a D^0 if the slow pion has positive charge, and a $\bar{D}^0$ otherwise. The $\tilde{D}^0$ mesons are studied in the decay channels $\tilde{D}^0 \to K_s\pi^+\pi^-$ and $\tilde{D}^0 \to K_sK^+K^-$, where the K_s has been reconstructed in the $K_s \to \pi^+\pi^-$ channel.

It is very important to realize that expression (31) shows that the terms that describe the $\tilde{D}^0$ decay time are not independent from those that describe the phase space and, for this reason, sensitivity to the mixing parameters is lost in a time integrated or a phase space integrated fit. Therefore, this analysis is devoted to obtain the mixing parameters x and y in a combined fit to the phase space $\tilde{A}_f$ and $\tilde{D}^0$ lifetime distribution of these flavor tagged $\tilde{D}^0$ mesons.

Another key point of this analysis is the fact that the kinematically allowed region of the phase space for the decay channels that have been considered is the same for both the D^0 and $\bar{D}^0$ mesons. Without this property, it would be impossible to get rid of an additional relative strong phase δ between the D^0 and $\bar{D}^0$ decay amplitudes to the same final state. Other searches for mixing are sensitive to the parameters x' and y', related to the mixing parameters as

$$\begin{pmatrix} x' \\ y' \end{pmatrix} = \begin{pmatrix} \cos\delta & \sin\delta \\ -\sin\delta & \cos\delta \end{pmatrix} \begin{pmatrix} x \\ y \end{pmatrix}. \tag{33}$$

The direct extraction of the mixing parameters x and y, with no strong phase ambiguities, is only possible in final states such as $K_s\pi^+\pi^-$, $K_sK^+K^-$, $\pi^+\pi^-\pi^0$, but not $K^+\pi^-\pi^0$, for example.

Expression (31) is used to study the $\tilde{D}^0$ proper lifetime dependence as a function of the position in the Dalitz plot. This provides sensitivity to the mixing parameters x and y directly, if CP conservation in the decay is assumed. An accurate phenomenological decay model for the variation of the amplitude over the Dalitz plot is needed in order to have sensitivity to x and y.

The time scale of mixing effects in the neutral D meson is two orders of magnitude larger than the D meson decay time itself. In other words, it decays much faster than it has time to undergo mixing. For this reason, events must be selected in such a way that the purity of the sample is as high as possible, also keeping, when it is possible, a large efficiency for signal events.

The events that have passed the selection criteria are characterized, i.e., functions have been found to describe the distributions of the relevant variables in the events. These variables have

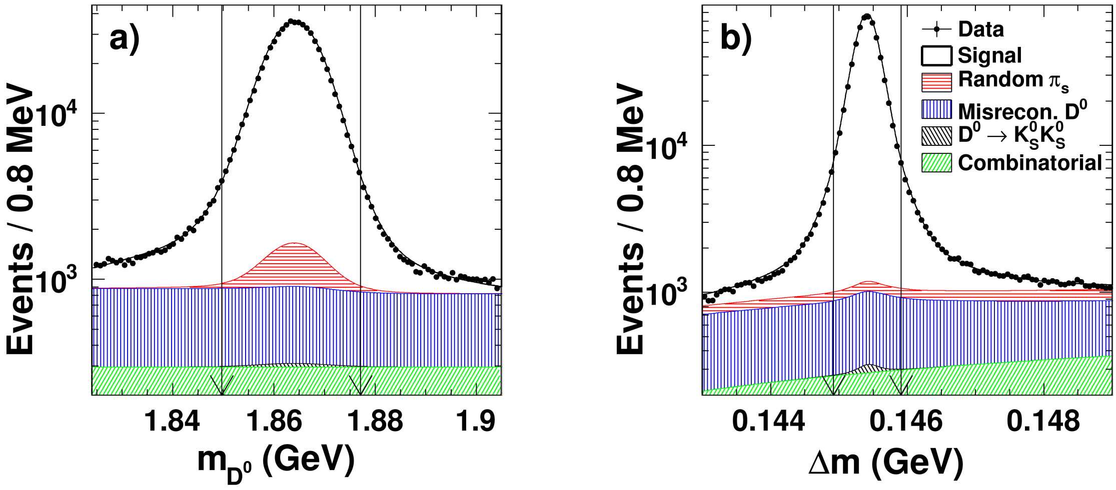

Figure 4: $K_s\pi^+\pi^-$ m_D and Δm distributions for data events.

been chosen to be m_D, defined as the $\tilde{D}^0$ mass, reconstructed from the 4-momenta of all its daughters, Δm, defined as the difference between the reconstructed $D^{\star\pm}$ and $\tilde{D}^0$ masses, the reconstructed $\tilde{D}^0$ lifetime t, obtained from its flight length, and the $\tilde{D}^0$ lifetime error σ_t. Several signal and background categories are introduced in order to simplify the description of the different components that contribute to the signal and background events. Additionally, the variables that identify an event in the phase space, commonly called Dalitz variables, are introduced in §2, as well as the decay model that describes them.

A D meson is considered to be a true one if the four charged particles of the signal channel have been reconstructed and matched correctly. A low momentum pion is considered to be true if its mother is a $D^\star$. The categories have been defined according to these definitions, and are shown in table 2.

Category	D	$\pi_s^\pm$	Description	Peaking behavior
1	true	true	Signal	m_D and Δm
2	true	false		m_D
3	false	true		Δm
4	false	false	Combinatoric background	Not peaking
5			$D^0 \to 4\pi/2\pi 2K$	m_D and Δm
6			$D^0 \to K_S^0 K_S^0$	m_D and Δm

Table 2: Signal and background categories.

For each category, the generic variables have been characterized separately. Figure 4 shows the BaBar distributions of m_D and Δm for data events.

In the analysis done by BaBar, the amplitude model is taken from a published BaBar paper on

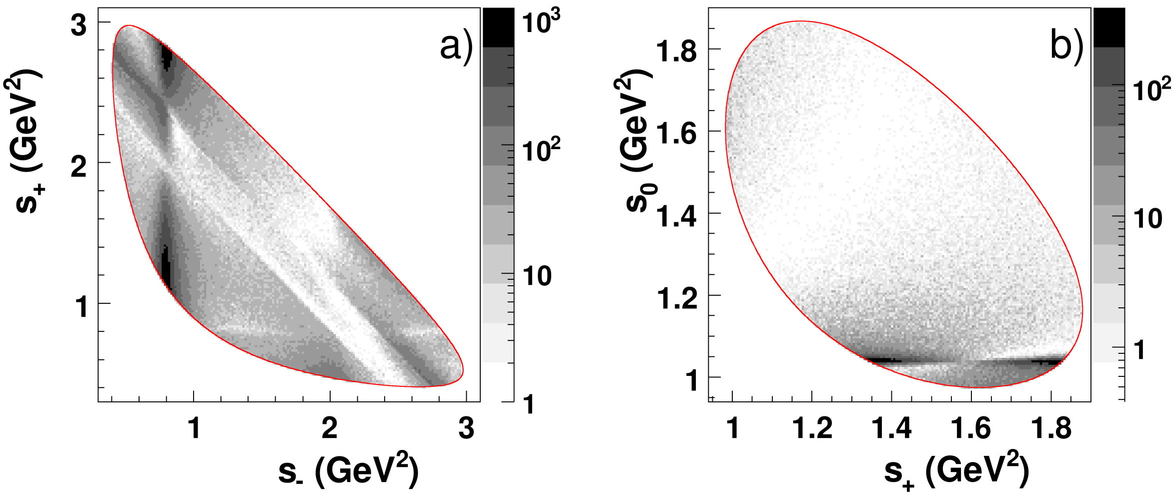

Figure 5: $K_s\pi^+\pi^-$ and $K_sK^+K^-$ Dalitz plots for data events.

the measurement of the CKM angle γ [23]. In this model, the amplitude is expressed as

$$\mathcal{M}_r = Z_l(m_{ab}^2, m_{ac}^2)B_l^{D^0c}(p, p_r)B_l^{ab}(q, q_r)\Delta_r(m_{ab}), \tag{34}$$

$$\mathcal{M} = \sum_r a_r e^{i\phi_r}\mathcal{M}_r, \tag{35}$$

where Z_λ describe the angular distribution of the decay products, $B_{\lambda,r}$ are the Blatt-Weisskopf penetration factors, and Δ_r is a propagator that describes the resonance. The most of the propagators are relativistic Breit-Wigner functions, except for a Gounaris-Sakurai function to describe the ρ^0 component and a combination of K-matrix and LASS formulations for a better description of overlapping $\pi\pi$ and $K\pi$ S-waves. Figure 5 shows the $K_s\pi^+\pi^-$ and $K_sK^+K^-$ Dalitz plots for data events.

An extended maximum likelihood fit is done to extract the mixing parameters x and y. This fit is split in three steps to facilitate fit convergence and reduce computing time, and is done to both real data and simulated Monte Carlo events.

The BaBar result for x and y is

$$x = (0.16 \pm 0.23 \text{ (stat)} \pm 0.12 \text{ (exp)} \pm 0.08 \text{ (mod)}) \cdot 10^{-2}, \tag{36}$$

$$y = (0.57 \pm 0.20 \text{ (stat)} \pm 0.13 \text{ (exp)} \pm 0.07 \text{ (mod)}) \cdot 10^{-2}, \tag{37}$$

where the first uncertainty is statistical, the second is experimental systematic, and the third is model related systematic.

The analysis done at BaBar is the first combined analysis of $K_s\pi^+\pi^-$ and $K_sK^+K^-$ events, and provides the most precise direct measurement of x and y up to date. It excludes the no-mixing

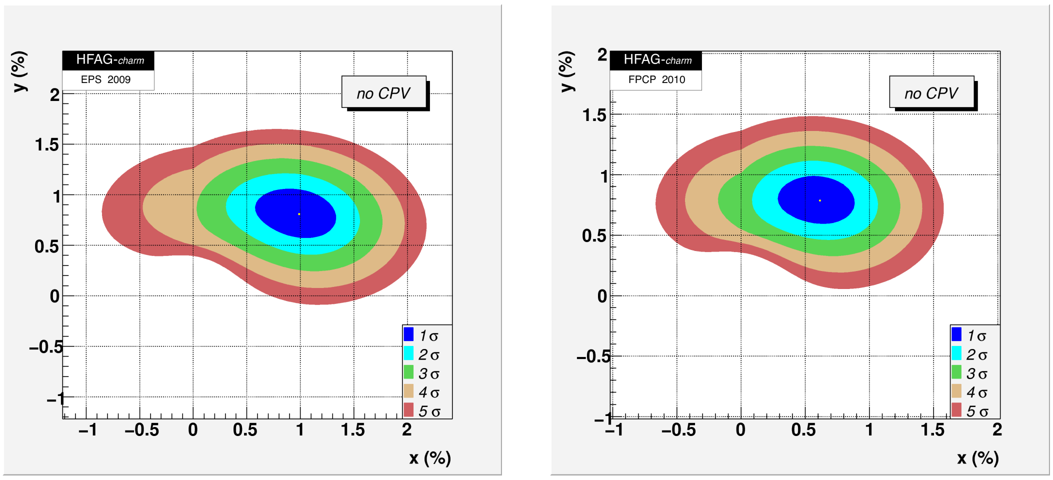

Figure 6: Heavy Flavor Averaging Group averages for x and y, before (left) and after (right) the last measurement from BaBar.

hypothesis with a significance of $1.9\,\sigma$, similarly to Belle [9], which excludes it at the level of $2.2\,\sigma$,

$$x = (0.80 \pm 0.29\ {}^{+0.09}_{-0.07}\ {}^{+0.10}_{-0.14}) \cdot 10^{-2}, \tag{38}$$

$$y = (0.33 \pm 0.24\ {}^{+0.08}_{-0.12}\ {}^{+0.06}_{-0.08}) \cdot 10^{-2}. \tag{39}$$

The analysis from Belle also fits for CP violation, yielding

$$\left|\frac{q}{p}\right| = (0.86\ {}^{+0.30}_{-0.29}\ {}^{+0.06}_{-0.08} \pm 0.08) \cdot 10^{-2}, \tag{40}$$

$$\phi_f = (-14\ {}^{+16}_{-18}\ {}^{+6}_{-3}\ {}^{+2}_{-4})^{\circ}. \tag{41}$$

The result from the BaBar collaboration favors a lower value for x than for y, which makes the central value move toward the standard model prediction. This can be seen in figure 6, which shows the Heavy Flavor Averaging Group significance levels at the first five standard deviations [22], obtained from all the available measurements before and after the last measurement from BaBar. A significant improvement in the current knowledge of the mixing parameters is also observed in these plots.

Document overview

The theoretical background on mixing and CP violation is explained in §1. The decay model used to describe the $\tilde{A}_f$ amplitudes is described in §2. On the experimental side, §3 describes the different parts of the BaBar detector. The event selection criteria are discussed in §4, and §5 discusses the signal and background characterization. The fit strategy is explained in §6, along with the tests performed on Monte Carlo events, including signal and background components. Finally, in §7, the several sources of systematic uncertainties have been explained, and the confidence regions and significance of the mixing results are evaluated in §8.

Chapter 1

Theoretical background

This chapter describes the concepts of mixing and CP symmetry violation in neutral D mesons.

1.1 Mixing of neutral D mesons

This section describes the quantum mechanics of a system of two neutral D mesons. The content of this section is model independent and is also valid for pairs of other self-conjugate neutral particles, such as kaons or B mesons.

For a system of a pair of neutral D mesons, different neutral states are relevant to the discussion of different processes:

- The two flavor eigenstates, $|D^0\rangle$ and $|\bar{D}^0\rangle$, have a definite quark content and are those relevant to particle production and decay processes. They are mixed with each other as they propagate through space and time, since they are not Hamiltonian eigenstates. The quark composition of neutral mesons is defined, by convention, in such a way that the particle is the isospin partner of the positively charged meson, and the antiparticle that of the negatively charged one. With this convention, $D^0 = c\bar{u}$ and $\bar{D}^0 = \bar{c}u$.

- The two Hamiltonian eigenstates, $|D_1\rangle$ and $|D_2\rangle$, have definite mass and lifetime, and they propagate through space and time in a definite way.

- If CP were preserved, the Hamiltonian eigenstates would also be CP eigenstates, namely $|D_+\rangle$ and $|D_-\rangle$. However, since CP is known to be violated, these states can be different.

For the system of the two neutral kaons, it is relevant to observe that their mass (Hamiltonian) eigenstates have very different lifetimes, although very similar masses, so it is very convenient to define their states as K_l and K_s for the long-lived and short-lived states, respectively.

For neutral D mesons, the mixing rate is much slower than the decay rate, so the flavor eigenstates are the most convenient basis for the derivation that follows.

In the flavor basis, the eigenstates are

$$|D^0\rangle = \begin{pmatrix} 1 \\ 0 \end{pmatrix}, \qquad |\bar{D}^0\rangle = \begin{pmatrix} 0 \\ 1 \end{pmatrix}. \tag{1.1}$$

An arbitrary linear combination of the neutral D flavor eigenstates,

$$a|D^0\rangle + b|\bar{D}^0\rangle, \tag{1.2}$$

evolves in time according to the time-dependent Schrödinger equation

$$i\frac{d}{dt}\begin{pmatrix} a \\ b \end{pmatrix} = \mathcal{H}\begin{pmatrix} a \\ b \end{pmatrix} \equiv \left(M - \frac{i}{2}\Gamma\right)\begin{pmatrix} a \\ b \end{pmatrix}, \tag{1.3}$$

where M and Γ are 2×2 Hermitian matrices.

It is important to notice that $\mathcal{H}$ is not a Hermitian matrix. If it was, there would be no way that equation (1.3) could describe a decay, since hermiticity would impose unitarity of the state in time. Therefore, equation (1.3) is an effective way to handle the evolution of a neutral D meson state, and has the noticeable feature that it does not require the explicit inclusion of any term representing the final state $|f\rangle$. For this reason, the $\mathcal{H}$ term in (1.3) is usually called **effective Hamiltonian**. A formal derivation of the effective Hamiltonian based on the time evolution of a generic state (with final state terms), can be found in [27, 28].

CPT invariance guarantees that $\mathcal{H}_{11} = \mathcal{H}_{22}$ [29].

The eigenvalues and eigenstates of the effective Hamiltonian are given by

$$\begin{pmatrix} M_{11} - \frac{i}{2}\Gamma_{11} & M_{12} - \frac{i}{2}\Gamma_{12} \\ M_{12}^\star - \frac{i}{2}\Gamma_{12}^\star & M_{11} - \frac{i}{2}\Gamma_{11} \end{pmatrix}\begin{pmatrix} \alpha \\ \beta \end{pmatrix} = \lambda_{1,2}\begin{pmatrix} \alpha \\ \beta \end{pmatrix}, \tag{1.4}$$

where $\lambda_{1,2} \equiv m_{1,2} - \frac{i}{2}\Gamma_{1,2}$, thus $m_{1,2} = \mathrm{Re}\,(\lambda_{1,2})$ and $\Gamma_{1,2} = -2\mathrm{Im}\,(\lambda_{1,2})$. The results of equation (1.4) are

$$\lambda_{1,2} = \left(M_{11} - \frac{i}{2}\Gamma_{11}\right) \pm \sqrt{\left(M_{12} - \frac{i}{2}\Gamma_{12}\right)\left(M_{12}^\star - \frac{i}{2}\Gamma_{12}^\star\right)}. \tag{1.5}$$

Therefore, the components of the eigenvectors verify that

$$\frac{\beta}{\alpha} = \pm\sqrt{\frac{M_{12}^\star - \frac{i}{2}\Gamma_{12}^\star}{M_{12} - \frac{i}{2}\Gamma_{12}}} = \pm\frac{q}{p}, \tag{1.6}$$

which defines q/p and, with no loss of genericity, it can be chosen that $|p|^2 + |q|^2 = 1$, in such a way that the two eigenstates are

$$\begin{pmatrix} \alpha \\ \beta \end{pmatrix}_\pm = \begin{pmatrix} p \\ \pm q \end{pmatrix}. \tag{1.7}$$

The diagonalized Hamiltonian matrix D is, therefore, given by $D = P^{-1}\mathcal{H}P$, with

$$P = \begin{pmatrix} p & p \\ q & -q \end{pmatrix}, \qquad P^{-1} = \frac{1}{2}\begin{pmatrix} \frac{1}{p} & \frac{1}{q} \\ \frac{1}{p} & -\frac{1}{q} \end{pmatrix}, \qquad D = \begin{pmatrix} \lambda_1 & 0 \\ 0 & \lambda_2 \end{pmatrix}. \tag{1.8}$$

So if a state is $|\Psi\rangle_H$ in the Hamiltonian basis, in the flavor basis it is

$$|\Psi\rangle_F = P\,|\Psi\rangle_H\,. \tag{1.9}$$

So the Hamiltonian eigenstates are written in the flavor basis as

$$|D_{1,2}\rangle_F = \begin{pmatrix} p \\ \pm q \end{pmatrix}, \tag{1.10}$$

so

$$|D_{1,2}\rangle = p\left|D^0\right\rangle \pm q\left|\bar{D}^0\right\rangle, \tag{1.11}$$

and

$$\begin{aligned} \left|D^0\right\rangle &= \frac{1}{2p}\left(|D_1\rangle + |D_2\rangle\right), \\ \left|\bar{D}^0\right\rangle &= \frac{1}{2q}\left(|D_1\rangle - |D_2\rangle\right). \end{aligned} \tag{1.12}$$

These last expressions are valid for any basis.

The time evolution of the Hamiltonian eigenstates is

$$|D_{1,2}(t)\rangle = e^{-i\lambda_{1,2}t}\,|D_{1,2}\rangle\,. \tag{1.13}$$

It is convenient to define

$$M = \frac{m_1+m_2}{2}, \qquad \Gamma = \frac{\Gamma_1+\Gamma_2}{2}, \qquad x = \frac{m_1-m_2}{\Gamma}, \qquad y = \frac{\Gamma_1-\Gamma_2}{2\Gamma}, \tag{1.14}$$

so

$$e^{-i\lambda_{1,2}t} = e^{-iMt}e^{-\frac{\Gamma t}{2}}e^{\mp\frac{(y+ix)\Gamma t}{2}}. \tag{1.15}$$

The term e^{-iMt} factors out of the expression of $e^{-i\lambda_{1,2}}$. This term is a pure phase that is common to both Hamiltonian eigenstates, and it can be canceled since it does not have any relevance in the expressions that follow. Therefore, with no loss of genericity,

$$e^{-i\lambda_{1,2}t} = e^{-\frac{\Gamma t}{2}}e^{\mp\frac{(y+ix)\Gamma t}{2}} = e^{-\frac{\Gamma t}{2}}h_{1,2}(t), \tag{1.16}$$

with

$$h_{1,2}(t) = e^{\mp\frac{(y+ix)\Gamma t}{2}}. \tag{1.17}$$

Therefore, the time evolution of the Hamiltonian eigenstates, given by (1.13) gets simplified to

$$|D_{1,2}(t)\rangle = e^{-\frac{\Gamma t}{2}} h_{1,2}(t)\,|D_{1,2}\rangle\,. \tag{1.18}$$

With this last expression and equations (1.12), the time evolution of the flavor eigenstates is given by

$$\begin{aligned} \left|D^0(t)\right\rangle &= e^{-\frac{\Gamma t}{2}} \left(\frac{h_1(t)+h_2(t)}{2}\left|D^0\right\rangle + \frac{q}{p}\frac{h_1(t)-h_2(t)}{2}\left|\bar{D}^0\right\rangle\right), \\ \left|\bar{D}^0(t)\right\rangle &= e^{-\frac{\Gamma t}{2}} \left(\frac{h_1(t)+h_2(t)}{2}\left|\bar{D}^0\right\rangle + \frac{p}{q}\frac{h_1(t)-h_2(t)}{2}\left|D^0\right\rangle\right). \end{aligned} \tag{1.19}$$

Only if $x = y = 0$, then $h_1(t) = h_2(t) = 1$, and the $\tilde{D}^0$ states would not mix with each other. These two parameters x and y completely describe the phenomenon of mixing, and are commonly called **mixing parameters**.

The time dependent amplitudes of a $|D^0\rangle$ and a $|\bar{D}^0\rangle$ decaying to a final state $\langle f|$ are, respectively,

$$\begin{aligned} \langle f|\mathcal{H}|D^0(t)\rangle &= e^{-\frac{\Gamma t}{2}} \langle f|\mathcal{H} \left(\frac{h_1(t)+h_2(t)}{2}\left|D^0\right\rangle + \frac{q}{p}\frac{h_1(t)-h_2(t)}{2}\left|\bar{D}^0\right\rangle\right), \\ \langle f|\mathcal{H}|\bar{D}^0(t)\rangle &= e^{-\frac{\Gamma t}{2}} \langle f|\mathcal{H} \left(\frac{h_1(t)+h_2(t)}{2}\left|\bar{D}^0\right\rangle + \frac{p}{q}\frac{h_1(t)-h_2(t)}{2}\left|D^0\right\rangle\right). \end{aligned} \tag{1.20}$$

It is useful to define

$$\begin{aligned} A_f &= \langle f|\mathcal{H}|D^0\rangle, \\ \bar{A}_f &= \langle f|\mathcal{H}|\bar{D}^0\rangle, \\ \chi &= \frac{q}{p}\frac{\bar{A}_f}{A_f}. \end{aligned} \tag{1.21}$$

The notation $\tilde{A}_f$ is used to refer to both the A_f and $\bar{A}_f$ amplitudes, similarly to the notation $\tilde{D}^0$, used to refer to both D^0 and $\bar{D}^0$.

With the definitions in (1.21), equations (1.20) become simplified to

$$\langle f|\mathcal{H}|\tilde{D}^0(t)\rangle = e^{-\frac{\Gamma t}{2}} \tilde{A}_f \left(\frac{1+\chi^{\pm 1}}{2} h_1(t) + \frac{1-\chi^{\pm 1}}{2} h_2(t)\right), \tag{1.22}$$

where ± 1 in the exponent of χ is $+1$ for the $|D^0\rangle$ and -1 for the $|\bar{D}^0\rangle$.

The term between parentheses in expression (1.22) depends on the mixing parameters x and y, and is 1 in case of no mixing. It is important to notice that this expression depends on both the lifetime and the amplitudes A_f and $\bar{A}_f$, and the measurement of the mixing parameters x and y requires a combined analysis of both. For this reason, a decay model is necessary to describe A_f and $\bar{A}_f$. This model is detailed in §2, and the time dependent phase space analysis is explained in §2.5. This analysis is devoted to measure the mixing parameters x and y defined in (1.14) by means of an amplitude study.

1.2 Phase conventions

A phase transformation acting on the flavor eigenstates,

$$\left|D^0_\zeta\right\rangle = e^{i\zeta}\left|D^0\right\rangle, \qquad \left|\bar{D}^0_\zeta\right\rangle = e^{-i\zeta}\left|\bar{D}^0\right\rangle, \tag{1.23}$$

does not have any physical effects, since the amplitudes defined in (1.21) are affected by this transformation as a global phase,

$$(A_f)_\zeta = e^{i\zeta}A_f, \qquad (\bar{A}_f)_\zeta = e^{-i\zeta}\bar{A}_f, \tag{1.24}$$

which has no physical significance.

The states $|D^0\rangle$ and $|\bar{D}^0\rangle$ are not CP eigenstates. The CP operator acting on these states transforms one into the other,

$$CP\left|D^0\right\rangle = e^{i\xi_D}\left|\bar{D}^0\right\rangle, \qquad CP\left|\bar{D}^0\right\rangle = e^{-i\xi_D}\left|D^0\right\rangle, \tag{1.25}$$

with ξ_D an arbitrary phase. This arbitrariness needs to be taken into account in the relation between the CP eigenstates ($|D_+\rangle$ and $|D_-\rangle$) and the flavor eigenstates ($|D^0\rangle$ and $|\bar{D}^0\rangle$), which also depends on this arbitrary phase ξ_D:

$$|D_\pm\rangle = \frac{1}{\sqrt{2}}\left(\left|D^0\right\rangle \pm e^{i\xi_D}\left|\bar{D}^0\right\rangle\right), \tag{1.26}$$

so

$$CP\,|D_\pm\rangle = \pm\,|D_\pm\rangle\,. \tag{1.27}$$

With the possible final states $|f\rangle$, an arbitrary phase ξ_f can be defined similarly.

1.3 The three types of CP violation in D meson decays

The possible manifestations of CP violation can be classified in a model-independent way:

- CP violation in the decay occurs in decays of both charged and neutral mesons. It occurs when the amplitude of a decay is different from that of the decay of its CP conjugate.
- CP violation in the mixing occurs in neutral meson decays, when the Hamiltonian eigenstates cannot be chosen to be also CP eigenstates.
- CP violation in the interference between decays with and without mixing occurs in decays into final states that are common to $|D^0\rangle$ and $|\bar{D}^0\rangle$.

For each of the three cases, there is a specific quantity that is a signature of CP violation and is independent of phase conventions.

1.3.1 CP violation in the decay

For any final state $|f\rangle$, the quantity

$$\left|\frac{\bar{A}_{\bar{f}}}{A_f}\right| \tag{1.28}$$

is independent of any phase conventions.

If a term in the Lagrangian density that contributes to the amplitude has complex parameters, then these parameters appear in complex conjugate form in the CP conjugate amplitude. Therefore, phases due to these terms appear in A_f and $\bar{A}_{\bar{f}}$ with opposite signs. In the standard model, only the terms from the CKM matrix, described in §1.4, can be complex parameters, so they are part of the electroweak sector of the theory. For this reason, phases arising from CKM matrix parameters are often called "weak phases".

Weak phases of single terms in the amplitude are convention dependent. However, the difference between the weak phases of different terms in A_f is convention independent.

A second type of phases can appear in the amplitude due to real terms in the Lagrangian density. These phases appear with the same sign in the CP conjugate amplitude. Usually, the dominant contribution to these phases comes from strong interaction terms in the Lagrangian density and, for this reason, they are often called "strong phases". As with weak phases, only the relative strong phases of different terms in the amplitude have physical content.

It is useful to write each contribution (indexed with k) to the amplitude in three parts: its magnitude A_k, its weak phase ϕ_k and its strong phase δ_k,

$$A_f = \sum_k A_k e^{i(\delta_k+\phi_k)}, \qquad \bar{A}_{\bar{f}} = e^{i(\xi_f-\xi_D)} \sum_k A_k e^{i(\delta_k-\phi_k)}. \tag{1.29}$$

The convention independent quantity (1.28) is, therefore,

$$\left|\frac{\bar{A}_{\bar{f}}}{A_f}\right| = \left|\frac{\sum_k A_k e^{i(\delta_k-\phi_k)}}{\sum_k A_k e^{i(\delta_k+\phi_k)}}\right|. \tag{1.30}$$

If CP is conserved, there can be no difference between any of the weak phases of the different terms in the amplitude or, in other words, the weak phases ϕ_k have to be equal. Therefore, (1.30) implies that

$$\left|\frac{\bar{A}_{\bar{f}}}{A_f}\right| \neq 1 \Rightarrow \text{ CP violation.} \tag{1.31}$$

This type of CP violation is called *CP violation in the decay*, and is consequence of the CP-violating interference between various terms in the decay amplitude.

From equation (1.30) it can also be seen that a CP violation of this type cannot be observed unless at least two terms in the amplitude with different weak phases acquire also different strong phases, since

$$|A_f|^2 - |\bar{A}_{\bar{f}}|^2 = -2 \sum_{jk} A_j A_k \sin(\phi_j - \phi_k) \sin(\delta_j - \delta_k). \tag{1.32}$$

Experimentally, CP violation in the decay can be measured in decays of charged particles to final states that are not CP eigenstates. For example, an asymmetry in charged B decays,

$$a_f = \frac{\Gamma\left(B^+ \to f\right) - \Gamma\left(B^- \to \bar{f}\right)}{\Gamma\left(B^+ \to f\right) + \Gamma\left(B^- \to \bar{f}\right)}, \tag{1.33}$$

can be written in terms of amplitudes as

$$a_f = \frac{1 - \left|\bar{A}_{\bar{f}}/A_f\right|^2}{1 + \left|\bar{A}_{\bar{f}}/A_f\right|^2}. \tag{1.34}$$

If a_f can be measured to be significantly different from zero, then a_f is an observation of CP violation in the decay.

CP violation in the decay can also occur in neutral meson decays, where it competes with the other two types of CP violation effects, described below.

1.3.2 CP violation in the mixing

The quantity

$$\left|\frac{q}{p}\right|^2 = \left|\frac{M_{12}^\star - \frac{i}{2}\Gamma_{12}^\star}{M_{12} - \frac{i}{2}\Gamma_{12}}\right| \tag{1.35}$$

is independent of phase conventions. When CP is conserved, the Hamiltonian eigenstates must be also CP eigenstates. From expressions (1.11) and (1.26), CP conservation implies that $|q/p| = 1$. Therefore,

$$\left|\frac{q}{p}\right| \neq 1 \Rightarrow \text{ CP violation.} \tag{1.36}$$

This type of CP violation is called *CP violation in the mixing*, and is the result of the Hamiltonian eigenstates being different from the CP eigenstates. This type of CP violation has been observed unambiguously in the neutral kaon system.

For the neutral D or B systems, this effect could be observed through the asymmetries in semileptonic decays,

$$a_{sl} = \frac{\Gamma\left(\bar{D}^0(t) \to \ell^+\nu X\right) - \Gamma\left(D^0(t) \to \ell^-\bar{\nu} X\right)}{\Gamma\left(\bar{D}^0(t) \to \ell^+\nu X\right) + \Gamma\left(D^0(t) \to \ell^-\bar{\nu} X\right)}, \tag{1.37}$$

which can be written in terms of $|q/p|$ as

$$a_{sl} = \frac{1 - |q/p|^4}{1 + |q/p|^4}. \tag{1.38}$$

Semileptonic channels have the particularity that there is only one term at leading order that contributes to the amplitude, which corresponds to the $W^\pm$ boson propagator. Therefore, semileptonic decays are clean from effects of CP violation in the decays, since these effects arise when there are relative phases between the different resonances of the decays, and semileptonic decays do not have leading resonances other than the $W^\pm$.

1.3.3 CP violation in the interference between decays with and without mixing

For any final state $|f\rangle$, the quantity

$$\frac{q}{p}\frac{\bar{A}_{\bar{f}}}{A_f} \tag{1.39}$$

depends only on the arbitrary phase ξ_f. In decays into final CP eigenstates, $f_{\mathrm{CP}} = \bar{f}_{\mathrm{CP}}$, it is necessary that $e^{i\xi_f} = \pm 1$, so

$$\lambda = \pm\frac{q}{p}\frac{\bar{A}_{f_{\mathrm{CP}}}}{A_{f_{\mathrm{CP}}}}, \tag{1.40}$$

where the $\pm$ sign is $+$ for CP even final states, and $-$ for CP odd final states, is independent of phase conventions and physically meaningful. Therefore, (1.40) implies that

$$\lambda \neq \pm 1 \Rightarrow \text{ CP violation.} \tag{1.41}$$

Note that both CP violation in the decay or in the mixing lead to (1.41) through $|\lambda| \neq 1$. However, it is possible that, to a good approximation, $|q/p| = 1$ and $\left|\bar{A}_{\bar{f}}/A_f\right| = 1$, yet there is CP violation.

This type of CP violation is called *CP violation in the interference between decays with and without mixing*. This type of CP violation has also been observed in the neutral kaon system. It can be observed by comparing decays into final CP eigenstates of a time evolving D neutral state that is created either as a D^0 or as a $\bar{D}^0$.

$$a_{f_{\mathrm{CP}}} = \frac{\Gamma\left(\bar{D}^0(t) \to f_{\mathrm{CP}}\right) - \Gamma\left(D^0(t) \to f_{\mathrm{CP}}\right)}{\Gamma\left(\bar{D}^0(t) \to f_{\mathrm{CP}}\right) + \Gamma\left(D^0(t) \to f_{\mathrm{CP}}\right)}, \tag{1.42}$$

1.4 CP violation in the standard model

In the standard model of $SU(3)_C \times SU(2)_L \times U(1)_Y$ gauge symmetry with three fermion generations, CP violation arises from a single phase in the mixing matrix for quarks [30, 31]. Each quark generation consists of three multiplets, written in the weak eigenstate basis as

$$Q_L = \begin{pmatrix} U_L \\ D_L \end{pmatrix} = (3,2)_{+1/3}, \quad U_R = (3,1)_{+4/3}, \quad D_R = (3,1)_{-2/3}, \tag{1.43}$$

where $(3,2)_{+1/3}$ denotes a triplet of $SU(3)_C$, doublet of $SU(2)_L$ with hypercharge $Y = 2(Q-T_3) = +1/3$, being Q the quark charge matrix and T_3 the third isospin component matrix.

The interactions of quarks with the $SU(2)_L$ gauge bosons are given by

$$\mathcal{L}_W = -\frac{1}{2}g\bar{Q}_{Li}\gamma^\mu\tau^a\mathbf{1}_{ij}Q_{Lj}W^a_\mu, \tag{1.44}$$

where γ^μ operates in Lorentz space, τ^a operates in $SU(2)_L$ space and $\mathbf{1}$ is the unit matrix operating in flavor space and is written explicitly to make the transformation to the mass eigenbasis clearer.

The masses and mixings of the quarks have a common origin in the standard model. They arise from the charged current Yukawa interactions of quarks with the Higgs scalar doublet $\phi(1,2)_{+1}$,

$$\mathcal{L}_Y = -Y^d_{ij}\bar{Q}_{Li}\phi D_{Rj} - Y^u_{ij}\bar{Q}_{Li}\tilde{\phi}U_{Rj} + \text{Hermitian conjugate}, \tag{1.45}$$

where $Y^{u,d}$ are 3×3 complex matrices and i, j label the quark generations. Spontaneous symmetry breaking, $SU(2)_L \times U(1)_Y \rightarrow U(1)_{EM}$, takes place when ϕ acquires vacuum expectation value, $\langle\phi\rangle = (0, v/\sqrt{2})$, and the two components of the quark doublet and the three members of the W^μ triplet become distinguishable. The charged current interaction becomes, in the weak eigenstate basis,

$$\mathcal{L}_W = -\sqrt{\frac{1}{2}}g\bar{U}_{Li}\gamma^\mu \mathbf{1}_{ij} D_{Lj} W^+_\mu + \text{Hermitian conjugate}, \tag{1.46}$$

and from the replacement $\text{Re}\left(\phi^0\right) \rightarrow \sqrt{\frac{1}{2}}(v + H^0)$ in equation (1.45), mass terms arise for the quarks, given by

$$\mathcal{L}_M = -\sqrt{\frac{1}{2}}Y^d_{ij}\bar{D}_{Li}D_{Rj} - \sqrt{\frac{1}{2}}Y^u_{ij}\bar{U}_{Li}U_{Rj} + \text{Hermitian conjugate}, \tag{1.47}$$

which defines

$$M_d = -\sqrt{\frac{1}{2}}Y^d_{ij}\bar{D}_{Li}D_{Rj}, \tag{1.48}$$

$$M_u = -\sqrt{\frac{1}{2}}Y^u_{ij}\bar{U}_{Li}U_{Rj}. \tag{1.49}$$

The phase information is now contained in these mass matrices. To transform to the mass eigenstate basis, four unitary matrices are defined, such that

$$V_{dL}M_d V^\dagger_{dR} = M^{\text{diag}}_d, \quad V_{uL}M_u V^\dagger_{uR} = M^{\text{diag}}_u, \tag{1.50}$$

where M^{diag}_q are diagonal and real, while V_{qL} and V_{qR} are complex. The charged current interactions (1.46) are given in the mass eigenbasis by

$$\mathcal{L}_W = -\sqrt{\frac{1}{2}}g\bar{U}_{Li}\gamma^\mu \bar{V}_{ij} D_{Lj} W^+_\mu + \text{Hermitian conjugate}, \tag{1.51}$$

where the matrix $\bar{V} = V_{uL}V^\dagger_{dL}$ is the unitary mixing matrix for the three quark generations. Notice the replacement of $\mathbf{1}$ in (1.46) with $\bar{V}_{ij}$ in (1.51).

Matrix V is called the Cabibbo-Kobayashi-Maskawa (CKM) matrix [30, 31], and has one irremovable phase, that gives rise to CP violation in the standard model. It is interesting to note that the same argument applied on a two-generation standard model Lagrangian density with a single Higgs field does not leave any CP-violation phases. Such a model could not accommodate CP violation without the addition of extra fields. It was this observation that led Kobayashi and Maskawa to suggest a third quark generation long before there was any experimental evidence for it.

1.4.1 Standard model predictions of D meson mixing and CPV

Mixing in the standard model originates from short and long distance contributions. Short distance contributions come from box diagrams with quarks and $W^{\pm}$ bosons. The standard model predicts small mixing effects because b quarks are CKM suppressed and s and d quarks are GIM suppressed [10, 32, 33, 34]. The main short distance contribution is to the x mixing parameter. Long distance contributions come from loop diagrams with hadronic intermediate states. These contributions are expected to be dominant, but still small. Since they are not perturbative, they are difficult to estimate, but predictions exist [11,12] that bound x and y in the range $[0.001, 0.01]$, with $|x| < |y|$.

New physics could arise through new particles in loops. For example, if $|x|$ was found to be much larger than $|y|$, this could be a hint of new physics.

The standard model predicts CPV in the D sector to be $\sim 10^{-3}$. If CPV was to be found with the current sensitivity ($\sim 10^{-2}$), this would also be a hint of new physics [12].

1.5 Mixing and CP violation searches

Mixing has been studied using a variety of suppressed hadronic decays: in the time dependence of the wrong sign events in $D^0 \to K^+\pi^-$ [2, 13, 3], in the ratio of lifetimes of $D^0 \to K^+K^-$ and $D^0 \to \pi^+\pi^-$ events with respect to $D^0 \to K^-\pi^+$ events [5, 4, 6], and in a D^0 time-dependent amplitude analysis of $D^0 \to K^+\pi^-\pi^0$ events [7]. Mixing has also been studied in semileptonic events [14,15,16] by the BaBar and Belle collaborations, and in a time-dependent amplitude analysis of $K_s\pi^+\pi^-$ events [8, 9].

D mesons are tagged at production by means of $D^{\star +} \to D^0\pi_s^+$ and its conjugate, where the charge of the low momentum pion $\pi_s^{\pm}$ tags the flavor of the produced D meson.

CP violation has been studied in single Cabibbo-suppressed decays with CP even final states $D^0 \to \pi^+\pi^-$ and $D^0 \to K^+K^-$ [17, 18] and $D^0 \to \pi^+\pi^-\pi^0$ [19, 20] and $D^0 \to K^+K^-\pi^0$ [19]. The standard model predicts CP violation in these modes to be $\sim 10^{-4} - 10^{-5}$, so evidence of CP violation in them, with the current sensitivity, would be a sign of physics beyond the standard model [12]. CP violation has also been studied in $D^0 \to K^+\pi^-\pi^0$ events [7, 21] and in $D^0 \to K^+K^-\pi^+\pi^-$ decays.

1.5.1 Mixing from D^0 lifetime measurements in $D^0 \to h^+h^-$ and $D^0 \to K^-\pi^+$

D meson mixing and CP violation alter the lifetime distributions of CP eigenstates h^+h^-. A good approximation for the average lifetime is

$$\tau^{\pm} = \tau_{K\pi}\left[1 + \left|\frac{q}{p}\right|^{\pm 1}(y\cos\phi_f \mp x\sin\phi_f)\right]^{-1}, \tag{1.52}$$

where τ^+ is the lifetime of $D^0 \to h^+h^-$, τ^- is the lifetime of $\bar{D}^0 \to h^+h^-$, $\tau_{K\pi}$ is the lifetime of $D^0 \to K^-\pi^+$, and

$$\phi_f = \arg\left(\frac{q}{p}\frac{\bar{A}_f}{A_f}\right). \tag{1.53}$$

The mixing and CP observables are

$$y_{CP} = y\cos\phi_f = \frac{\tau_{K\pi}}{\langle\tau_{hh}\rangle} - 1, \qquad \Delta y = y\sin\phi_f = \frac{\tau_{K\pi}}{\langle\tau_{hh}\rangle}A_\tau, \tag{1.54}$$

where

$$\langle\tau_{hh}\rangle = \frac{\tau^+ + \tau^-}{2}, \qquad A_\tau = \frac{\tau^+ - \tau^-}{\tau^+ + \tau^-}, \tag{1.55}$$

are the lifetime average and the asymmetry, respectively.

Belle's results [4] are

$$y_{CP} = (1.31 \pm 0.32\ (\text{stat}) \pm 0.25\ (\text{syst})) \cdot 10^{-2}, \tag{1.56}$$
$$A_\tau = (0.01 \pm 0.30\ (\text{stat}) \pm 0.15\ (\text{syst})) \cdot 10^{-2}, \tag{1.57}$$

which provide evidence of D meson mixing at $3.2\,\sigma$.

BaBar published the result of a tagged analysis [5],

$$y_{CP} = (1.03 \pm 0.33\ (\text{stat}) \pm 0.19\ (\text{syst})) \cdot 10^{-2}, \tag{1.58}$$
$$\Delta y = (-0.26 \pm 0.36\ (\text{stat}) \pm 0.08\ (\text{syst})) \cdot 10^{-2}, \tag{1.59}$$

and also a combined result of an analysis of a combined set of disjoint tagged and untagged events [6],

$$y_{CP} = (1.13 \pm 0.22\ (\text{stat}) \pm 0.18\ (\text{syst})) \cdot 10^{-2}, \tag{1.60}$$

which shows the largest significant evidence up to date of D meson mixing at $4.1\,\sigma$.

The Heavy Flavor Averaging Group [22] averages for y_{CP} are shown in figure 1.1.

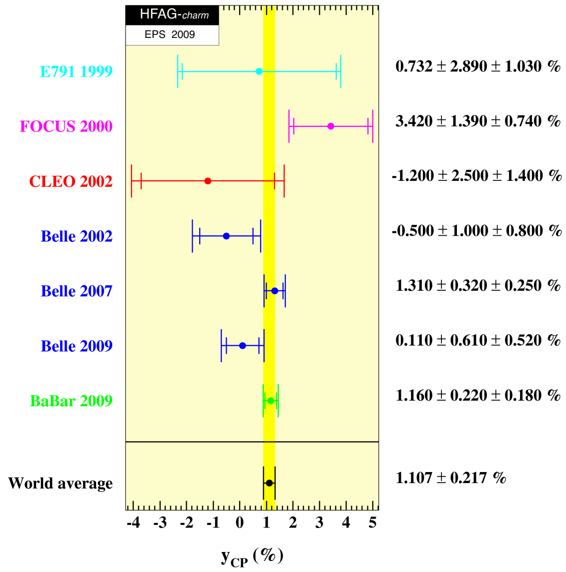

Figure 1.1: Heavy Flavor Averaging Group averages for y_{CP}.

Chapter 2

Decay model

The three-body decay width of a $D^0 \to ABC$ decay is given by

$$d\Gamma = \frac{|\mathcal{M}|^2}{32(2\pi)^3 m_D^3}\, dm_{ab}^2\, dm_{ac}^2, \tag{2.1}$$

where m_D is the mass of the $\tilde{D}^0$ meson, m_{ab} and m_{ac} are the invariant masses of the pairs ab and ac, respectively, and $\mathcal{M}$ is the Lorentz-invariant decay amplitude.

In the general case of a three-body decay of a particle X, this expression is written as

$$d\Gamma = \frac{\overline{|\mathcal{M}|^2}}{32(2\pi)^3 m_X^3}\, dm_{ab}^2\, dm_{ac}^2, \tag{2.2}$$

where $\overline{|\mathcal{M}|^2}$, indicates the average of the decay amplitude over the spin states of the decaying particle X. In the case of this analysis, the mother particle is a scalar particle and, therefore, there is just one spin amplitude and no averaging is required.

The graphical representation of the modulus squared amplitude $|\mathcal{M}|^2$ in terms of pairs of invariant masses (ab and ac in this analysis) is called **Dalitz plot** [35, 36], and is a very useful tool to understand the underlying physics in the decay process. If $|\mathcal{M}|^2$ is constant, the kinematically allowed region of the Dalitz plot will be uniformly populated with events. Any variation in the population over the Dalitz plot is due to dynamical rather than kinematical effects.

The parameterization of the decay amplitude used in this analysis attempts to describe the magnitude $|\mathcal{M}|^2$. It is important to remark that the fundamental description of a $\tilde{D}^0$ decay involves calculations with strong interactions, i.e. involving quarks and gluons, and these calculations are very hard to perform. Therefore, the formulation used in this analysis is, strictly speaking, a model that tries to describe these interactions in a simpler but non-fundamental way. For this reason, these kind of analyses are often said to be **model dependent**, because other non-fundamental models can also be accurate descriptions of the observation, but only one of them is picked as the nominal one.

The choice of the nominal model arises the question of what would be the values of the measured magnitudes if the choice had been different. The effect of imposing a model rather than another is accounted for as a specific source of systematic uncertainty, and is described in detail in §7.2.

The three body $\tilde{D}^0$ decay has been mostly modeled as a superposition of quasi-two-body decays $D^0 \to rc$, and $r \to ab$, being a, b and c pseudo-scalars. This way of modeling the decays makes it easy to visualize intermediate resonances simply by looking at the most populated regions of the Dalitz plot. The amplitude for this process is given by

$$\mathcal{M}_r = \sum_{\lambda} \langle ab|r_\lambda\rangle \Delta_r(m_{ab}) \langle cr_\lambda|D^0\rangle = Z_l(m_{ab}^2, m_{ac}^2) B_l^{D^0c}(p, p_r) B_l^{ab}(q, q_r) \Delta_r(m_{ab}), \tag{2.3}$$

where the sum is over the helicity states λ of the resonance r, l is the orbital angular momentum number between r and c and, since a, b and c are scalar particles, it is also the orbital angular momentum number between a and b (which is the same as the spin of the resonance), $\vec{p}$ is the momentum of c in the rest frame of the $\tilde{D}^0$, $\vec{q}$ is the momentum of a (or b) in the rest frame of the system ab, $p = |\vec{p}|$, $q = |\vec{q}|$, p_r and q_r are the values of p and q if $m_{ab} = m_r$, and m denotes invariant masses of the particles or pairs of particles.

The values of p and q can be obtained in terms of invariant masses of the pairs of particles involved in the event:

$$p = \frac{\lambda^{\frac{1}{2}}(m_{ab}^2, m_D^2, m_c^2)}{2m_D} = \frac{\sqrt{[m_{ab}^2 - (m_D + m_c)^2][m_{ab}^2 - (m_D - m_c)^2]}}{2m_D}, \tag{2.4}$$

$$q = \frac{\lambda^{\frac{1}{2}}(m_{ab}^2, m_a^2, m_b^2)}{2m_{ab}} = \frac{\sqrt{[m_{ab}^2 - (m_a + m_b)^2][m_{ab}^2 - (m_a - m_b)^2]}}{2m_{ab}}, \tag{2.5}$$

$$\lambda(x, y, z) = x^2 + y^2 + z^2 - 2xy - 2xz - 2yz. \tag{2.6}$$

Alternatively, the momentum $\vec{p}$ can be evaluated in the rest frame of the resonant pair ab. The effect of changing the reference frame with respect to which this momentum is computed, is accounted for as a source of systematic uncertainty, and is described in detail in §7.2.1 and §7.2.3.

The function $Z_l(m_{ab}^2, m_{ac}^2)$ describes the angular distribution of the decay products, $B_l^{D^0c}$ is the centrifugal barrier factor for the primary vertex (rc production), B_l^{ab} is the centrifugal barrier factor for the secondary vertex (ab production), and Δ_r is the dynamical function (propagator) that describes the resonance r. These terms are described in detail in the following sections.

Notice that ab denotes the resonant pair and that this resonant pair is, in general, not the same for different resonances. For example, for the contribution from the ρ^0 resonance in the $K_s\pi^+\pi^-$ decay, the resonant pair is the dipion $\pi^+\pi^-$, but for the contribution from the $K^{\star -}$ resonance, the resonant pair is the system $K_s\pi^-$.

The total amplitude of the decay process is expressed as a complex linear combination of amplitudes for individual resonances, i.e.

$$\mathcal{M} = \sum_r a_r e^{i\phi_r} \mathcal{M}_r, \tag{2.7}$$

where a_r and ϕ_r are real parameters, and ϕ_r is an additional individual global[1] phase for each resonance (notice that $\mathcal{M}_r$ is a complex number, too). Equation (2.7) is the mathematical expression of what is known as **isobar model**, where the total amplitude is modeled as a linear combination of individual amplitudes, each corresponding to one single resonance.

It is important to notice that individual phases do not contain any physical information, but the differences between any pair of phases do. For this reason, the phase that corresponds to the ρ resonance is fixed to be 0 in this analysis, with no physical implications, and the values of the other phases have to be understood to be with respect to this one.

2.1 Angular distribution

The expressions for the angular distribution of the decay products are derived from the spin sum rules and the Feynman rules. Resonances with different helicities have different expressions for the angular distribution of the decay products.

The spin sum rule is an expression that appears in the calculation of the Feynman diagrams and involves the polarization of the resonance.

For scalar resonances, there is no polarization and, therefore, the angular distribution is uniform:

$$Z_0 = 1. \tag{2.8}$$

For vector resonances, the spin sum rule is

$$\sum_\lambda \epsilon_\lambda^{\mu\star} \epsilon_\lambda^{\nu}. \tag{2.9}$$

Since polarization vectors have 4 components, but represent particles with spin number 1, it is necessary for them to have only 3 degrees of freedom. This is achieved by imposing the transversality condition, so

$$\sum_\lambda \epsilon_\lambda^{\mu\star} \epsilon_\lambda^{\nu} \to -g^{\mu\nu} + \frac{p^\mu p^\nu}{m^2}, \tag{2.10}$$

where p^μ is the 4-momentum of the resonant pair and $g^{\mu\nu}$ is the metric tensor.

Here, a right arrow is used instead of the equal sign. This means that the spin sum is not the right part of the expression, but it can be replaced with it with no physical implication. This is why this is called a *rule*, and not an equality.

For tensor resonances, the spin sum rule is given by

$$\sum_\lambda \epsilon_\lambda^{\mu\nu\star} \epsilon_\lambda^{\alpha\beta}. \tag{2.11}$$

Since two-index tensors have, in general, 16 components, but polarization vectors have to represent particles with spin number 2, they must have only 5 degrees of freedom. This is achieved by

[1]In the sense that it does not depend on the point in the phase space, while $\mathcal{M}_r$ does.

imposing the following conditions:

- It must be symmetric, $\epsilon^{\mu\nu} = \epsilon^{\nu\mu}$, which imposes 6 constraints.
- It must be transverse, $\epsilon^{\mu\nu} p_\nu = 0$, which imposes 4 constraints.
- It must be traceless, $\epsilon^{\mu\mu} = 0$, which imposes 1 constraint.

The spin sum rule for a tensor resonance is, therefore,

$$\sum_\lambda \epsilon_\lambda^{\mu\nu\star} \epsilon_\lambda^{\alpha\beta} \to \frac{1}{2}\left(T^{\mu\alpha}T^{\nu\beta} + T^{\mu\beta}T^{\nu\alpha}\right) - \frac{1}{3} T^{\mu\nu}T^{\alpha\beta}, \quad T^{\mu\nu} = -g^{\mu\nu} + \frac{p^\mu p^\nu}{m^2}. \tag{2.12}$$

Knowing the spin sum rules for the different spin quantum numbers of the resonances under consideration, the Lorentz-invariant spin factor Z is obtained by contracting these quantities with the corresponding current [37],

$$Z_0 = 1 \tag{2.13}$$

$$Z_1 = m_{bc}^2 - m_{ac}^2 + \frac{\left(m_D^2 - m_c^2\right)\left(m_a^2 - m_b^2\right)}{m_{ab}^2} \tag{2.14}$$

$$\begin{aligned} Z_2 = &\left[m_{bc}^2 - m_{ac}^2 + \frac{\left(m_D^2 - m_c^2\right)\left(m_a^2 - m_b^2\right)}{m_{ab}^2}\right]^2 - \\ &- \frac{1}{3}\left[m_{ab}^2 - 2\left(m_D^2 + m_c^2\right) + \frac{\left(m_D^2 - m_c^2\right)^2}{m_{ab}^2}\right]\left[m_{ab}^2 - 2\left(m_a^2 + m_b^2\right) + \frac{\left(m_a^2 - m_D^2\right)^2}{m_{ab}^2}\right] \end{aligned} \tag{2.15}$$

The derivation of these expressions has been done enforcing transversality of the polarization vector by means of terms of the form

$$-g^{\mu\nu} + \frac{p^\mu p^\nu}{m_{ab}^2}, \tag{2.16}$$

and expressions (2.13), (2.14) and (2.15) constitute what is called the Zemach formalism [38,39,40]. However, enforcing transversality on, for example, the vector W boson propagator, cancels out the amplitude of the $\pi^- \to W^- \to \mu^- \nu_\mu$. The helicity formalism [40,41,42,43] relaxes the transversality condition by means of terms of the form

$$-g^{\mu\nu} + \frac{p^\mu p^\nu}{m_r^2}, \tag{2.17}$$

where m_r is the mass parameter of the propagator of the resonant particle. Since both approaches are reasonable, this analysis uses the Zemach formalism, but the helicity formalism is accounted for as a component of the systematic uncertainty, as described in §7.2.1 and §7.2.3.

2.2 Partial wave analysis

The mathematical description of a particle 3-body decay with a resonance is equivalent to the description of a 2-body scattering with a 2-body final state. The Feynman diagrams of both phenomena are exactly the same and, therefore, the study of one phenomenon is often useful to describe some properties of the other.

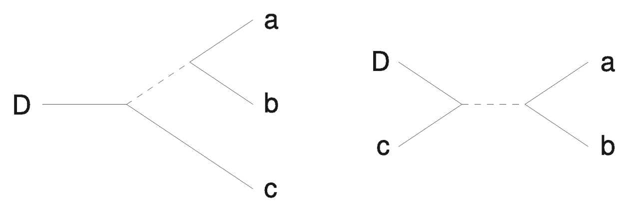

Figure 2.1: The amplitudes of a particle 3-body decay with a resonance and of a 2-body scattering with a 2-body final state are the same, since they have equal Feynman diagrams.

The formalism of the partial wave analysis was introduced as a method to compute scattering amplitudes. For a scattering potential confined in a finite volume in space and the detectors very far from the region containing the potential, the wave function of an incident plane wave with momentum $\vec{q}$ at infinite distance can be written as

$$\psi_{r\to\infty}(\vec{r}) = e^{i\vec{q}\vec{r}} + f(\theta, q)\frac{e^{iqr}}{r}, \tag{2.18}$$

with θ the angle between the incident and scattered directions, and $f(\theta, q)$ the scattering amplitude.

It is well known that the solution for $f(\theta, q)$ can be written as

$$f(\theta, q) = \frac{1}{q}\sum_{l=0}^{\infty}(2l+1)\, e^{i\delta_l}\sin\delta_l P_l(\cos\theta), \tag{2.19}$$

where δ_l are functions that may depend on q and P_l are the Legendre polynomials of order l.

The method of the partial wave expansion breaks down the initial wave function into an infinite sum over angular momentum components labeled by the quantum number l. The contribution from each l to the scattering amplitude is calculated separately and called **partial wave scattering amplitude**. The total scattering amplitude is obtained by summing over all the partial wave scattering amplitudes.

The δ_l functions in (2.19) are phase shifts between components with different angular momentum.

The relationship between the Lorentz-invariant amplitude $\mathcal{M}$ in (2.1) and the scattering amplitude $f(\theta, q)$ in (2.19) is given [44, 45] by

$$\mathcal{M} = 8\pi m_{ab} f(\theta, q), \tag{2.20}$$

where, in the case of a three-body decay, rather than a scattering process, m_{ab} is the invariant mass of the resonant pair ab and q is the momentum of a (or b) in the rest frame of the resonant pair ab.

By defining

$$\mathcal{T} = \sum_{l=0}^{\infty} (2l+1)\, e^{i\delta_l} \sin\delta_l P_l(\cos\theta), \tag{2.21}$$

$$\rho = \frac{2q}{m_{ab}}, \tag{2.22}$$

$$\hat{\mathcal{T}} = \frac{\mathcal{T}}{\rho}, \tag{2.23}$$

where ρ is called the **phase space factor**, expression (2.20) can be written as

$$\mathcal{M} = 16\pi\hat{\mathcal{T}}. \tag{2.24}$$

2.3 Centrifugal barrier factors

In scattering experiments, an approximate description of the interaction of two particles is given by

$$U_l(r) = V(r) + \frac{l(l+1)}{2\mu r^2} \qquad \text{for } r > R, \tag{2.25}$$

$$U_l(r) \simeq -U_0 \qquad \text{for } r < R, \tag{2.26}$$

where r is the separation of the two particles, R is the effective nuclear radius, $U_l(r)$ is the particle potential, l is its orbital angular momentum quantum number, μ is the reduced mass of the two particle system and $V(r)$ is the interaction potential. The second term in (2.25) is called **centrifugal potential** and depends on the orbital angular momentum quantum number l. The term $V(r)$ is also usually called **potential barrier**, and the centrifugal potential is also called **centrifugal barrier**.

From the effective potential expression (2.25) it is clear, with no need to solve the Schrödinger equation, that the larger is the angular momentum of the system, the harder is for the two particles to get close and undergo interaction.

In the case of a decay, rather than a scattering, a higher angular momentum or a smaller particle radius creates a higher centrifugal barrier that lowers the transition probability.

The Blatt-Weisskopf functions $F_l(q)$ [24,46] weight the amplitudes $\mathcal{M}_r$ to account for this effect. For the lowest l numbers, these functions are given by

$$F_0(q) = 1, \tag{2.27}$$

$$F_1(q) = \sqrt{\frac{2z^2}{z^2+1}}, \tag{2.28}$$

$$F_2(q) = \sqrt{\frac{13z^4}{z^4+3z^2+9}}, \tag{2.29}$$

where $z = Rq$, R is the Blatt-Weisskopf effective radius, and $F_l(q)$ are normalized to be 1 for $z = 1$. The Blatt-Weisskopf centrifugal barrier factors B_l in (2.3) are

$$B_l(q, q_r) = \frac{F_l(q)}{F_l(q_r)}, \tag{2.30}$$

where q_r is the value of q when $m_{ab} = m_r$, with m_r the mass of the resonant particle r.

In this analysis, the effective radius of the Blatt-Weisskopf parameters is fixed to $R = 1.5\,\mathrm{GeV}^{-1}$.

2.4 Scattering propagators and the K-matrix formalism

The non-resonant contribution to $D^0 \to abc$ is parameterized as a constant (S-wave) with no variations in magnitude or phase across the Dalitz plot.

The dynamical function Δ_r is derived from the S-matrix formalism. The amplitude of an initial state $|i\rangle$ coupling with a final state $\langle f|$ is

$$S_{fi} = \langle f|S|i\rangle. \tag{2.31}$$

The S matrix is usually written in terms of the transition matrix T as

$$S = I + 2iT, \tag{2.32}$$

where the identity matrix I describes events where no interaction is undergone, and the transition matrix T describes events where interactions occur.

The scattering operator S and the transition operator T contain a normalization term and also ensure 4-momentum conservation, which can be factored out to define the $\mathcal{S}$ and $\mathcal{T}$ matrices,

$$\langle f|S|i\rangle = (2\pi)^4\delta^{(4)}(p_f - p_i)\langle f|\mathcal{S}|i\rangle, \tag{2.33}$$
$$\langle f|T|i\rangle = (2\pi)^4\delta^{(4)}(p_f - p_i)\langle f|\mathcal{T}|i\rangle, \tag{2.34}$$

with p_f and p_i being the final and initial 4-momenta, respectively.

The scattering operator $\mathcal{S}$ is unitary, $\mathcal{S}\mathcal{S}^\dagger = \mathcal{S}^\dagger\mathcal{S} = I$, which implies that

$$\mathcal{T}^{-1} + iI = (\mathcal{T}^{-1} + iI)^\dagger. \tag{2.35}$$

This defines the K-matrix as

$$K^{-1} \equiv \mathcal{T}^{-1} + iI. \tag{2.36}$$

The K-matrix is Hermitian by definition. Since both $\mathcal{S}$ and $\mathcal{T}$ are invariant under time reversal, it turns out that both $\mathcal{S}$ and $\mathcal{T}$ have to be also symmetric, and therefore so must be the K-matrix. So since the K-matrix is Hermitian and symmetric, it is also implied that it must be real.

Solving (2.36) for $\mathcal{T}$ yields

$$\mathcal{T} = (I - iK)^{-1}K = K(I - iK)^{-1}. \tag{2.37}$$

From the unitarity condition (2.32) it is also required that

$$\mathcal{T} - \mathcal{T}^{\dagger} = 2i\mathcal{T}^{\dagger}\mathcal{T}. \tag{2.38}$$

Since $\mathcal{T}$ is symmetric, this expression reduces to the **optical theorem**,

$$\mathrm{Im}\,(\mathcal{T}) = |\mathcal{T}|^2\,. \tag{2.39}$$

It is convenient to express the $\mathcal{S}$ matrix in a different way

$$\mathcal{S} = I + 2i\rho^{\frac{1}{2}}\hat{\mathcal{T}}\rho^{\frac{1}{2}}, \tag{2.40}$$

where the phase space matrix ρ is the diagonal matrix $\rho = \mathrm{diag}(\rho_j)$, with ρ_j the phase space factor for channel j, defined in (2.22).

With this definition, in the single-channel S-wave, $\mathcal{S} = e^{2i\delta}$ satisfies unitarity and

$$\hat{\mathcal{T}} = \frac{1}{\rho}e^{i\delta}\sin\delta, \tag{2.41}$$

so this $\hat{\mathcal{T}}$ can be identified with $\hat{\mathcal{T}}$ in (2.23). For waves with non-zero angular momentum, the angular distribution term, described in §2.1, has to be additionally accounted for in this last expression of $\hat{\mathcal{T}}$.

Equivalently, the $\hat{K}$ matrix is

$$\hat{K}^{-1} = \hat{\mathcal{T}}^{-1} + i\rho. \tag{2.42}$$

In processes with multiple resonances that are assumed to dominate the amplitude, these have to appear as a sum of poles in the K-matrix, and are typically parameterized by

$$K_{ij} = \sum_{\alpha} \frac{g_{\alpha i}(m_{ab})g_{\alpha j}(m_{ab})}{m_{\alpha}^2 - m_{ab}^2}, \tag{2.43}$$

and

$$\hat{K}_{ij} = \sum_{\alpha} \frac{g_{\alpha i}(m_{ab})g_{\alpha j}(m_{ab})}{(m_{\alpha}^2 - m_{ab}^2)\sqrt{\rho_i(m_{ab})\rho_j(m_{ab})}}, \tag{2.44}$$

where the sum on α goes over the number of resonances, with masses m_α, and the **residue functions** (with energy dimensions) for channel i are given by

$$g_{\alpha i}^2(m_{ab}) = m_{\alpha}\Gamma_{\alpha i}(m_{ab}). \tag{2.45}$$

It is important to notice that this expression does not imply that $g_{\alpha i}$ are positively defined. Actually, some of these matrix elements take negative values in practice.

The width $\Gamma_\alpha(m_{ab})$ is

$$\Gamma_\alpha(m_{ab}) = \sum_i \Gamma_{\alpha i}(m_{ab}) \tag{2.46}$$

for each resonance α.

If there is a sharp separation at R (the effective Blatt-Weisskopf radius) between an outer region, where the interactions are negligible in comparison with the centrifugal barrier, and an inner region, where they dominate, it is useful to factor the Blatt-Weisskopf factors out of the partial decay width as an approximate representation of the centrifugal barrier effects. It is also useful to take a phase space factor out of the partial decay width, so

$$\Gamma_{\alpha i}(m_{ab}) = \frac{g^2_{\alpha i}(m_{ab})}{m_\alpha} = \gamma^2_{\alpha i}\Gamma^0_\alpha \rho_i(m_{ab}) B^2_l(q_i, q_{\alpha i}), \tag{2.47}$$

and

$$g_{\alpha i}(m_{ab}) = \gamma_{\alpha i}\sqrt{m_\alpha \Gamma^0_\alpha}\sqrt{\rho_i(m_{ab})} B_l(q_i, q_{\alpha i}), \tag{2.48}$$

where $\gamma_{\alpha i}$ are real (not necessarily positive) constants subject to the normalization condition $\sum_i \gamma^2_{\alpha i} = 1$.

Equation (2.47) is an attempt to separate the unknown dynamics within the interaction region from the well understood kinematical dependence of $\Gamma_{\alpha i}$ due to phase space and the centrifugal barrier outside of R [46]. This is done with the hope that the variation of Γ^0_α might be a lower order effect in comparison with the variation of B_l. In this analysis, it is assumed that Γ^0_α are constants.

It is practical to take as fit parameters the **base residue functions**,

$$g^0_{\alpha i} = \gamma_{\alpha i}\sqrt{m_\alpha \Gamma^0_\alpha}, \tag{2.49}$$

and express the residue functions more simply as

$$g_{\alpha i}(m_{ab}) = g^0_{\alpha i}\sqrt{\rho_i(m_{ab})} B_l(q_i, q_{\alpha i}). \tag{2.50}$$

In terms of base residue functions and pole masses, the $\hat{K}$-matrix has a simpler form

$$\hat{K}_{ij} = \sum_\alpha \frac{g^0_{\alpha i} g^0_{\alpha j} B_l(q_i, q_{\alpha i}) B_l(q_j, q_{\alpha j})}{m^2_\alpha - m^2_{ab}}. \tag{2.51}$$

The K**-matrix partial widths** $\tilde{\Gamma}_{\alpha i}$ and a K**-matrix total width** $\tilde{\Gamma}_\alpha$ are defined by

$$\tilde{\Gamma}_{\alpha i} = \Gamma_{\alpha i}(m_\alpha) = \gamma^2_{\alpha i}\Gamma^0_\alpha \rho_i(m_\alpha), \tag{2.52}$$

$$\tilde{\Gamma}_\alpha = \Gamma_\alpha(m_\alpha) = \Gamma^0_\alpha \sum_i \gamma^2_{\alpha i}\rho_i(m_\alpha), \tag{2.53}$$

which yield

$$\gamma^2_{\alpha i} = \frac{\tilde{\Gamma}_{\alpha i}}{\Gamma^0_\alpha \rho_i(m_\alpha)}. \tag{2.54}$$

The mass-dependent decay width can, therefore, be written as

$$\Gamma_\alpha(m_{ab}) = \sum_i \tilde{\Gamma}_{\alpha i} \frac{\rho_i(m_{ab})}{\rho_i(m_\alpha)} B_l^2(q_i, q_{\alpha i}) = \Gamma_\alpha^0 \sum_i \gamma_{\alpha i}^2 \rho_i(m_{ab}) B_l^2(q_i, q_{\alpha i}). \tag{2.55}$$

It is possible to parameterize a non-resonant background in each K-matrix element by adding a real dimensionless term b_{ij} to the sum of pole terms (2.51) with no risk of breaking unitarity,

$$\hat{K}_{ij} \to \hat{K}_{ij} + b_{ij}. \tag{2.56}$$

2.4.1 Production of resonances in P-vector approach

The K-matrix formalism describes the formation of resonances in two-body scattering processes $ab \to ab$, but it can be generalized to cover the case of the production of resonances in the decays of neutral D mesons.

It is necessary to assume that, in the production process, the two-body system in the final state does not interact with the rest of the final state.

According to Aitchison [47], the production part of the decay process is parameterized by a production vector P, and should result in an amplitude F according to

$$F = (I - iK)^{-1} P = T K^{-1} P, \tag{2.57}$$

or

$$\hat{F} = (I - i\hat{K}\rho)^{-1} \hat{P} = \hat{T} \hat{K}^{-1} \hat{P}. \tag{2.58}$$

Here, $\hat{P}$ characterizes the production of a resonance and $\hat{F}$ is the resulting invariant amplitude.

Expression (2.57) makes evident that P must have the same poles as K, since otherwise the amplitude F would vanish at the positions of the poles.

In expression (2.58), the term $(I - i\hat{K}\rho)^{-1}$ may be considered as the scattering propagator, thus carrying the states produced through $\hat{P}$ to the final state.

$\hat{P}$ and $\hat{F}$ are both column vectors and, similarly to (2.43) and (2.44),

$$P_j = \sum_\alpha \frac{\beta_\alpha^0 g_{\alpha j}(m_{ab})}{m_\alpha^2 - m_{ab}^2}, \tag{2.59}$$

and

$$\hat{P}_j = \sum_\alpha \frac{\beta_\alpha^0 g_{\alpha j}(m_{ab})}{(m_\alpha^2 - m_{ab}^2)\sqrt{\rho_j(m_{ab})}}, \tag{2.60}$$

where β_α^0 are complex production parameters, with energy dimensions.

Expression (2.60) gets simplified to

$$\hat{P}_j = \sum_\alpha \frac{\beta_\alpha^0 g_{\alpha j}^0 B_l(q_j, q_{\alpha j})}{m_\alpha^2 - m_{ab}^2}. \tag{2.61}$$

2.4.2 Single isolated resonance

For a process with a single isolated resonance with mass m_r,

$$K = \frac{m_r \Gamma_r(m_{ab})}{m_r^2 - m_{ab}^2}. \tag{2.62}$$

From (2.55),

$$\Gamma_r(m_{ab}) = \Gamma_r^0 \rho(m_{ab}) B_l^2(q, q_r), \tag{2.63}$$

so, leaving the angular dependence aside,

$$\mathcal{T}_r = \left[\frac{m_r \Gamma_r^0}{m_r^2 - m_{ab}^2 - i m_r \Gamma_r(m_{ab})}\right] \rho(m_{ab}) B_l^2(q, q_r). \tag{2.64}$$

The term between brackets is the well known **Breit-Wigner** propagator, $\rho(m_{ab})$ is the phase space factor, and $B_l(q, q_r)$ is the Blatt-Weisskopf centrifugal barrier factor.

The $\hat{\mathcal{T}}$-matrix element for this resonance is, therefore,

$$\hat{\mathcal{T}}_r = \left[\frac{m_r \Gamma_r^0}{m_r^2 - m_{ab}^2 - i m_r \Gamma_r(m_{ab})}\right] B_l^2(q, q_r). \tag{2.65}$$

For the resonances that are treated according to the isobar model, all the propagators that are used in this analysis are Breit-Wigner propagators, with the exception of the ρ^0 in the model of the $\tilde{D}^0 \to K_s \pi^+ \pi^-$, where a Gounaris-Sakurai propagator [25] has been used,

$$\hat{\mathcal{T}}_\rho = \frac{m_\rho^2 + d m_\rho \Gamma_\rho^0}{m_\rho^2 - m_{ab}^2 + f(m_{ab}^2) - i m_{ab} \Gamma_\rho(m_{ab})}, \tag{2.66}$$

where

$$f(m_{ab}^2) = \frac{\Gamma_\rho^0 m_\rho^2}{q_\rho} \left\{ \left(\frac{q}{q_\rho}\right)^2 \left[h(m_{ab}^2) - h(m_\rho^2)\right] + h'(m_\rho^2)\left(m_\rho^2 - m_{ab}^2\right) \right\}, \tag{2.67}$$

where q is the pion momentum in the dipion rest frame, as defined in (2.5), which gets simplified because the resonant particles have equal mass:

$$q = \sqrt{\frac{m_{ab}^2}{4} - m_\pi^2}, \tag{2.68}$$

$$q_\rho = \sqrt{\frac{m_\rho^2}{4} - m_\pi^2}, \tag{2.69}$$

and

$$h(m^2) = \frac{2q}{\pi m} \ln\left(\frac{m+2q}{2m_\pi}\right), \tag{2.70}$$

$$h'(m_\rho^2) = \left.\frac{dh}{d\,(m^2)}\right|_{m^2=m_\rho^2} = h(m_\rho^2)\left(\frac{1}{8q_\rho^2} - \frac{1}{2m_\rho^2}\right) + \frac{1}{2\pi m_\rho^2}, \tag{2.71}$$

and d is chosen to satisfy the condition $\mathcal{T}_\rho(m_{ab}=0)=1$, and depends on the mass of the resonant particle,

$$d = \frac{3m_\pi^2}{\pi q_\rho^2} \ln\left(\frac{m_\rho + 2q_\rho}{2m_\pi}\right) + \frac{m_\rho}{2\pi q_\rho} - \frac{m_\pi^2 m_\rho}{\pi q_\rho^3}. \tag{2.72}$$

2.4.3 Overlapping resonances

For a single-channel process with two resonances with pole masses m_1 and m_2, the K-matrix can be written as

$$K = \frac{m_1\Gamma_1(m_{ab})}{m_1^2 - m_{ab}^2} + \frac{m_2\Gamma_2(m_{ab})}{m_2^2 - m_{ab}^2}. \tag{2.73}$$

In the limit where m_1 and m_2 are far apart (in terms of widths), the propagator of both resonances can be approximated by a sum of Breit-Wigner functions,

$$\mathcal{T}_{1+2} \approx \mathcal{T}_1 + \mathcal{T}_2. \tag{2.74}$$

However, the more the resonances overlap, the more this approximation violates unitarity. In the limit where $m_1 = m_2 \equiv m_r$,

$$\mathcal{T}_{1+2} = \frac{m_r\left[\Gamma_1(m_{ab}) + \Gamma_2(m_{ab})\right]}{m_r^2 - m_{ab}^2 - i m_r\left[\Gamma_1(m_{ab}) + \Gamma_2(m_{ab})\right]}. \tag{2.75}$$

This result has the form of a single Breit-Wigner function, but with a total width equal to the sum of the widths of the two resonances.

2.4.4 Coupled channels

For a two-channel process with a single resonance with pole mass m_r, the K-matrix can be written as

$$K_r = \frac{1}{m_r^2 - m_{ab}^2}\begin{pmatrix} g_{r1}^2 & g_{r1}g_{r2} \\ g_{r1}g_{r2} & g_{r2}^2 \end{pmatrix}, \tag{2.76}$$

with $g_{ri}(m_{ab})$ defined in (2.45). From this expression,

$$\mathcal{T}_r = \frac{1}{m_r^2 - m_{ab}^2 - i(g_{r1}^2 + g_{r2}^2)}\begin{pmatrix} g_{r1}^2 & g_{r1}g_{r2} \\ g_{r1}g_{r2} & g_{r2}^2 \end{pmatrix}. \tag{2.77}$$

In the specific case where $l = 0$,

$$\hat{\mathcal{T}}_r = \frac{m_r \Gamma_r^0}{m_r^2 - m_{ab}^2 - i m_r \left[\Gamma_{r1}(m_{ab}) + \Gamma_{r2}(m_{ab})\right]} \begin{pmatrix} \gamma_{r1}^2 & \gamma_{r1}\gamma_{r2} \\ \gamma_{r1}\gamma_{r2} & \gamma_{r2}^2 \end{pmatrix} \tag{2.78}$$

$$= \frac{m_r \Gamma_r^0}{m_r^2 - m_{ab}^2 - i m_r \Gamma_r^0 \left(\gamma_{r1}^2 \rho_1 + \gamma_{r2}^2 \rho_2\right)} \begin{pmatrix} \gamma_{r1}^2 & \gamma_{r1}\gamma_{r2} \\ \gamma_{r1}\gamma_{r2} & \gamma_{r2}^2 \end{pmatrix} \tag{2.79}$$

In this analysis, the expression for coupled channels is used in the $K_s K^+ K^-$ mode, where the $a_0^{\pm}(980)$ and $a_0^0(908)$ resonances are taken into account. The mass of the a_0 particles is close to the $K_s K^{\pm}$ and K^+K^- production thresholds, and they decay mostly through $a_0^{\pm} \to \eta\pi^{\pm}$ or $a_0^0 \to \eta\pi^0$.

The K^+K^- and $K^0\bar{K}^0$ channels are assumed to have the same base residue function. The $a_0^{\pm} \to \eta\pi^{\pm}$ and $a_0^0 \to \eta\pi^0$ channels are also considered to have the same base residue function. Therefore, $\gamma_{r1} = \gamma_{KK}$ and $\gamma_{r2} = \gamma_{\eta\pi}$.

The phase space factor $\rho_{\eta\pi}$ is computed by means of (2.5). The phase space factor for the $K_s K^{\pm}$ and K^+K^- production uses the approximation of equal mass for both the neutral and charged kaons, $m_K \equiv m_{K^{\pm}} = m_{K^0}$, so it takes the form

$$\rho_{KK} \simeq \sqrt{1 - \frac{4m_K^2}{m_{ab}^2}}. \tag{2.80}$$

Since the mass of the a_0 particles is very close to the $K_s K^{\pm}$ and K^+K^- production thresholds, it is expected to find some events where $m_{ab} < 2m_K$, so an analytical continuation of the phase space factor is required,

$$\rho_{KK} \simeq i\sqrt{\frac{4m_K^2}{m_{ab}^2} - 1}. \tag{2.81}$$

2.4.5 Resonances in the P-vector approach

In this analysis, for the $\pi\pi$ S-wave, a common formulation of the $\hat{K}$-matrix has been used

$$\hat{K}_{ij} = \left(\sum_{\alpha} \frac{g_{\alpha i}^0 g_{\alpha j}^0}{m_\alpha^2 - m_{ab}^2} + f_{ij}^{sc} \frac{1\mathrm{GeV}^2 - s_0^{sc}}{m_{ab}^2 - s_0^{sc}}\right) \left[\frac{1\mathrm{GeV}^2 - s_0^A}{m_{ab}^2 - s_0^A}\left(m_{ab}^2 - \frac{s_A m_\pi^2}{2}\right)\right], \tag{2.82}$$

where $g_{\alpha i}^0$ are the real base residue functions for pole m_α and channel i, the real parameters f_{ij}^{sc} and s_0^{sc} describe a smooth background part of the K-matrix, and the term between brackets is called the **Adler zero** [48] and suppresses a false kinematical singularity near the $\pi\pi$ threshold.

This formulation for the $\hat{K}$-matrix is just the expression of (2.51) for an S-wave, with a non-resonant background term, according to (2.56), and corrected by the Adler zero term.

The five channels $\pi^+\pi^-$, $K\bar{K}$, 4π, $\eta\eta$ and $\eta\eta'$ have been taken into account. All the parameters of the $\hat{K}$-matrix, including the ones that parameterize the background and the ones that parameterize the Adler zero term, are fixed by scattering experiments [49, 50],

$$
g^0_{\alpha i} = \begin{array}{c} \begin{array}{ccccc} g^0_{\alpha,\pi^+\pi^-} & g^0_{\alpha,K\bar{K}} & g^0_{\alpha,4\pi} & g^0_{\alpha,\eta\eta} & g^0_{\alpha,\eta\eta'} \end{array} \\ \begin{pmatrix} 0.22889 & -0.55377 & 0.00000 & -0.39899 & -0.34639 \\ 0.94128 & 0.55095 & 0.00000 & 0.39065 & 0.31503 \\ 0.36856 & 0.23888 & 0.55639 & 0.18340 & 0.18681 \\ 0.33650 & 0.40907 & 0.85679 & 0.19906 & -0.00984 \\ 0.18171 & -0.17558 & -0.79658 & -0.00355 & 0.22358 \end{pmatrix} \end{array} \mathrm{GeV}, \quad m_\alpha = \begin{pmatrix} 0.65100 \\ 1.20360 \\ 1.55817 \\ 1.21000 \\ 1.82206 \end{pmatrix} \mathrm{GeV},
$$

$$
f^{sc}_{ij} = \begin{array}{c} \begin{array}{ccccc} f^{sc}_{i,\pi^+\pi^-} & f^{sc}_{i,K\bar{K}} & f^{sc}_{i,4\pi} & f^{sc}_{i,\eta\eta} & f^{sc}_{i,\eta\eta'} \end{array} \\ \begin{pmatrix} 0.23399 & 0.15044 & -0.20545 & 0.32825 & 0.35412 \\ 0.15044 & 0 & 0 & 0 & 0 \\ -0.20545 & 0 & 0 & 0 & 0 \\ 0.32825 & 0 & 0 & 0 & 0 \\ 0.35412 & 0 & 0 & 0 & 0 \end{pmatrix} \end{array}, \quad \begin{array}{l} s^{sc}_0 = -3.92637 \ \mathrm{GeV}^2, \\ s^A_0 = -0.15 \ \mathrm{GeV}^2, \\ s_A = 1. \end{array} \tag{2.83}
$$

Similarly to the $\hat{K}$-matrix, the production vector $\hat{P}$ has been parameterized as

$$
\hat{P}_j = \sum_\alpha \frac{\beta^0_\alpha g^0_{\alpha j}}{m^2_\alpha - m^2_{ab}} + f^{pr}_{\pi\pi,j} \frac{1\mathrm{GeV}^2 - s^{pr}_0}{m^2_{ab} - s^{pr}_0}, \tag{2.84}
$$

where the β^0_α complex production parameters and the production background parameters $f^{pr}_{\pi\pi,j}$ and s^{pr}_0 are allowed to float in the fit. The rest of the parameters of the $\hat{P}$-vector are shared with the parameterization of the $\hat{K}$-matrix and, therefore, are also fixed.

Usually, an Adler zero factor, identical to the one in the parameterization of the $\hat{K}$-matrix, is also included in the parameterization of the $\hat{P}$-vector, but in this analysis it has been included only in the $\hat{K}$-matrix parameterization, and not in the $\hat{P}$-vector.

2.4.6 LASS-like parameterization

The LASS experiment at the SLAC National Accelerator Laboratory found a broad, spinless resonance in the $K^-\pi^+$ spectrum in $K^-p \to K^-\pi^+\eta$ scattering experiments [26], centered around a pole at 1430 MeV, which could not be correctly described by the usual Breit-Wigner line shape. An effective range parameterization for the $K\pi$ S-wave was used,

$$
\mathcal{T}_{\mathrm{LASS}} = \sin\delta_R e^{i\delta_R} e^{2i\delta_B} + \sin\delta_B e^{i\delta_B} = \sin(\delta_R + \delta_B) e^{i(\delta_R+\delta_B)}, \tag{2.85}
$$

where

$$\tan\delta_R = \frac{m_r\Gamma(m_{ab})}{m_r^2 - m_{ab}^2}, \tag{2.86}$$

$$\cot\delta_B = \frac{1}{aq} + \frac{rq}{2}, \tag{2.87}$$

where the background is described by means of an effective range parameterization, with a the scattering length, r the effective range, and q the momentum of any of the resonant particles in the reference frame of the resonant pair, as expressed in (2.5). Neither the scattering length a nor the effective range r are defined to be positive [51].

$\mathcal{T}_{\mathrm{LASS}}$ is unitary and can be considered a special case of the two-body single channel K-matrix formalism with $K = \tan(\delta_R + \delta_B)$.

The parameterization in (2.85) is valid for $K^- p \to K^- \pi^+ \eta$ elastic scattering experiments, but can be generalized to production experiments as

$$\mathcal{T}_{\mathrm{gLASS}} = R\sin\delta_R e^{i(\delta_R+\phi_R)} e^{2i(\delta_B+\phi_B)} + B\sin(\delta_B+\phi_B) e^{i(\delta_B+\phi_B)}, \tag{2.88}$$

where B, R, ϕ_B and ϕ_R are real parameters, and (2.88) reduces to the elastic scattering expression when $B = R = 1$ and $\phi_B = \phi_R = 0$.

Using that

$$e^{i\delta}\sin\delta = \frac{1}{\cot\delta - i}, \tag{2.89}$$

$$e^{2i\delta} = \frac{\cot\delta + i}{\cot\delta - i}, \tag{2.90}$$

expression (2.88) can be written as

$$\begin{aligned}\mathcal{T}_{\mathrm{gLASS}} =& R e^{i\phi_R} e^{2i\phi_B}\left(\frac{\cot\delta_B + i}{\cot\delta_B - i}\right)\frac{m_r\Gamma(m_{ab})}{m_r^2 - m_{ab}^2 - i m_r\Gamma(m_{ab})} + \\ & B e^{i\phi_B}\frac{\cos\phi_B + \sin\phi_B\cot\delta_B}{\cot\delta_B - i},\end{aligned} \tag{2.91}$$

and, therefore,

$$\begin{aligned}\hat{\mathcal{T}}_{\mathrm{gLASS}} =& R e^{i\phi_R} e^{2i\phi_B}\left(\frac{q\cot\delta_B + iq}{q\cot\delta_B - iq}\right)\frac{m_r\Gamma_r^0}{m_r^2 - m_{ab}^2 - i m_r\Gamma(m_{ab})} + \\ & B\frac{m_{ab}}{2} e^{i\phi_B}\frac{\cos\phi_B + \sin\phi_B\cot\delta_B}{q\cot\delta_B - iq}.\end{aligned} \tag{2.92}$$

Since q can approach zero, it is practical for computer usage to modify the LASS expressions in such a way that they explicitly contain $q\cot\delta_B$, in which the dependence on the inverse of q, in (2.87), is explicitly cancelled. For this reason $q\cot\delta_B$ is kept in expression (2.92), although q can be simplified or factored out in some of its terms.

2.4.7 Fit fractions

The fit fraction of resonance r is usually defined as

$$f_r = \frac{\int \left|a_r e^{i\delta_r} \mathcal{T}_r\right|^2 \, dm_{ab}^2 \, dm_{ac}^2}{\int \left|\sum_k a_k e^{i\delta_k} \mathcal{T}_k\right|^2 \, dm_{ab}^2 \, dm_{ac}^2}, \tag{2.93}$$

where the integrals are performed in the kinematically allowed phase space, i.e., inside the boundaries of the Dalitz plot.

Since the rate of a single process is proportional to the square of the relevant matrix element, as seen in (2.1), the fit fraction is expected to give an idea of the amount of each resonance the model contains.

When the K-matrix or the generalized LASS parameterizations are used to describe a wave (e.g. the $\pi\pi$ S-wave and the $K\pi$ S-wave), then $\mathcal{M}_r$ refers to the entire wave, since there are no individual resonances.

In general, the sum of all the fit fractions for all the resonances will not be 1 due to interference.

2.4.8 Decay model summary

2.4.8.1 $K_s\pi^+\pi^-$

The decay model used in this analysis has already been used in BaBar for the measurement of the CKM angle γ [23]. The amplitude for the $K_s\pi^+\pi^-$ mode is given by

$$\mathcal{T} = \mathcal{T}_{\pi\pi} + \mathcal{T}_{K\pi} + \sum_{P,D-\text{waves}} a_r e^{i\phi_r} \mathcal{T}_r, \tag{2.94}$$

where $\mathcal{T}_{\pi\pi}$ is the contribution of the $\pi\pi$ K-matrix with a P-vector approach for the production part, and $\mathcal{T}_{K\pi}$ is the contribution of the $K\pi$ generalized LASS function, described in 2.4.6. The terms inside the sum are the isobar model part, where $a_r e^{i\phi_r}$ are the complex coefficients of the linear combination of the amplitude terms $\mathcal{T}_r$ of each resonance r. These complex coefficients are parameters of the fit described in §6.

The contributions of the model are:

- The $\pi\pi$ S-wave, expressed as a K-matrix combined with a production vector, as explained in §2.4.5, with the values of the poles and base residue functions taken from [50] and summarized in expressions (2.83). The K-matrix parameters are fixed. The fifth P-vector pole mass, m_5, and the $\eta\eta'$ production energy threshold are both far beyond the kinematic range of the dipion invariant mass $(m_D - m_{K_s})$. For this reason, there is little sensitivity to their associated parameters β_5 and $f_{\pi\pi,\eta\eta'}$, so both of them have been fixed to zero in the nominal fit. The parameters $f_{i,j}^{pr}$ for $i \neq \pi\pi$ have been fixed to zero, since they are not related to the $\pi\pi$ production process. The parameter $f_{\pi\pi,\eta\eta}^{pr}$ has also been fixed to zero, and s_0^{pr} has been fixed to s_0^{sc}, since there is also little sensitivity to these parameters in the data.

- The $K\pi$ S-wave, represented by the $K_0^{\star\pm}(1430)$, and expressed as a generalized LASS amplitude, described in §2.4.6.
- The P-wave contribution, represented by the $\rho(770)$, $\omega(782)$ and both the Cabibbo allowed and doubly suppressed $K^{\star\pm}(892)$ and $K^{\star\pm}(1680)$.
- The D-wave contribution, represented by the $K_2^{\star\pm}(1430)$ and the $f_2^0(1270)$.

The P and D waves are assumed to be dominated by narrow and isolated resonances and, therefore, these waves are described by the isobar model with relativistic Breit-Wigner functions, except for the ρ^0 resonance, that is described by a Gounaris-Sakurai function [25].

2.4.8.2 $K_sK^+K^-$

The amplitude for the $K_sK^+K^-$ mode is given by

$$\mathcal{T} = \sum_{P,D-\text{waves}} a_r e^{i\phi_r}\mathcal{T}_r, \tag{2.95}$$

where the complete amplitude has been mostly described as an isobar model, where $a_r e^{i\phi_r}$ are the complex coefficients of the linear combination of the amplitude terms $\mathcal{T}_r$ of each resonance r. These complex coefficients are parameters of the fit described in §6. The $a_0(980)$ resonances have been described according to a coupled channel formulation, explained in §2.4.4.

The contributions of the model are:

- The S-wave, represented by the $a_0^0(980)$, $a_0^\pm(980)$, $f_0^0(1370)$, $a_0^0(1450)$ and $a_0^+(1450)$ for D^0 and $a_0^-(1450)$ for $\bar{D}^0$. The $a_0^\pm(1450)$ doubly Cabibbo suppressed channel is not included in the nominal model. However, it is considered in an alternative model that contributes to assign systematic uncertainties, as described in detail in §7.2.
  - The $a_0^\pm(980)$ and $a_0^0(980)$ particles have a mass very close to the $K_sK^\pm$ and K^+K^- production thresholds, and are expressed as a coupled channel formulation, described in §2.4.4. The parameters of their mass and base residue functions have been extracted from a Crystal Barrel measurement [52], $m_{a_0} = 999 \pm 2\,\text{MeV}$, $g^0_{\eta\pi} = 324 \pm 15\,\text{MeV}$. In order to reduce the systematic uncertainty associated to fixing γ_{KK}, it has been left to float in the fit. A previous toy Monte Carlo study shows that it is possible to extract γ_{KK} with the data sample used in this analysis.
  - The parameters of the $f_0^0(1370)$ are taken from a BES measurement [53], with mass $1350 \pm 50\,\text{MeV}$ and width $265 \pm 40\,\text{MeV}$. Alternative parameters from an E791 measurement [54], with mass $1434 \pm 18\,\text{MeV}$ and width $173 \pm 32\,\text{MeV}$, are used to associate a systematic uncertainty to this choice of values, as described in §7.2.
- The P-wave, represented by the $\phi(1020)$ particle. It is described by a relativistic Breit-Wigner propagator. The mass and width parameters of this resonance have been left to float in the fit in order to account for mass resolution effects.

- The D-wave, represented by the $f_2^0(1270)$ particle. It is expressed as a relativistic Breit-Wigner propagator.

- The parameters of the rest of the resonances have been extracted from the Particle Data Group review of particle physics [55].

For $l = 0, 2$, only states with odd isospin are allowed to couple strongly to K^+K^-. For this reason, the particles $f_0^0(980)$, $f_0^0(1370)$ and $f_2^0(1270)$ are expected to have a very small contribution to the decay model. This is supported by a previous publication of the measurement of the CKM angle γ [23]. The reference decay model includes $f_0^0(1370)$ and $f_2^0(1270)$, but excludes $f_0^0(980)$, which is considered in an alternative model that contributes to assign a systematic uncertainty to this exclusion, and is described in §7.2.3.

2.5 Time dependent phase space analysis

The squared time-dependent amplitudes, which depend on the point in the phase space and the time, are

$$\left|\langle f|\mathcal{H}|\tilde{D}^0(t)\rangle\right|^2 = \left|\tilde{A}_f\right|^2 e^{-\Gamma t}\left|\frac{1+\chi^{\pm 1}}{2}h_1(t) + \frac{1-\chi^{\pm 1}}{2}h_2(t)\right|^2 \tag{2.96}$$

$$\begin{aligned} &= \left|\tilde{A}_f\right|^2 e^{-\Gamma t}\left[\frac{1+|\chi|^{\pm 2}}{2}\cosh(y\Gamma t) + \frac{1-|\chi|^{\pm 2}}{2}\cos(x\Gamma t) - \right. \\ &\qquad \left. \mathrm{Re}\left(\chi^{\pm 1}\right)\sinh(y\Gamma t) + \mathrm{Im}\left(\chi^{\pm 1}\right)\sin(x\Gamma t)\right], \end{aligned} \tag{2.97}$$

where $\tilde{D}^0$ and $\tilde{A}_f$ represent both D^0 and A_f or $\bar{D}^0$ and $\bar{A}_f$, and the $\pm$ signs in the exponents of χ are $+1$ for D^0 and -1 for $\bar{D}^0$.

If mixing did not exist ($x = y = 0$),

$$\left|\langle f|\mathcal{H}|\tilde{D}^0(t)\rangle\right|^2 = \left|\tilde{A}_f\right|^2 e^{-\Gamma t}, \tag{2.98}$$

where the $\tilde{D}^0$ lifetime dependence and the decay model dependence factorize.

Expression (2.96) is probably the simplest way to express the time evolution of the flavor eigenstates. However, expression (2.97) becomes useful for the practical reason of computing the norm of the PDF.

In practice, the $\tilde{D}^0$ lifetime dependent amplitude gets corrected by reconstruction efficiency non-uniformities across the phase space, expressed with a term $\epsilon(m^2_{AB}, m^2_{AC})$, and by $\tilde{D}^0$ lifetime resolution effects, expressed with a resolution function $R(t, \sigma_t)$, which depends on both the lifetime t and its per-event error σ_t. The time-dependent amplitude PDF is, therefore, expressed as

$$p^{D,t,\sigma_t} = \frac{1}{N_D}\epsilon(m^2_{ab}, m^2_{ac})\left(\left|\langle f|\mathcal{H}|\tilde{D}^0(t)\rangle\right|^2 \otimes_t R(t,\sigma_t)\right) p^{\sigma_t}_{nc}, \tag{2.99}$$

where N_D is a normalization constant, $p_{nc}^{\sigma_t}$ is the projection of the PDF over σ_t, $\otimes_t$ denotes convolution over t, and

$$\int_{-\infty}^{\infty} R(t,\sigma_t)\,dt = 1, \quad \forall\sigma_t. \tag{2.100}$$

The term for efficiency non-uniformities $\epsilon(m^2_{AB}, m^2_{AC})$ and the resolution function R are described in detail in §5.2.2 and §5.2.3.

The normalization of the PDF is an important issue, since it is of crucial importance in the fitting procedure. The following definitions of integrals over the phase space simplify this computation.

$$I_1 = \int \epsilon\left|A_f\right|^2 d\mathcal{P} \tag{2.101}$$

$$I_\chi = \frac{1}{I_1}\int \epsilon\left|A_f\right|^2 \chi\, d\mathcal{P} = \frac{q}{p}\frac{1}{I_1}\int \epsilon A_f^\star \bar{A}_f\, d\mathcal{P} \tag{2.102}$$

$$I_{\chi^2} = \frac{1}{I_1}\int \epsilon\left|A_f\right|^2 \left|\chi\right|^2 d\mathcal{P} = \left|\frac{q}{p}\right|^2 \frac{1}{I_1}\int \epsilon\left|\bar{A}_f\right|^2 d\mathcal{P}. \tag{2.103}$$

These integrals have to be done numerically. A description of several techniques on how to make these calculations can be found on §B.

2.5.1 Sensitivity to x and y over the phase space

If the $\tilde{D}^0$ lifetime is selected in a range that spans the most of the area under the lifetime PDF, it is a good approximation to consider

$$\int_{t_{\min}}^{t_{\max}} dt\left[e^{-\Gamma t}\,{}^{\sin}_{\cos}(x\Gamma t)\otimes_t R(t,\sigma_t)\right] \approx \int_0^\infty e^{-\Gamma t}\,{}^{\sin}_{\cos}(x\Gamma t)\,dt, \tag{2.104}$$

$$\int_{t_{\min}}^{t_{\max}} dt\left[e^{-\Gamma t}\,{}^{\sinh}_{\cosh}(y\Gamma t)\otimes_t R(t,\sigma_t)\right] \approx \int_0^\infty e^{-\Gamma t}\,{}^{\sinh}_{\cosh}(y\Gamma t)\,dt. \tag{2.105}$$

Such approximation has not been used in the actual analysis, but these expressions are useful to discuss which regions of the phase space are most sensitive to the mixing parameters x and y.

Using that

$$\int_0^\infty e^{-\Gamma t}\,{}^{\sin}_{\cos}(x\Gamma t)\,dt = \frac{1}{\Gamma}\frac{{}^{x}_{1}}{1+x^2}, \tag{2.106}$$

$$\int_0^\infty e^{-\Gamma t}\,{}^{\sinh}_{\cosh}(y\Gamma t)\,dt = \frac{1}{\Gamma}\frac{{}^{y}_{1}}{1-y^2}, \tag{2.107}$$

the norm of the PDF can be approximated as

$$N_D \approx \frac{I_1}{\Gamma}\left[\left(\frac{1+I_{\chi^2}}{2} - y\mathrm{Re}\left(I_\chi\right)\right)\frac{1}{1-y^2} + \left(\frac{1-I_{\chi^2}}{2} + x\mathrm{Im}\left(I_\chi\right)\right)\frac{1}{1+x^2}\right]. \tag{2.108}$$

If the efficiency is symmetric under the exchange of two squared invariant masses and there is no direct CP violation, then $I_{\chi^2} = |q/p|^2$. With the definitions in expressions (2.101-2.103), the projection of the PDF over the $\tilde{D}^0$ lifetime and its error can be approximated as

$$p^{t,\sigma_t} \approx \frac{I_1}{N_D} e^{-\Gamma t} \left[\frac{1+I_{\chi^2}}{2} \cosh(y\Gamma t) + \frac{1-I_{\chi^2}}{2} \cos(x\Gamma t) - \right. \\ \left. \mathrm{Re}\,(I_\chi) \sinh(y\Gamma t) + \mathrm{Im}\,(I_\chi) \sin(x\Gamma t) \right] \otimes_t R(t,\sigma_t)\, p_{nc}^{\sigma_t}. \tag{2.109}$$

The projection of the PDF over the amplitude variables can be approximated using expressions (2.106) and (2.107) as

$$p^D \approx \frac{\epsilon\,|A_f|^2}{N_D \Gamma} \left[\left(\frac{1+|\chi|^2}{2} - y\mathrm{Re}\,(\chi) \right) \frac{1}{1-y^2} + \left(\frac{1-|\chi|^2}{2} + x\mathrm{Im}\,(\chi) \right) \frac{1}{1+x^2} \right]. \tag{2.110}$$

In the approximation of CP conservation on equation (2.110), and imposing $y = 0$,

$$p^D \approx \frac{\epsilon}{I_1\,(1+x^2)} \left[|A_f|^2 + x\mathrm{Im}\left(A_f^\star \bar{A}_f\right) + x^2 \left(\frac{|A_f|^2 + \left|\bar{A}_f\right|^2}{2} \right) \right]. \tag{2.111}$$

The term that multiplies x in this expression shows that there is sensitivity to the x mixing parameter in regions that are symmetric over the Dalitz plot, which contain mainly neutral resonances. These regions are essential to provide sensitivity to the sign of x. The term that multiplies x^2 shows that there is also sensitivity in regions where the amplitude of the D^0, A_f, or of the $\bar{D}^0$, $\bar{A}_f$, are large (both charged and neutral resonances).

Similarly, imposing $x = 0$,

$$p^D \approx \frac{\epsilon}{I_1\,(1-y\mathrm{Re}\,(I_\chi))} \left[|A_f|^2 - y\mathrm{Re}\left(A_f^\star \bar{A}_f\right) - y^2 \left(\frac{|A_f|^2 - \left|\bar{A}_f\right|^2}{2} \right) \right]. \tag{2.112}$$

The term that multiplies y in this expression shows that there is sensitivity to the y mixing parameter in regions that are symmetric over the Dalitz plot, which contain mainly neutral resonances. These regions are also essential to provide sensitivity to the sign of y. The term that multiplies y^2 shows that there is also sensitivity in regions of the phase space where the decay amplitudes of the D^0, A_f, and of the $\bar{D}^0$, $\bar{A}_f$, have a large difference in moduli (charged resonances).

In summary, sensitivity to x and y over the phase space comes from regions with large values of the amplitude moduli, including both charged and neutral resonances. The latter are essential to provide sensitivity to the signs of x and y.

Chapter 3

The BaBar detector

3.1 Detector overview

The design of the BaBar detector is optimized for studies of CP violating asymmetries in the decay of neutral B mesons to CP eigenstates. In addition, the detector is well suited for other physics topics, such as precision measurements of decays of bottom and charm mesons and of τ leptons, and also searches for rare processes that become accessible with the high luminosity of the PEP-II B factory.

The PEP-II B factory is an asymmetric e^+e^- collider that, from 1999 to 2008, has successfully operated up to four times its design luminosity of $3 \cdot 10^{33}\,\mathrm{cm}^{-2}\mathrm{s}^{-1}$. The collisions take place at a center of mass energy of 10.58 GeV, which corresponds to the mass of the $\Upsilon(4S)$. At this energy, a resonant $\Upsilon(4S)$ is produced, which decays exclusively to $B^0\bar{B}^0$ and B^+B^- coherent pairs. This provides an ideal laboratory for the study of B mesons.

In PEP-II, the electron high energy beam of 9.0 GeV collides head on with the positron low energy beam of 3.1 GeV, resulting in a Lorenz boost of the center of mass frame of $\beta\gamma = 0.56$. This boost makes it possible to reconstruct the decay vertices of the two B mesons and to determine their relative decay times.

The BaBar detector [56] was designed and built by a large international team of scientists and engineers.

Figure 3.1 shows a longitudinal section through the detector center, and figure 3.2 shows and end view.

To maximize the geometric acceptance of the boosted B meson decays, the whole detector is offset relative to the beam to beam interaction point by 0.37 m in the direction of the lower energy beam.

The innermost part of the detector consists of a silicon vertex tracker (SVT), a drift chamber (DCH), a detector of internally reflected Čerenkov light (DIRC), and a CsI electromagnetic calorimeter (EMC). These systems are surrounded by a superconducting solenoid that generates

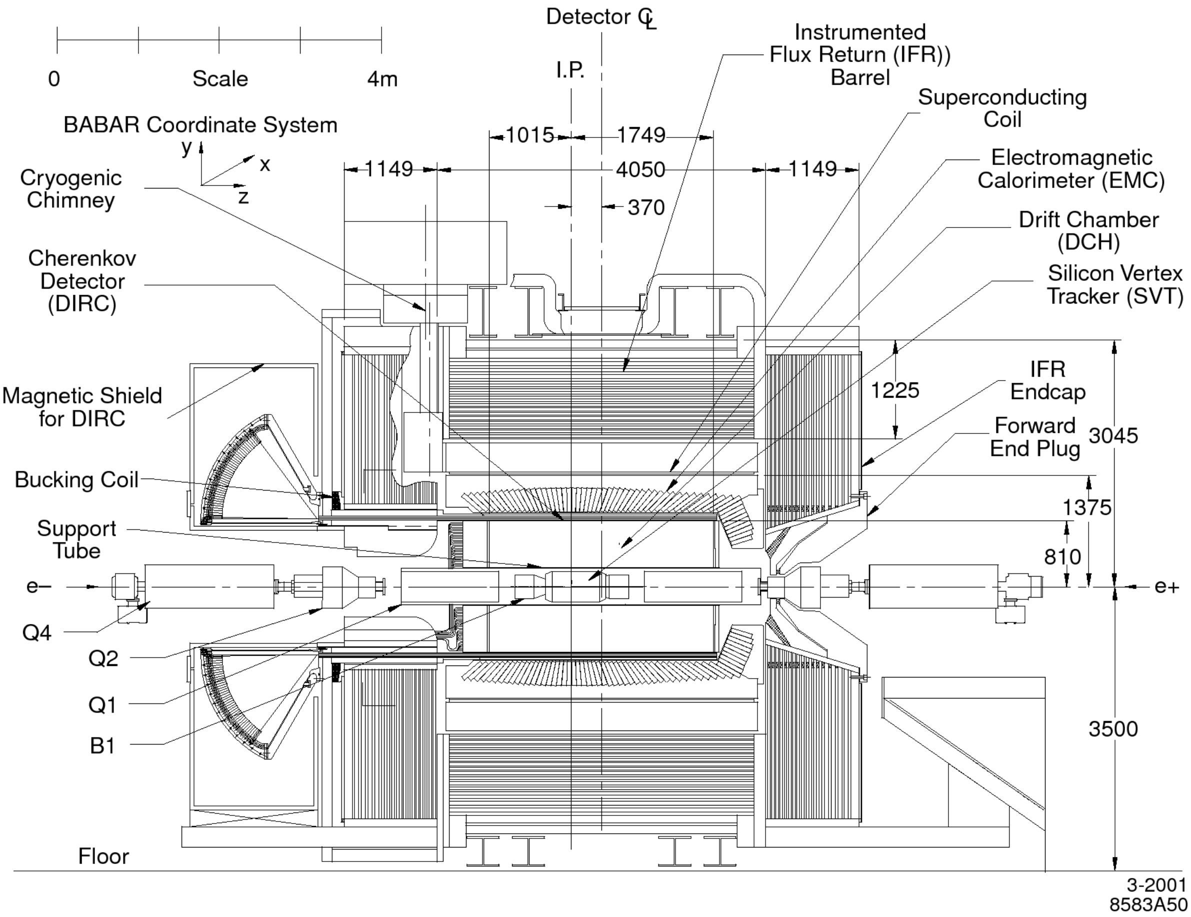

Figure 3.1: BaBar detector longitudinal view.

a magnetic field of 1.5 T. The region where the flux of the magnetic field returns is instrumented (IFR) for muon and neutral hadron detection.

The polar angle coverage extends to 350 mrad in the forward direction and 400 mrad in the backward direction, with respect to the direction of the high energy beam.

As plotted in figures 3.1 and 3.2, the right handed coordinate system has its z axis longitudinal to the principal axis of the drift chamber. This axis is offset to the beam axis by about 20 mrad in the horizontal plane. The x axis is horizontal to the floor and points away from the center of the PEP-II storage rings, and the y axis points upward.

The forward and backward acceptance of the tracking system are constrained by components of PEP-II, a pair of dipole magnets (B1) followed by a pair of quadrupole magnets (Q1). The vertex detector and these magnets are placed inside a support tube that is 4.5 m long and has 0.217 m of inner diameter. The central section of this tube is fabricated from a carbon fiber composite.

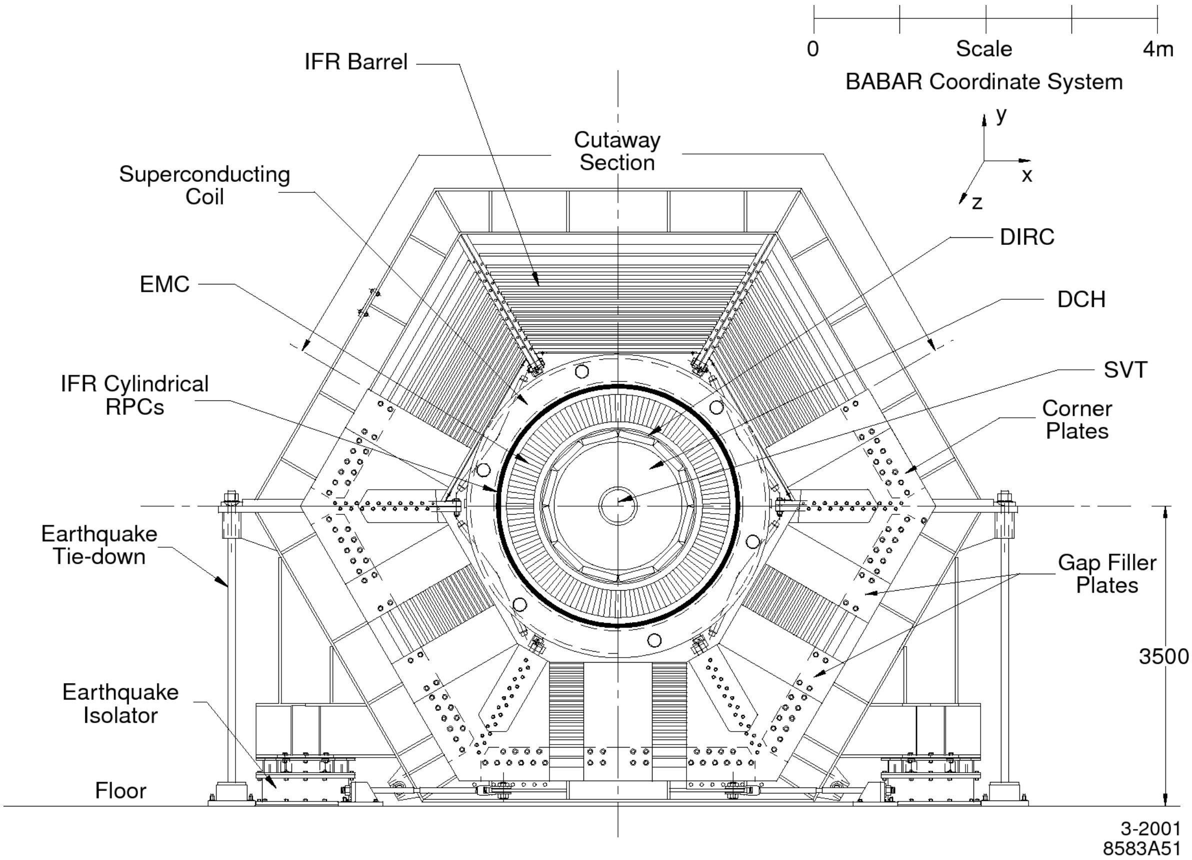

Figure 3.2: BaBar detector end view.

3.2 Silicon vertex tracker (SVT)

The charged particle tracking system is composed of the silicon vertex tracker (SVT) and the drift chamber (DCH). Their principal purpose is the efficient detection of charged particles and the precision measurement of their momenta. These precision measurements allow for the reconstruction of exclusive B and D meson decays with high momentum and vertex resolution and minimal background. The reconstruction of multiple decay vertices of weakly decaying B and D mesons is crucial for the physics goals of the experiment.

Track measurements are also important to match their extrapolation with the measurements obtained at the DIRC, EMC, and IFR. The most critical measurements are the angles at the DIRC, since the uncertainties in the charged particle track parameters add to the uncertainty in the measurement of the Čerenkov angle. For this reason, the track errors from the combined SVT and DCH measurements should be small compared to the average DIRC Čerenkov angle measurements.

The SVT was designed to measure angles and positions of charged particles just outside the beam pipe, very close to the interaction region. It is composed of five layers of double sided silicon strip detectors that are assembled as modules. The readout of these modules is situated at both ends, thus keeping the inactive material in the acceptance volume at the smallest possible level.

The SVT is critical for the measurement of the time dependent CP asymmetries. To avoid any significant impact of the detector resolution to CP sensitive measurements, the mean vertex resolution along the z axis for a fully reconstructed B decay is better than $80\,\mu$m.

In the plane perpendicular to the beam line, the SVT provides a resolution of the order of $\sim 100\,\mu$m. This requirement comes from the need to reconstruct final states in B, τ and charm decays. For example, in decays of the type $B^0 \to D^+D^-$, the distance between the two D mesons in the plane perpendicular to the beam line is typically $\sim 275\,\mu$m.

Some of the decay products of B and D mesons have low transverse momentum, p_t. The SVT provides standalone tracking for particles with transverse momentum less than 120 MeV, the minimum measurable with the DCH alone. This feature is also fundamental for the identification of slow pions from $D^\star$ meson decays, which the analysis presented here relies upon. A tracking efficiency of 70 % or more is necessary for tracks with a transverse momentum in the range from 50 MeV to 120 MeV.

The standalone tracking capability and the need to link SVT tracks to the DCH were crucial in choosing the number of layers.

The inner three layers are mounted as close as possible to the water cooled beryllium beam pipe. This minimizes the impact of multiple scattering in the beam pipe on the extrapolation of the tracks to the vertex. The inner three layers primarily provide position and angle information for the measurement of the vertex position.

The outer two layers are at much larger radii. This provides the coordinate and angle measurements needed for linking SVT and DCH tracks.

To fulfill the requirements on vertex precision, the spatial resolution of the three inner layers is $10 - 15\,\mu$m and about $40\,\mu$m in the two outer layers. The inner three layers perform the impact parameter measurements, and the outer ones are necessary for pattern recognition and low p_t tracking.

The SVT withstands a maximum of 1 rad/day of ionizing radiation in the horizontal plane immediately outside the beam pipe, where the highest radiation is concentrated, and 0.1 rad/day on average elsewhere.

The SVT is not accessible during normal detector operations. The time needed for any replacement is estimated to be 4 to 5 months. For this reason, reliability and robustness are mandatory. All the components of the SVT inside the support tube have a long mean time to failure, and redundancies are built in whenever possible.

The SVT is water cooled to remove the heat generated by the electronics.

3.2.1 Layout

The five layers of silicon strip sensors of the SVT are organized in modules. The three inner layers have 6 modules each, while the 4th and 5th layers have 16 and 18 modules, respectively.

A photograph of the SVT is shown in figure 3.3.

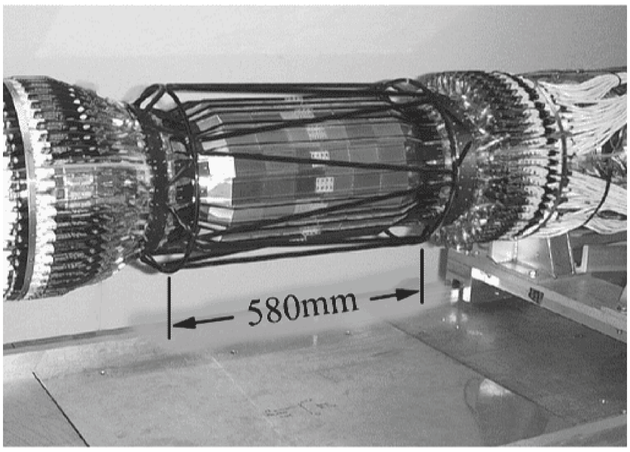

Figure 3.3: Fully assembled SVT. The silicon sensors of the outer layer are visible, as is the carbon fiber space frame that surrounds the silicon (black structure).

The strips on the opposite sides of each sensor are oriented perpendicularly to each other. The strips measuring the azimuthal angle (ϕ strips) run parallel to the beam, and the z measuring strips (z strips) are oriented transversely to the beam axis.

The modules of the inner 3 layers are straight, and those of layers 4 and 5 are arch shaped (figures 3.4 and 3.5). This arch shaped design was chosen to minimize the amount of silicon required to cover the solid angle and to increase the crossing angle for particles near the edges of acceptance. A photograph of an outer layer arch module is shown in figure 3.6

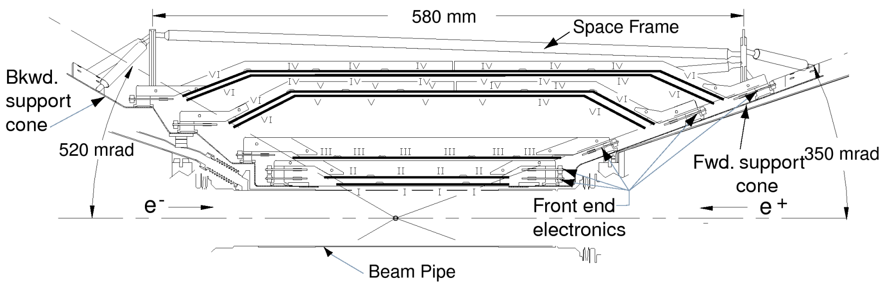

Figure 3.4: Schematic view of the longitudinal section of the SVT. The roman numerals label the six different types of sensors.

The inner modules are tilted in ϕ by 5°, allowing an overlap region between adjacent modules. This provides full azimuthal coverage and has advantages for alignment. The arch geometry does not allow the outer modules to be tilted. For this reason, and for the same purpose of having an overlap in the ϕ coordinate and to avoid gaps, layers 4 and 5 are divided into two sub-layers and placed at slightly different radii (see figure 3.5).

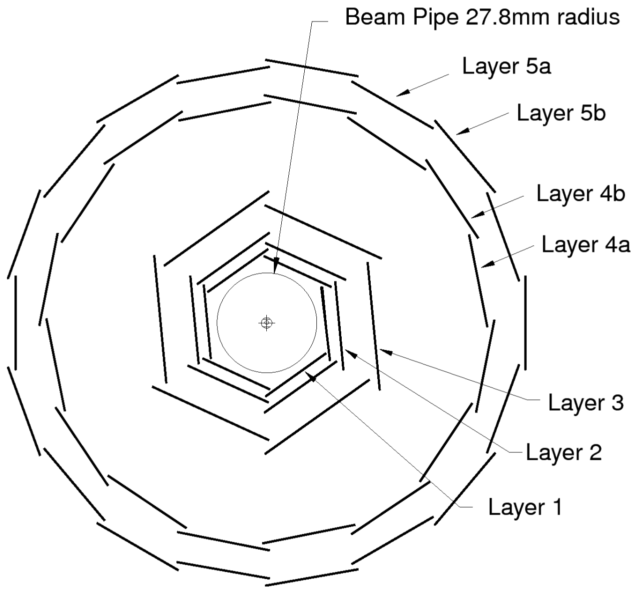

Figure 3.5: Schematic view of the transverse section of the SVT.

3.2.2 Radiation monitoring

Radiation monitoring is extremely important to ensure that the SVT does not exceed its radiation budget, which could cause irreversible damage to the detector. This radiation budged was not exceeded at the time of the shutdown of BaBar.

3.2.3 Defects

Due to a series of minor mishaps occurred during the installation of the SVT, nine out of 208 readout sections (each corresponding to one side of a half module) were damaged and not functioning. The reasons for these damages are various: defective connectors, mishandling during installation, and not fully understood problems on the front end electronics. There has been no module failure due to radiation damage.

The presence of defective modules has had a very small impact on the physics analyses that have been carried on within the BaBar collaboration.

Figure 3.6: Picture of an SVT arch module.

3.3 Drift chamber (DCH)

The main purpose of the DCH is the momentum measurement of charged particles. Additionally, it provides information for the charged particle trigger and a measurement of dE/dx (energy loss per unit of flight length), useful for particle identification (PID).

The DCH complements the measurements of the impact parameter and the directions of charged tracks provided by the SVT.

At low momenta, the DCH measurements dominate the errors on the extrapolation of the charged tracks to the DIRC, EMC, and IFR.

The reconstruction of decay and interaction vertices outside of the SVT volume relies strongly on the DCH. For this reason, the chamber is able to measure not only the transverse momenta and positions, but also the longitudinal position of track, with a resolution of $\sim 1\,\mathrm{mm}$.

The DCH also supplies information for the charged particle trigger.

For low momentum particles, the DCH provides particle identification by measurement of ionization energy loss per unit length (dE/dx). A resolution of about $7\,\%$ allows π/K separation for momenta up to $700\,\mathrm{MeV}$.

The particle identification capability complements the performance of the DIRC in the barrel region. In the extreme forward and backward directions, the DCH is the only device that provides discrimination of particles with different mass.

Since the average momentum of charged particles produced in B and D decays is less than 1 GeV, multiple scattering is a significant limitation on the track parameter resolution. Multiple scattering inside the DCH is minimized by means of a choice of low mass wires and a helium based gas mixture. In addition, the material in front and inside the chamber volume has been minimized in such a way that the DCH represents only $0.002X_0$, being X_0 one radiation length.

The design of the DCH is compact. It has 40 layers of small approximately hexagonal cells. Longitudinal information is derived from 24 out of the 40 wires placed at small angles to the principal axis. For particles with transverse momentum greater than 180 MeV, this provides up to 40 spatial and energy loss measurements.

Material in the outer wall and in the forward direction is minimum to avoid degrading the performance of the DIRC and the EMC. To minimize the amount of material in front of the calorimeter endcap, the readout electronics of the DCH are mounted on the backward endplate of the chamber.

A longitudinal cross section and dimensions of the DCH are shown in figure 3.7.

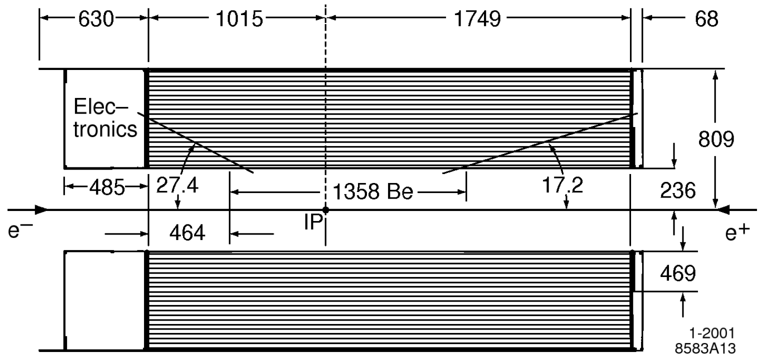

Figure 3.7: Longitudinal section of the DCH with principal dimensions. The chamber is offset by 370 mm from the interaction point (IP).

3.3.1 Drift cells

The DCH consists of a total of 7104 small drift cells, arranged in 40 cylindrical layers. These layers are grouped by four into ten super-layers. These super-layers have the same wire orientation and equal number of cells in each layer. Sequential layers are staggered by half a cell. This arrangement enables local segment finding and left-right ambiguity resolution within a super-layer, even if one out of four signals is missing.

The stereo angles of the super-layers alternate between axial (A) and stereo (U,V) pairs, in the order AUVAUVAUVA, as shown in figure 3.8. The stereo angles vary between ±45 mrad and ±76 mrad.

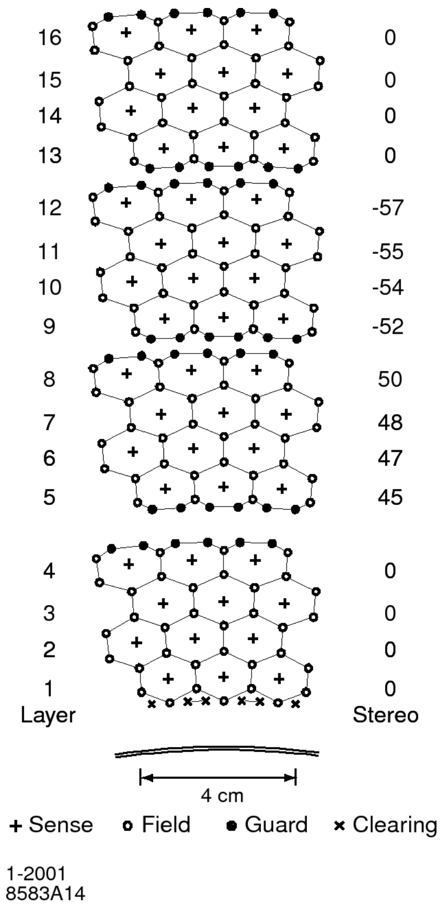

Figure 3.8: Schematic layout of the drift cells for the four innermost super-layers. The numbers on the right side give the stereo angles in $mrad$ of sense wires in each layer.

The drift cells are hexagonal in shape, approximately 11.9 mm along the radial direction, and 19.0 mm in the azimuthal direction. The hexagonal cell configuration provides an approximate circular symmetry over a large portion of the cell (figure 3.9).

Each cell consists of one sense wire surrounded by six field wires, as shown in figure 3.8. Field wires are at ground potential, and a positive high voltage is applied to the sense wires. An avalanche gain of approximately $5 \cdot 10^4$ is obtained at a typical operating voltage of 1960 V.

For cells at the inner or outer boundary of a super-layer, two guard wires are added to improve the electrostatic performance of the cell and to match the gain of the boundary cells to those of the cells in the inner layers.

At the innermost boundary of layer 1 and the outermost boundary of layer 40, two clearing wires are added per cell to collect charges created through photon conversions in the material of the walls.

The specific energy loss, dE/dx per track traversing the DCH is computed as a truncated mean from the lowest 80% of the individual measurements of charge deposited in each drift cell. Corrections are also applied to remove sources of bias that degrade the accuracy of the primary

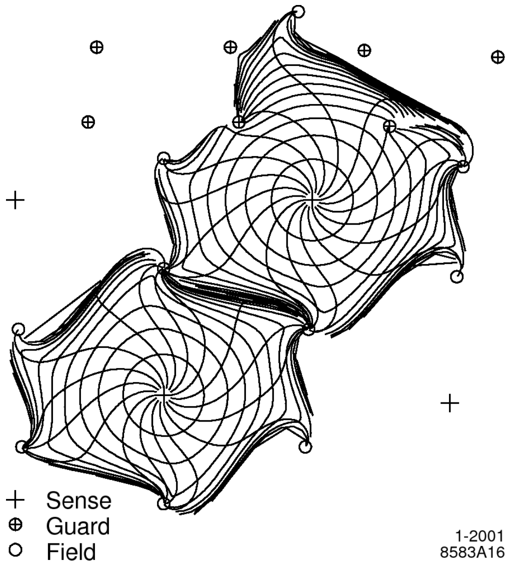

Figure 3.9: Drift cell isochrones (contours of equal drift times of ions) in cells of layers 3 and 4 of an axial super-layer. The isochrones are spaced by 100 ns.

ionization measurement, such as changes in gas pressure and temperature, differences in cell geometry and charge collection, signal saturation, non linearities and variation of cell charge collection as a function of the entrance angle.

3.4 Detector of internally reflected Čerenkov light (DIRC)

The study of CP violation requires the ability to tag the flavor of the mesons by means of their decay products. The momenta of the kaons used for flavor tagging extends up to 2 GeV, though the most of them is below 1 GeV. Besides, pions and kaons of the specific decays $B^0 \rightarrow \pi^+\pi^-$ and $B^0 \rightarrow K^+\pi^-$ must be well distinguished. Their momenta ranges from 1.7 GeV to 4.2 GeV. This momentum is strongly related with their polar angle distribution, due to the boost of the center of mass frame.

The detector of internally reflected Čerenkov light (DIRC) [57] is intended to identify separately pions and kaons with momentum from above 500 MeV to the kinematic limit of 4.5 GeV. For momenta below 700 MeV, particle identification relies on the dE/dx measurements in the DCH and SVT.

Čerenkov light is produced in 4.9 m long bars of synthetic fused silica of rectangular cross section of $1.7\,cm \times 3.5$ cm. This light is transported by total internal reflection to an array of photomultiplier tubes, and the angle of emission is preserved along this transportation process. This array forms the backward wall of a toroidal water tank located beyond the backward end of the magnet. Images of the Čerenkov rings are reconstructed from the position and time of arrival of the light signals to the photomultiplier tubes.

Since the calorimeter is located right after the DIRC, the particle identification (PID) system has been designed thin and uniform in terms of radiation lengths.

The DIRC provides separation of pions and kaons at the level of $\sim 4\sigma$ or larger for all tracks from B meson decays.

The DIRC is based on the fact that the magnitudes of angles are preserved upon reflection on a flat surface. Figure 3.10 shows a schematic of the DIRC geometry that illustrates the principles of light production, transport, and imaging.

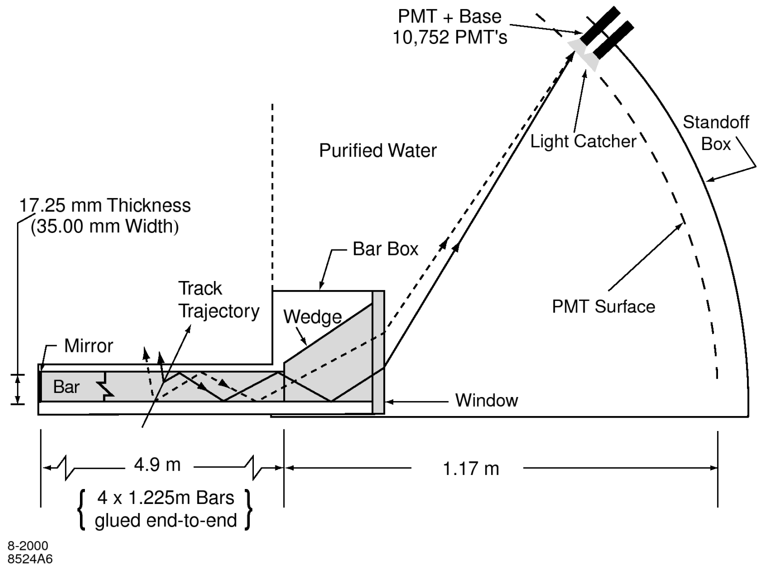

Figure 3.10: Schematics of the DIRC radiator bar and imaging region.

With β being the velocity of a particle in units of the speed of light, and n the refraction index of the radiator material, the Čerenkov angle θ_c verifies the relation $\cos\theta_c = 1/n\beta$. The larger is the refraction index of the radiator material, the more sensitive is the device to the measurement of the velocity of the particle.

The radiator material of the DIRC is synthetic fused silica in the form of long, thin bars with rectangular cross section. These bars are also light pipes for the light trapped in the radiator by total internal reflection. Synthetic fused silica is chosen because of its resistance to ionizing radiation, long attenuation length, large index of refraction, and low chromatic dispersion within the wavelength acceptance of the DIRC.

A fused silica wedge at the exit of the bar reflects photons at large angles relative to the bar axis.

Particles travelling close to the speed of light ($\beta \approx 1$), some photons are transported to either one or both ends of the bar, depending on the particle incident angle. To avoid instrumenting both ends of the bar with photon detectors, a mirror is placed at the forward end, perpendicular to the bar axis, so photons travelling forward are reflected to the backward instrumented end.

At the instrumented end region, there is a water filled tank called the *standoff box*. The photons are detected by an array of densely packed photomultiplier tubes (PMT), each of them surrounded by reflecting *light catcher* cones to capture light that otherwise could miss the active area of a PMT.

The PMTs are placed at a distance of about 1.2 m from the bar ends. The expected Čerenkov light pattern at this surface is a conic section, where the cone opening angle is the Čerenkov production angle modified by refraction at the exit from the fused silica window.

3.5 Electromagnetic calorimeter (EMC)

The electromagnetic calorimeter (EMC) is designed to measure electromagnetic showers with excellent efficiency, and with a high energy and angular resolution over the energy range from 20 MeV to 9 GeV. This allows the detection of photons from π^0 and η decays as well as high energy photons and electrons from electromagnetic, weak, and radiative processes.

By identifying electrons, the EMC contributes to the flavor tagging of neutral B mesons via semileptonic decays, to the reconstruction of vector mesons, like $\psi(1S)$, and to the study of semileptonic and rare decays of B and D mesons, and τ leptons.

3.5.1 Layout

The measurement of extremely rare decays of B mesons, like $B^0 \to \pi^0\pi^0$, poses strong requirements on energy resolution, namely of order $1-2\,\%$. Such requirements lead to the choice of a hermetic total absorption calorimeter, composed of a finely segmented array of 6580 thallium-doped cesium iodide crystals (CsI(Tl)). These crystals are arranged in modules that are supported individually from an external support structure. This structure consists of a barrel and a forward endcap. There is no backward endcap, since the front end assembly electronics of the drift chamber is located there. The crystals are read out by silicon photodiodes that are matched to the spectrum of scintillation light and mounted on the rear surface. To maintain the desired performance, low noise analog circuits are used, and the electronics and energy response of the EMC are calibrated frequently.

The EMC consists of a cylindrical barrel and a conical forward endcap. It has full coverage in azimuth, and extends from 15.8° to 141.8° in polar angle, which corresponds to a 90 % solid angle coverage in the center of mass reference frame.

The barrel contains 5760 crystals arranged in 48 rings with 120 identical crystals each. The endcap holds 820 crystals arranged in 8 rings. Figure 3.11 shows a longitudinal view of the EMC layout.

The crystals have a trapezoidal cross section, and their length ranges from 29.6 cm in the backward to 32.4 cm in the forward direction, corresponding to $16-17.5$ times the radiation length. This limits the effects of shower leakage from increasingly higher energy particles. The silicon photodiodes are glued to a transparent polystyrene substrate with a thickness of 1.2 mm that, in turn, is glued to the center of the rear face of the crystal by an optical epoxy to maximize light transmission.

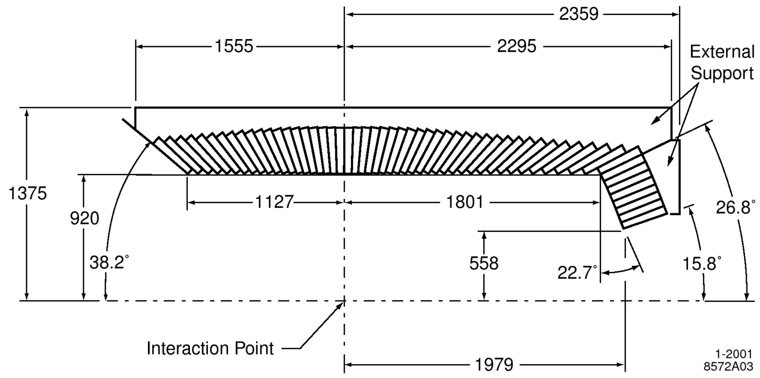

Figure 3.11: Longitudinal cross section of the top half of the EMC, indicating the arrangement of the 56 crystal rings. The detector is axially symmetric around the z axis. All dimensions are given in mm.

During data taking, the data acquisition imposes a single crystal lower readout threshold of 1 MeV in order to keep the data volume at an acceptable level. During stable colliding beam conditions, on average 1000 crystals are read out, corresponding to an average occupancy of 16 %. A typical hadronic event contributes signals in 150 crystals.

With the exception of minor cable damage during installation, which left two channels inoperative, all the readout channels have met their reliability requirements.

3.5.2 Reconstruction algorithms

A typical electromagnetic shower spreads over many adjacent crystals, forming a cluster of energy deposits. Pattern recognition algorithms have been developed to identify these clusters and to determine if they are generated by a charged or a neutral particle.

Clusters are required to contain at least one seed crystal with an energy above 10 MeV. Surrounding crystals are considered part of the cluster if their energy exceeds 1 MeV, or if they are contiguous neighbors of a crystal with at least 3 MeV.

3.5.3 Energy and angular resolution

The EMC has an energy resolution given by

$$\frac{\sigma_E}{E} = \frac{(2.32 \pm 0.30) \cdot 10^{-2}}{\sqrt[4]{E/GeV}} \oplus (1.85 \pm 0.12) \cdot 10^{-2}. \tag{3.1}$$

This expression is derived from several processes depending on the energy range. At high energy it is derived from Bhabha scattering, where the energy of the detected shower can be predicted from the polar angle of the $e^{\pm}$. At low energy it is measured with an radioactive source or with specific decay channels.

The angular resolution of the EMC is given by

$$\sigma_\theta = \sigma_\phi = \left(\frac{3.87 \pm 0.07}{\sqrt{E/GeV}} \oplus (0.00 \pm 0.04) \right) \text{ mrad.} \tag{3.2}$$

3.6 Instrumented flux return (IFR)

The instrumented flux return was designed to identify muons with high efficiency and good purity, and to detect long lived neutral hadrons over a wide range of momenta and angles, mostly K_l and neutrons. For this purpose, the steel in the magnet flux return, both in the barrel and the two endcap doors, is segmented into layers with thicknesses ranging from 2 cm in the inside to 10 cm at the outside. Between these steel absorbers, single gap resistive plate chambers (RPC) [58] detect streamers from ionizing particles by means of external capacitive readout strips.

Muons are important for tagging the flavor of neutral B mesons via semileptonic decays, for the reconstruction of vector mesons, like $\psi(1S)$, and for the study of semileptonic and rare decays involving leptons from B and D decays and τ leptons. K_l detection allows the study of exclusive B decays, in particular CP eigenstates.

3.6.1 Design

The IFR uses the steel flux return of the magnet as a muon filter and hadron absorber. Single gap resistive plate chambers (RPC) with two coordinate readout have been chosen as detectors. The RPCs are installed in the gaps of the finely segmented steel of the barrel and the end doors of the flux return, as illustrated in figure 3.12.

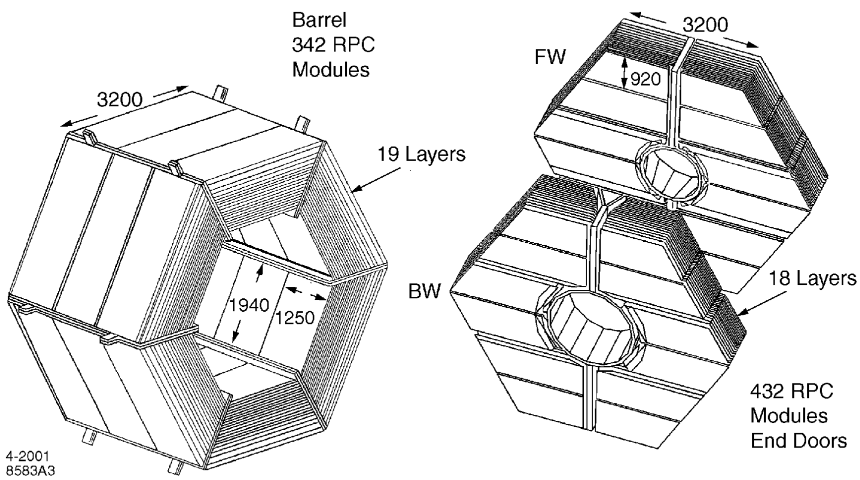

Figure 3.12: Overview of the barrel sectors and forward and backward end doors of the IFR. The shape of the RPC modules and their dimensions in mm are indicated.

The planar RPCs consist of two bakelite sheets, with a thickness of 2 mm and separated by a gap of 2 mm. The external surfaces are coated with graphite, connected to a high voltage (~ 8 kV) and ground. The internal surfaces, facing the gap, are treated with linseed oil. RPCs detect streamers from ionizing particles via capacitive readout strips. They operate with a non-flammable gas mixture, typically 56.7 % argon, 38.8 % freon 134a (1,1,1,2 tetrafluoroethane), and 4.5 % isobutane, within the two layers of bakelite.

The steel is segmented into 18 plates, increasing in thickness from 2 cm for the inner nine plates to 10 cm for the outermost plates. The nominal gap between the steel plates is 3.5 cm in the inner layers of the barrel and 3.2 cm elsewhere. There are 19 RPC layers in the barrel and 18 in the endcaps. In addition, two layers of cylindrical RPCs with four readout planes are installed between the EMC and the magnet cryostat to detect particles exiting the EMC.

There are 806 RPC modules, 57 in each of the six barrel sectors, 108 in each of the four half end doors, and 32 in the two cylindrical layers. Each barrel module has 32 strips running perpendicular to the beam axis to measure the z coordinate and 96 strips parallel to the beam axis extending over three modules to measure ϕ.

During the first year of operation, a large fraction of the RPC modules had suffered significant losses in efficiency. It was found that linseed oil droplets had formed on the inner surface of the bakelite plates, some bridging the gap and forming electric-short spots and leaving serious permanent damage to their performance. [59]

The resistive plate chambers have been replaced with limited streamer tubes (LST). The LSTs consist of gas-filled tubes with a single wire at high voltage. An LST cell consists of a silver plated sense wire 100 mm in diameter, located at the center of a cell of 9 mm^2 section. A charged particle passing through the cell ionizes the gas and a streamer builds up, which can be read out from the wire. Simultaneously, a signal is induced on the plane mounted below the tube, which is detected using strips perpendicular to the wire direction. The wire direction is mounted on BaBar longitudinally to the z axis, thus providing the ϕ coordinate. The strips provide the z coordinate. The mixture of gas is 89 % CO_2, 3 % argon and 8 % isobutane.

The first installation phase of the LSTs was done from August to October 2004. The RPCs from the inner 18 layers of the top and bottom sextants were removed (19th layer was unaccessible). LSTs were installed in 12 of the 18 layers, and brass was installed in the other 6 to increase the total absorption length. The second installation phase was done in autumn 2006, and the replacement of RPCs with LSTs was completed.

Figure 3.13 shows the pion rejection rate as a function of the muon efficiency for high energy muons ($p \in (2, 4)$ GeV) for years 2000, 2004 and 2005. During 2005, there were data from both RPCs and LSTs. With the LSTs, the overall performance is even better than the initial performance of the RPCs in the first year of operation.

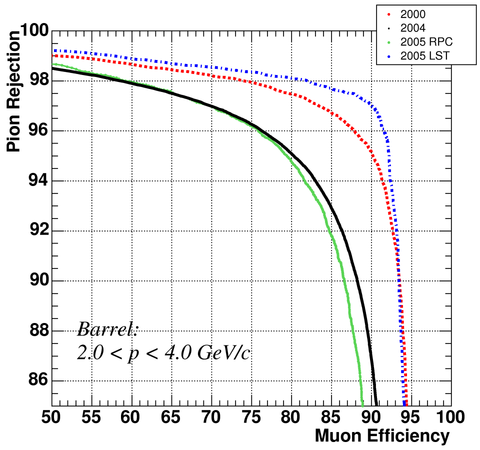

Figure 3.13: Pion rejection rate of the IFR as a function of the muon efficiency for years 2000 (red), 2004 (black) and 2005 for RPCs (green) and 2005 for LSTs (blue).

3.7 Trigger

The basic function of the trigger is to select events of interest with a high, stable, and well-understood efficiency while rejecting background events and keeping the total event rate under 120 Hz.

The trigger efficiency is larger than 99 % for all $B\bar{B}$ events and larger than 95 % for continuum events. Other event types, such as $\tau^+\tau^-$ events, have a less stringent requirement of about $90-95$ % efficiency, depending on the specific $\tau^\pm$ decay channel.

The trigger system is robust and flexible in order to function even under extreme background situations. It can also operate in an environment with dead or noisy channels.

The trigger is implemented as a two-level hierarchy, the Level 1 (L1) in hardware followed by the Level 3 (L3) in software. The L1 trigger decision is based on charged tracks in the DCH above a preset transverse momentum, showers in the EMC, and tracks detected in the IFR. The DCH trigger (DCT), the EMC trigger (EMT), and the IFR trigger (IFT) generate trigger *primitives*, summary data on the position and energy of particles, that are sent to the global trigger (GLT) every 134 ns. The GLT processes all trigger primitives to form specific triggers and then delivers them to the Fast Control and Timing System (FCTS).

The L3 trigger software comprises event reconstruction and classification, a set of event selection filters, and monitoring. This software runs on the online computer cluster. The filters have access to the complete event data for making their decision.

Chapter 4

Event selection

The time scale of mixing effects in the neutral D meson is two orders of magnitude larger than the D meson decay time itself. In other words, it decays much faster than it has time to undergo mixing. For this reason, the event selection must guarantee that the purity of the sample is as high as possible, also keeping, when it is possible, a large efficiency for signal events.

The $\tilde{D}^0$ meson is tagged at production as D^0 or $\bar{D}^0$ by means of the decay

$$D^{\star +} \to D^0 \pi_s^+, \tag{4.1}$$

$$D^{\star -} \to \bar{D}^0 \pi_s^-. \tag{4.2}$$

The low-momentum pion $\pi_s^\pm$ is commonly called **soft pion**, and its charge is used to tag the flavor of the $\tilde{D}^0$ meson.

This analysis studies the $\tilde{D}^0$ resonant structure by means of a Dalitz analysis dependent on the $\tilde{D}^0$ proper lifetime. The two decays

$$\tilde{D}^0 \to K_s \pi^+ \pi^-, \tag{4.3}$$

$$\tilde{D}^0 \to K_s K^+ K^-, \tag{4.4}$$

are reconstructed, where $K_s \to \pi^+\pi^-$.

To refer to both $K_s\pi^+\pi^-$ and $K_sK^+K^-$ decay modes, usually the compact notation $K_sh^+h^-$ is used, where $h = \pi, K$.

A Monte Carlo simulated event is considered to be a signal one if the whole decay chain $D^{\star\pm} \to \tilde{D}^0\pi_s^\pm$, $\tilde{D}^0 \to K_sh^+h^-$, $K_s \to \pi^+\pi^-$ is reconstructed, and all the reconstructed charged particles in the final state are matched with their respective Monte Carlo generated ones.

4.1 Data and Monte Carlo samples

The data sample used in this analysis is summarized in table 4.1, with the integrated luminosity specified for each of the six BaBar run periods. A total of $468.5\,\text{fb}^{-1}$ of data is used.

Run period	Luminosity (fb^{-1})	
	On peak	Off peak
Run 1	20.4	2.6
Run 2	61.6	6.9
Run 3	31.8	2.5
Run 4	100.3	10.1
Run 5	133.3	14.5
Run 6	78.8	7.9
Total	424.1	44.4
	468.5	

Table 4.1: Integrated luminosities for data, with the detailed contributions from each run period.

The Monte Carlo production is composed by five background samples ($B^0\bar{B}^0$, B^+B^-, $c\bar{c}$, uds and $\tau^+\tau^-$), and the signal samples of the $K_s\pi^+\pi^-$ and $K_sK^+K^-$ $\tilde{D}^0$ decay modes. For each of the two $\tilde{D}^0$ decay modes, three signal samples have been produced, with different characteristics: the *flat* samples contain signal events where the phase space has been modeled as a constant with respect to m^2_{ab} and m^2_{ac} defined in §2, i.e., with no resonances implemented in their production. The mixing parameters of this sample are forced to be $x = y = 0$. The *nomix* samples contain signal events produced with an isobar decay model composed of a linear combination of relativistic Breit-Wigner propagators, with the mixing parameters being forced to be $x = y = 0$. The *mix* samples contain signal events produced with the same model than the *nomix* sample, but with the mixing parameters being forced to be $x = y = 10^{-2}$. Monte Carlo $\tilde{D}^0$ decays have been generated with the `EvtGen` package [60], and the interactions between the generated particles and the detector material are simulated with the `GEANT4` package [61]. The resulting samples are processed in the same was as the real data recorded by the detector. The implementation of the model used in this analysis in `EvtGen` is described in §C.

Since $c\bar{c}$ background events can also contain signal events, these are removed from the $c\bar{c}$ sample so the background can be studied separately from the signal.

The Monte Carlo sample is summarized in table 4.2. The values of the luminosity column have been calculated using the values of the cross sections and branching ratios of table 4.3.

Channel		Events (10^6)	Luminosity (fb^{-1})
	$B^0\bar{B}^0$	718.0	1305.5
	B^+B^-	708.7	1288.7
	$c\bar{c}$	1237.9	952.2
	uds	999.0	478.0
	$\tau^+\tau^-$	430.3	483.5
	flat	5.678	720.6
$K_s\pi^+\pi^-$ signal	*nomix*	7.952	1009.1
	mix	7.952	1009.1
	flat	1.894	1521.3
$K_sK^+K^-$ signal	*nomix*	1.982	1592.0
	mix	1.982	1592.0

Table 4.2: Number of generated Monte Carlo events for the different background and signal samples, with their corresponding integrated luminosities. For signal, the reported number of events is the sum of D^0 and $\bar{D}^0$ events.

Magnitude	Value	Units
$\sigma_{b\bar{b}}$	1.1	nb
$\sigma_{c\bar{c}}$	1.3	nb
σ_{uds}	2.09	nb
$\sigma_{\tau^+\tau^-}$	0.89	nb
$\sigma_{D^\star X}$	580 $\pm$ 70	pb
$R(D^{\star\pm} \to \tilde{D}^0\pi^\pm)$	0.677 ± 0.005	
$R(\tilde{D}^0 \to K_s\pi^+\pi^-)$	$(2.88 \pm 0.19) \cdot 10^{-2}$	
$R(\tilde{D}^0 \to K_sK^+K^-)$	$(4.55 \pm 0.34) \cdot 10^{-3}$	
$R(K_s \to \pi^+\pi^-)$	$(6.920 \pm 0.005) \cdot 10^{-1}$	

Table 4.3: Cross sections for $b\bar{b}$ production ($\sigma_{b\bar{b}}$), $c\bar{c}$ production ($\sigma_{c\bar{c}}$), light quark production (σ_{uds}), τ pair production ($\sigma_{\tau^+\tau^-}$) and $D^{\star\pm}$ production ($\sigma_{D^\star X}$), in e^+e^- events, and branching fractions R for the different decays involved in the signal decay chain.

4.2 Event reconstruction and preselection

All the information used in this analysis is kept in data files that contain all the necessary information on the reconstructed events. Information on the complete true Monte Carlo particle family tree and truth match information are also added to the data files.

A charged particle is considered to be correctly truth matched if its position in the decay family tree is the same for the reconstructed and the true events. This family tree is allowed to have radiative decays, where one or two photons are emitted in the $D^{\star\pm}$, $\tilde{D}^0$ or K_s decays.

In some cases, the pions of the final state, daughters of the $D^{\star\pm}$, $\tilde{D}^0$ or K_s, may decay in flight,

$$\pi^{\pm} \to \mu^{\pm}\tilde{\nu}_{\mu}, \tag{4.5}$$

where $\tilde{\nu}_{\mu}$ may represent both a ν_{μ} or a $\bar{\nu}_{\mu}$, depending on the charge of the decaying pion. Since the masses of the $\pi^{\pm}$ and the $\mu^{\pm}$ are very similar, the neutrino $\tilde{\nu}_{\mu}$ can only carry a small fraction of the momentum from this decay, so the energy and momentum of the $\pi^{\pm}$ and the $\mu^{\pm}$ are very similar. For this reason, if a reconstructed pion is matched with a $\mu^{\pm}$ that is the daughter of a $\pi^{\pm}$ from the correct family tree, the particle is also considered to be correctly truth matched.

Since several cuts need to be applied for the final event selection, a first preselection with looser cuts is done during the reconstruction of the K_s, $\tilde{D}^0$ and $D^{\star\pm}$, thus reducing the size of the data files. The details on the reconstruction of the K_s, $\tilde{D}^0$ and $D^{\star\pm}$ and the preselection cuts applied are reported below.

4.2.1 K_s reconstruction

K_s candidates are formed by combining two pion tracks with opposite electric charge. The reconstruction algorithm constrains the K_s daughters to originate from a common vertex. A K_s mass (m_{K_s}) window cut of 25 MeV is applied with respect to the nominal K_s mass [55].

4.2.2 $\tilde{D}^0$ reconstruction

$\tilde{D}^0$ candidates are formed by combining K_s candidates with two pion or kaon tracks with opposite electric charge. $\tilde{D}^0$ daughters are constrained to originate from a common vertex. Particle identification is used for the charged $\tilde{D}^0$ candidate daughters. A $\tilde{D}^0$ mass (m_D) window cut of 40 MeV is applied with respect to the nominal $\tilde{D}^0$ mass value [55]. An additional cut on the $\tilde{D}^0$ momentum in the incident e^+e^- center of mass reference frame, $p^{\star}_{D} > 2.2$ GeV is also applied. A beam spot constraint is applied on the $\tilde{D}^0$ production vertex in order to improve the resolution on m_D.

4.2.3 $D^{\star\pm}$ reconstruction

$D^{\star\pm}$ candidates are formed by combining $\tilde{D}^0$ candidates with charged pion tracks. The beam spot constraint applied to the $\tilde{D}^0$ production vertex also improves the resolution on Δm. K_s and

m_D mass constraints are not requested. A Δm window cut of 15 MeV is applied with respect to the nominal Δm value [55].

4.3 Final selection criteria

The final selection criteria for $K_s\pi^+\pi^-$ and $K_sK^+K^-$ events are almost identical, except for the particle identification of the charged tracks coming from the $\tilde{D}^0$ decay.

- The reconstructed mass of the $\tilde{D}^0$ is required to satisfy $m_D \in (1824.5, 1904.5)$ MeV.
- The difference between the masses of the reconstructed $D^{\star\pm}$ and $\tilde{D}^0$ mesons is required to satisfy $\Delta m \in (143.0, 149.0)$ MeV.
- In order to guarantee a minimum quality of the decay vertices, the vertex reconstruction algorithm provides a $\chi^2_{\rm fit}$ for each of them, with its corresponding number of degrees of freedom, $n_{\rm dof}$. The area under the tail of a χ^2 distribution beyond the observed $\chi^2_{\rm fit}$ of the $D^{\star\pm}$, $\tilde{D}^0$ and K_s decay vertices is required to satisfy $1 - P_{\chi^2}\left(\chi^2, n_{\rm dof}\right) > 0.0001$, where the χ^2 cumulative distribution function, P_{χ^2}, is described in §A.
- In order to reject true $\tilde{D}^0$ from B decays, the $\tilde{D}^0$ momentum in the center of mass frame is required to verify $p^\star_D > 2.5$ GeV, being 2.5 GeV the upper kinematic limit of $\tilde{D}^0$ momentum in B decays. On preselected events, this cut has $\sim 85\,\%$ efficiency for signal events and rejects $\sim 95\,\%$ of correctly reconstructed $\tilde{D}^0$ from $B\bar{B}$ decays.
- The K_s candidate is required to have a reconstructed invariant mass within 9 MeV of the nominal K_s mass [55], $m_{K_s} = m^{PDG}_{K_s} \pm 9$ MeV.
- To guarantee that the soft pion reaches the drift chamber, its transverse momentum p_t is required to be $p_t > 100$ MeV. This condition is also applied to the charged pion or kaon daughters of the $\tilde{D}^0$ and to the pion daughters of the K_s.
- To reduce contamination from $\tilde{D}^0 \to 4\pi$ (for $K_s\pi^+\pi^-$) and $\tilde{D}^0 \to \pi\pi KK$ (for $K_sK^+K^-$) events, where two pions in the final state can be wrongly associated to the daughters of a non-existent K_s, it has been required that $\cos\theta_{K_s} > 0.99$, being θ_{K_s} the collinearity angle of the reconstructed K_s, defined as the angle between its flight direction ($\vec{x}_{K_s}$) and its momentum ($\vec{p}_{K_s}$), in the laboratory rest frame.
- With the same purpose of the cut on $\cos\theta_{K_s}$, it has been required that $\frac{l_{K_s}}{\sigma_{l_{K_s}}} > 10$, being l_{K_s} the projected flight length of the K_s ($\vec{x}_{K_s}$) along its momentum vector ($\vec{p}_{K_s}$), computed as

$$l_{K_s} = \frac{\vec{p}_{K_s} \cdot \vec{x}_{K_s}}{|\vec{p}_{K_s}|}, \tag{4.6}$$

  and $\sigma_{l_{K_s}}$ being its error.
- The $\tilde{D}^0$ charged daughters in $K_sK^+K^-$ events are required to have particle identification incompatible with the pion hypothesis. This reduces combinatorial background and keeps a high efficiency for signal.

- In order to reject $\tilde{D}^0$ mesons with poor vertex reconstruction, the soft pion is required to have some hit in the drift chamber, and the pion or kaon daughters of the $\tilde{D}^0$ are required to have, at least, 2 ϕ or Z hits in the first two layers of the SVT.
- The $\tilde{D}^0$ lifetime is required to satisfy $t \in (-6, 6)$ ps.
- The per-event $\tilde{D}^0$ proper lifetime error is required to satisfy $\sigma_t < 1$ ps.

After applying all the selection criteria, 744000 $K_s\pi^+\pi^-$ and 96000 $K_sK^+K^-$ candidates on data are kept. It is important to remark that the region defined by the selection cuts on m_D and Δm is used in §6.1 to define the center and size of the so-called signal box region, where events are restricted in a tighter region within twice the measured resolution around the mean m_D and Δm values. The only purpose of the selection region on m_D and Δm is to define this signal box, and once this purpose is fulfilled, the analysis proceeds with the events in the signal box region.

4.4 Best candidate choice

In the events where there are multiple $\tilde{D}^0$ candidates, the only one that is kept is the one with the largest area under the tail of a χ^2 distribution beyond the observed $\chi^2_{\rm fit}$ of the $D^{\star\pm}$ geometrical decay vertex.

The average multiplicity of candidates per event on signal events after imposing all the selection cuts is 1.105 for $K_s\pi^+\pi^-$ and 1.034 for $K_sK^+K^-$.

The probability of making the correct choice, defined as the ratio between the number of truth matched events selected after the choice and the total number of events with multiple candidates, is 52.7 % for $K_s\pi^+\pi^-$ and 54.5 % for $K_sK^+K^-$.

The criteria used for the best candidate choice has negligible impact on the distribution of the variables used in the final mixing fit, since the probability of making the correct choice is just slightly larger that 50 % and, therefore, the effect of choosing the best candidate is almost statistically equivalent to selecting one randomly. For this reason, no experimental systematic uncertainty is assigned to the selection of the best candidate.

4.5 Signal and background categories

Several signal and background components contribute in the m_D and Δm distributions. These components have been classified into different categories, where different behaviors are expected. The definition of the categories is based on the correctness of the reconstruction of the $\tilde{D}^0$ or the soft pion $\pi_s^\pm$.

A $\tilde{D}^0$ is considered to be correctly reconstructed if all its charged daughters are correctly truth matched. The exact meaning of a correct truth match is explained in §4.2. Notice the exceptions allowed on the radiative decays or decays with pions decaying in flight.

A soft pion is considered to be correctly reconstructed if, together with a $\tilde{D}^0$, these are the only two sisters of a $D^{\star\pm}$ mother, regardless of how well reconstructed is the $\tilde{D}^0$. Notice that this definition does not imply that the reconstructed $\tilde{D}^0$ and the soft pion are sisters.

Four categories are defined with respect to the correctness of the reconstruction of the $\tilde{D}^0$ and the soft pion, and two additional categories are defined for specific events that have the same final state particles than the signal:

- **Category 1** events have both a correctly reconstructed $\tilde{D}^0$ and soft pion. These are mostly signal events and are, therefore, expected to peak both in m_D and Δm. Events where the reconstructed $\tilde{D}^0$ and soft pion are not sisters have the same peaking behavior.
- **Category 2** events have a correctly reconstructed $\tilde{D}^0$, but an incorrectly reconstructed soft pion. These events are expected to peak in m_D because the m_D reconstruction does not depend on the properties of the soft pion, but are not expected to peak in Δm.
- **Category 3** events have a correctly reconstructed soft pion, but an incorrectly reconstructed $\tilde{D}^0$. These events have a small peaking component in Δm because there are mismatches of the $\tilde{D}^0$ daughters with $\omega \to \pi^+\pi^-\gamma$ events where the ω is the daughter of a $\tilde{D}^0$ meson.
- **Category 4** events are combinatorial background events, where neither the $\tilde{D}^0$ nor the soft pion are correctly reconstructed. It is shown in §4.6 that, in the selection region, these events present a peaking component in m_D, but do not have any peaking behavior in m_D or Δm in the signal box region.
- **Category 5** events have their charged particles matched to the pions from $\tilde{D}^0 \to \pi^+\pi^-\pi^+\pi^-$ decays (for $K_s\pi^+\pi^-$) or the pions and kaons from $\tilde{D}^0 \to \pi^+\pi^-K^+K^-$ decays (for $K_sK^+K^-$). These events are expected to peak in both m_D and Δm. The cuts on $\cos\theta_{K_s}$ and $\frac{l_{K_s}}{\sigma_{l_{K_s}}}$ get rid of almost all these events, and those remaining represent a negligible amount.
- **Category 6** events have their charged particles matched to the pion K_s daughters produced in $\tilde{D}^0 \to K_sK_s$ events. These events are expected to peak in both m_D and Δm. Only events in the $K_s\pi^+\pi^-$ $\tilde{D}^0$ decay mode can fit into this category. The cuts on $\cos\theta_{K_s}$ and $\frac{l_{K_s}}{\sigma_{l_{K_s}}}$ are not effective to reduce this source of background to a negligible amount, but they represent a 0.1 % of signal events.

Since the final selection cuts make the events in category 5 negligible, in the rest of this document, this category is no longer considered. However, the naming of the categories follows the numerical order for the historical reason that these were defined in an early stage of this analysis, so K_sK_s events keep the classification as category 6, though there is no longer a category 5.

4.6 Misreconstructed signal events

Misreconstructed signal events have been studied with signal Monte Carlo reconstructed events that are not correctly truth matched. Figure 4.1 shows the m_D histogram of these events for the different background categories, for both $K_s\pi^+\pi^-$ and $K_sK^+K^-$ $\tilde{D}^0$ decay modes, and figure 4.2 shows the Δm projections.

The m_D histograms for events in category 2 are consistent with a correctly reconstructed $\tilde{D}^0$ meson, and those for events in category 3 are consistent with a combinatorial behavior. However, there is a peak in m_D for $K_s\pi^+\pi^-$ events in category 4, shifted towards lower values of m_D than its nominal mass, which is not consistent with a combinatorial behavior. This peaking behavior is due to signal events where the soft pion has been misreconstructed as a $\tilde{D}^0$ daughter. The average lower momentum of the soft pion with respect to the $\tilde{D}^0$ daughter pions originates this peaking behavior, while preserving the peak shape, since the rest of the $\tilde{D}^0$ daughters are correctly reconstructed. This effect is completely negligible in the signal box region.

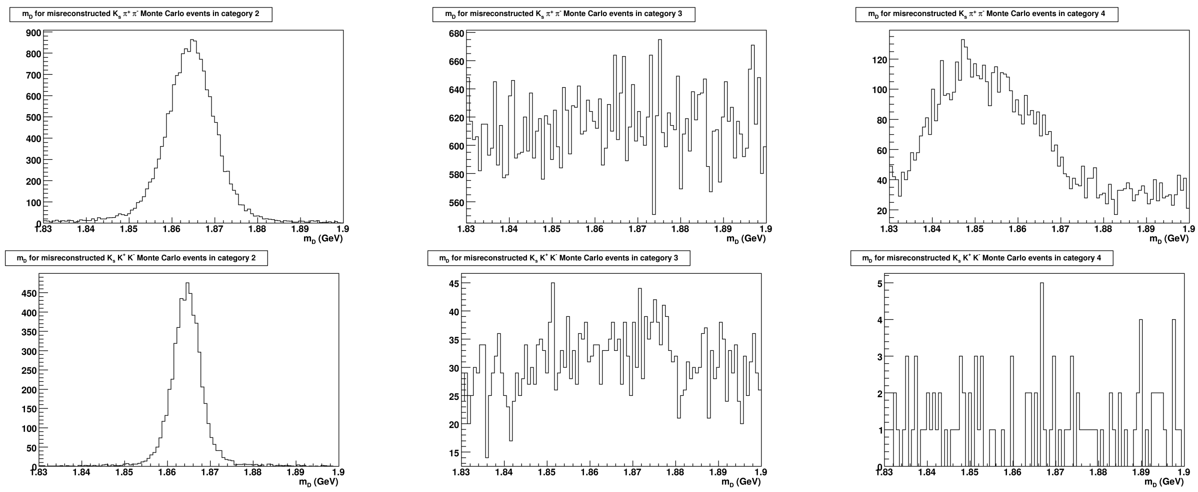

Figure 4.1: m_D misreconstructed signal events in the selection region for categories 1 (left column), 2 (middle column) and 3 (right column) for $K_s\pi^+\pi^-$ (top row) and $K_sK^+K^-$ (bottom row).

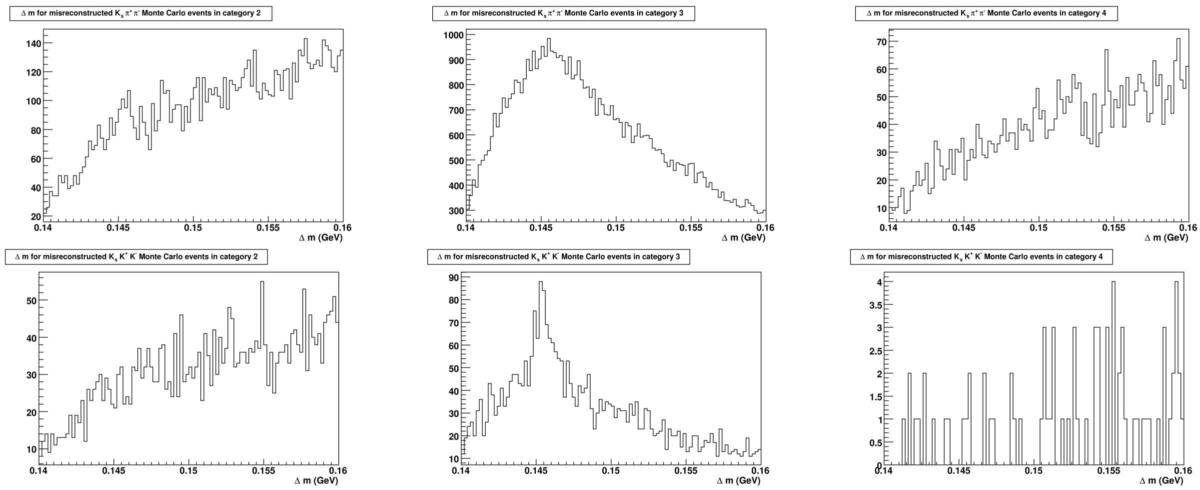

Figure 4.2: Δm misreconstructed signal events in the selection region for categories 1 (left column), 2 (middle column) and 3 (right column) for $K_s\pi^+\pi^-$ (top row) and $K_sK^+K^-$ (bottom row).

4.7 Comparison of data and Monte Carlo events

The comparison of the data and Monte Carlo samples in the selection region is shown in figure 4.3 for $K_s\pi^+\pi^-$ events and in figure 4.4 for $K_sK^+K^-$ events. Though some differences are observed, the shapes of the variable distributions are the same, and equal parameterizations, yet with different values of the parameters, are assumed for both data and Monte Carlo events. The parameterization for the different categories is described in §5.

It is important to remark that this analysis does not rely on the Monte Carlo samples. In the few steps where some values obtained from Monte Carlo are used in the fit to data, it is accounted for as a specific source of systematic uncertainty, and described in §7.

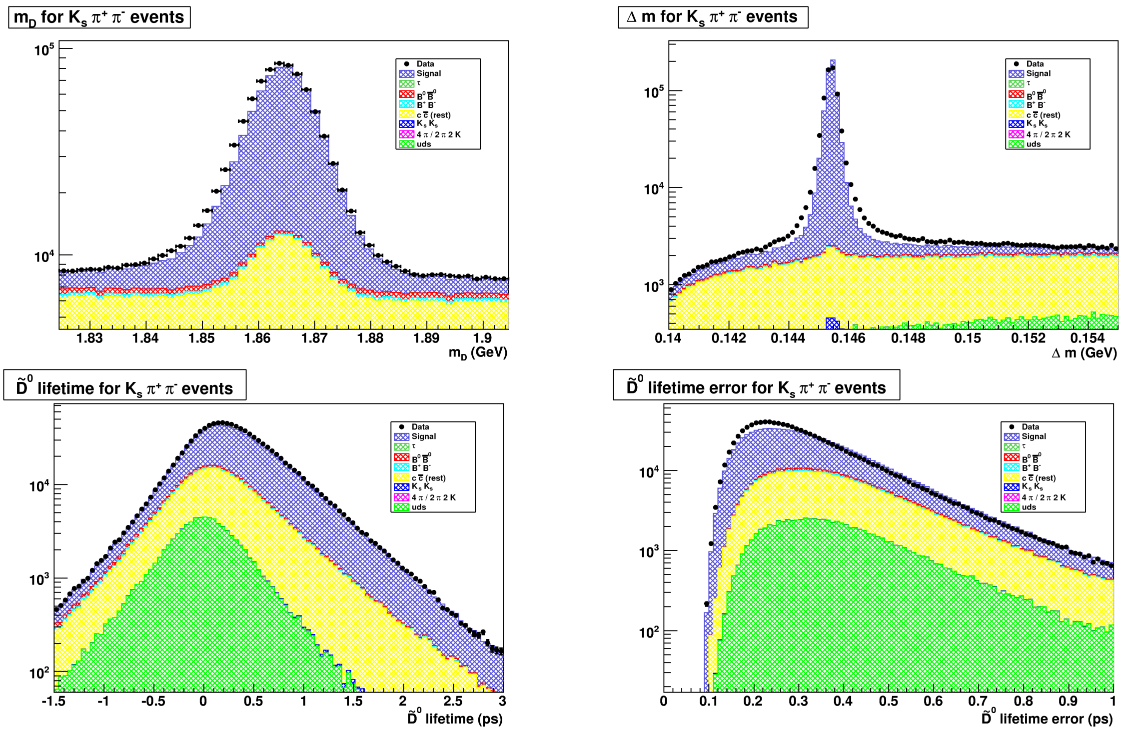

Figure 4.3: Data and Monte Carlo comparison of reconstructed m_D (top left), Δm (top right), $\tilde{D}^0$ lifetime (bottom left) and $\tilde{D}^0$ lifetime error (bottom right) for $K_s\pi^+\pi^-$ events. The Monte Carlo signal and background components are normalized to data luminosity.

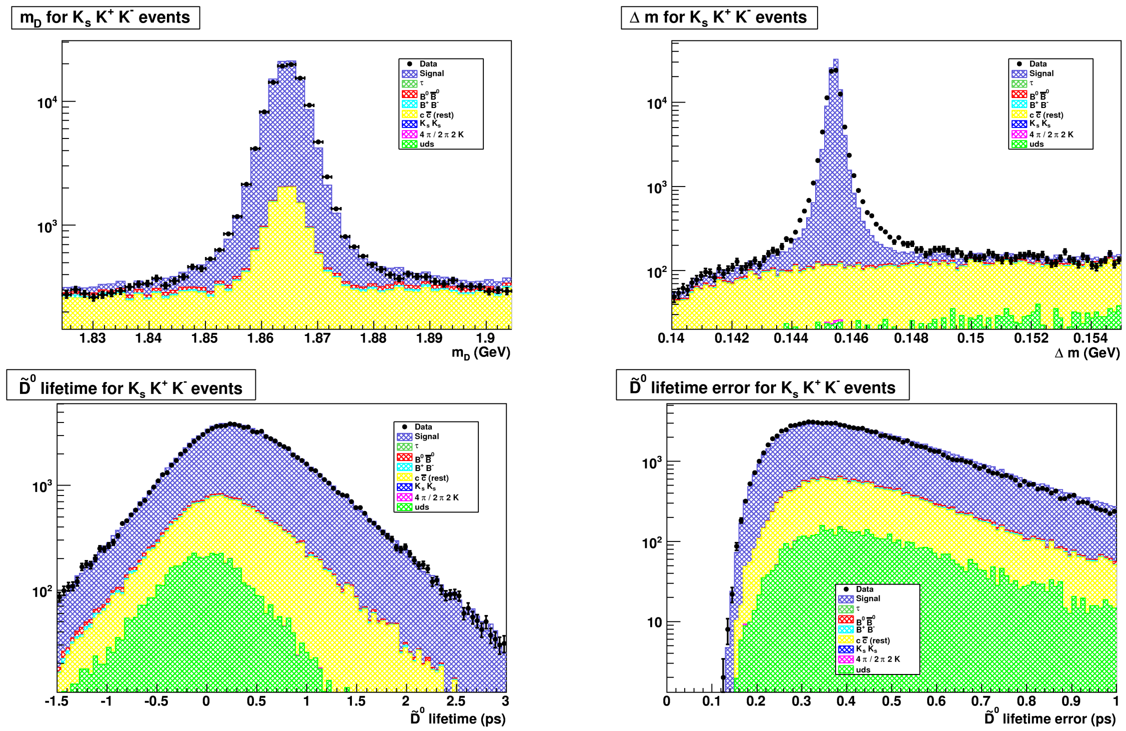

Figure 4.4: Data and Monte Carlo comparison of reconstructed m_D (top left), Δm (top right), $\tilde{D}^0$ lifetime (bottom left) and $\tilde{D}^0$ lifetime error (bottom right) for $K_sK^+K^-$ events. The Monte Carlo signal and background components are normalized to data luminosity.

Chapter 5

Signal and background characterization

The signal and background characterization is the search for probability distribution functions (PDF) that accurately describe the generic variables of the analysis, namely m_D, Δm, t and σ_t, for both the signal and background samples, as well as the PDFs that describe the variables of the decay model, m^2_{ab} and m^2_{ac}.

The characterization of the signal and background events described in this chapter has been done with the *flat* Monte Carlo sample, described in §4.1 and summarized in table 4.2.

5.1 Basic distributions

There are five basic distributions that compose the PDFs of the generic variables. The notation for them consists of a name, that identifies the function, and the list of arguments between parentheses. These arguments are, first, a block of comma separated variables, and second a block of comma separated parameters of the PDF. Both blocks are separated with a semicolon. For example, $G(x; \mu, \sigma)$ is a Gaussian function on the variable x, with mean μ and width σ.

The Gaussian is the simplest of all the basic distributions that compose the PDFs used to characterize the generic variables for signal and background,

$$G(x; \mu, \sigma) = \frac{1}{\sigma\sqrt{2\pi}} \exp\left[-\frac{(x-\mu)^2}{2\sigma^2}\right]. \tag{5.1}$$

The Gaussian distribution is normalized to 1 if the variable x ranges from $-\infty$ to ∞. In the cases where the range of variation of the variable x is bounded, $x \in (x^{\min}, x^{\max})$, the norm of the Gaussian is given by

$$N_G(\mu, \sigma) = \frac{1}{2}\text{erf}\left(\frac{x-\mu}{\sigma\sqrt{2}}\right)_{x^{\min}}^{x^{\max}}. \tag{5.2}$$

For signal events, the distribution of Δm gets wider as m_D gets further from its central value. To account for this correlation, a modified two-variable Gaussian implementing width correlation has been defined as [62]

$$G_c(x,y;\mu_x,\sigma_x,\mu_y,\sigma_y,\kappa) = \frac{1}{2\pi\sigma_x\sigma_y\,(1+\kappa)}\exp\left[-\frac{(x-\mu_x)^2}{2\sigma_x^2}\right]\exp\left[-\frac{(y-\mu_y)^2}{2\sigma_y^2\left[1+\kappa\left(\frac{x-\mu_x}{\sigma_x}\right)^2\right]^2}\right]. \tag{5.3}$$

This distribution is normalized to 1 if both x and y range from $-\infty$ to ∞. If the range of variation of x is bounded, the normalization of G_c has to be done numerically.

If y is allowed to take values in the range $(-\infty,\infty)$, the G_c projection on x is

$$G_c(x;\mu_x,\sigma_x,\kappa) = \int_{-\infty}^{\infty} dy\, G_c(x,y;\mu_x,\sigma_x,\mu_y,\sigma_y,\kappa) = \frac{1+\kappa\left(\frac{x-\mu_x}{\sigma_x}\right)^2}{\sigma_x\sqrt{2\pi}\,(1+\kappa)}\exp\left[-\frac{(x-\mu_x)^2}{2\sigma_x^2}\right]. \tag{5.4}$$

If the range of variation of y is bounded, this projection depends also on μ_y and σ_y. In any case, it is important to notice that it is not a Gaussian. The G_c projection on y must be done numerically, and is not a Gaussian either.

For the evaluation of the component of the systematic uncertainty due to the error on the signal and background yields, described in §7.1.3, a bifurcated Gaussian is used,

$$G_b(x;\mu,\sigma_l,\sigma_r) = \begin{cases} \dfrac{2\sigma_l}{\sigma_l+\sigma_r}G(x;\mu,\sigma_l) & \text{for } x<\mu, \\ \dfrac{2\sigma_r}{\sigma_l+\sigma_r}G(x;\mu,\sigma_r) & \text{for } x\geq\mu. \end{cases} \tag{5.5}$$

The Johnson unbounded distribution [63] allows for a range of skewness and kurtosis that cannot be achieved with a Gaussian distribution,

$$J_{S_U}(x;\mu,\sigma,\gamma,\delta) = \frac{\delta}{\sigma\sqrt{2\pi}\sqrt{1+\left(\frac{x-\mu}{\sigma}\right)^2}}\exp\left\{-\frac{1}{2}\left[\gamma+\delta\operatorname{arcsinh}\left(\frac{x-\mu}{\sigma}\right)\right]^2\right\}. \tag{5.6}$$

The Johnson unbounded distribution is normalized to 1 if x ranges from $-\infty$ to ∞. If the range of variation of x is bounded, $x\in(x^{\min},x^{\max})$, the norm of this distribution is given by

$$N_J(\mu,\sigma,\gamma,\delta) = \frac{1}{2}\operatorname{erf}\left\{\frac{1}{\sqrt{2}}\left[\gamma+\delta\operatorname{arcsinh}\left(\frac{x-\mu}{\sigma}\right)\right]\right\}_{x^{\min}}^{x^{\max}}. \tag{5.7}$$

The Argus distribution [64] is a bounded PDF with $x\in(0,c)$,

$$A(x;c,\chi) = \frac{2\chi^3}{\gamma\left(\frac{3}{2},\chi^2\right)}\frac{x}{c^2}\sqrt{1-\frac{x^2}{c^2}}\exp\left[-\chi^2\left(1-\frac{x^2}{c^2}\right)\right], \tag{5.8}$$

where $\gamma(p,\chi)$ is the lower incomplete gamma function, c is the maximum value of x and χ controls the curvature of the function. It can be generalized to describe a different peaking behavior with

$$A_p(x;c,\chi) = \frac{2\chi^{2(p+1)}}{\gamma\left(p+1,\chi^2\right)} \frac{x}{c^2}\left(1-\frac{x^2}{c^2}\right)^p \exp\left[-\chi^2\left(1-\frac{x^2}{c^2}\right)\right]. \tag{5.9}$$

This distribution is normalized to 1 for any values of p if x is allowed to take values in the entire range, $x \in (0,c)$. If the range of variation of x is more limited, $x \in (x^{\min}, x^{\max})$, the norm of the distribution is given by

$$N_{A_p}(c,\chi) = -\frac{\gamma\left[p+1,\chi^2\left(1-\frac{x^2}{c^2}\right)\right]_{x^{\min}}^{x^{\max}}}{\gamma\left(p+1,\chi^2\right)}. \tag{5.10}$$

The Argus distribution can be expressed as $A(x;c,\chi) = A_{1/2}(x;c,\chi)$, and the lower incomplete gamma function for this particular case can be computed using the relation

$$\gamma\left(\frac{3}{2},\chi^2\right) = \frac{\sqrt{\pi}}{2}\operatorname{erf}(\chi) - \chi e^{-\chi^2}. \tag{5.11}$$

Based on (5.9), a lower-bounded PDF can be defined as

$$B_p(x;c,\chi) = \frac{2\chi^{2(p+1)}}{\Gamma\left(p+1\right)} \frac{x}{c^2}\left(\frac{x^2}{c^2}-1\right)^p \exp\left[-\chi^2\left(\frac{x^2}{c^2}-1\right)\right], \tag{5.12}$$

where $\Gamma(p)$ is the Γ function and $x \in (c,\infty)$. This PDF is normalized to 1 if x is allowed to take values in the entire range. If not, its norm is given by

$$N_{B_p}(c,\chi) = \frac{\gamma\left[p+1,\chi^2\left(\frac{x^2}{c^2}-1\right)\right]_{x^{\min}}^{x^{\max}}}{\Gamma\left(p+1\right)}. \tag{5.13}$$

The PDF $B(x;c,\chi) = B_{1/2}(x;c,\chi)$ has been used to describe a part of the background,

$$B(x;c,\chi) = \frac{4\chi^3}{\sqrt{\pi}} \frac{x}{c^2}\sqrt{\frac{x^2}{c^2}-1}\exp\left[-\chi^2\left(\frac{x^2}{c^2}-1\right)\right]. \tag{5.14}$$

In the A_p and B_p functions explained above, the term inside the exponential must be negative for the PDF to be normalized. For this reason, the χ parameter is squared in this exponential. However, for historical reasons, usually $\xi = \chi^2$ is used and, therefore,

$$B(x;c,\xi) = \frac{4\xi^{3/2}}{\sqrt{\pi}} \frac{x}{c^2}\sqrt{\frac{x^2}{c^2}-1}\exp\left[-\xi\left(\frac{x^2}{c^2}-1\right)\right]. \tag{5.15}$$

Finally, the n-th degree polynomials $P_n(x;a_0,a_1,\dots)$ have also been used, where a_k are the coefficients of the k-th power of x. Since polynomials can not be normalized within an infinite range, it has to be understood that they are defined only in the range of variation of the variable that they describe and that they are normalized within this range.

Table 5.1 summarizes the basic PDFs that have been used to characterize generic variables, either for signal or background.

$G(x;\mu,\sigma)$	$\frac{1}{\sigma\sqrt{2\pi}}\exp\left[-\frac{(x-\mu)^2}{2\sigma^2}\right]$
$G_c(x,y;\mu_x,\sigma_x,\mu_y,\sigma_y,\kappa)$	$\frac{1}{2\pi\sigma_x\sigma_y(1+\kappa)}\exp\left[-\frac{(x-\mu_x)^2}{2\sigma_x^2}\right]\exp\left[-\frac{(y-\mu_y)^2}{2\sigma_y^2\left[1+\kappa\left(\frac{x-\mu_x}{\sigma_x}\right)^2\right]^2}\right]$
$G_b(x;\mu,\sigma_l,\sigma_r)$	$\begin{cases}\frac{2\sigma_l}{\sigma_l+\sigma_r}G(x;\mu,\sigma_l) & \text{for } x<\mu,\\ \frac{2\sigma_r}{\sigma_l+\sigma_r}G(x;\mu,\sigma_r) & \text{for } x\geq\mu.\end{cases}$
$J_{S_U}(x;\mu,\sigma,\delta,\gamma)$	$\frac{\delta}{\sigma\sqrt{2\pi}\sqrt{1+\left(\frac{x-\mu}{\sigma}\right)^2}}\exp\left\{-\frac{1}{2}\left[\gamma+\delta\text{arcsinh}\left(\frac{x-\mu}{\sigma}\right)\right]^2\right\}$
$B(x;c,\xi)$	$\frac{4\xi^{3/2}}{\sqrt{\pi}}\frac{x}{c^2}\sqrt{\frac{x^2}{c^2}-1}\exp\left[-\xi\left(\frac{x^2}{c^2}-1\right)\right]$
$P_n(x;a_0,a_1,\dots)$	$\sum_k a_k x^k$

Table 5.1: Basic PDFs used to characterize the generic variables.

5.2 Signal characterization

To avoid confusion, the names of the variables have a superindex indicating the magnitude they refer to and the number of category, as described in §4.5, and a subindex to distinguish the parameters of the different components of the PDF. For example, $\sigma_2^{m_D,1}$ is the width of the second Gaussian that is used in the signal (category 1) m_D PDF.

The name of the PDF for a given variable consists of the letter p, with a superindex indicating the variable described and a subindex indicating the number of the category. For example, $p_2^{m_D}$ is the category 2 PDF for m_D.

Since the number of parameters of the PDFs can be very large, they are not written explicitly.

When a linear combination of normalized distribution functions is used, for the result to be normalized each term is multiplied by a fit fraction term, which is also a parameter. The name of this fit fraction is the letter f, followed by the same superindex and subindex than the parameters of the distribution function it multiplies.

Many plots in this document contain a region with the normalized residuals, computed as the Poisson likelihood χ^2 described in [65], $\chi^2 = 2(n_{\text{mod}} - n) + 2n\ln(n/n_{\text{mod}})$, being n the number of events in a given bin and n_{mod} the number of events predicted by the model to be in this bin. The residual has been signed, where the sign is taken positive for $n \geq n_{\text{mod}}$ and negative otherwise. The normalized residuals have, by assumption of a Poisson distribution of the bin contents, an error of one unit, and are a useful tool to visualize the goodness of fit in specific plot regions. In some plots, they have been used to identify the regions of the model that have the largest disagreement with data. This same definition of the residuals has also been used in the search for mixing in $D^0 \to K^+\pi^-$ decays [2], which showed first evidence of this phenomenon.

5.2.1 Signal m_D and Δm characterization

The Δm distribution for signal truth matched events (category 1) gets wider as m_D gets further from its central value. The resolution on Δm varies quadratically with m_D. To account for this correlation between m_D and Δm, shown in figures 5.1 and 5.2, a two-variable PDF has been defined for them. This PDF has a term that uses non-correlated functions for m_D and Δm, and a term that uses two Gaussians with width correlation defined in equation (5.3).

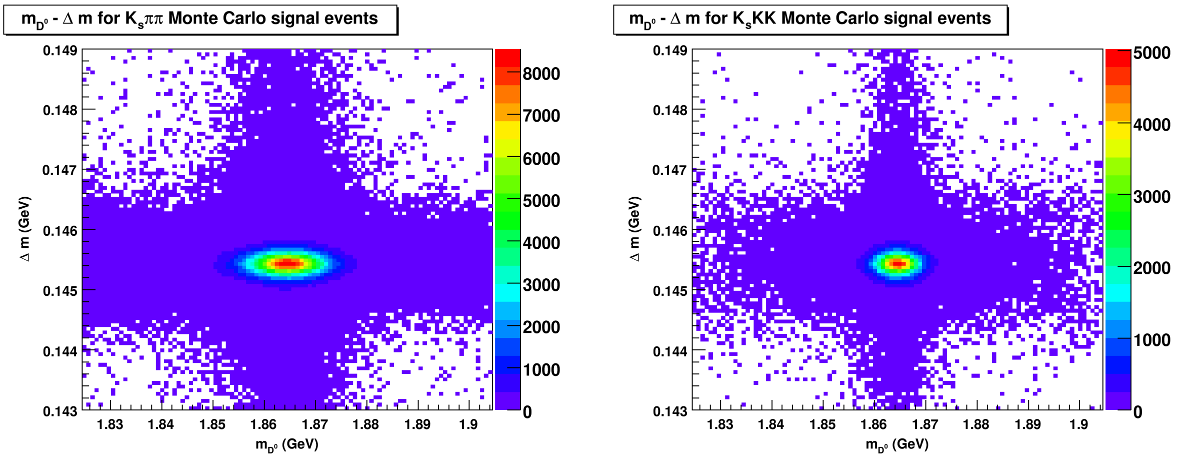

Figure 5.1: Correlation between m_D and Δm for truth matched $K_s\pi^+\pi^-$ (left plot) and $K_sK^+K^-$ (right plot) signal events.

In this specific case, the term that implements the correlation is named $p_c^{m_D,\Delta m}$ and the non-correlated functions of the other term are named $p_{nc}^{m_D}$ for m_D and $p_{nc}^{\Delta m}$ for Δm. The two-variable PDF is named $p_1^{m_D,\Delta m}$. Therefore, there is no $p_1^{m_D}$ or $p_1^{\Delta m}$.

All the expressions are valid for both $K_s\pi^+\pi^-$ and $K_sK^+K^-$ modes, with any small differences explained in the text. All the objects, therefore, should have another index dedicated to the $\tilde{D}^0$ decay mode, but it has been omitted for clarity.

For $K_s\pi^+\pi^-$, the term with no correlation for m_D is a sum of two Gaussian distributions with different means and widths. The one with largest width parameterizes the lower mass tail dominated by radiative events $D^0 \to K_s\pi^+\pi^- + n\gamma$, where energy is lost in the reconstruction. For $K_sK^+K^-$, it is a sum of three Gaussians, instead of two. Therefore, for $K_s\pi^+\pi^-$,

$$\begin{aligned} p_{nc}^{m_D} = \quad & f_1^{m_D} \cdot G\left(m_D; \mu_1^{m_D,nc}, \sigma_1^{m_D,nc}\right) + \\ & (1 - f_1^{m_D}) \cdot G\left(m_D; \mu_2^{m_D,nc}, \sigma_2^{m_D,nc}\right), \end{aligned} \tag{5.16}$$

and for $K_sK^+K^-$,

$$\begin{aligned} p_{nc}^{m_D} = \quad & f_{12}^{m_D} \cdot [\quad f_1^{m_D} \cdot G\left(m_D; \mu_1^{m_D,nc}, \sigma_1^{m_D,nc}\right) + \\ & \qquad (1 - f_1^{m_D}) \cdot G\left(m_D; \mu_2^{m_D,nc}, \sigma_2^{m_D,nc}\right)] + \\ & (1 - f_{12}^{m_D}) \qquad \cdot G\left(m_D; \mu_3^{m_D,nc}, \sigma_3^{m_D,nc}\right). \end{aligned} \tag{5.17}$$

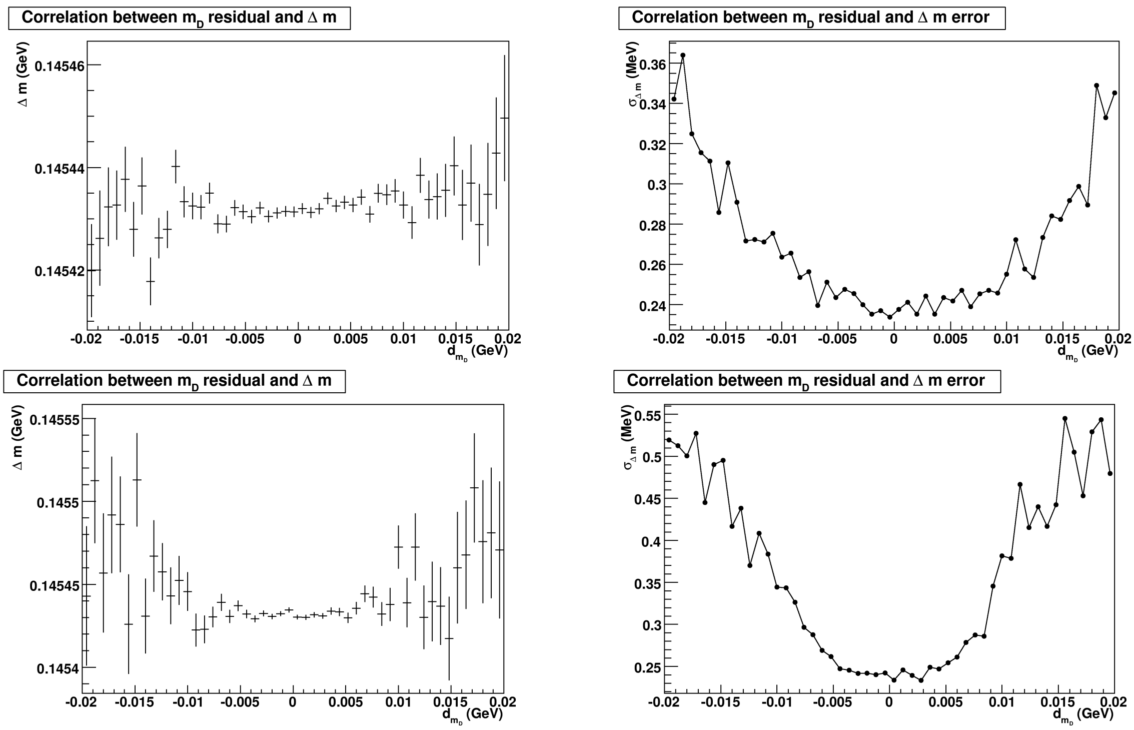

Figure 5.2: Correlation between m_D residual with Δm (left column) and resolution on Δm (right column) for truth matched signal events for $K_s\pi^+\pi^-$ (top row) and $K_sK^+K^-$ (bottom row). The mean value of Δm does not present correlation with m_D, but its resolution varies quadratically with m_D.

The term with no correlation for Δm is

$$\begin{aligned} p_{nc}^{\Delta m} = \quad & f_J^{\Delta m} \quad \cdot J_{S_U}\left(\Delta m; \mu_J^{\Delta m,nc}, \sigma_J^{\Delta m,nc}, \gamma_J^{\Delta m,nc}, \delta_J^{\Delta m,nc}\right) + \\ & \left(1 - f_J^{\Delta m}\right) \cdot G\left(\Delta m; \mu_J^{\Delta m,nc}, \sigma_G^{\Delta m,nc}\right), \end{aligned} \tag{5.18}$$

where the Johnson S_U function and the Gaussian share the parameter $\mu_J^{\Delta m,nc}$.

The term with correlation is

$$\begin{aligned} p_c^{m_D,\Delta m} = \quad & f_1^c \quad \cdot G_c\left(m_D, \Delta m; \mu_1^{m_D,c}, \sigma_1^{m_D,c}, \mu_1^{\Delta m,c}, \sigma_1^{\Delta m,c}, \kappa_1\right) + \\ & (1 - f_1^c) \cdot G_c\left(m_D, \Delta m; \mu_2^{m_D,c}, \sigma_2^{m_D,c}, \mu_2^{\Delta m,c}, \sigma_2^{\Delta m,c}, \kappa_2\right). \end{aligned} \tag{5.19}$$

The signal PDF that combines both terms with and without correlation for m_D and Δm is

$$p_1^{m_D,\Delta m} = f_{nc}^{m_D,\Delta m} \cdot p_{nc}^{m_D} \cdot p_{nc}^{\Delta m} + \left(1 - f_{nc}^{m_D,\Delta m}\right) \cdot p_c^{m_D,\Delta m}. \tag{5.20}$$

Figure 5.3 shows the projections of the m_D and Δm fit to truth matched Monte Carlo signal events.

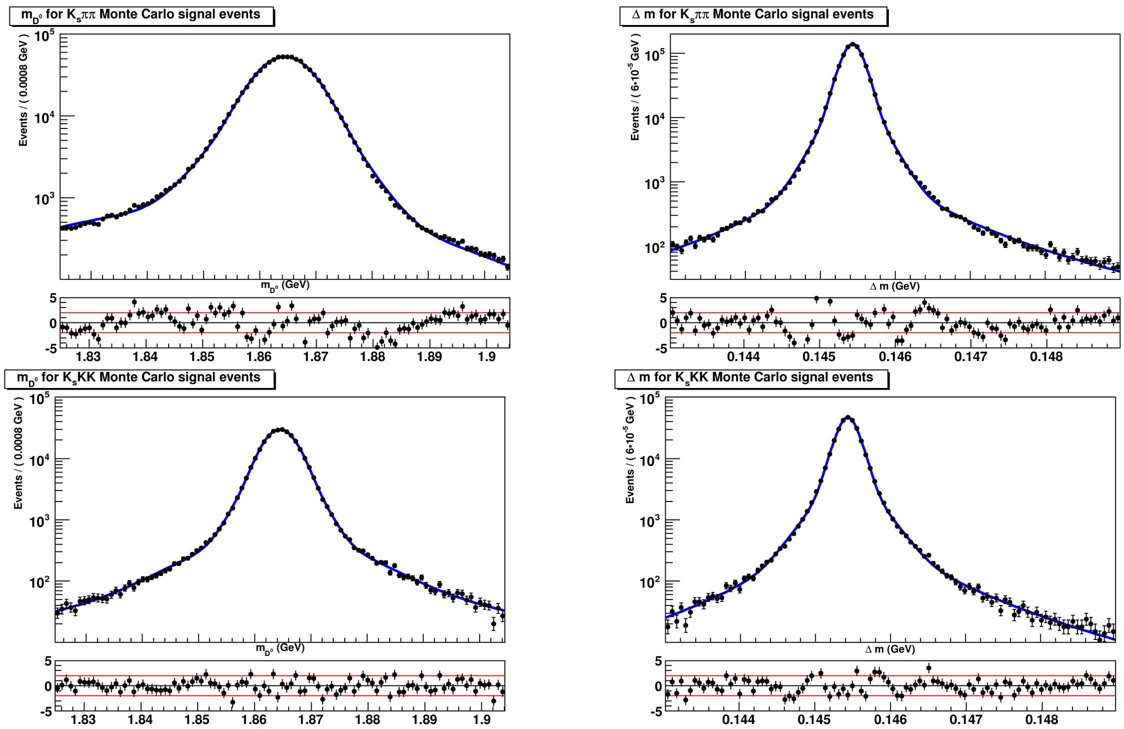

Figure 5.3: m_D (left column) and Δm (right column) projections of the fit to truth matched signal events for $K_s\pi^+\pi^-$ (top row) and $K_sK^+K^-$ (bottom row).

5.2.2 Signal t and σ_t characterization

Apart from the physical information contained in the $\tilde{D}^0$ decay law, described in §2.5, resolution effects have to be also taken into account. The resolution function used in this analysis for the $\tilde{D}^0$ lifetime takes the per-event $\tilde{D}^0$ lifetime error σ_t. Similarly to the m_D and Δm variables, the $\tilde{D}^0$ lifetime t distribution for signal events (category 1) also has a correlation with its uncertainty σ_t, and the naming of the magnitudes of the PDF for t and σ_t follows a similar rule. If mixing is considered, it is not possible to factorize the terms of the time-dependent amplitude that depend on the $\tilde{D}^0$ lifetime from those that depend on the decay model. In this case, it is necessary to describe these terms by means of an expression that combines them all, as is done in §5.2.3. However, for a sample with no mixing, a two-variable PDF for t and σ_t is defined as

$$p_1^{t,\sigma_t} = p_c^{t,\sigma_t} \cdot p_{nc}^{\sigma_t}. \tag{5.21}$$

Both terms p_c^{t,σ_t} and $p_{nc}^{\sigma_t}$ are normalized independently, i.e.

$$\int_{t^{\min}}^{t^{\max}} p_c^{t,\sigma_t}\, dt = 1 \quad \forall \sigma_t, \tag{5.22}$$

$$\int_{\sigma_t^{\min}}^{\sigma_t^{\max}} p_{nc}^{\sigma_t}\, d\sigma_t = 1. \tag{5.23}$$

Therefore,

$$\int_{t^{\min}}^{t^{\max}} \int_{\sigma_t^{\min}}^{\sigma_t^{\max}} p_1^{t,\sigma_t}\, dt\, d\sigma_t = 1. \tag{5.24}$$

It is important to realize that σ_t is one of the variables of this analysis and, therefore, it is necessary to construct a PDF that describes it properly, like with any other variable. Failing to do so would result in a Punzi bias [66].

The term p_c^{t,σ_t}, that depends on both t and σ_t, is the convolution over t of the true lifetime dependence T with a resolution function R,

$$p_c^{t,\sigma_t} = T(t) \otimes_t R(t, \sigma_t), \tag{5.25}$$

where $\otimes_t$ denotes convolution over t.

The true amplitude dependence on the $\tilde{D}^0$ lifetime t is the one expressed in (1.22) and, therefore, is the one to be convoluted with the resolution function. This chapter is not devoted to find the expression of T because it is given by the theory, as described in §2.5. However, in any Monte Carlo sample with no mixing implemented, like the *flat* sample used in this chapter, the $\tilde{D}^0$ lifetime term factors out of the time-dependent $\tilde{D}^0$ decay amplitude, and is given by

$$T(t;\tau) = \begin{cases} \dfrac{1}{\tau} \exp\left(-\dfrac{t}{\tau}\right) & \text{for } t \geq 0, \\ 0 & \text{for } t < 0, \end{cases} \tag{5.26}$$

where τ would be the lifetime of a $\tilde{D}^0$ that does not undergo mixing.

The $\tilde{D}^0$ lifetime resolution function has been studied and characterized. Figure 5.4 shows the correlation of the $\tilde{D}^0$ lifetime error σ_t with the $\tilde{D}^0$ lifetime residual and its resolution. Though the relationship between σ_t and the resolution on the $\tilde{D}^0$ lifetime residual is shown to be linear, a scale factor is applied to σ_t in order to better reproduce the resolution function. On the other hand, the $\tilde{D}^0$ lifetime residual slightly depends on σ_t.

The main component of the resolution function R is constructed by scaling the width of a Gaussian using the per-event error,

$$\frac{1}{k\sigma_t\sqrt{2\pi}} \exp\left(-\frac{(t-b)^2}{2(k\sigma_t)^2}\right), \tag{5.27}$$

where b introduces a bias to the lifetime measurement and k is a scale factor.

The resolution function used in this analysis is a sum of three terms, describing a core, tail and outliers, respectively. The core and the tail components use the per-event error, while the outliers component uses a global width.

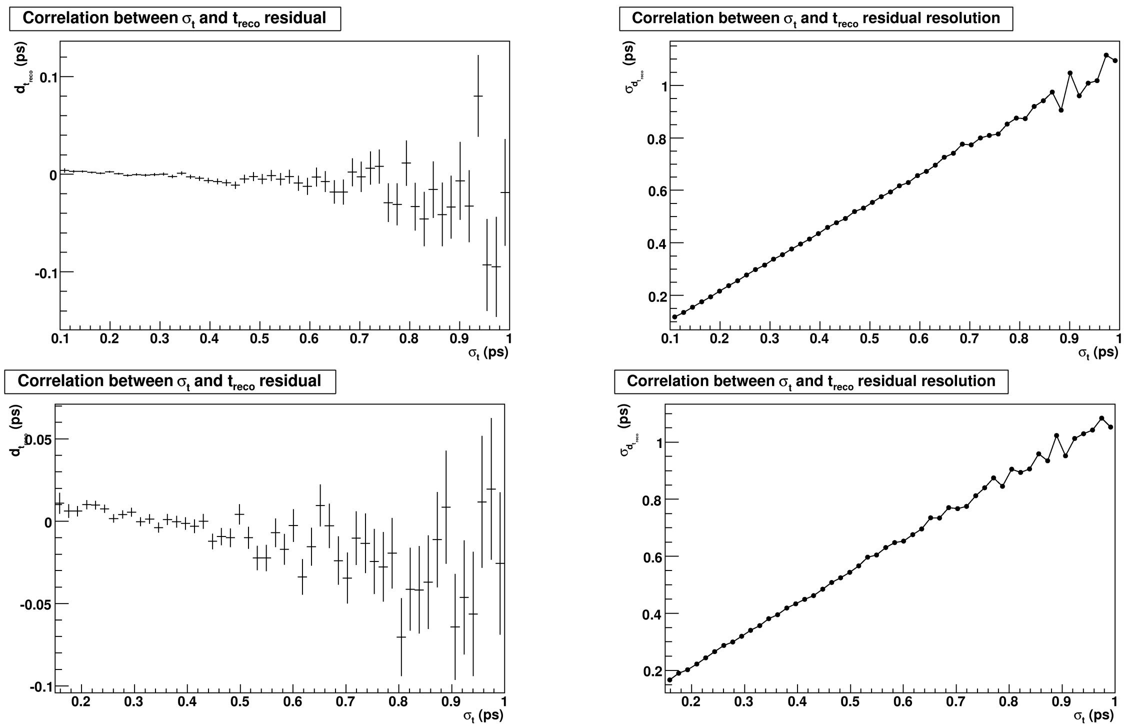

Figure 5.4: Correlation between $\tilde{D}^0$ lifetime residual with σ_t (left column) and resolution on $\tilde{D}^0$ lifetime residual (right column) for truth matched $K_s\pi^+\pi^-$ (top row) and $K_sK^+K^-$ (bottom row) signal events.

$$
\begin{aligned}
R(t, \sigma_t; b_{[cto]}, k_{[ct]}, \sigma_o, f_{[co]}) = \qquad & f_c \cdot \frac{1}{k_c\sigma_t\sqrt{2\pi}} \exp\left(-\frac{(t-b_c)^2}{2(k_c\sigma_t)^2}\right) + \\
(1 - f_c - f_o) \cdot & \frac{1}{k_t\sigma_t\sqrt{2\pi}} \exp\left(-\frac{(t-b_t)^2}{2(k_t\sigma_t)^2}\right) + \\
& f_o \cdot \frac{1}{\sigma_o\sqrt{2\pi}} \exp\left(-\frac{(t-b_o)^2}{2\sigma_o^2}\right).
\end{aligned}
\tag{5.28}
$$

Figure 5.5 shows the projections of the reconstructed $\tilde{D}^0$ lifetime fit to truth matched Monte Carlo signal events.

The σ_t distribution $p_{nc}^{\sigma_t}$ is described by a Johnson function,

$$
p_{nc}^{\sigma_t} = J_{S_U}\left(\sigma_t; \mu^{\sigma_t,nc}, \sigma^{\sigma_t,nc}, \gamma^{\sigma_t,nc}, \delta^{\sigma_t,nc}\right). \tag{5.29}
$$

The fit to σ_t has been done separately from the fit described in §6. For the Monte Carlo sample, the parameters of $p_{nc}^{\sigma_t}$ have been fixed from a fit to *flat* Monte Carlo signal events, while for data they have been fixed from a fit to data events in the signal box region, which is a region around the nominal values of m_D and Δm where most of the signal events are found, and is defined in §6. Once the values of the parameters are found in these events, they are fixed in the mixing fit.

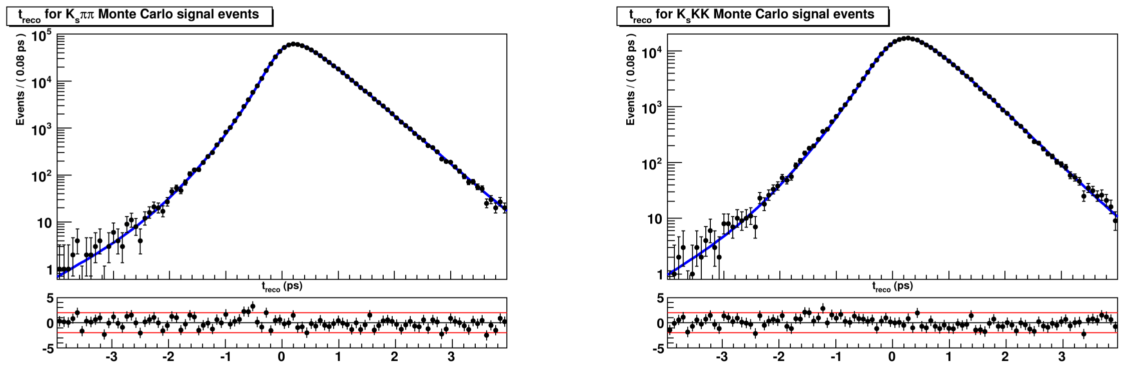

Figure 5.5: Reconstructed t projections of the fit to truth matched signal Monte Carlo events for $K_s\pi^+\pi^-$ (left plot) and $K_sK^+K^-$ (right plot).

Figure 5.6 shows that σ_t is not constant across the phase space. To account for this correlation, in the last step of the mixing fit, described in §6, the Dalitz plot has been divided in 16×16 boxes for $K_s\pi^+\pi^-$ and 16 slices for $K_sK^+K^-$, and σ_t has been fit to a Johnson function separately in each box or slice.

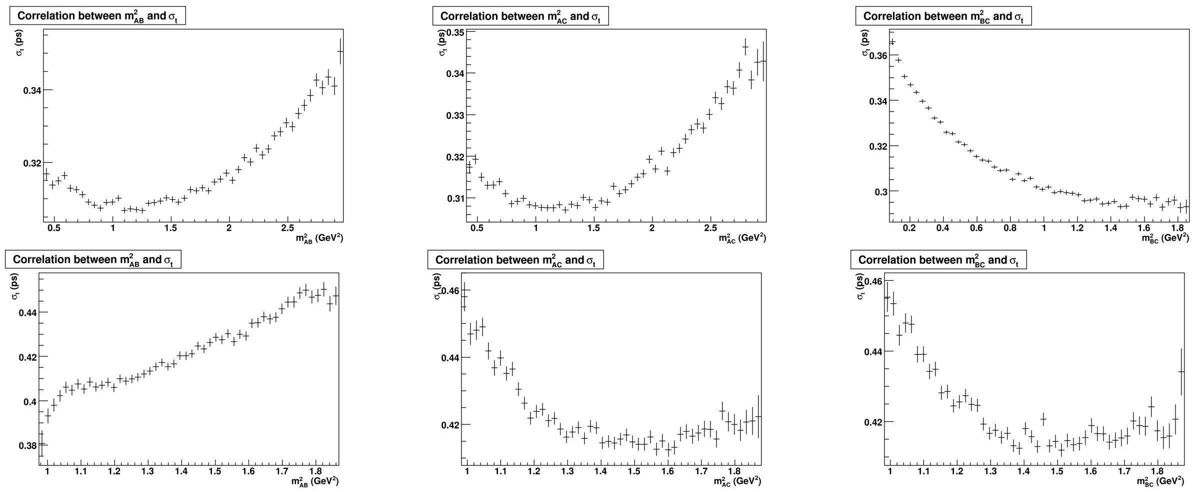

Figure 5.6: Correlation between the Dalitz plot variables and the $\tilde{D}^0$ lifetime resolution, σ_t, for truth matched signal events for $K_s\pi^+\pi^-$ (top row) and $K_sK^+K^-$ (bottom row) events.

Figure (5.7) shows the σ_t projections of the fit to truth matched Monte Carlo signal events.

5.2.3 Signal decay model characterization

The true amplitude dependence on t, m^2_{ab} and m^2_{ac} is expressed in (1.22). The decay model time-dependent PDF is proportional to the square modulus of the time dependent amplitude, but it has to be corrected by the efficiency non-uniformities $\epsilon(m^2_{AB}, m^2_{AC})$ across the phase space, and

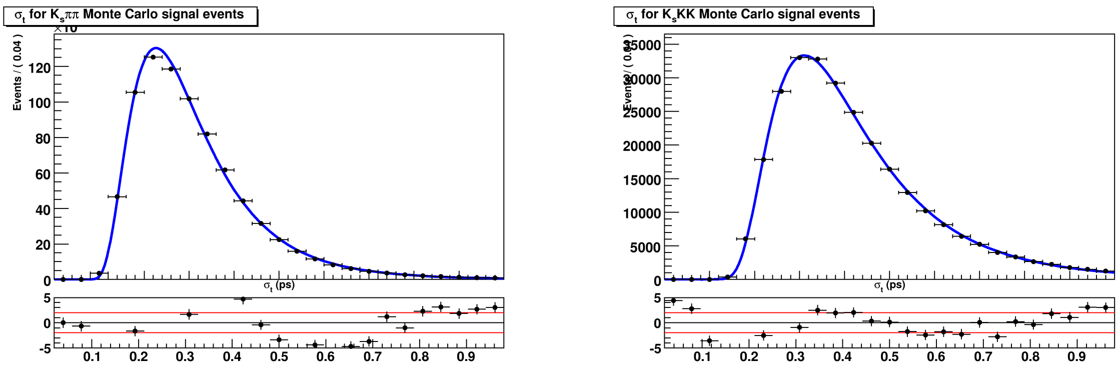

Figure 5.7: Reconstructed σ_t projections of the fit to truth matched signal Monte Carlo $K_s\pi^+\pi^-$ (left plot) and $K_sK^+K^-$ (right plot) events.

$\tilde{D}^0$ lifetime resolution effects, characterized in §5.2.2, have to be taken into account,

$$p_1^{D,t,\sigma_t} = \frac{1}{N_D}\epsilon(m^2_{ab}, m^2_{ac})\left(\left|\langle f|\mathcal{H}|\tilde{D}^0(t)\rangle\right|^2 \otimes_t R(t,\sigma_t)\right) p_{nc}^{\sigma_t}, \tag{5.30}$$

where N_D is the norm of the decay model PDF after the correction and the superindex D refers to the Dalitz variables m^2_{ab} and m^2_{ac}.

Here, the pairs of squared invariant masses of the $\tilde{D}^0$ daughters are defined as $(m^2_{ab}, m^2_{ac}) = (m^2_{K_s\pi^+}, m^2_{K_s\pi^+-})$ for $K_s\pi^+\pi^-$ and $(m^2_{ab}, m^2_{ac}) = (m^2_{K_sK^+}, m^2_{K^+K^-})$ for $K_sK^+K^-$.

The efficiency has been obtained by performing an unbinned maximum likelihood fit on *flat* Monte Carlo events, presented in §4.1.

For $K_s\pi^+\pi^-$, $\epsilon(m^2_{AB}, m^2_{AC})$ has been modeled by a two-variable symmetric third degree polynomial,

$$\begin{aligned}\epsilon(m^2_{ab}, m^2_{ac}) =& 1 + a_1(m^2_{ab} + m^2_{ac}) + a_2(m^4_{ab} + m^4_{ac} + m^2_{ab}m^2_{ac}) + \\ & a_3(m^6_{ab} + m^6_{ac} + m^4_{ab}m^2_{ac} + m^2_{ab}m^4_{ac}),\end{aligned} \tag{5.31}$$

and for $K_sK^+K^-$, it has been modeled by a two-variable non-symmetric second degree polynomial,

$$\epsilon(m^2_{ab}, m^2_{ac}) = 1 + a_{10}m^2_{ab} + a_{01}m^2_{ac} + a_{11}m^2_{ab}m^2_{ac} + a_{20}m^4_{ab} + a_{02}m^4_{ac}. \tag{5.32}$$

The best fit values of the coefficients of these polynomials are reported in table 5.2 for $K_s\pi^+\pi^-$ and in table 5.3 for $K_sK^+K^-$. In both tables, the nominal coefficients, obtained from the sample of both D^0 and $\bar{D}^0$ events, are compared to those obtained for D^0 and $\bar{D}^0$ events only. No significant differences are observed between those obtained for D^0 and $\bar{D}^0$ events only.

The projections of the efficiency distributions and their fits are shown in figure 5.8. These plots show that the symmetric two-variable polynomial used for the $K_s\pi^+\pi^-$ efficiency parameterization has some difficulties reproducing inefficiencies in some borders of the Dalitz plot, which also become evident in the fit projections of the Dalitz plots for steps 2b and 3, described below. These imperfections in the efficiency characterization are accounted for as a source of systematic uncertainty and are described in §7.1.6.

	$a_1\,(\mathrm{GeV}^{-2})$	$a_2\,(\mathrm{GeV}^{-4})$	$a_3\,(\mathrm{GeV}^{-6})$
$D^0 \to K_s\pi^+\pi^-$	0.019 ± 0.070	0.104 ± 0.023	-0.032 ± 0.003
$\bar{D}^0 \to K_s\pi^+\pi^-$	0.029 ± 0.067	0.090 ± 0.022	-0.029 ± 0.003
$\tilde{D}^0 \to K_s\pi^+\pi^-$	0.017 ± 0.048	0.099 ± 0.016	-0.031 ± 0.002

Table 5.2: Best fit values and errors of the parameters of the efficiency over the phase space symmetrized third degree polynomial for $K_s\pi^+\pi^-$.

	$a_{10}\,(\mathrm{GeV}^{-2})$	$a_{01}\,(\mathrm{GeV}^{-2})$	$a_{11}\,(\mathrm{GeV}^{-4})$	$a_{20}\,(\mathrm{GeV}^{-4})$	$a_{02}\,(\mathrm{GeV}^{-4})$
$D^0 \to K_sK^+K^-$	53.7 ± 9.1	24.9 ± 6.4	-4.7 ± 2.0	-17.4 ± 3.0	-9.1 ± 2.4
$\bar{D}^0 \to K_sK^+K^-$	49.5 ± 9.5	38.6 ± 8.1	-2.4 ± 2.1	-16.6 ± 3.3	-15.4 ± 3.1
$\tilde{D}^0 \to K_sK^+K^-$	47.5 ± 6.1	28.7 ± 4.7	-3.3 ± 1.3	-15.6 ± 2.0	-11.1 ± 1.8

Table 5.3: Best fit values and errors of the parameters of the efficiency over the phase space second degree polynomial for $K_sK^+K^-$.

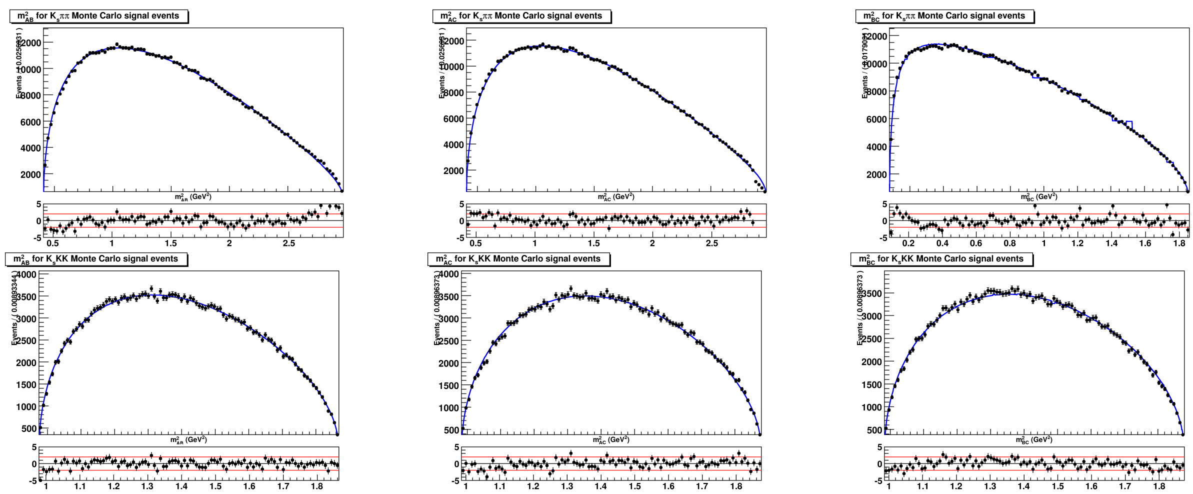

Figure 5.8: Dalitz plot projections of the efficiency over the phase space for $K_s\pi^+\pi^-$ (top row) and $K_sK^+K^-$ (bottom row) events.

5.3 Background characterization

5.3.1 Background m_D and Δm characterization

Since there is no evident correlation between m_D and Δm for Monte Carlo background events (figure 5.9), except for category 3, the m_D and Δm PDFs for background categories is described as a product of one-variable PDFs, chosen differently for each category.

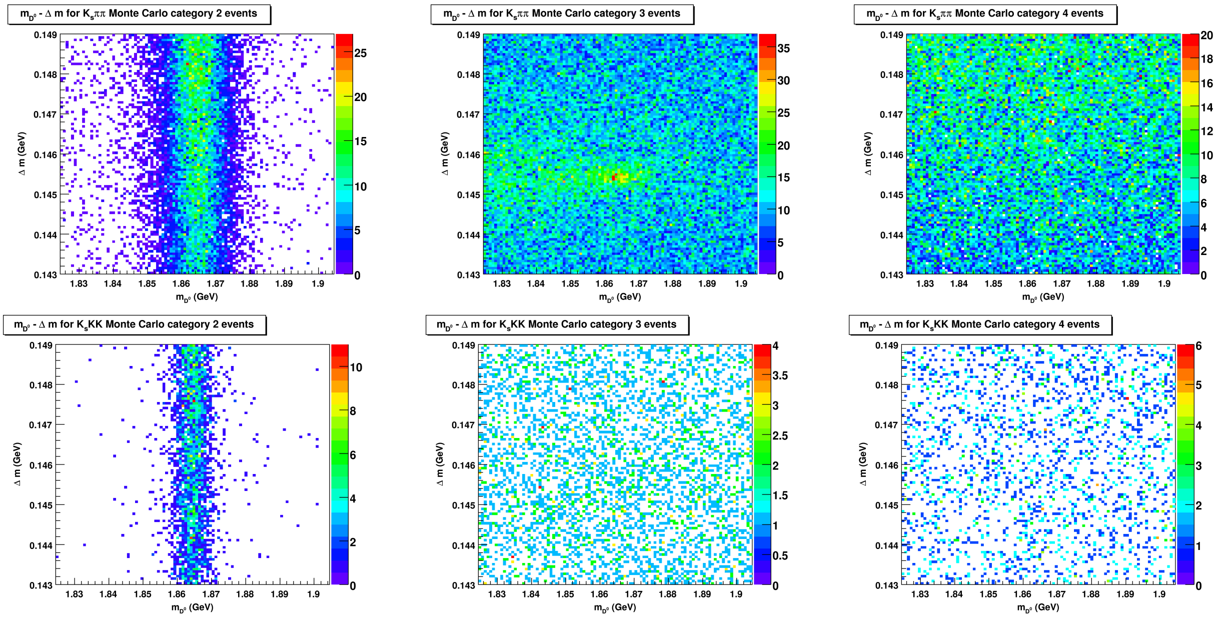

Figure 5.9: Correlation between m_D and Δm for Monte Carlo background events for $K_s\pi^+\pi^-$ (top row) and $K_sK^+K^-$ (bottom row).

Since category 2 consists of correctly reconstructed $\tilde{D}^0$ mesons, the m_D PDF for this category is taken from category 1,

$$\begin{aligned} p_2^{m_D} &= \int p_1^{m_D,\Delta m}\, d\Delta m \\ &= f_{nc}^{m_D,\Delta m} \cdot p_{nc}^{m_D} + (1 - f_{nc}^{m_D,\Delta m}) \cdot \int p_c^{m_D,\Delta m}\, d\Delta m. \end{aligned} \tag{5.33}$$

The parameters used in $p_2^{m_D}$ take the same values than those used in $p_1^{m_D,\Delta m}$.

The category 2 Δm PDF is a single modified Argus function (5.15) with the minimum value fixed to the nominal mass of the charged pion,

$$p_2^{\Delta m} = B\left(\Delta m; m_\pi, \xi^{\Delta m,2}\right). \tag{5.34}$$

Figure 5.10 shows the m_D and Δm projections of the fit to background Monte Carlo events in category 2.

As observed in the top middle plot of figure 5.9, there is a small correlation between m_D and Δm for events in category 3, where an overpopulation of events appears in the lower m_D sideband. This overpopulation corresponds to events with a true soft pion where one of the two charged pion daughters of the $\tilde{D}^0$ has been matched with one of the true charged pions from $\omega \to \pi^+\pi^-\gamma$ decays from the $\tilde{D}^0 \to K_s\omega$ channel.

To describe this correlation, a non-parametric PDF (a two-variable histogram) has been used, constructed with category 3 Monte Carlo background events correctly weighted to their composition

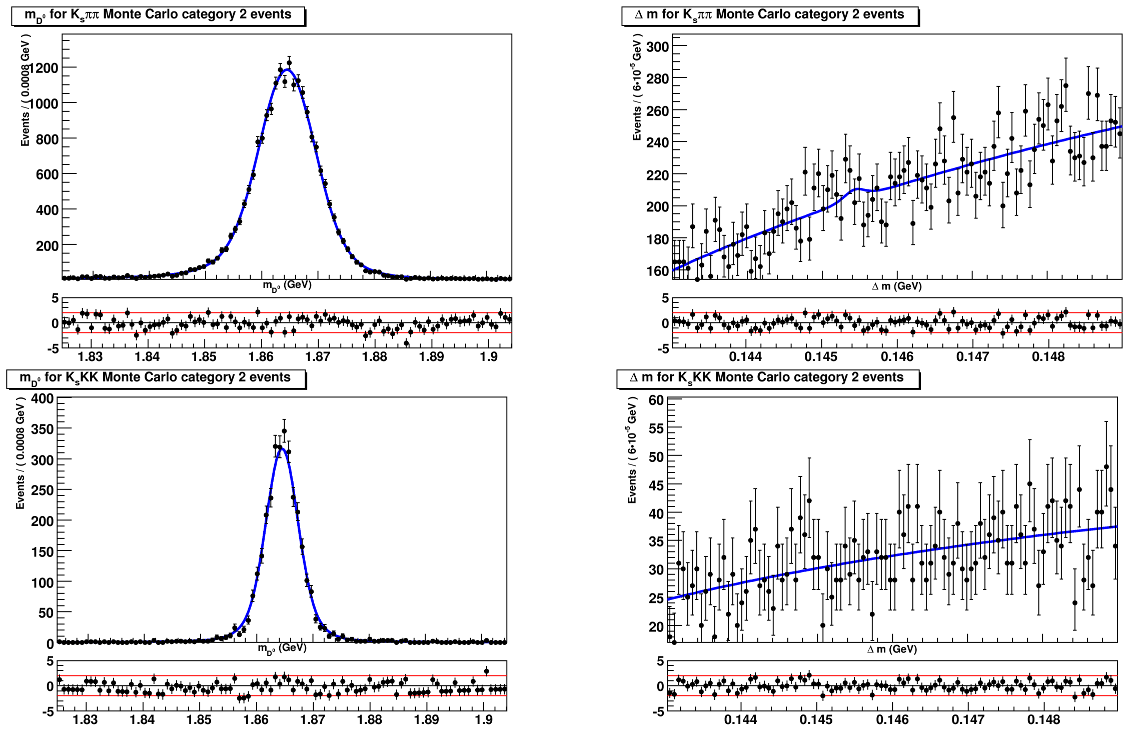

Figure 5.10: m_D (left column) and Δm (right column) projections of the fit to background Monte Carlo category 2 events for $K_s\pi^+\pi^-$ (top row) and $K_sK^+K^-$ (bottom row).

from $B^0\bar{B}^0$, B^+B^-, $c\bar{c}$, uds, $\tau^+\tau^-$ and wrongly reconstructed signal events.

m_D and Δm fit projections of background Monte Carlo category 3 events are shown in figure 5.11.

The category 4 PDF for m_D is given by

$$p_4^{m_D} = f_{P_1}^{m_D,4} \cdot P_1(m_D; a_0^{m_D,4}, a_1^{m_D,4}) + (1 - f_{P_1}^{m_D,4}) \cdot G\left(m_D; \mu^{m_D,4}, \sigma^{m_D,4}\right). \tag{5.35}$$

m_D and Δm fit projections of background Monte Carlo events in category 4 are shown in figure 5.12.

The m_D distribution shows a small peak due to signal-like reconstructed $\tilde{D}^0$ mesons, mostly from events where the soft pion has been incorrectly reconstructed as a $\tilde{D}^0$ daughter. However, in the nominal fit, the fraction corresponding to the polynomial is fixed to $f_{P_1} = 1$. To account for a small m_D peaking background component in category 4 events, this fraction is varied up to 0.9 and a source of systematic uncertainty is associated to this variation, as explained in §7.1.3.

The category 4 PDF for Δm is given by

$$p_4^{\Delta m} = B\left(\Delta m; m_\pi, \xi^{\Delta m,4}\right). \tag{5.36}$$

As verified in Monte Carlo, it is assumed that $\xi^{\Delta m,2} = \xi^{\Delta m,4}$.

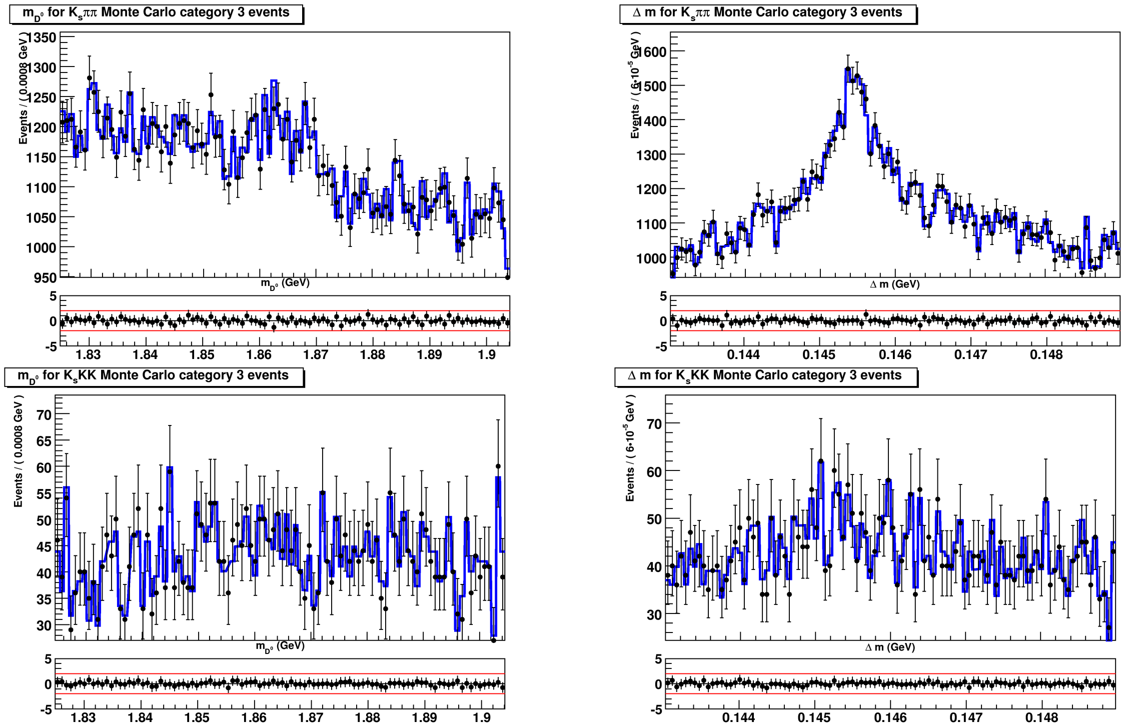

Figure 5.11: m_D (left column) and Δm (right column) projections of the fit to background Monte Carlo category 3 events for $K_s\pi^+\pi^-$ (top row) and $K_sK^+K^-$ (bottom row).

Due to the geometry of $\tilde{D}^0 \to K_sK_s$ events, these decays have a peaking component in both m_D and Δm variables. This behavior is described with

$$\begin{aligned} p_6^{m_D} = \quad & f_1^{m_D,6} \quad \cdot G\left(m_D; \mu_1^{m_D,6}, \sigma_1^{m_D,6}\right) + \\ & (1 - f_1^{m_D,6}) \cdot G\left(m_D; \mu_2^{m_D,6}, \sigma_2^{m_D,6}\right), \end{aligned} \tag{5.37}$$

and

$$\begin{aligned} p_6^{\Delta m} = \quad & f_J^{\Delta m,6} \quad \cdot J_{S_U}\left(\Delta m; \mu_J^{\Delta m,6}, \sigma_J^{\Delta m,6}, \gamma_J^{\Delta m,6}, \delta_J^{\Delta m,6}\right) + \\ & (1 - f_J^{\Delta m,6}) \cdot G\left(\Delta m; \mu_G^{\Delta m,6}, \sigma_G^{\Delta m,6}\right). \end{aligned} \tag{5.38}$$

m_D and Δm fit projections of background Monte Carlo category 6 events are shown in figure 5.13.

5.3.2 Background t and σ_t characterization

Events in category 2 contain real $\tilde{D}^0$ mesons, but present no sensitivity to mixing, since the $\tilde{D}^0$ mesons have a random flavor tag. The t and σ_t PDF is taken to be the same as for signal events, but with the mixing parameters fixed to $x = y = 0$, since the resolution function is dominated by

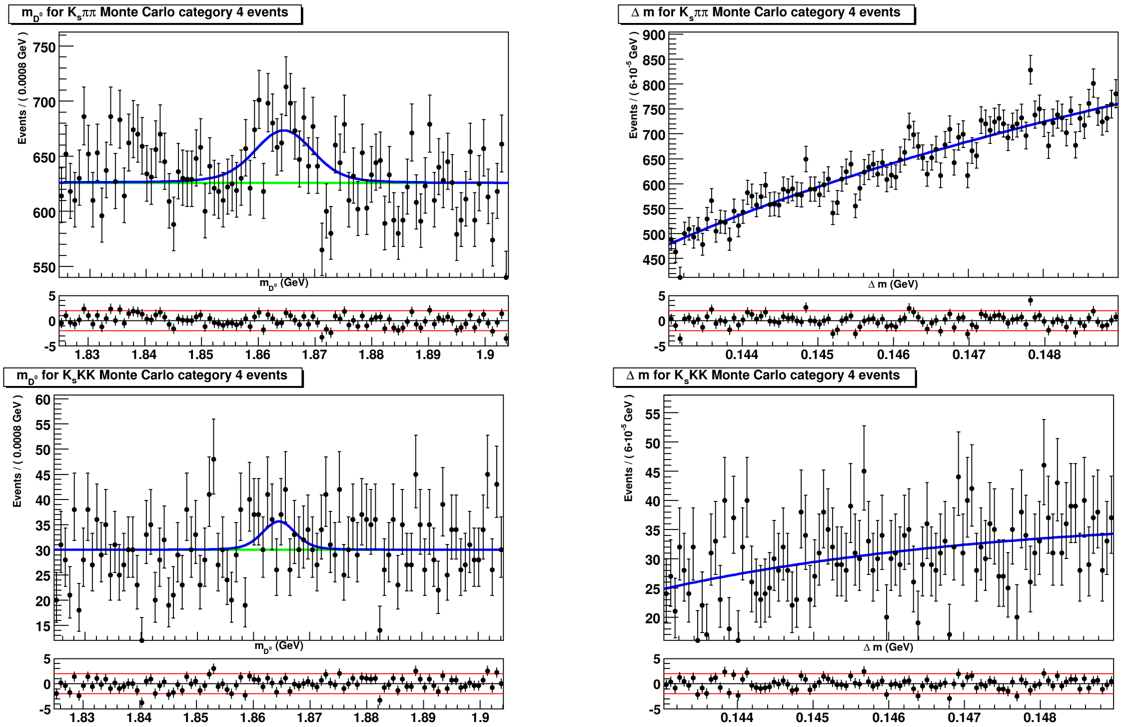

Figure 5.12: m_D (left column) and Δm (right column) projections of the fit to background Monte Carlo category 4 events for $K_s\pi^+\pi^-$ (top row) and $K_sK^+K^-$ (bottom row). The green curve in the left plots corresponds to fixing $f_{P_1} = 1$, and the blue curve accounts for a small Gaussian peak.

the real $\tilde{D}^0$ and the fake soft pion has negligible impact,

$$p_2^{t,\sigma_t} = p_c^{t,\sigma_t} \cdot p_{nc}^{\sigma_t}, \tag{5.39}$$

with

$$\begin{aligned} p_c^{t,\sigma_t} &= T(t) \otimes_t R(t, \sigma_t), & (5.40)\\ p_{nc}^{\sigma_t} &= J_{S_U}\left(\sigma_t; \mu^{\sigma_t,nc}, \sigma^{\sigma_t,nc}, \gamma^{\sigma_t,nc}, \delta^{\sigma_t,nc}\right). & (5.41)\end{aligned}$$

For categories 3 and 4, a common parameterization is used, since both contain fake $\tilde{D}^0$. Here, no correlation between t and σ_t is expected and, therefore, the PDF for these categories is

$$p_{3,4}^{t,\sigma_t} = p_{3,4}^{t} \cdot p_{3,4}^{\sigma_t}. \tag{5.42}$$

The $\tilde{D}^0$ lifetime distribution for $K_s\pi^+\pi^-$ has been parameterized as

$$\begin{aligned} p_{3,4}^{t} = \quad & f_J^{t,3,4} \cdot J_{S_U}\left(t; \mu_J^{t,3,4}, \sigma_J^{t,3,4}, \gamma_J^{t,3,4}, \delta_J^{t,3,4}\right) + \\ & (1 - f_J^{t,3,4}) \cdot G\left(t; \mu_G^{t,3,4}, \sigma_G^{t,3,4}\right) \end{aligned} \tag{5.43}$$

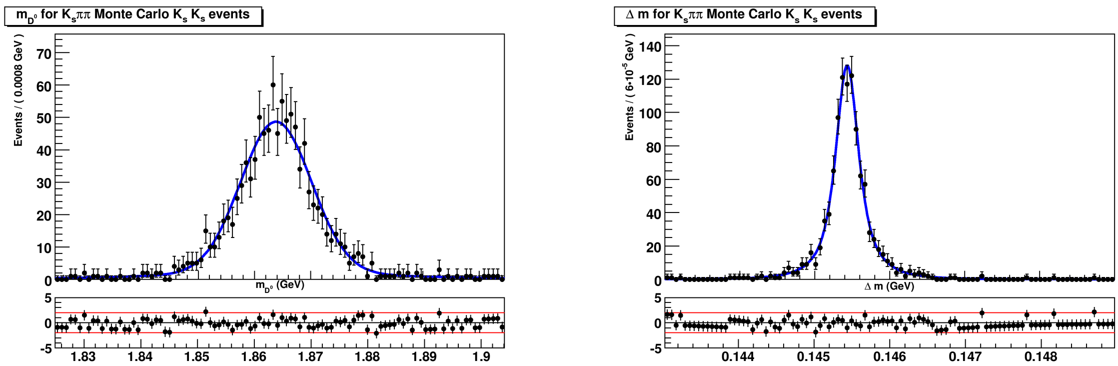

Figure 5.13: m_D (left plot) and Δm (right plot) projections of the fit to background Monte Carlo category 6 events for $K_s\pi^+\pi^-$.

and for $K_sK^+K^-$ as

$$p^t_{3,4} = J_{S_U}\left(t;\mu_J^{t,3,4},\sigma_J^{t,3,4},\gamma_J^{t,3,4},\delta_J^{t,3,4}\right). \tag{5.44}$$

The σ_t distribution is parameterized as a Johnson S_U function,

$$p^{\sigma_t}_{3,4} = J_{S_U}\left(\sigma_t;\mu^{\sigma_t,3,4},\sigma^{\sigma_t,3,4},\gamma^{\sigma_t,3,4},\delta^{\sigma_t,3,4}\right). \tag{5.45}$$

The values of the parameters of these PDFs take the same values for both categories 3 and 4.

For categories 3 and 4, the fit to the $\tilde{D}^0$ lifetime has been done separately from the fit described in §6. The $\tilde{D}^0$ lifetime PDF $p^t_{3,4}$ has been fit to *flat* Monte Carlo background events in categories 3 and 4, and its parameters have been fixed in the mixing fit. Since it is reasonable to use either Monte Carlo or data m_D sidebands to fix the parameters of $p^t_{3,4}$, this choice is considered a source of systematic uncertainty and is explained in detail in §7.1.5.

The fit to σ_t has been done separately from the fit described in §6. For the Monte Carlo sample, the parameters of $p^{\sigma_t}_{3,4}$ have been fixed from a fit to *flat* Monte Carlo fake $\tilde{D}^0$ events in the signal box region, while for data they have been fixed from a fit to data events in the m_D sideband region, defined in §6. Once the values of the parameters are found in these events, they are fixed in the mixing fit.

Fit to $\tilde{D}^0$ lifetime projections of background Monte Carlo fake $\tilde{D}^0$ events are shown in figure 5.14.

The $\tilde{D}^0$ lifetime parameterization of the category 6 events uses a Johnson S_U function and a Gaussian, sharing the same parameter $\mu_J^{t,6}$.

$$\begin{aligned} p^t_6 = \quad & f_J^{t,6} \cdot J_{S_U}\left(t;\mu_J^{t,6},\sigma_J^{t,6},\gamma_J^{t,6},\delta_J^{t,6}\right) + \\ & (1-f_J^{t,6})\cdot G\left(t;\mu_J^{t,6},\sigma_G^{t,6}\right). \end{aligned} \tag{5.46}$$

The $\tilde{D}^0$ lifetime projection of the fit to background Monte Carlo K_sK_s events is shown in figure

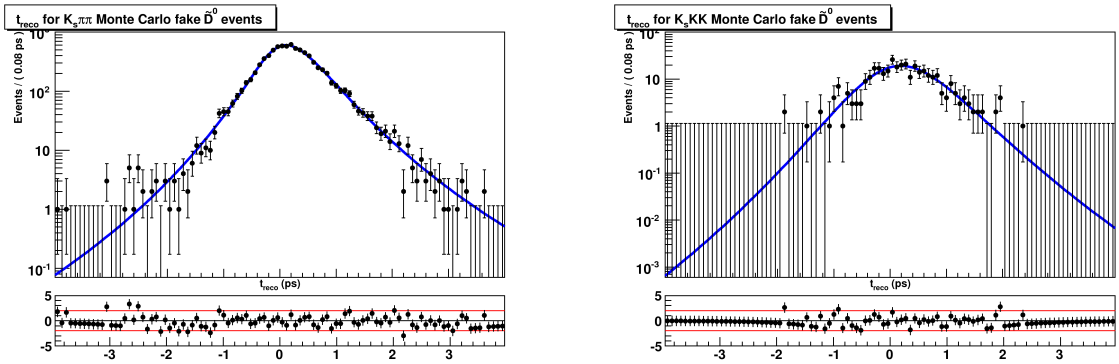

Figure 5.14: $\tilde{D}^0$ lifetime projections of the fit to background Monte Carlo fake $\tilde{D}^0$ events for $K_s\pi^+\pi^-$ (left plot) and $K_sK^+K^-$ (right plot).

5.15.

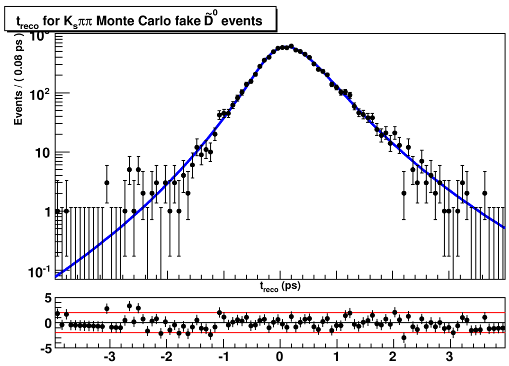

Figure 5.15: $\tilde{D}^0$ lifetime projections of the fit to background Monte Carlo K_sK_s events.

The σ_t distribution is parameterized as a Johnson S_U function,

$$p_6^{\sigma_t} = J_{S_U}\left(\sigma_t; \mu^{\sigma_t,6}, \sigma^{\sigma_t,6}, \gamma^{\sigma_t,6}, \delta^{\sigma_t,6}\right). \tag{5.47}$$

5.3.3 Background decay model characterization

Since category 2 events contain real $\tilde{D}^0$ mesons, the same decay model used in signal events can be used in category 2 events. However, events in this category present no sensitivity to mixing, since the $\tilde{D}^0$ mesons have a random flavor tag. The decay model PDF for this category is the same as in equation (5.30), but with the mixing parameters fixed to $x = y = 0$,

$$p_2^{D,t,\sigma_t} = \frac{1}{N_D}\epsilon(m_{ab}^2, m_{ac}^2)\left|\tilde{A}_f\right|^2\left(e^{-\Gamma t}\otimes_t R(t,\sigma_t)\right)p_{nc}^{\sigma_t}. \tag{5.48}$$

The fake soft pion in events in category 2 has an effect on the mistag fraction and is discussed in §6.2.2.3.

The shapes of the background amplitude PDFs for events in categories 3 and 4, with fake $\tilde{D}^0$ mesons, are non-parametric. The different sources considered to extract these PDFs are described in §6.2.2.2.

For events in category 6, the decay model is parameterized as a single relativistic Breit-Wigner K_s resonance with mass and width parameters determined from a fit to *nomix* Monte Carlo events in category 6. The systematic uncertainty associated to this rough approach is considered to be included in the one associated to the yield of category 6 events, described in §7.1.3.

The background amplitude PDF for categories 3, 4 and 6 is constructed as the product of the Dalitz and $\tilde{D}^0$ lifetime and σ_t PDFs,

$$p_{3,4}^{D,t,\sigma_t} = p_{3,4}^{D} \cdot p_{3,4}^{t,\sigma_t}, \tag{5.49}$$

$$p_{6}^{D,t,\sigma_t} = p_{6}^{D} \cdot p_{6}^{t,\sigma_t}, \tag{5.50}$$

5.4 Summary of signal and background characterization

Table 5.4 summarizes all the PDFs used for signal and background characterization.

Category	Magnitude	PDF	$\tilde{D}^0$ decay mode
1	m_D,Δm	$f_{nc}^{m_D,\Delta m} \cdot p_{nc}^{m_D} \cdot p_{nc}^{\Delta m} + \left(1 - f_{nc}^{m_D,\Delta m}\right) \cdot p_c^{m_D,\Delta m}$	
		$p_{nc}^{m_D} = \begin{cases} f_1^{m_D} \cdot G\left(m_D; \mu_1^{m_D,nc}, \sigma_1^{m_D,nc}\right) + \left(1 - f_1^{m_D}\right) \cdot G\left(m_D; \mu_2^{m_D,nc}, \sigma_2^{m_D,nc}\right) \\ f_{12}^{m_D} \cdot [f_1^{m_D} \cdot G\left(m_D; \mu_1^{m_D,nc}, \sigma_1^{m_D,nc}\right) + \left(1 - f_1^{m_D}\right) \cdot G\left(m_D; \mu_2^{m_D,nc}, \sigma_2^{m_D,nc}\right)] + \left(1 - f_{12}^{m_D}\right) \cdot G\left(m_D; \mu_3^{m_D,nc}, \sigma_3^{m_D,nc}\right) \end{cases}$	$K_s\pi^+\pi^-$ $K_sK^+K^-$
		$p_{nc}^{\Delta m} = f_J^{\Delta m} \cdot J_{S_U}\left(\Delta m; \mu_J^{\Delta m,nc}, \sigma_J^{\Delta m,nc}, \gamma_J^{\Delta m,nc}, \delta_J^{\Delta m,nc}\right) + \left(1 - f_J^{\Delta m}\right) \cdot G\left(\Delta m; \mu_J^{\Delta m,nc}, \sigma_G^{\Delta m,nc}\right)$	
		$p_c^{m_d,\Delta m} = f_1^c \cdot G_c\left(m_D, \Delta m; \mu_1^{m_D,c}, \sigma_1^{m_D,c}, \mu_1^{\Delta m,c}, \sigma_1^{\Delta m,c}, \kappa_1\right) + \left(1 - f_1^c\right) \cdot G_c\left(m_D, \Delta m; \mu_2^{m_D,c}, \sigma_2^{m_D,c}, \mu_2^{\Delta m,c}, \sigma_2^{\Delta m,c}, \kappa_2\right)$	
	R	$f_c \cdot \frac{1}{k_c\sigma_t\sqrt{2\pi}} \exp\left(-\frac{(t-b_c)^2}{2(k_c\sigma_t)^2}\right) + (1 - f_c - f_o) \cdot \frac{1}{k_c\sigma_t\sqrt{2\pi}} \exp\left(-\frac{(t-b_t)^2}{2(k_t\sigma_t)^2}\right) + f_o \cdot \frac{1}{\sigma_o\sqrt{2\pi}} \exp\left(-\frac{(t-b_o)^2}{2\sigma_o^2}\right)$	
	σ_t	$J_{S_U}\left(\sigma_t; \mu^{\sigma_t,nc}, \sigma^{\sigma_t,nc}, \gamma^{\sigma_t,nc}, \delta^{\sigma_t,nc}\right)$	
2	m_D	$\int p_1^{m_D,\Delta m}\, d\Delta m$	
	Δm	$B\left(\Delta m; m_\pi, \xi^{\Delta m,2}\right)$	
	R	$f_c \cdot \frac{1}{k_c\sigma_t\sqrt{2\pi}} \exp\left(-\frac{(t-b_c)^2}{2(k_c\sigma_t)^2}\right) + (1 - f_c - f_o) \cdot \frac{1}{k_c\sigma_t\sqrt{2\pi}} \exp\left(-\frac{(t-b_t)^2}{2(k_t\sigma_t)^2}\right) + f_o \cdot \frac{1}{\sigma_o\sqrt{2\pi}} \exp\left(-\frac{(t-b_o)^2}{2\sigma_o^2}\right)$	
	σ_t	$J_{S_U}\left(\sigma_t; \mu^{\sigma_t,nc}, \sigma^{\sigma_t,nc}, \gamma^{\sigma_t,nc}, \delta^{\sigma_t,nc}\right)$	
3	m_D	Non-parametric	
	Δm	Non-parametric	
	t	$\begin{cases} f_J^{t,3,4} \cdot J_{S_U}\left(t; \mu_J^{t,3,4}, \sigma_J^{t,3,4}, \gamma_J^{t,3,4}, \delta_J^{t,3,4}\right) + \left(1 - f_J^{t,3,4}\right) \cdot G\left(t; \mu_G^{t,3,4}, \sigma_G^{t,3,4}\right) \\ J_{S_U}\left(t; \mu_J^{t,3,4}, \sigma_J^{t,3,4}, \gamma_J^{t,3,4}, \delta_J^{t,3,4}\right) \end{cases}$	$K_s\pi^+\pi^-$ $K_sK^+K^-$
	σ_t	$J_{S_U}\left(\sigma_t; \mu^{\sigma_t,3,4}, \sigma^{\sigma_t,3,4}, \gamma^{\sigma_t,3,4}, \delta^{\sigma_t,3,4}\right)$	
4	m_D	$f_{P_1}^{m_D,4} \cdot P_1\left(m_D; a_0^{m_D,4}, a_1^{m_D,4}\right) + \left(1 - f_{P_1}^{m_D,4}\right) \cdot G\left(m_D; \mu^{m_D,4}, \sigma^{m_D,4}\right)$	
	Δm	$B\left(\Delta m; m_\pi, \xi^{\Delta m,2}\right)$	
	t	$\begin{cases} f_J^{t,3,4} \cdot J_{S_U}\left(t; \mu_J^{t,3,4}, \sigma_J^{t,3,4}, \gamma_J^{t,3,4}, \delta_J^{t,3,4}\right) + \left(1 - f_J^{t,3,4}\right) \cdot G\left(t; \mu_G^{t,3,4}, \sigma_G^{t,3,4}\right) \\ J_{S_U}\left(t; \mu_J^{t,3,4}, \sigma_J^{t,3,4}, \gamma_J^{t,3,4}, \delta_J^{t,3,4}\right) \end{cases}$	$K_s\pi^+\pi^-$ $K_sK^+K^-$
	σ_t	$J_{S_U}\left(\sigma_t; \mu^{\sigma_t,3,4}, \sigma^{\sigma_t,3,4}, \gamma^{\sigma_t,3,4}, \delta^{\sigma_t,3,4}\right)$	
6	m_D	$f_1^{m_D,6} \cdot G\left(m_D; \mu_1^{m_D,6}, \sigma_1^{m_D,6}\right) + \left(1 - f_1^{m_D,6}\right) \cdot G\left(m_D; \mu_2^{m_D,6}, \sigma_2^{m_D,6}\right)$	
	Δm	$f_J^{\Delta m,6} \cdot J_{S_U}\left(\Delta m; \mu_J^{\Delta m,6}, \sigma_J^{\Delta m,6}, \gamma_J^{\Delta m,6}, \delta_J^{\Delta m,6}\right) + \left(1 - f_J^{\Delta m,6}\right) \cdot G\left(\Delta m; \mu_G^{\Delta m,6}, \sigma_G^{\Delta m,6}\right)$	
	t	$f_J^{t,6} \cdot J_{S_U}\left(t; \mu_J^{t,6}, \sigma_J^{t,6}, \gamma_J^{t,6}, \delta_J^{t,6}\right) + \left(1 - f_J^{t,6}\right) \cdot G\left(t; \mu_J^{t,6}, \sigma_G^{t,6}\right)$	
	σ_t	$J_{S_U}\left(\sigma_t; \mu^{\sigma_t,6}, \sigma^{\sigma_t,6}, \gamma^{\sigma_t,6}, \delta^{\sigma_t,6}\right)$	

Table 5.4: Summary of PDF components for signal and background.

Chapter 6

Fit

This chapter describes the unbinned extended maximum likelihood fit that is done on m_D, Δm, $\tilde{D}^0$ lifetime t, lifetime error σ_t, and Dalitz plot variables m^2_{ab} and m^2_{ac}.

The nominal model uses the PDFs described in §5 and summarized in table 5.4, and the decay model described in §2.4.8. In this model, both D^0 and $\bar{D}^0$ events, and both $K_s\pi^+\pi^-$ and $K_sK^+K^-$ $\tilde{D}^0$ decay modes are fit together, with the same decay model parameters, mixing parameters x and y, and average lifetime τ.

The full extended log-likelihood is

$$\ln \mathcal{L}_{\text{ext}} = -\sum_c n_c + \sum_{i=1}^{N} \ln \left[\sum_c n_c p_c \left(\vec{x}_i ; \vec{p} \right) \right], \tag{6.1}$$

where i indexes the events and c the categories ($c = \{1, 2, 3, 4, 6\}$). $\vec{x}_i$ is the vector of variables evaluated for the i-th candidate, $\vec{p}$ is the vector of parameters, p_c is the PDF for category c, N is the total number of candidates and n_c is the yield of events in category c.

After applying the selection criteria described in §4.3, two different regions in $(m_D, \Delta m)$ are considered:

- The **large box** is limited in both Monte Carlo and data samples by $m_D \in [1824.5, 1904.5]$ MeV and $\Delta m \in [143.0, 149.0]$ MeV, which correspond to the selection criteria on m_D and Δm, described in §4.3.
- The **signal box** is limited to $\pm 2\sigma$ from the mean value of the m_D and Δm distributions. The limits of this box on m_D and Δm are different for Monte Carlo and data. The procedure to obtain the m_D and Δm limits of the signal box is explained in §6.1.2 below. The choice of the $\pm 2\sigma$ window has been adopted with the purpose to maximize the purity of the data sample while keeping a high signal efficiency. In §7.1.2 below, it is shown that an alternative window at $\pm 3\sigma$ only increases the signal yield by 9.7 % for $K_s\pi^+\pi^-$ and 6.4 % for $K_sK^+K^-$, while the background yields increase between 52.3 % and 124.0 %, depending on the category. With this extended window, the overall purity of the sample changes from 98.5 % to 97.4 % for $K_s\pi^+\pi^-$ and from 99.2 % to 98.7 % for $K_sK^+K^-$.

To minimize computer power, while guaranteeing a high sensitivity to mixing, the fit is divided in three steps. The vector of variables $\vec{x}_i$ is different in each of the steps.

- In **step 1**, $\vec{x} = (m_D, \Delta m)$ and $\vec{p}$ are all the signal and background shape parameters, described in §5.2.1 and §5.3.1, and summarized in table 5.4. This step is divided into two sub-steps:
  - In **step 1a**, a fit for $(m_D, \Delta m)$ is performed in the large box region. The signal and background PDF parameters and the yields are extracted and serve as an initial value for the subsequent steps.
  - In **step 1b**, the yields for signal and background categories in the signal box region are evaluated by scaling the **step 1a** results found in the large box according to the PDFs integral ratio. To reduce computer power, the yields are fixed in the subsequent steps to those obtained here. This step does not involve an actual fitting procedure.

  The PDF of **step 1** is validated with the Monte Carlo sample, where the amount of signal and background is known.

- In **step 2**, initial values for the parameters used in the following **step 3** are evaluated. This facilitates the fit convergence and reduces the needed computing power. This step is divided into two sub-steps:
  - In **step 2a**, a Dalitz-integrated fit for $\vec{x} = (t, \sigma_t)$ is performed. Here, $\vec{p}$ are the parameters of the $\tilde{D}^0$ lifetime resolution function and the parameters of the $\tilde{D}^0$ background lifetime PDF, presented in §5.2.2 and §5.3.2 and summarized in table 5.4. The initial values of the $\tilde{D}^0$ lifetime resolution function and $\tilde{D}^0$ lifetime background are extracted. Notice that the parameters of the σ_t distribution are extracted separately from this fit process, as explained in §5.2.2 and §5.3.2.
  - In **step 2b**, a time-integrated fit for $\vec{x} = (m^2_{ab}, m^2_{ac})$ is performed. In this analysis, the pairs of squared invariant masses of the $\tilde{D}^0$ daughters are defined as $(m^2_{ab}, m^2_{ac}) = (m^2_{K_s\pi^+}, m^2_{K_s\pi^-})$ for $K_s\pi^+\pi^-$ and $(m^2_{ab}, m^2_{ac}) = (m^2_{K_sK^+}, m^2_{K^+K^-})$ for $K_sK^+K^-$. $\vec{p}$ are, therefore, the parameters of the decay model described in §2.4.8.

  The results of the two sub-steps of **step 2** are used as initial values for the following step.

- In **step 3**, a time-dependent Dalitz plot for $\vec{x} = (t, \sigma_t, m^2_{ab}, m^2_{ac})$ is performed in the signal box region. The results found in **step 2** are taken as initial values for this fit. Here, $\vec{p}$ are the parameters of the $\tilde{D}^0$ lifetime resolution function, the $\tilde{D}^0$ average lifetime τ, the mixing parameters x and y, and the most of the complex terms of the linear combination of resonances, as explained in §2.4.8. Category yields and background PDF parameters are fixed to the values found in the previous steps.

All the parameterizations used in the different steps of the fit have been tuned using the Monte Carlo samples shown in table 4.2, where the background samples have been weighted to the luminosity of the $c\bar{c}$ sample because this is the sample where more events can pass the cuts and, therefore, is the one with the highest relevance.

The fit is performed on both data and Monte Carlo samples, which are reported in §4.1. The data sample has a luminosity of $468.5\,\mathrm{fb}^{-1}$.

The next sections explain in detail the three steps of the fit, and the mixing fit validation is discussed in detail in §6.5.

6.1 Step 1

The fit described in this section uses the *flat* Monte Carlo sample for the signal, described in §4.1 and detailed in table 4.2.

6.1.1 Step 1a

The m_D and Δm PDF for correctly truth matched signal events and for background events has been described in §5.2.1 and §5.3.1, and summarized in table 5.4.

The fit projections to the combination of all the background Monte Carlo samples are shown in figure 6.1.

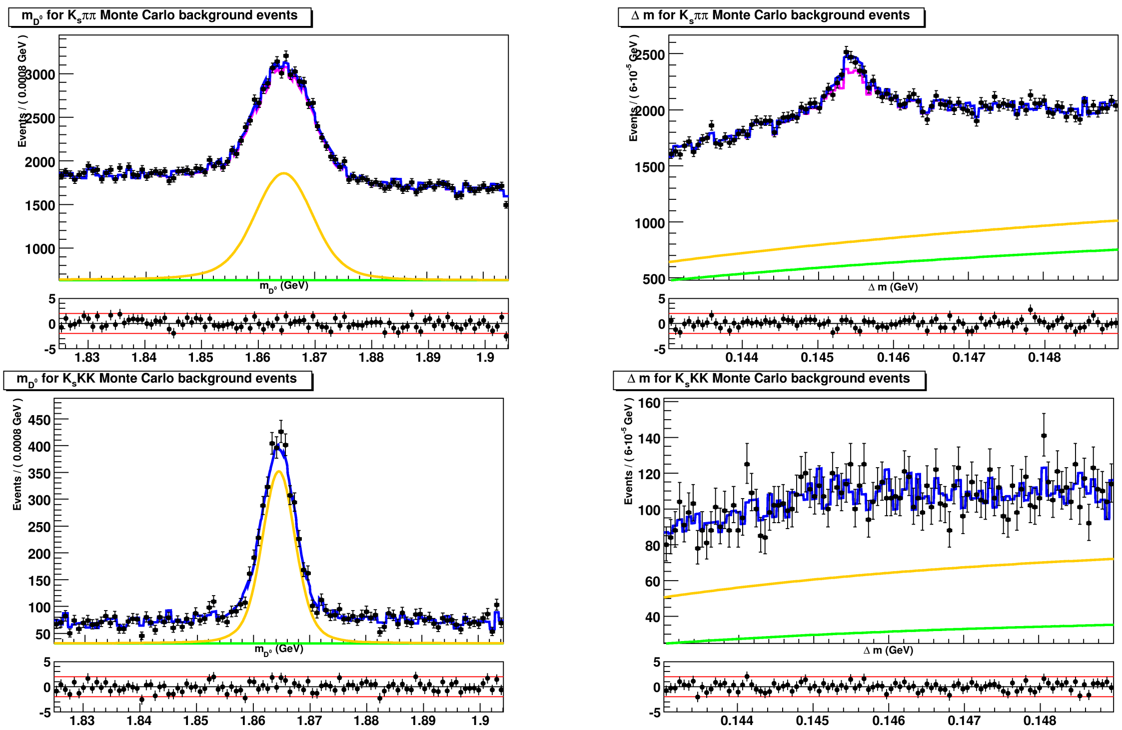

Figure 6.1: m_D (left column) and Δm (right column) projections of the fit to background events for $K_s\pi^+\pi^-$ (top row) and $K_sK^+K^-$ (bottom row). The colors represent the contribution of category 2 (yellow), category 3 (red) and category 4 (green). The blue line is the total PDF projection.

The fit projections to the combination of both background and truth matched signal Monte Carlo samples are shown in figure 6.2.

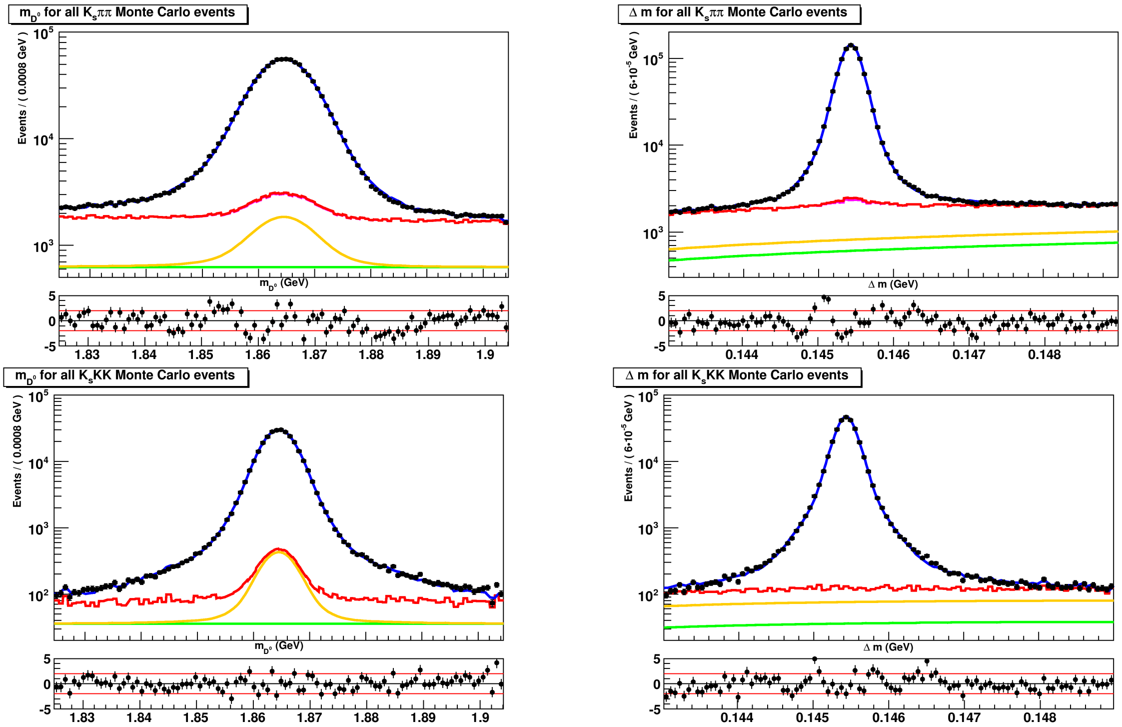

Figure 6.2: m_D (left column) and Δm (right column) projections of the fit to truth matched signal events and background events for $K_s\pi^+\pi^-$ (top row) and $K_sK^+K^-$ (bottom row). The colors represent the contribution of category 2 (yellow), category 3 (red) and category 4 (green). The blue line is the total PDF projection.

Since the fit has many parameters, those that present the largest correlations are fixed in the fit to the values found in a fit to signal Monte Carlo events. These are $\{\sigma_1^{m_D,c}, \sigma_1^{\Delta m,c}, \sigma_J^{\Delta m,nc}, \gamma_J^{\Delta m,nc}, \delta_J^{\Delta m,nc}\}$. The results of the fit on Monte Carlo are reported in table 6.1 for $K_s\pi^+\pi^-$ and in table 6.2 for $K_sK^+K^-$. The parameters of the PDF of categories 4 and 6 are fixed to the values found on fits to Monte Carlo events in these categories.

To validate the step 1a, the obtained fitted yields have been compared to the yields obtained by counting the events that have been matched to each category. The results are shown in table 6.3.

There is a reasonable agreement between the fitted yields and those obtained by counting on Monte Carlo. The largest discrepancies affect categories 2 and 4, because the combinatorial shape of the m_D PDF for category 4 is very similar to the tail component of the m_D PDF for category 2.

The yield of category 3 events is fixed to the one obtained by counting on Monte Carlo, since this yield is fully correlated with the one for category 4 because both m_D and Δm PDFs are very similar in these categories.

The results of the fit on data are reported in table 6.4 for $K_s\pi^+\pi^-$ and in table 6.5 for $K_sK^+K^-$, and the projections of this fit are shown in figure 6.3.

Parameter	Value	Limits	Units
n_1	936513 ± 1188	$(10^{-4}, 10^8)$	
n_2	21579 ± 611	$(10^{-4}, 10^8)$	
n_4	62697 ± 651	$(10^{-4}, 10^8)$	
$f_{nc}^{m_D,\Delta m}$	$0.2038 \pm 4.0 \cdot 10^{-3}$	$(0, 1)$	
$f_1^{m_D,nc}$	$0.3313 \pm 8.2 \cdot 10^{-3}$	$(0, 1)$	
$\mu_1^{m_D,nc}$	$1.85661 \pm 2.7 \cdot 10^{-4}$	$(1.7, 2)$	GeV
$\sigma_1^{m_D,nc}$	$2.229 \cdot 10^{-2} \pm 3.7 \cdot 10^{-4}$	$(10^{-4}, 0.1)$	GeV
$\mu_2^{m_D,nc}$	$1.86437 \pm 4.0 \cdot 10^{-5}$	$(1.7, 2)$	GeV
$\sigma_2^{m_D,nc}$	$4.852 \cdot 10^{-3} \pm 6.0 \cdot 10^{-5}$	$(10^{-4}, 0.1)$	GeV
$f_J^{\Delta m,nc}$	$0.2739 \pm 8.6 \cdot 10^{-3}$	$(0, 1)$	
$\mu_J^{\Delta m,nc}$	$0.145424 \pm 1.5 \cdot 10^{-6}$	$(0.14, 0.15)$	GeV
$\sigma_G^{\Delta m,nc}$	$3.234 \cdot 10^{-4} \pm 4.0 \cdot 10^{-6}$	$(10^{-5}, 0.01)$	GeV
$f_1^{m_D,\Delta m,c}$	$0.2556 \pm 2.9 \cdot 10^{-3}$	$(0, 1)$	
$\mu_1^{m_D,c}$	$1.86398 \pm 3.0 \cdot 10^{-5}$	$(1.7, 2)$	GeV
$\mu_1^{\Delta m,c}$	$0.145433 \pm 7.6 \cdot 10^{-7}$	$(0.14, 0.15)$	GeV
κ_1	$0.2568 \pm 4.2 \cdot 10^{-3}$	$(0, 1)$	
$\mu_2^{m_D,c}$	$1.86455 \pm 1.2 \cdot 10^{-5}$	$(1.7, 2)$	GeV
$\sigma_2^{m_D,c}$	$4.507 \cdot 10^{-3} \pm 1.3 \cdot 10^{-5}$	$(10^{-4}, 0.1)$	GeV
$\mu_2^{\Delta m,c}$	$0.145428 \pm 3.6 \cdot 10^{-7}$	$(0.14, 0.15)$	GeV
$\sigma_2^{\Delta m,c}$	$1.4418 \cdot 10^{-4} \pm 5.8 \cdot 10^{-7}$	$(10^{-5}, 0.01)$	GeV
κ_2	$6.12 \cdot 10^{-2} \pm 2.2 \cdot 10^{-3}$	$(0, 1)$	
$\xi^{\Delta m,2}$	0.93 ± 0.24	$(0, 100)$	

Table 6.1: Results of the step 1a fit to all the Monte Carlo $K_s\pi^+\pi^-$ events.

6.1.2 Step 1b

The signal box has been defined as the region enclosed within two average widths around the mean values of m_D and Δm, $m_D = \langle\mu^{m_D}\rangle \pm 2\langle\sigma^{m_D}\rangle$ and $\Delta m = \langle\mu^{\Delta m}\rangle \pm 2\langle\sigma^{\Delta m}\rangle$. The average mean values $\langle\mu\rangle$ and average widths $\langle\sigma\rangle$ have been calculated separately for the Monte Carlo and data samples by weighting the mean and width of each component of the PDF by their corresponding fit fraction.

The values found in the $K_s\pi^+\pi^-$ Monte Carlo sample are $\langle\mu^{m_D}\rangle = 1.86387\,\text{GeV}$, $\langle\sigma^{m_D}\rangle = 0.00634\,\text{GeV}$, $\langle\mu^{\Delta m}\rangle = 0.14543\,\text{GeV}$, $\langle\sigma^{\Delta m}\rangle = 0.00018\,\text{GeV}$. For the $K_sK^+K^-$ Monte Carlo sample, the same range of values has been adopted to allow further fits to run on both $K_s\pi^+\pi^-$ and $K_sK^+K^-$ datasets together.

The values found in the data sample are $\langle\mu^{m_D}\rangle = 1.86340\,\text{GeV}$, $\langle\sigma^{m_D}\rangle = 0.00685\,\text{GeV}$, $\langle\mu^{\Delta m}\rangle = 0.14541\,\text{GeV}$, $\langle\sigma^{\Delta m}\rangle = 0.00025\,\text{GeV}$.

Therefore, the definition of the signal box region is shown in table 6.6.

The yields in the signal box region n_c^{SB}, for each category c, have been evaluated by scaling the yields found in the large box region (n_c^{LB}) by the ratio of the PDF integrals in the two regions.

Parameter	Value	Limits	Units
n_1	299426 ± 601	$(10^{-4}, 10^{8})$	
n_2	3971 ± 220	$(10^{-4}, 10^{8})$	
n_4	3594 ± 125	$(10^{-4}, 10^{8})$	
$f_{nc}^{m_D,\Delta m}$	$0.1833 \pm 3.4 \cdot 10^{-3}$	$(0, 1)$	
$f_{12}^{m_D,nc}$	$0.708 \pm 3.0 \cdot 10^{-2}$	$(0, 1)$	
$f_{1}^{m_D,nc}$	$0.191 \pm 4.0 \cdot 10^{-2}$	$(0, 1)$	
$\mu_{1}^{m_D,nc}$	$1.86465 \pm 5.5 \cdot 10^{-4}$	$(1.7, 2)$	GeV
$\sigma_{1}^{m_D,nc}$	$2.13 \cdot 10^{-2} \pm 2.4 \cdot 10^{-3}$	$(10^{-4}, 0.1)$	GeV
$\mu_{2}^{m_D,nc}$	$1.86450 \pm 3.5 \cdot 10^{-5}$	$(1.7, 2)$	GeV
$\sigma_{2}^{m_D,nc}$	$2.618 \cdot 10^{-3} \pm 5.0 \cdot 10^{-5}$	$(10^{-4}, 0.1)$	GeV
$\mu_{3}^{m_D,nc}$	$1.86423 \pm 1.8 \cdot 10^{-4}$	$(1.7, 2)$	GeV
$\sigma_{3}^{m_D,nc}$	$1.040 \cdot 10^{-2} \pm 6.2 \cdot 10^{-4}$	$(10^{-4}, 1)$	GeV
$f_{J}^{\Delta m,nc}$	$0.2575 \pm 1.25 \cdot 10^{-2}$	$(0, 1)$	
$\mu_{J}^{\Delta m,nc}$	$0.145428 \pm 2.5 \cdot 10^{-6}$	$(0.14, 0.15)$	GeV
$\sigma_{G}^{\Delta m,nc}$	$3.705 \cdot 10^{-4} \pm 5.1 \cdot 10^{-6}$	$(10^{-5}, 0.01)$	GeV
$f_{1}^{m_D,\Delta m,c}$	$0.2844 \pm 4.9 \cdot 10^{-3}$	$(0, 1)$	
$\mu_{1}^{m_D,c}$	$1.86449 \pm 2.4 \cdot 10^{-5}$	$(1.7, 2)$	GeV
$\mu_{1}^{\Delta m,c}$	$0.145432 \pm 9.8 \cdot 10^{-7}$	$(0.14, 0.15)$	GeV
κ_1	$0.2293 \pm 6.5 \cdot 10^{-3}$	$(0, 1)$	
$\mu_{2}^{m_D,c}$	$1.86451 \pm 1.0 \cdot 10^{-5}$	$(1.7, 2)$	GeV
$\sigma_{2}^{m_D,c}$	$2.515 \cdot 10^{-3} \pm 1.3 \cdot 10^{-5}$	$(10^{-4}, 0.1)$	GeV
$\mu_{2}^{\Delta m,c}$	$0.145428 \pm 5.7 \cdot 10^{-7}$	$(0.14, 0.15)$	GeV
$\sigma_{2}^{\Delta m,c}$	$1.44295 \cdot 10^{-4} \pm 7.1 \cdot 10^{-7}$	$(10^{-5}, 0.01)$	GeV
κ_2	$7.1209 \cdot 10^{-2} \pm 3.1 \cdot 10^{-3}$	$(0, 1)$	
$\xi^{\Delta m,2}$	4.05 ± 0.68	$(0, 100)$	

Table 6.2: Results of the step 1a fit to all the Monte Carlo $K_s K^+ K^-$ events.

The errors on the yields in the signal box region have been evaluated using two different techniques.

- As a first approximation, the error obtained from the fitter, $\sigma_{n_c}^{LB}$ has been split into two contributions: a Poisson error ($\sqrt{n_c^{LB}}$) due to the statistical fluctuations of the yields in the sample, and a contribution from the fit difficulties in distinguishing different event categories, $\sigma_{f,c}^{LB}$, i.e., ${\sigma_{n_c}^{LB}}^2 = n_c^{LB} + {\sigma_{f,c}^{LB}}^2$. The $\sigma_{f,c}^{LB}$ contribution has been rescaled with the ratio of the PDF integrals in the two regions and the resulting value, $\sigma_{f,c}^{SB}$, has been added in quadrature to the Poisson error on the yields in the signal box, $\sqrt{n_c^{SB}}$, so the total error in the signal box region is $\sigma_{n_c}^{SB} = \sqrt{n_c^{SB} + {\sigma_{f,c}^{SB}}^2}$.
- As a more appropriate technique, 300 toy Monte Carlo experiments have been generated using the values of the PDF parameters and yields obtained in step 1a for data. The datasets produced in these toy Monte Carlo experiments have been fit to the same PDF used to

$\tilde{D}^0$ decay mode	Category	n_c from fit	n_c from Monte Carlo	Discrepancy
$K_s\pi^+\pi^-$	1	936513 ± 1188	936442	0.06
	2	21579 ± 611	21060	0.84
	3		113785	
	4	62697 ± 651	63442	-1.14
	6		1043	
$K_sK^+K^-$	1	299426 ± 601	300726	-2.16
	2	3971 ± 220	3201	3.50
	3		4291	
	4	3594 ± 125	3059	4.28

Table 6.3: Comparison of the fitted yields to those obtained by counting on Monte Carlo. Discrepancy is defined as the difference of both yields over the error on the fitted one.

generate them, allowing to float the same PDF parameters and yields as in the fit to data. The fitted values of the yields to these toy Monte Carlo datasets have been scaled from the large box region to the signal box region. The error of the yield has been taken as the root mean squared of the distribution of the yields in the signal box region.

The second technique is more appropriate and properly propagates the uncertainties on the yields from the large box region to the signal box region, while it also allows to calculate the full statistical covariance matrix for the yields in the signal box region. Therefore, this technique is the one that has been used to propagate the uncertainties on the yields to the mixing parameters.

The first technique has been applied in both Monte Carlo and data, and has to be considered as just a first fast approximation to the uncertainty.

The yields and errors obtained in both large and signal box regions are summarized in tables 6.7 and 6.8. For Monte Carlo, only the first approximation to the uncertainty has been used, while for data, both of them are reported, though only the toy Monte Carlo technique is used to propagate the uncertainties from the large box region to the signal box region. The values in table 6.8 show that the first technique overestimates the correct uncertainties given by the toy Monte Carlo technique.

The statistical covariance and correlation matrices for the yields in the signal box region, calculated from the toy Monte Carlo sample, are

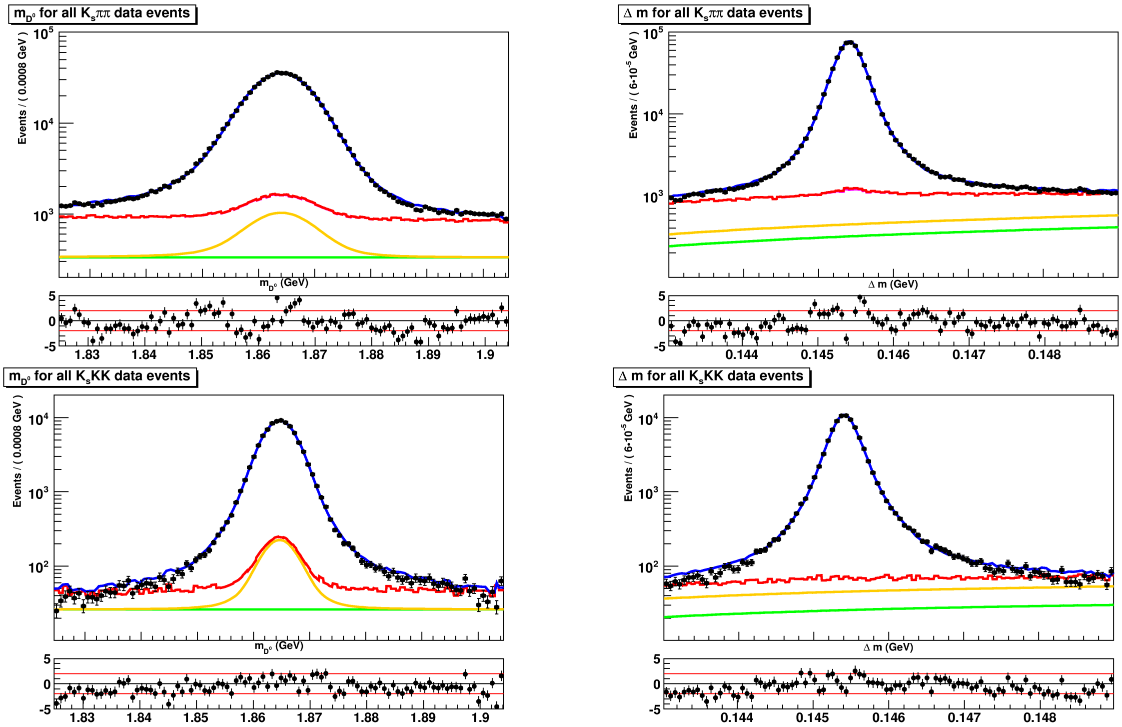

Figure 6.3: m_D (left column) and Δm (right column) projections of the fit to all data events for $K_s\pi^+\pi^-$ (top row) and $K_sK^+K^-$ (bottom row). The colors represent the contribution of category 2 (yellow), category 3 (red) and category 4 (green). The blue line is the total PDF projection.

$$V_{K_s\pi^+\pi^-} = \begin{array}{c} \begin{array}{ccc} n_1 & n_2 & n_4 \end{array} \\ \begin{pmatrix} 612178 & -1709.68 & 1611.13 \\ -1709.68 & 6023.8 & 537.849 \\ 1611.13 & 537.849 & 11773.3 \end{pmatrix} \end{array}, \quad \rho_{K_s\pi^+\pi^-} = \begin{array}{c} \begin{array}{ccc} n_1 & n_2 & n_4 \end{array} \\ \begin{pmatrix} 1.0000 & -0.0282 & 0.0190 \\ -0.0282 & 1.0000 & 0.0639 \\ 0.0190 & 0.0639 & 1.0000 \end{pmatrix} \end{array}, \tag{6.2}$$

$$V_{K_sK^+K^-} = \begin{array}{c} \begin{array}{ccc} n_1 & n_2 & n_4 \end{array} \\ \begin{pmatrix} 88353.7 & -248.146 & 15.4935 \\ -248.146 & 871.604 & 72.9307 \\ 15.4935 & 72.9307 & 154.557 \end{pmatrix} \end{array}, \quad \rho_{K_sK^+K^-} = \begin{array}{c} \begin{array}{ccc} n_1 & n_2 & n_4 \end{array} \\ \begin{pmatrix} 1.0000 & -0.0283 & 0.0042 \\ -0.0283 & 1.0000 & 0.1987 \\ 0.0042 & 0.1987 & 1.0000 \end{pmatrix} \end{array}. \tag{6.3}$$

Parameter	Value	Limits	Units
n_1	643502 ± 1020	$(10^{-4}, 10^8)$	
n_2	13317 ± 577	$(10^{-4}, 10^8)$	
n_4	33286 ± 494	$(10^{-4}, 10^8)$	
$f_{nc}^{m_D,\Delta m}$	$0.3254 \pm 5.6 \cdot 10^{-3}$	$(0, 1)$	
$f_1^{m_D,nc}$	$0.2743 \pm 6.8 \cdot 10^{-3}$	$(0, 1)$	
$\mu_1^{m_D,nc}$	$1.85782 \pm 2.5 \cdot 10^{-4}$	$(1.7, 2)$	GeV
$\sigma_1^{m_D,nc}$	$2.079 \cdot 10^{-2} \pm 3.7 \cdot 10^{-4}$	$(10^{-4}, 0.1)$	GeV
$\mu_2^{m_D,nc}$	$1.86381 \pm 3.5 \cdot 10^{-5}$	$(1.7, 2)$	GeV
$\sigma_2^{m_D,nc}$	$5.393 \cdot 10^{-3} \pm 5.4 \cdot 10^{-5}$	$(10^{-4}, 0.1)$	GeV
$f_J^{\Delta m,nc}$	$0.4012 \pm 8.6 \cdot 10^{-3}$	$(0, 1)$	
$\mu_J^{\Delta m,nc}$	$0.145425 \pm 1.7 \cdot 10^{-6}$	$(0.14, 0.15)$	GeV
$\sigma_G^{\Delta m,nc}$	$3.580 \cdot 10^{-4} \pm 4.5 \cdot 10^{-6}$	$(10^{-5}, 0.01)$	GeV
$f_1^{m_D,\Delta m,c}$	$0.2500 \pm 4.8 \cdot 10^{-3}$	$(0, 1)$	
$\mu_1^{m_D,c}$	$1.86351 \pm 4.4 \cdot 10^{-5}$	$(1.7, 2)$	GeV
$\mu_1^{\Delta m,c}$	$0.145412 \pm 1.15 \cdot 10^{-6}$	$(0.14, 0.15)$	GeV
κ_1	$0.3104 \pm 6.7 \cdot 10^{-3}$	$(0, 1)$	
$\mu_2^{m_D,c}$	$1.86416 \pm 1.85 \cdot 10^{-5}$	$(1.7, 2)$	GeV
$\sigma_2^{m_D,c}$	$4.895 \cdot 10^{-3} \pm 2.5 \cdot 10^{-5}$	$(10^{-4}, 0.1)$	GeV
$\mu_2^{\Delta m,c}$	$0.145405 \pm 6.3 \cdot 10^{-7}$	$(0.14, 0.15)$	GeV
$\sigma_2^{\Delta m,c}$	$1.7655 \cdot 10^{-4} \pm 9.7 \cdot 10^{-7}$	$(10^{-5}, 0.01)$	GeV
κ_2	$4.06 \cdot 10^{-2} \pm 3.0 \cdot 10^{-3}$	$(0, 1)$	
$\xi^{\Delta m,2}$	0.24 ± 0.33	$(0, 100)$	

Table 6.4: Results of the step 1a fit to all the data $K_s\pi^+\pi^-$ events.

Parameter	Value	Limits	Units
n_1	90329 ± 345	$(10^{-4}, 10^8)$	
n_2	2037 ± 162	$(10^{-4}, 10^8)$	
n_4	2636 ± 91	$(10^{-4}, 10^8)$	
$f_{nc}^{m_D,\Delta m}$	$0.313 \pm 1.2 \cdot 10^{-2}$	$(0, 1)$	
$f_{12}^{m_D,nc}$	$0.734 \pm 2.4 \cdot 10^{-2}$	$(0, 1)$	
$f_1^{m_D,nc}$	$0.150 \pm 2.3 \cdot 10^{-2}$	$(0, 1)$	
$\mu_1^{m_D,nc}$	$1.86617 \pm 5.9 \cdot 10^{-4}$	$(1.7, 2)$	GeV
$\sigma_1^{m_D,nc}$	$1.60 \cdot 10^{-2} \pm 1.1 \cdot 10^{-3}$	$(10^{-4}, 0.1)$	GeV
$\mu_2^{m_D,nc}$	$1.86471 \pm 4.8 \cdot 10^{-5}$	$(1.7, 2)$	GeV
$\sigma_2^{m_D,nc}$	$2.616 \cdot 10^{-3} \pm 8.0 \cdot 10^{-5}$	$(10^{-4}, 0.1)$	GeV
$\mu_3^{m_D,nc}$	$1.86456 \pm 1.9 \cdot 10^{-4}$	$(1.7, 2)$	GeV
$\sigma_3^{m_D,nc}$	$6.82 \cdot 10^{-3} \pm 4.6 \cdot 10^{-4}$	$(10^{-4}, 1)$	GeV
$f_J^{\Delta m,nc}$	$0.393 \pm 2.0 \cdot 10^{-2}$	$(0, 1)$	
$\mu_J^{\Delta m,nc}$	$0.145434 \pm 4.3 \cdot 10^{-6}$	$(0.14, 0.15)$	GeV
$\sigma_G^{\Delta m,nc}$	$3.75 \cdot 10^{-4} \pm 1.1 \cdot 10^{-5}$	$(10^{-5}, 0.01)$	GeV
$f_1^{m_D,\Delta m,c}$	$0.213 \pm 1.2 \cdot 10^{-2}$	$(0, 1)$	
$\mu_1^{m_D,c}$	$1.86466 \pm 7.2 \cdot 10^{-5}$	$(1.7, 2)$	GeV
$\mu_1^{\Delta m,c}$	$0.145404 \pm 2.9 \cdot 10^{-6}$	$(0.14, 0.15)$	GeV
κ_1	$0.267 \pm 2.0 \cdot 10^{-2}$	$(0, 1)$	
$\mu_2^{m_D,c}$	$1.86464 \pm 2.3 \cdot 10^{-5}$	$(1.7, 2)$	GeV
$\sigma_2^{m_D,c}$	$2.689 \cdot 10^{-3} \pm 3.3 \cdot 10^{-5}$	$(10^{-4}, 0.1)$	GeV
$\mu_2^{\Delta m,c}$	$0.145406 \pm 1.5 \cdot 10^{-6}$	$(0.14, 0.15)$	GeV
$\sigma_2^{\Delta m,c}$	$1.721 \cdot 10^{-4} \pm 2.4 \cdot 10^{-6}$	$(10^{-5}, 0.01)$	GeV
κ_2	$5.64 \cdot 10^{-2} \pm 6.8 \cdot 10^{-3}$	$(0, 1)$	
$\xi^{\Delta m,2}$	1.98 ± 0.80	$(0, 100)$	

Table 6.5: Results of the step 1a fit to all the data $K_s K^+ K^-$ events.

	Monte Carlo	Data
m_D (GeV)	$[1.85119, 1.87656]$	$[1.84970, 1.87711]$
Δm (GeV)	$[0.14506, 0.14579]$	$[0.14492, 0.14591]$

Table 6.6: Definition of the signal box for Monte Carlo and data.

$\tilde{D}^0$ decay mode	Category	n_c^{LB} from fit	n_c^{SB} from approximation
$K_s\pi^+\pi^-$	1	936513 ± 1188	802033 ± 1073
	2	21579 ± 611	2300 ± 80
	3	113785	6334
	4	62697 ± 651	2340 ± 53
	6	1043	772
$K_sK^+K^-$	1	299426 ± 601	268578 ± 563
	2	3971 ± 220	162 ± 16
	3	4291	196
	4	3594 ± 125	138 ± 13

Table 6.7: Yields with errors in the large and signal box regions for Monte Carlo.

$\tilde{D}^0$ decay mode	Category	n_c^{LB} from fit	n_c^{SB}	$\sigma_{n_c}^{SB}$ from approximation	$\sigma_{n_c}^{SB}$ from toy Monte Carlo
$K_s\pi^+\pi^-$	1	643502 ± 1020	540789	906	782
	2	13317 ± 577	1941	93	78
	3	55983	4388		
	4	33286 ± 494	1804	49	108
	6	316	258		
$K_sK^+K^-$	1	90329 ± 345	79908	320	297
	2	2037 ± 162	320	30	30
	3	2111	140		
	4	2636 ± 91	146	13	12

Table 6.8: Yields with errors in the large and signal box regions for data.

6.2 Step 2

The purpose of this step of the fit is to evaluate the initial values of the parameters used in the following step 3.

Step 2a is a time-dependent Dalitz-integrated fit to evaluate the parameters of the $\tilde{D}^0$ lifetime resolution function and the parameters of the $\tilde{D}^0$ background lifetime PDF, presented in §5.2.2 and §5.3.2 and summarized in table 5.4.

Notice that the parameters of the σ_t distribution are extracted separately from this fit process, as explained in §5.2.2 and §5.3.2.

Step 2b is a time-integrated fit for the parameters of the Dalitz decay model, described in §2.4.8.

The results of the two sub-steps of **step 2** are used as initial values for the following step 3.

6.2.1 Step 2a

The fit described in this section uses the *nomix* Monte Carlo sample for the signal, described in §4.1 and detailed in table 4.2. The reason of this choice is that more statistics is available in comparison with the *flat* sample. In the signal box region, 1104994 $K_s\pi^+\pi^-$ and 283561 $K_sK^+K^-$ events are retained after applying all the cuts described in §4.3.

6.2.1.1 True $\tilde{D}^0$ lifetime fit

To determine if the selection criteria defined in §4.3 induce any bias in the measurement of the average $\tilde{D}^0$ lifetime τ, a fit has been done to the true $\tilde{D}^0$ lifetime distributions in signal truth matched Monte Carlo, which has been generated with $\tau_{\text{gen}} = 0.4116\,\text{ps}$. The results of this fit for all the signal samples are shown in table 6.9. In all cases, the acceptance bias is small.

Figure 6.4 shows the lifetime distribution fit to the generated Monte Carlo signal events.

$\tilde{D}^0$ decay mode	Sample	τ (ps)
$K_s\pi^+\pi^-$	*flat*	0.4128 ± 0.0005
	nomix	0.4123 ± 0.0004
	mix	0.4121 ± 0.0004
$K_sK^+K^-$	*flat*	0.4120 ± 0.0008
	nomix	0.4106 ± 0.0008
	mix	0.4116 ± 0.0008

Table 6.9: Measured average lifetimes in true signal Monte Carlo samples.

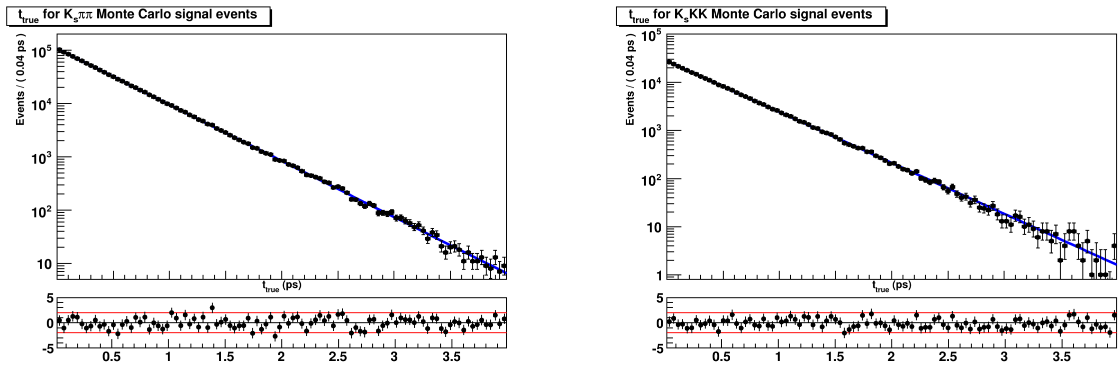

Figure 6.4: Fit to the true $\tilde{D}^0$ lifetime of signal truth matched $K_s\pi^+\pi^-$ (left plot) and $K_sK^+K^-$ (right plot) events.

6.2.1.2 Signal Monte Carlo fit

The $\tilde{D}^0$ lifetime resolution function expressed in (5.28) has three bias parameters. These parameters present a clear anti-correlation, since the expected average lifetime is

$$\langle t \rangle = \Gamma^{-1} + f_c b_c + (1 - f_c - f_o)b_t + f_o b_o. \tag{6.4}$$

Parameters that present correlation make the fit harder to converge, so the less of them involved in the minimization process, the easier the convergence. To determine which of them are necessary in step 3, three kinds of fits are performed on the three available signal Monte Carlo samples: first, only the core bias parameter is allowed to float and the rest are fixed to zero, second, the core and tail bias parameters are allowed to float and the outliers bias parameter is fixed to zero, and last, all the three bias parameters are allowed to float.

The results of these fits are shown in table 6.10. These results show that considering the bias parameter in the tail component improves the overall $\tilde{D}^0$ lifetime fit results. Since the fit does not present sensitivity to the bias parameter in the outliers component, this parameter is fixed to zero in the nominal fit.

However, the effect of considering non-zero bias parameters for the tail and outliers components has a very small impact on the measurement of the x and y mixing parameters. For example, for the *mix* Monte Carlo $K_sK^+K^-$ sample, where the need for b_t is more evident, table 6.11 shows that, allowing only the core bias parameter to float, makes a small difference in the measured values of x and y, with respect to allowing all the bias parameters to float. The fraction and width parameters of the outliers components have been fixed in the nominal mixing fit to the values reported in table 6.11.

The signal fit $\tilde{D}^0$ lifetime projections for $K_s\pi^+\pi^-$ and $K_sK^+K^-$ events are shown in figure 6.5, and the results of this fit are shown in table 6.12 and 6.13.

$\tilde{D}^0$ decay mode	Sample	Magnitude	b_c floated	$b_{[ct]}$ floated	$b_{[cto]}$ floated
$K_s\pi^+\pi^-$	*flat*	τ (ps)	0.4114 ± 0.0008	0.4100 ± 0.0011	0.4101 ± 0.0011
		b_c (ps)	0.0005 ± 0.0007	0.0002 ± 0.0007	0.0001 ± 0.0007
		b_t (ps)		0.034 ± 0.016	0.034 ± 0.017
		b_o (ps)			-0.15 ± 0.47
	nomix	τ (ps)	0.4114 ± 0.0007	0.4124 ± 0.0008	0.4120 ± 0.0009
		b_c (ps)	-0.0003 ± 0.0005	0.00009 ± 0.0006	0.0002 ± 0.0006
		b_t (ps)		-0.024 ± 0.011	-0.023 ± 0.011
		b_o (ps)			0.23 ± 0.19
	mix	τ (ps)	0.4116 ± 0.0007	0.4116 ± 0.0008	0.4108 ± 0.0009
		b_c (ps)	-0.0005 ± 0.0006	-0.0005 ± 0.0006	-0.0003 ± 0.0006
		b_t (ps)		0.0009 ± 0.012	0.003 ± 0.011
		b_o (ps)			0.38 ± 0.14
$K_sK^+K^-$	*flat*	τ (ps)	0.4130 ± 0.0017	0.4061 ± 0.0026	0.4056 ± 0.0027
		b_c (ps)	-0.0006 ± 0.0016	0.0002 ± 0.0017	0.0005 ± 0.0017
		b_t (ps)		0.102 ± 0.027	0.101 ± 0.027
		b_o (ps)			0.93 ± 1.61
	nomix	τ (ps)	0.4115 ± 0.0017	0.4102 ± 0.0026	0.4112 ± 0.0026
		b_c (ps)	-0.0004 ± 0.0017	-0.0005 ± 0.0017	-0.0011 ± 0.0017
		b_t (ps)		0.016 ± 0.023	0.015 ± 0.022
		b_o (ps)			-0.52 ± 0.51
	mix	τ (ps)	0.4810 ± 0.0015	0.4103 ± 0.0027	0.4094 ± 0.0029
		b_c (ps)	-0.0073 ± 0.0013	-0.0081 ± 0.0014	-0.0079 ± 0.0014
		b_t (ps)		0.062 ± 0.016	0.064 ± 0.016
		b_o (ps)			0.17 ± 0.15

Table 6.10: $\tilde{D}^0$ proper lifetime fits to signal Monte Carlo samples, to account for different bias components in the resolution function. The mixing parameters x and y are fixed to 0 in all these fits.

Magnitude	b_c floated	$b_{[cto]}$ floated
τ (ps)	0.4158 ± 0.0015	0.4074 ± 0.0029
x	0.0058 ± 0.0050	0.0059 ± 0.0051
y	0.0104 ± 0.0031	0.0107 ± 0.0032

Table 6.11: Results of the fit to $\tilde{D}^0$ lifetime and mixing parameters for the $K_sK^+K^-$ *mix* signal Monte Carlo sample, with different bias components allowed to float.

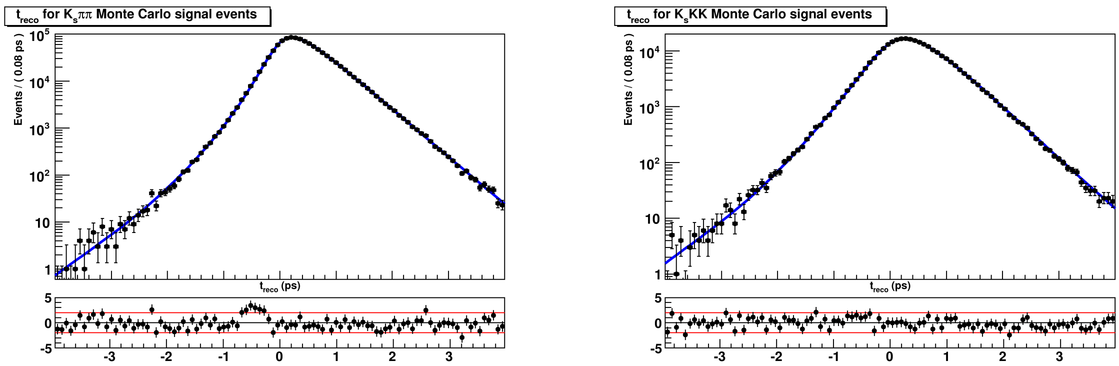

Figure 6.5: $\tilde{D}^0$ lifetime projections of the fit to signal truth matched *nomix* events for $K_s\pi^+\pi^-$ (left plot) and $K_sK^+K^-$ (right plot).

Parameter	Value	Limits	Units
τ	$0.41235 \pm 7.9 \cdot 10^{-4}$	$(0.1, 1)$	ps
f_c	$0.9445 \pm 5.4 \cdot 10^{-3}$	$(0, 1)$	
b_c	$8.7 \cdot 10^{-5} \pm 6.2 \cdot 10^{-4}$	$(-1, 1)$	ps
k_c	$0.9653 \pm 3.4 \cdot 10^{-3}$	$(0.001, 2)$	
b_t	$-2.4 \cdot 10^{-2} \pm 1.1 \cdot 10^{-2}$	$(-1, 1)$	ps
k_t	$1.812 \pm 4.1 \cdot 10^{-2}$	$(0.001, 5)$	
f_o	$6.1 \cdot 10^{-4} \pm 1.5 \cdot 10^{-4}$	$(0, 1)$	
k_o	1.42 ± 0.13	$(0, 20)$	

Table 6.12: Results of the step 2a fit to all the signal Monte Carlo $K_s\pi^+\pi^-$ events.

6.2.1.3 Background Monte Carlo fit

The t and σ_t PDF for correctly truth matched signal events and for background events has been described in §5.2.2 and §5.3.2, and summarized in table 5.4.

For categories 3 and 4, the fit to the $\tilde{D}^0$ lifetime has been done separately from the fit to the rest of the parameters. The parameters of the background $\tilde{D}^0$ lifetime PDF for these events, with fake $\tilde{D}^0$ mesons, can be extracted from three different sources:

- Data m_D sidebands.
- Monte Carlo m_D sidebands.
- Fake Monte Carlo $\tilde{D}^0$ events in the signal box region.

The upper and lower m_D sidebands have been defined as the region between 60 MeV and 100 MeV above and below the nominal $\tilde{D}^0$ mass [55], respectively, with no restrictions on the values of Δm.

- Upper m_D sideband: $m_D \in [1.8645 + 0.060, 1.8645 + 0.100]$ GeV.

Parameter	Value	Limits	Units
τ	$0.4102 \pm 2.6 \cdot 10^{-3}$	$(0.1, 1)$	ps
f_c	$0.913 \pm 1.2 \cdot 10^{-2}$	$(0, 1)$	
b_c	$-5.2 \cdot 10^{-4} \pm 1.7 \cdot 10^{-3}$	$(-1, 1)$	ps
k_c	$0.9729 \pm 6.5 \cdot 10^{-3}$	$(0.001, 2)$	
b_t	$1.6 \cdot 10^{-2} \pm 2.3 \cdot 10^{-2}$	$(-1, 1)$	ps
k_t	$1.825 \pm 5.9 \cdot 10^{-2}$	$(0.001, 5)$	
f_o	$1.11 \cdot 10^{-3} \pm 4.2 \cdot 10^{-4}$	$(0, 1)$	
k_o	1.85 ± 0.22	$(0, 20)$	

Table 6.13: Results of the step 2a fit to all the signal Monte Carlo $K_sK^+K^-$ events.

- Lower m_D sideband: $m_D \in [1.8645 - 0.100, 1.8645 - 0.060]$ GeV.

The lifetime distributions of events from the three different sources proposed are compared in figure 6.6.

The $\tilde{D}^0$ lifetime PDF $p^t_{3,4}$ has been fit to *nomix* Monte Carlo background events in categories 3 and 4 in the signal box region, and the parameters obtained are fixed in the mixing fit to both data and Monte Carlo events. Since it is reasonable to use either Monte Carlo or data m_D sidebands to fix the parameters of $p^t_{3,4}$, this choice is considered a source of systematic uncertainty and is explained in detail in §7.1.4.

The fit projections to the combination of all the background samples are shown in figure 6.7.

The $\tilde{D}^0$ lifetime projection of the fit to background Monte Carlo K_sK_s events is shown in figure 6.8. The parameters obtained from this fit are also fixed in the nominal mixing fit to both data and Monte Carlo events.

The results of the fit on Monte Carlo are reported in table 6.14 for $K_s\pi^+\pi^-$, in table 6.15 for $K_sK^+K^-$, and in table 6.16 for category 6 $K_s\pi^+\pi^-$ events.

Parameter	Value	Limits	Units
f^t_J	0.94 ± 0.73	$(0, 1)$	
μ^t_J	0.08 ± 0.11	$(-10, 10)$	ps
σ^t_J	0.66 ± 0.18	$(0, 10)$	ps
γ^t_J	0.24 ± 0.11	$(-10, 10)$	
δ^t_J	-1.39 ± 0.14	$(-10, 10)$	
μ^t_G	-0.03 ± 0.25	$(-10, 10)$	ps
σ^t_G	0.23 ± 0.30	$(0, 10)$	ps

Table 6.14: Results of the step 2a fit to Monte Carlo background $K_s\pi^+\pi^-$ events in categories 3 and 4.

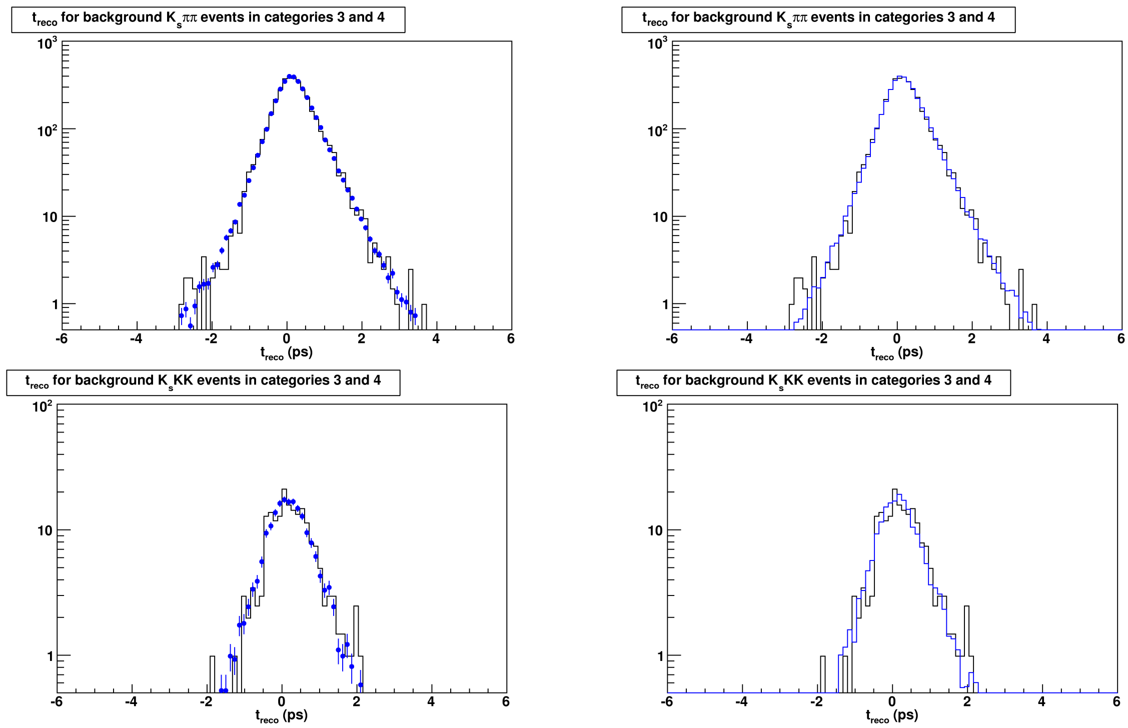

Figure 6.6: Compared $\tilde{D}^0$ lifetime projections of the fake Monte Carlo events in the signal box (black curves) with data (blue points) and Monte Carlo (blue histograms) events in the sidebands, for $K_s\pi^+\pi^-$ (top row) and $K_sK^+K^-$ (bottom row) events.

6.2.1.4 Signal and background Monte Carlo and data fit

Since the bias parameters of the $\tilde{D}^0$ lifetime resolution function are very correlated between them and with the $\tilde{D}^0$ average lifetime, the presence of background would make difficult the discrimination between the real background events and the wide tail components of the resolution function for true $\tilde{D}^0$ events. For this reason, the bias parameter of the tail component has been fixed in the complete Monte Carlo and data sets to the values obtained in the signal Monte Carlo fit, summarized in tables 6.12 and 6.13.

This decision is backed up by a set of toy Monte Carlo experiments tuned to data. Figure 6.9 shows the residual values of b_c, b_t and τ, defined as the difference between the fitted and the generated values, for 100 signal toy Monte Carlo samples. Figure 6.10 shows the residual values of the same magnitudes for 100 toy Monte Carlo samples, with both signal and background. The effect of floating the tail bias component produces a lifetime offset of $\sim 1\,\mathrm{fs}$ due to the anti-correlation between the bias parameters and the lifetime, which remarks the inability of a correct discrimination of the signal and the background when the latter is included. However, this discrimination is improved in step 3, because the Dalitz variables enhance the ability to perform this discrimination. Figure 6.11 shows the fitted b_c and τ residual values for 100 toy Monte Carlo samples, with both signal and background, and with b_t fixed to the value obtained in the signal Monte Carlo fit, and proves that no significant bias is expected in b_c or τ due to fixing b_t.

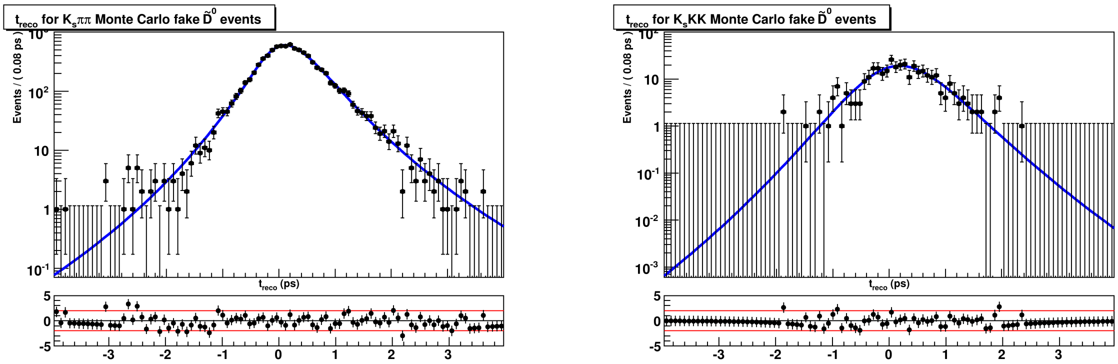

Figure 6.7: $\tilde{D}^0$ lifetime projections of the fit to Monte Carlo background events in categories 3 and 4 for $K_s\pi^+\pi^-$ (left plot) and $K_sK^+K^-$ (right plot).

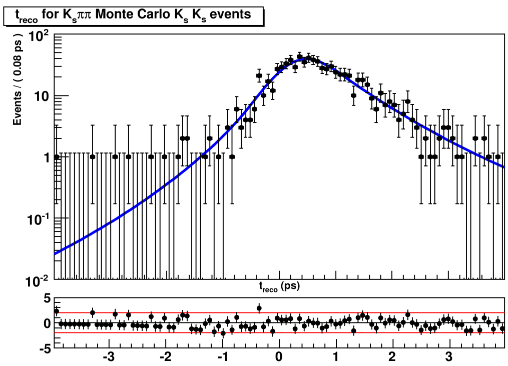

Figure 6.8: $\tilde{D}^0$ lifetime projections of the fit to background Monte Carlo K_sK_s events.

The effect of fixing the tail and outliers bias components is accounted for as a source of systematic uncertainty and is described in §7.1.4.

The fit projections to the complete Monte Carlo sample, with both signal and background, and to data, are shown in figure 6.12. The results of the fit to Monte Carlo events are shown in table 6.17 for $K_s\pi^+\pi^-$ and in table 6.18 for $K_sK^+K^-$. The results of the fit to data events are shown in table 6.19 for $K_s\pi^+\pi^-$ and in 6.20 for $K_sK^+K^-$.

No significant core bias component is observed in Monte Carlo, which is consistent with the hypothesis of no misalignment effects in this sample. However, a significant core bias component is found on data, at the level of $7\,\sigma$ for $K_s\pi^+\pi^-$ and $2.2\,\sigma$ for $K_sK^+K^-$. This observation can be explained as vertex detector (SVT) misalignment effects.

No significant lifetime bias is observed in Monte Carlo. In data, the deviation from the world average [55] is $(\tau - \tau_{\mathrm{PDG}}) = (0.0012 \pm 0.0018)$ for $K_s\pi^+\pi^-$ and $(\tau - \tau_{\mathrm{PDG}}) = (0.0043 \pm 0.0037)$ for $K_sK^+K^-$, which shows no evidence of any significant bias in the measurement of the $\tilde{D}^0$ lifetime in the data sample.

Parameter	Value	Limits	Units
μ_J^t	0.08 ± 0.15	$(-10, 10)$	ps
σ_J^t	1.09 ± 0.30	$(0, 10)$	ps
γ_J^t	0.26 ± 0.25	$(-10, 10)$	
δ_J^t	-1.96 ± 0.44	$(-10, 10)$	

Table 6.15: Results of the step 2a fit to Monte Carlo background $K_s K^+ K^-$ events in categories 3 and 4.

Parameter	Value	Limits	Units
$f_J^{t,6}$	0.81 ± 0.21	$(0, 1)$	
$\mu_J^{t,6}$	0.37 ± 0.095	$(-10, 10)$	ps
$\sigma_J^{t,6}$	0.83 ± 0.24	$(0, 10)$	ps
$\gamma_J^{t,6}$	-0.46 ± 0.09	$(-10, 0)$	
$\delta_J^{t,6}$	1.19 ± 0.16	$(-10, 10)$	
$\sigma_G^{t,6}$	0.40 ± 0.11	$(0, 10)$	ps

Table 6.16: Results of the step 2a fit to Monte Carlo background $K_s \pi^+ \pi^-$ events in category 6.

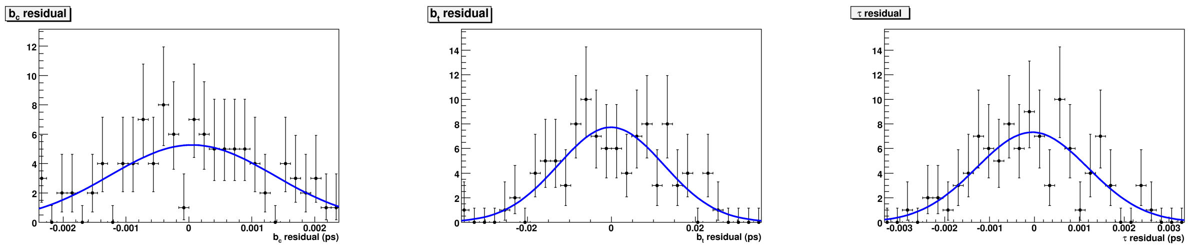

Figure 6.9: Residual distributions of fitted b_c (left plot), b_t (center plot) and $\tilde{D}^0$ average lifetime τ (right plot) for a set of 100 signal Monte Carlo experiments tuned to data.

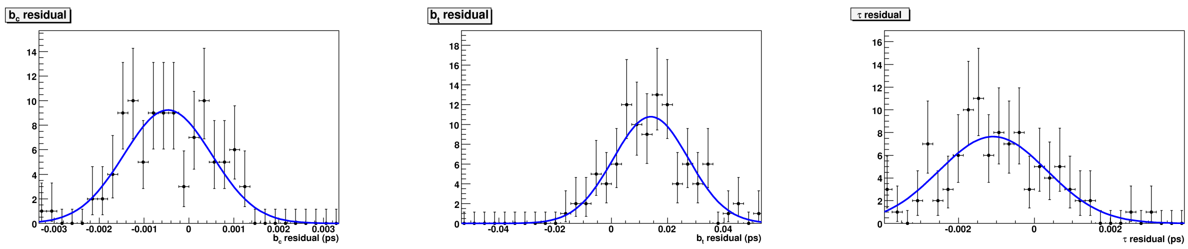

Figure 6.10: Residual distributions of fitted b_c (left plot), b_t (center plot) and $\tilde{D}^0$ average lifetime τ (right plot) for a set of 100 Monte Carlo experiments, with both signal and background, tuned to data.

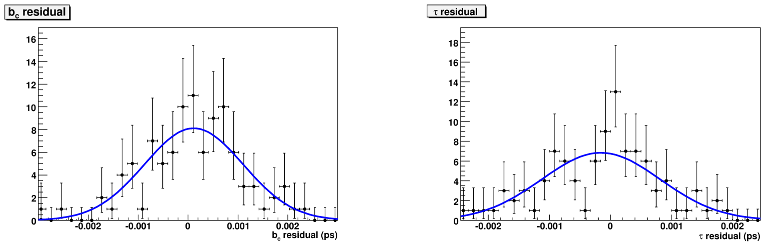

Figure 6.11: Residual distributions, with b_t fixed, of fitted b_c (left plot) and $\tilde{D}^0$ average lifetime τ (right plot) for a set of 100 Monte Carlo experiments, with both signal and background, tuned to data.

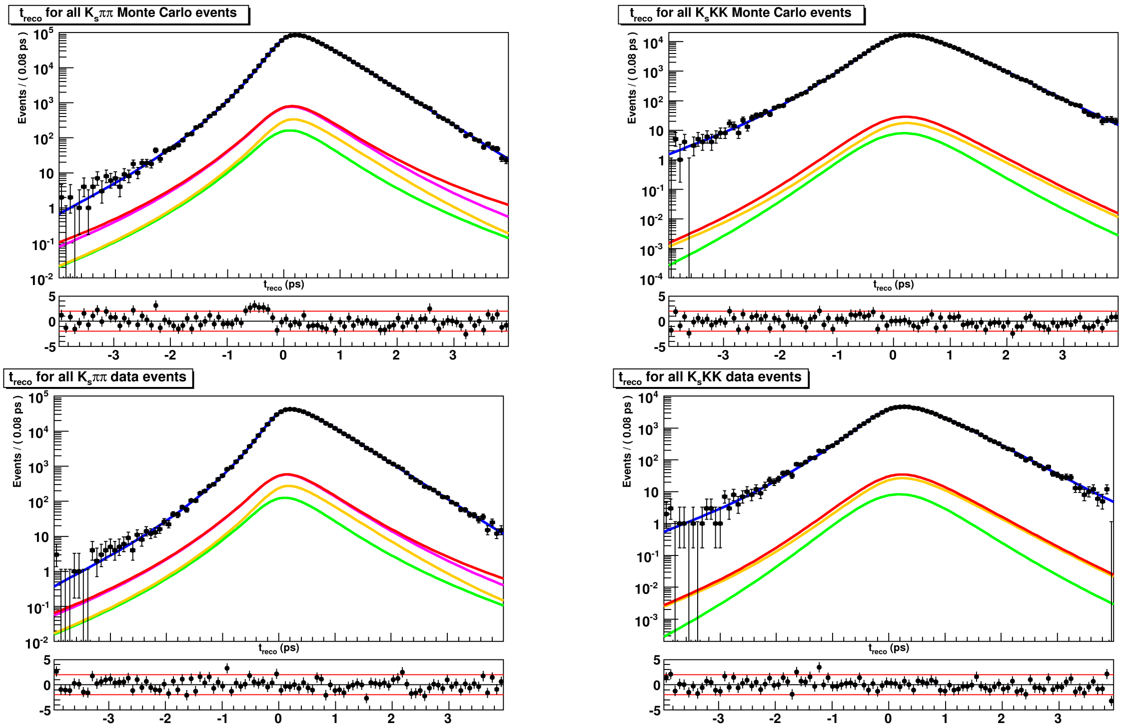

Figure 6.12: $\tilde{D}^0$ lifetime projections of the fit to all Monte Carlo (top row) and data (bottom row) $K_s\pi^+\pi^-$ (left column) and $K_sK^+K^-$ (right column) events. The colors represent the contribution of category 2 (yellow), category 3 (red) and category 4 (green). The blue line is the total PDF projection.

Parameter	Value	Limits	Units
τ	$0.41207 \pm 6.7 \cdot 10^{-4}$	$(0.1, 1)$	ps
f_c	$0.9434 \pm 5.7 \cdot 10^{-3}$	$(0, 1)$	
b_c	$5.9 \cdot 10^{-4} \pm 5.9 \cdot 10^{-4}$	$(-1, 1)$	ps
k_c	$0.9662 \pm 3.4 \cdot 10^{-3}$	$(0.001, 2)$	
k_t	$1.735 \pm 4.0 \cdot 10^{-2}$	$(0.001, 5)$	

Table 6.17: Results of the step 2a fit to all Monte Carlo $K_s\pi^+\pi^-$ events.

Parameter	Value	Limits	Units
τ	$0.4102 \pm 1.7 \cdot 10^{-3}$	$(0.1, 1)$	ps
f_c	$0.9129 \pm 9.9 \cdot 10^{-3}$	$(0, 1)$	
b_c	$-5.2 \cdot 10^{-4} \pm 1.7 \cdot 10^{-3}$	$(-1, 1)$	ps
k_c	$0.9729 \pm 6.0 \cdot 10^{-3}$	$(0.001, 2)$	
k_t	$1.819 \pm 4.8 \cdot 10^{-2}$	$(0.001, 5)$	

Table 6.18: Results of the step 2a fit to all Monte Carlo $K_s K^+ K^-$ events.

Parameter	Value	Limits	Units
τ	$0.40893 \pm 9.6 \cdot 10^{-4}$	$(0.1, 1)$	ps
f_c	$0.921 \pm 1.3 \cdot 10^{-2}$	$(0, 1)$	
b_c	$6.18 \cdot 10^{-3} \pm 8.9 \cdot 10^{-4}$	$(-1, 1)$	ps
k_c	$0.9974 \pm 6.2 \cdot 10^{-3}$	$(0.001, 2)$	
k_t	$1.626 \pm 5.1 \cdot 10^{-2}$	$(0.001, 5)$	

Table 6.19: Results of the step 2a fit to all $K_s \pi^+ \pi^-$ data events.

Parameter	Value	Limits	Units
τ	$0.4058 \pm 3.4 \cdot 10^{-3}$	$(0.1, 1)$	ps
f_c	$0.918 \pm 1.8 \cdot 10^{-2}$	$(0, 1)$	
b_c	$7.3 \cdot 10^{-3} \pm 3.3 \cdot 10^{-3}$	$(-1, 1)$	ps
k_c	$1.033 \pm 1.2 \cdot 10^{-2}$	$(0.001, 2)$	
k_t	1.95 ± 0.10	$(0.001, 5)$	

Table 6.20: Results of the step 2a fit to all $K_s K^+ K^-$ data events.

6.2.2 Step 2b

The fit described in this section is a $\tilde{D}^0$ lifetime-integrated fit to find initial values for the parameters of the decay model, described in §2.4.8, to be used in step 3. The parameterization of the background is also discussed.

6.2.2.1 Signal decay model PDF

The complete PDF for the decay model has been described in expression (5.30) of §5.2.3.

The fit described in this section is a $\tilde{D}^0$ lifetime-integrated fit, and no mixing is yet considered. Therefore, the $\tilde{D}^0$ lifetime-integrated amplitude PDF becomes

$$p_1^D = \frac{1}{N_D}\epsilon(m_{ab}^2, m_{ac}^2)\left|\tilde{A}_f\right|^2, \tag{6.5}$$

where $\tilde{A}_f$ is the amplitude described in §2.4.8.

6.2.2.2 Background decay model PDF

The decay model PDF for events in category 2 has been described in §5.3.3.

The shapes of the background phase space PDF for events in categories 3 and 4, with fake $\tilde{D}^0$ mesons, are non-parametric and can be extracted from the same three sources as the parameters of the $\tilde{D}^0$ lifetime PDF, namely data sidebands, Monte Carlo sidebands, and fake Monte Carlo $\tilde{D}^0$ mesons in the signal box region.

Figures 6.13 and 6.14 show the Dalitz plot projections of the upper and lower m_D sidebands for the Monte Carlo and data samples, respectively. It is observed that they present a different resonant structure due to their different background composition.

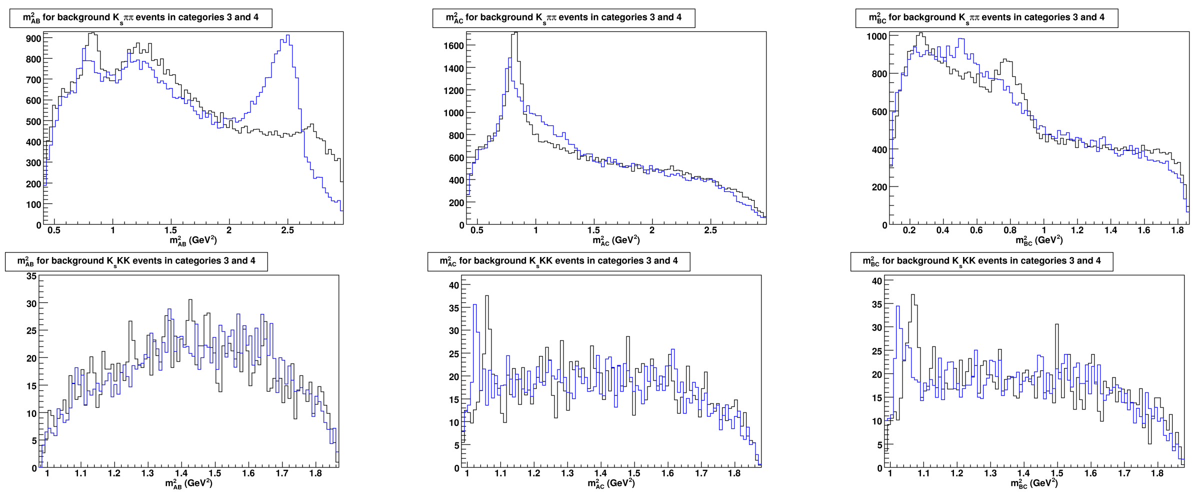

Figure 6.13: Dalitz plot projections of the **Monte Carlo** upper (blue histograms) and lower (black histograms) m_D sidebands for $K_s\pi^+\pi^-$ (top row) and $K_sK^+K^-$ (bottom row) events.

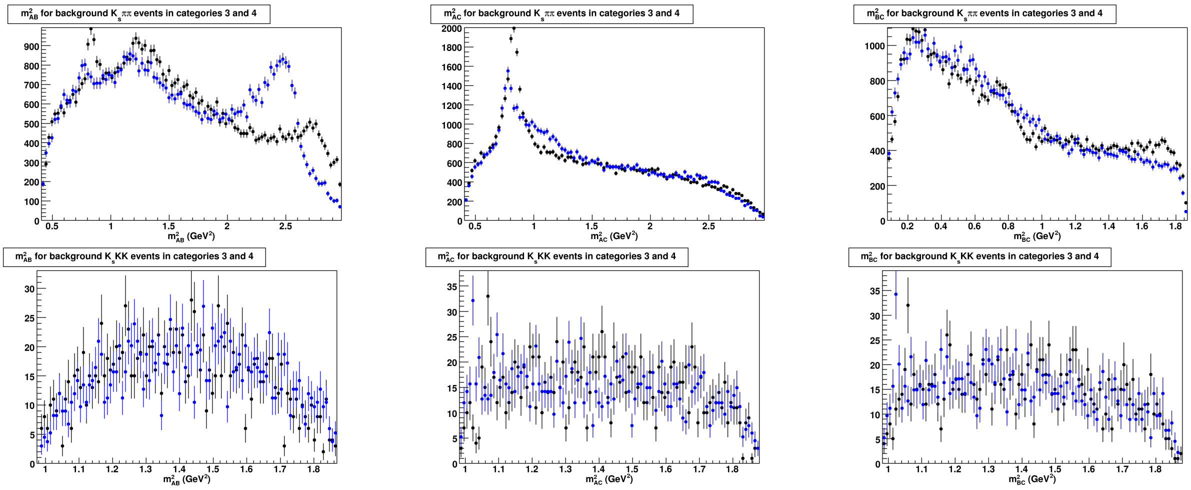

Figure 6.14: Dalitz plot projections of the **data** upper (blue points) and lower (black points) m_D sidebands for $K_s\pi^+\pi^-$ (top row) and $K_sK^+K^-$ (bottom row) events.

Figure 6.15 shows the Dalitz plot projections of the merged upper and lower m_D sidebands for the Monte Carlo and data samples. It can be observed that the agreement between Monte Carlo and data samples is good.

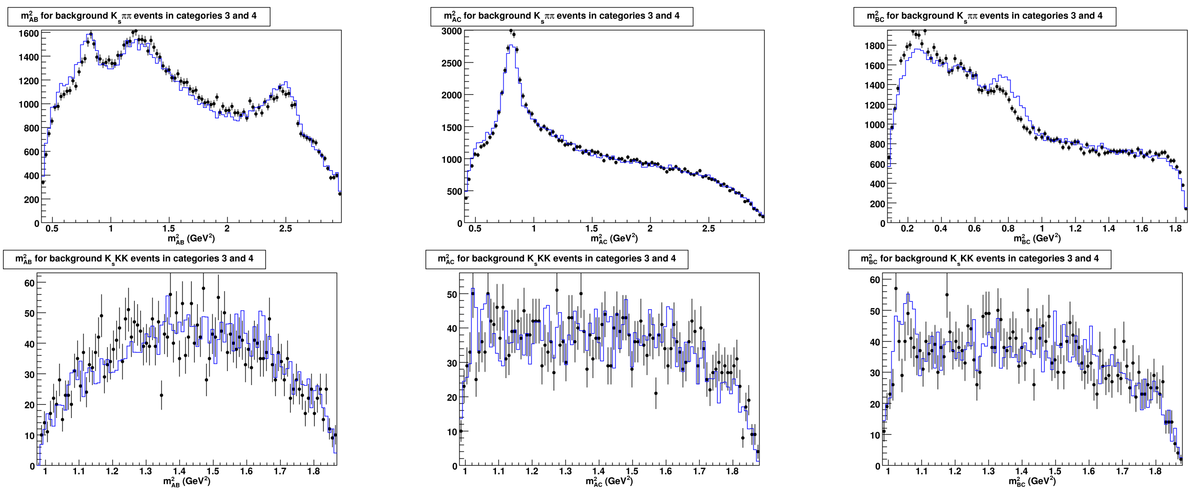

Figure 6.15: Dalitz plot projections of the **Monte Carlo** (blue histograms) and **data** (black points) merged upper and lower m_D sidebands for $K_s\pi^+\pi^-$ (top row) and $K_sK^+K^-$ (bottom row) events.

The Dalitz plot projections of the fake $\tilde{D}^0$ Monte Carlo events (categories 3 and 4) in the signal box region are compared with the Dalitz plot projections of the merged upper and lower m_D sidebands for Monte Carlo events, in figure 6.16, and for data events, in figure 6.17.

Since the purity in the signal box region is very large, the background is highly reduced in this region and large statistical fluctuations become evident in the histograms bin-to-bin variation. However, the data in the m_D sidebands have a much larger statistics and their Dalitz plot pro-

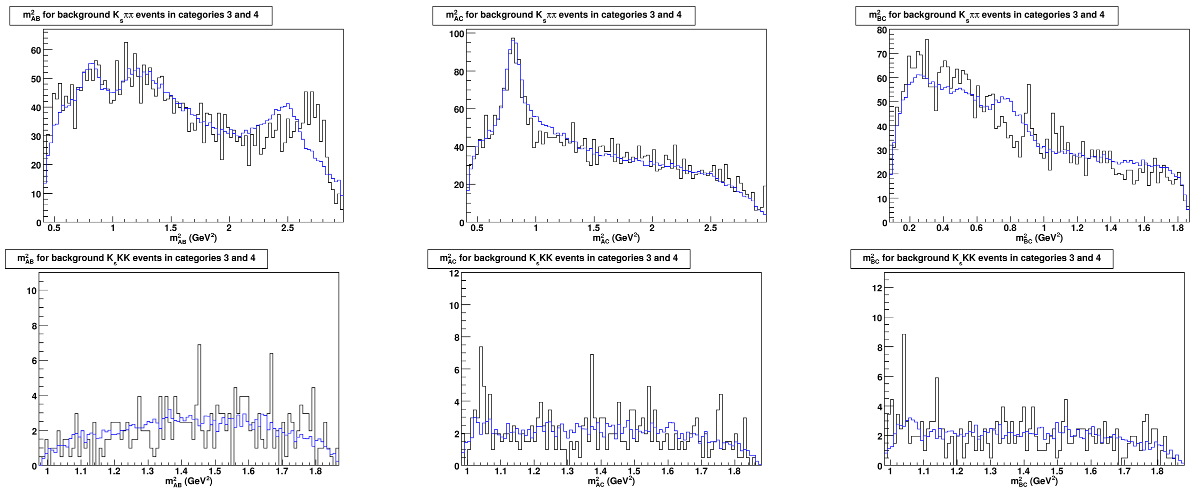

Figure 6.16: Dalitz plot projections of the fake $\tilde{D}^0$ Monte Carlo events in the signal box region (black points) and of the merged upper and lower **Monte Carlo** m_D sidebands (blue points) for $K_s\pi^+\pi^-$ (top row) and $K_sK^+K^-$ (bottom row) events.

jections are in good agreement with those of the fake $\tilde{D}^0$ Monte Carlo events in the signal box region.

For this reason, the nominal fit uses the background profiles obtained from the data m_D sidebands for the data sample, and those obtained from Monte Carlo background with fake $\tilde{D}^0$ in the signal box region, for the Monte Carlo sample. This choice is made in both steps 2b and 3. No analytical parameterization is introduced for the description of these background profiles, so a non-parametric PDF is used.

The approaches to the phase space background profiles that are not used in the nominal fit are accounted for as a source of systematic uncertainty and are reported in §7.1.10.

6.2.2.3 Mistag fractions

Mistagged events are events with a true $\tilde{D}^0$ where the soft pion has been reconstructed with opposite charge with respect to its $D^{\star\pm}$ mother. Since these $\tilde{D}^0$ mesons have the wrong tag, their distribution in the phase space is the one that corresponds to their flavor, but they are fitted to the distribution that corresponds to the opposite flavor. This creates a fake mixing effect and, therefore, these events are potentially dangerous.

Table 6.21 shows the fraction of events in Monte Carlo categories 1 and 2 where the soft pion has the right sign charge.

In category 1, mistagged events are those where the soft pion and the $\tilde{D}^0$ are not sisters. This effect is very small, as can be seen in table 6.21, and is neglected in the nominal fit.

In category 2, the soft pion is fake and its charge is random, so the fraction of mistagged events in this category is expected to be around $\sim 50\,\%$. Table 6.21 shows that these fractions for both

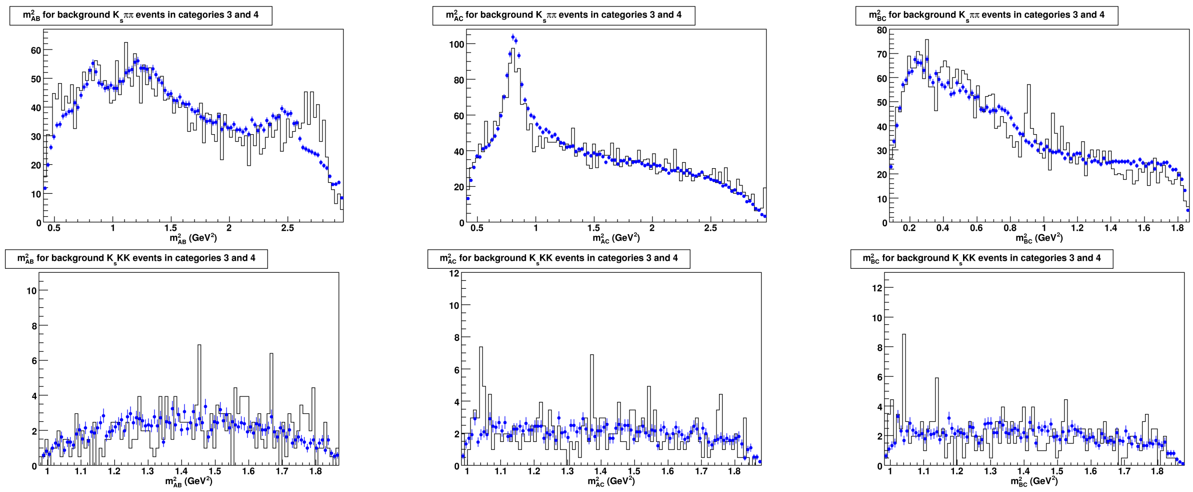

Figure 6.17: Dalitz plot projections of the fake $\tilde{D}^0$ Monte Carlo events in the signal box region (black points) and of the merged upper and lower **data** m_D sidebands (blue points) for $K_s\pi^+\pi^-$ (top row) and $K_sK^+K^-$ (bottom row) events.

$K_s\pi^+\pi^-$ and $K_sK^+K^-$ events deviate very slightly from 50 %, so a value of 50 % is assumed in the nominal fit.

Category	$K_s\pi^+\pi^-$	$K_sK^+K^-$
1	0.99876 ± 0.00006	0.99979 ± 0.00006
2	0.539 ± 0.014	0.512 ± 0.046

Table 6.21: Fractions of correctly tagged $\tilde{D}^0$ mesons in categories 1 and 2, extracted from Monte Carlo events.

In categories 3 and 4, the background decay model PDF is the same for both D^0 and $\bar{D}^0$, so there are no mistag fractions to consider.

6.2.2.4 Results for $K_s\pi^+\pi^-$

As described in §2.4.8, the P-vector parameters β^0_α, s^{pr}_0 and $f^{pr}_{\pi\pi,j}$ in expression (2.84) are left to float in the fit, and the parameters $f^{pr}_{i,j}$ for $i \neq \pi\pi$ have been fixed to zero, since they are not related to the $\pi\pi$ production process. Also, $f^{pr}_{\pi\pi,\eta\eta}$ and $f^{pr}_{\pi\pi,\eta\eta'}$ have also been fixed to zero, and s^{pr}_0 has been fixed to s^{sc}_0, since there is little sensitivity to this parameters in the data.

The $f^{pr}_{i,j}$ parameters obtained in this step 2b have been fixed in the nominal mixing fit performed in step 3.

The parameterization of the $K\pi$ S-wave has been studied in detail by fitting the data sample to different alternative parameterizations. These parameterizations include

- expression (2.92) itself, where elastic unitarity is not enforced,

- the same expression with unitarity imposed ($R = B = 1$, $\phi_R = \phi_B = 0$), and
- the same expression without the background phase shift ($\phi_B = 0$).

A significant improvement of about 20 units in $-\ln \mathcal{L}_{\text{ext}}$ is observed between the first two, which favors the first option. Therefore, the parameterization in expression (2.92) is adopted in the nominal model.

The parameters of the $K\pi$ S-wave obtained in this step 2b have been fixed in the nominal mixing fit performed in step 3.

The results of the step 2b fit on $K_s\pi^+\pi^-$ data events are shown in table 6.22 for the isobar component parameters, in table 6.23 for the P-vector parameters, and in table 6.24 for the $K\pi$ S-wave parameters. The total fit fraction adds up to 103.27 %, with $\chi^2/\text{ndof} = 10429.2/(8626 - 41) = 1.2148$. Since a statistically significant number of events is necessary to make the χ^2 evaluation meaningful, this χ^2/ndof has been obtained using an adaptive binning with the purpose of producing uniformly populated bins across the phase space. The algorithm starts with a single rectangular bin enclosing the whole phase space. Then, the centroid of the events populating the bin is calculated and used to divide the bin in four smaller bins. This process is repeated recursively until some of the bins contains less than a certain number of events, that has been set to 30 in this evaluation. The average number of events per bin is 64.

The Dalitz plot projections of the fit to $K_s\pi^+\pi^-$ data events to the nominal model are shown in figure 6.18. The normalized residuals of this fit across the Dalitz plot are shown in figure 6.19, with an adaptive and a uniform binning. Two regions in the normalized residuals plot present a large discrepancy between the data and the model: on one hand, the small diagonal red region corresponds to the low energy region of the $\pi^+\pi^-$ projection, around 0.1 GeV^2, and is caused by invariant mass resolution effects not explicitly accounted for in the nominal model. On the other hand, the red region in the bottom right corner of the Dalitz plot is due to imperfections in the parameterization of the efficiency non-uniformities across the phase space. These regions, however, have no sensitivity to mixing.

Component	Re $\left(a_r e^{i\phi_r}\right)$	Im $\left(a_r e^{i\phi_r}\right)$	f_r (%)	m_r (GeV)	Γ_r (GeV)
$K_0^{\star -}(1430)$	0.20 ± 0.07	2.62 ± 0.03	6.13	1.422 ± 0.002	0.247 ± 0.003
$K_0^{\star +}(1430)$	−0.03 ± 0.02	0.14 ± 0.01	0.02		
$K^{\star -}(892)$	−1.193 ± 0.008	1.255 ± 0.007	56.98	0.89370 ± 0.00007	0.0467 ± 0.0001
$K^{\star +}(892)$	0.123 ± 0.003	−0.117 ± 0.003	0.55		
$\rho^0(770)$	1 ± 0	0 ± 0	21.07		
$\omega(782)$	−0.0192 ± 0.0007	0.0375 ± 0.0005	0.61		
$K^{\star -}(1680)$	−0.87 ± 0.05	−0.15 ± 0.05	0.28		
$K_2^{\star -}(1430)$	−1.04 ± 0.01	0.78 ± 0.02	1.94		
$K_2^{\star +}(1430)$	−0.10 ± 0.01	0.04 ± 0.01	0.01		
$f_2^0(1270)$	−0.40 ± 0.01	0.10 ± 0.01	0.26		

Table 6.22: Results of the isobar component parameters from the step 2b fit to all $K_s\pi^+\pi^-$ data events.

Parameter	Re	Im
β_1	5.52 ± 0.05	-0.23 ± 0.06
β_2	-15.58 ± 0.10	-0.3 ± 0.1
β_3	-40.7 ± 0.7	17.0 ± 0.9
β_4	-6.2 ± 0.3	6.9 ± 0.3
$f^{pr}_{\pi\pi,\pi\pi}$	11.4 ± 0.1	-0.1 ± 0.1
$f^{pr}_{\pi\pi,KK}$	6.6 ± 0.4	-14.0 ± 0.4
$f^{pr}_{\pi\pi,4\pi}$	3.8 ± 0.7	5.8 ± 0.8

Table 6.23: Results of the P-vector parameters from the step 2b fit to all $K_s\pi^+\pi^-$ data events. The total fit fraction of the P-vector contribution is $f_r = 15.4\,\%$.

Parameter	Value
ϕ_B	-0.100 ± 0.010
ϕ_R	-2.04 ± 0.02
$a\,(\mathrm{GeV}^{-1})$	0.224 ± 0.003
$r\,(\mathrm{GeV}^{-1})$	-15.0 ± 0.1
B	-0.62 ± 0.04

Table 6.24: Results of the $K\pi$ S-wave parameters from the step 2b fit to all $K_s\pi^+\pi^-$ data events.

The goodness of fit of the nominal model is found to be better than that of other alternative models considered as sources of decay model systematic uncertainties and described in §7.2. However, this goodness of fit is rather poor. At least three contributions can be stressed:

- The description of the data does not take into account the limited mass resolution effects. The contribution of this effect to the χ^2/ndof can be estimated from the difference of χ^2/ndof values between fits to both the reconstructed and true Dalitz variables of the same Monte Carlo events, generated and fitted with the same decay model. These fits are also used to assign a systematic uncertainty to the bias introduced by the experimental effects that are not properly accounted for in the fit procedure, and are explained in detail in §7.1.1. This difference is $\Delta\chi^2/\mathrm{ndof} = 0.0948$.
- The parameterization of the efficiency non-uniformities across the phase space shows imperfections at its boundaries, as discussed in 6.2.2.1. These effects are evident in the projections shown in figure 6.18, and also in figure 6.22. The contribution of this effect to the χ^2/ndof can be estimated from the difference of χ^2/ndof values between fits to both generated and reconstructed Dalitz variables of the same Monte Carlo events, i.e., with no reconstruction and selection the former, and passing the event reconstruction and selection the latter. This sample is not available for this analysis but, as a first approximation, an independent high statistics generated sample is used to obtain $\Delta\chi^2/\mathrm{ndof} = 0.0603$.
- The imperfections in the decay model description of the data.

The sum of the first two contributions, of experimental nature, is $\Delta\chi^2/\mathrm{ndof} = 0.1551$. If this estimate is used to correct the χ^2/ndof of the nominal model fit, $\chi^2/\mathrm{ndof} = 1.2148 - 0.1551 =$

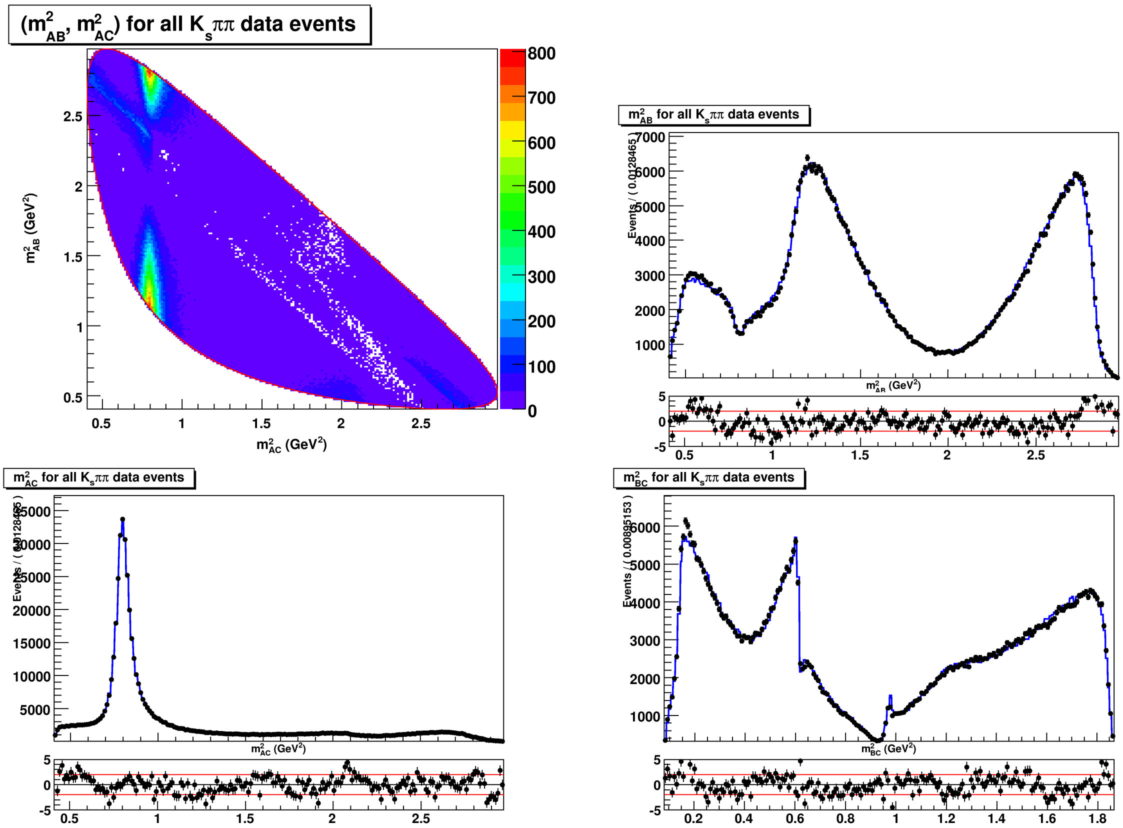

Figure 6.18: Dalitz plot projections of the step 2b fit to **data** $K_s\pi^+\pi^-$ events to the nominal model.

1.0597, this represents a significant improvement in the goodness of fit, and the remaining excess of χ^2/ndof can only be attributed to the decay model.

6.2.2.5 Results for $K_sK^+K^-$

The results of the step 2b fit on $K_sK^+K^-$ data are shown in table 6.25. The total fit fraction adds up to 163.4 %, with $\chi^2/\text{ndof} = 1511.2/(1195-17) = 1.2829$, obtained using the same adaptive binning algorithm used for $K_s\pi^+\pi^-$, with the same minimum of 30 events per bin, which results in an average of 67 events per bin.

The base residue function $g^0_{K\bar{K}}$ obtained from the fit, $g^0_{K\bar{K}} = (0.537 \pm 0.009)$ GeV, is larger than the previously measured value by the Crystal Barrel collaboration [52], but is compatible with the result from the BaBar collaboration [67].

In the subsequent fits, the coefficients for $f_0^0(1370)$, $a_0^0(1450)$ and $a_0^+(1450)$ ($a_0^-(1450)$ for $\bar{D}^0$) have been fixed to the values found in this step of the fit.

The Dalitz plot projections of the fit to $K_sK^+K^-$ data events to the nominal model are shown in figure 6.20. The normalized residuals of this fit across the Dalitz plot are shown in figure 6.21, with an adaptive and a uniform binning. The red bin in the center of the normalized residuals plot corresponds to an almost empty region, which has no sensitivity to mixing.

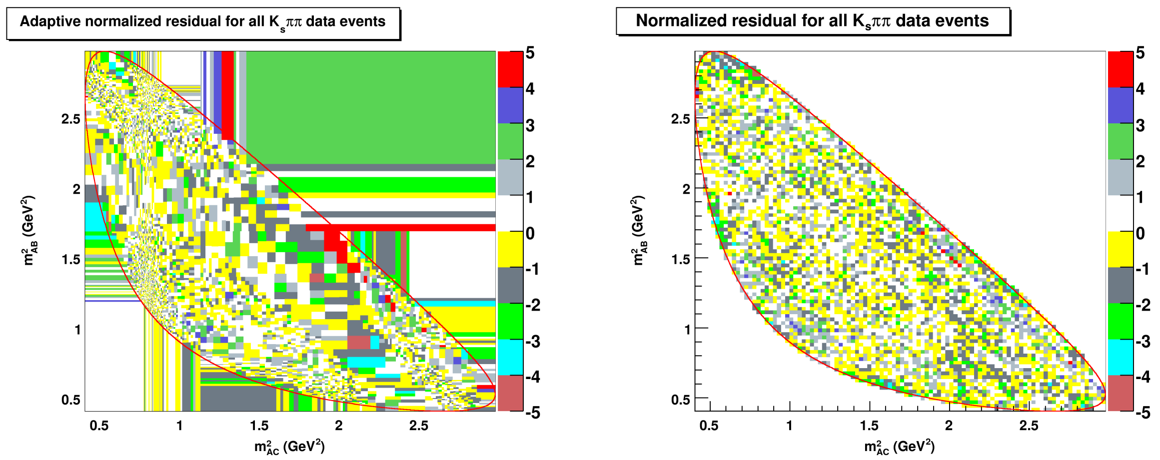

Figure 6.19: Normalized residuals of the step 2b fit to **data** $K_s\pi^+\pi^-$ events to the nominal model, computed with an adaptive (left plot) and a uniform 100×100(right plot) binning.

Component	Re $\left(a_r e^{i\phi_r}\right)$	Im $\left(a_r e^{i\phi_r}\right)$	f_r (%)	m_r (GeV)	Γ_r (GeV)
$a_0^0(980)$	1 ± 0	0 ± 0	51.81		
$a_0^+(980)$	-0.62 ± 0.02	-0.14 ± 0.02	19.45		
$a_0^-(980)$	-0.10 ± 0.01	0.08 ± 0.01	0.74		
$f_0^0(1370)$	0.16 ± 0.05	0.02 ± 0.03	1.74		
$a_0^0(1450)$	-0.3 ± 0.1	-0.77 ± 0.08	19.28		
$a_0^+(1450)$	-0.09 ± 0.06	0.93 ± 0.03	25.57		
$\phi(1020)$	0.131 ± 0.003	-0.193 ± 0.005	44.10	1.01955 ± 0.00002	0.00460 ± 0.00004
$f_2^0(1270)$	0.38 ± 0.02	0.02 ± 0.02	0.72		

Table 6.25: Results of the parameters from the step 2b fit to all $K_sK^+K^-$ data events. The result for the $K\bar{K}$ base residue function used in the coupled channel formalism for $a_0(980)$ is $g^0_{K\bar{K}} = (0.537 \pm 0.009)$ GeV.

6.2.2.6 Direct CP violation test

This step allows for a test of direct CP violation (see §1.3). This is accomplished by comparing the amplitudes and phases extracted from a time integrated decay model fit on data to the separate D^0 and $\bar{D}^0$ samples. Since sensitivity to mixing comes from the time-dependent analysis, in this time-integrated fit, no mixing or CP violation in the mixing are allowed, i.e., it has been imposed that $q/p = 1$ and $x = y = 0$. The standard model predicts very small CP violation effects in $K_s\pi^+\pi^-$ and $K_sK^+K^-$ decays, and these are mainly due to $K^0\bar{K}^0$ mixing [68]. A measurement from the CLEO collaboration [69] shows no evidence of direct CP violation in $K_s\pi^+\pi^-$ decays.

It is important to remark that the fit performed in this step is not intended to be a measurement of CP violation in $\tilde{D}^0$ mesons, but a verification of the no direct CP violation hypothesis that is assumed in the nominal mixing fit. The results of the fit are shown in tables 6.26 and 6.27 for $K_s\pi^+\pi^-$, and in table 6.28 for $K_sK^+K^-$, where the quoted values are the differences between

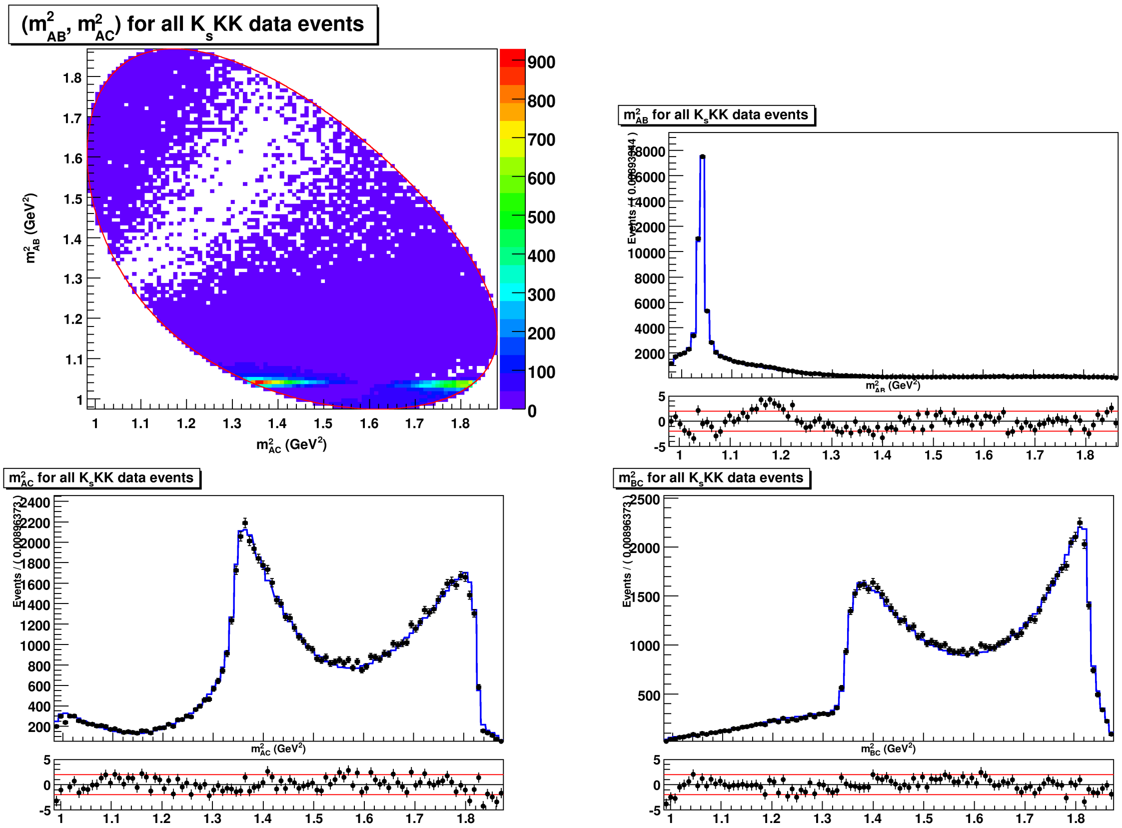

Figure 6.20: Dalitz plot projections of the step 2b fit to **data** $K_sK^+K^-$ events to the nominal model.

the D^0 and $\bar{D}^0$ results, and the errors are statistical only. No evidence of direct CP violation in $K_s\pi^+\pi^-$ and $K_sK^+K^-$ events is found in this test.

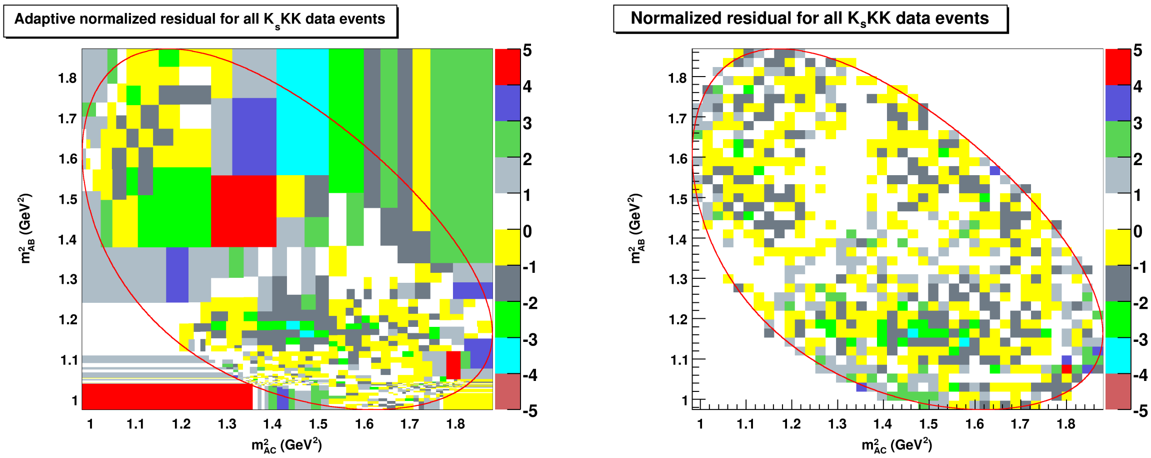

Figure 6.21: Normalized residuals of the step 2b fit to **data** $K_sK^+K^-$ events to the nominal model, computed with an adaptive (left plot) and a uniform 40×40 (right plot) binning.

Component	Re $\left(a_r e^{i\phi_r}\right)$	Im $\left(a_r e^{i\phi_r}\right)$
$K_0^{\star -}(1430)$	-0.039 ± 0.036	-0.004 ± 0.031
$K_0^{\star +}(1430)$	-0.002 ± 0.029	-0.039 ± 0.028
$K^{\star -}(892)$	-0.010 ± 0.011	0.0036 ± 0.0125
$K^{\star +}(892)$	-0.0108 ± 0.0056	-0.0035 ± 0.0049
ω	0.0011 ± 0.0013	$-1.2 \cdot 10^{-5} \pm 0.0011$
$K^{\star -}(1680)$	0.050 ± 0.064	0.050 ± 0.078
$K_2^{\star -}(1430)$	-0.039 ± 0.025	0.0664 ± 0.0325
$K_2^{\star +}(1430)$	0.029 ± 0.026	-0.004 ± 0.026
$f_2^0(1270)$	-0.009 ± 0.024	-0.029 ± 0.026

Table 6.26: Differences between the D^0 and $\bar{D}^0$ results of the isobar component parameters from the step 2b fit to all $K_s\pi^+\pi^-$ data events.

Parameter	Re	Im
β_1	0.11 ± 0.11	-0.07 ± 0.08
β_2	-0.12 ± 0.11	0.25 ± 0.14
β_3	-1.345 ± 1.97	1.03 ± 1.48
β_4	0.375 ± 0.46	-0.53 ± 0.35

Table 6.27: Differences between the D^0 and $\bar{D}^0$ results of the P-vector parameters from the step 2b fit to all $K_s\pi^+\pi^-$ data events.

Component	$\mathrm{Re}\left(a_r e^{i\phi_r}\right)$	$\mathrm{Im}\left(a_r e^{i\phi_r}\right)$
$a_0^+(980)$	-0.0019 ± 0.0098	0.028 ± 0.018
$a_0^-(980)$	0.002 ± 0.013	-0.0025 ± 0.011
ϕ	-0.0062 ± 0.0033	-0.0019 ± 0.0026
$f_2^0(1270)$	-0.036 ± 0.030	0.019 ± 0.0275

Table 6.28: Differences between the D^0 and $\bar{D}^0$ results of the parameters from the step 2b fit to all $K_sK^+K^-$ data events.

6.3 Step 3

The fit described in this section is the fit to the mixing parameters, and depends on t, σ_t and the Dalitz variables m^2_{ab} and m^2_{ac}.

The complete PDF for the decay model has been described in expression (5.30) of §5.2.3. Since the $\tilde{D}^0$ lifetime-dependence of the amplitude is not integrated out in this step of the fit, time resolution effects are taken into account. The $\tilde{D}^0$ lifetime resolution function and the characterization of σ_t are explained in detail in §5.2.2. Resolution effects in the Dalitz variables have not been implemented in the characterization and are accounted for as a source of systematic uncertainty and detailed in §7.1.9.

The core bias parameters (for $K_s\pi^+\pi^-$ and $K_sK^+K^-$) of the $\tilde{D}^0$ lifetime resolution function are allowed to float in this step. The tail bias parameters for $K_s\pi^+\pi^-$ and $K_sK^+K^-$ have been fixed to the values obtained in the fit to signal Monte Carlo, as explained in §6.2.1.4 and summarized in tables 6.12 and 6.13. The outliers bias parameters have been fixed to zero, as explained in §6.2.1.2.

The scale factor parameters of the core and tail components of the resolution function have been left to float. The global width that describes the outliers component has been fixed to the value found in fits to signal Monte Carlo events.

6.4 Mixing fit results

The main purpose of the fit to data is to extract the mixing parameters x and y while imposing no, CP violation, and is reported in §6.4.1. However, a test is performed for possible effects of CP violation on the measurement of the mixing parameters, which is reported in §6.4.2.

To avoid experimenter's bias, the result of the fit has been hidden from the analysts. This process is usually called **blinding** and, to accomplish it, unknown values δ_x and δ_y have been added to the results of x and y, respectively. The output of the fitter, therefore, has been $x_b = x + \delta_x$ and $y_b = y + \delta_y$, instead of x and y. The values δ_x and δ_y are calculated with an algorithm that transforms known strings of characters into real numbers. These numbers can be easily calculated from the provided strings with the help of a small program that operates on them at byte level, but are hard to calculate without a computer.

The parameters of the fit have been set as follows:

- The yields of all the categories have been fixed to the values found in step 1b.
- The parameters of the $\tilde{D}^0$ lifetime PDF for categories 3 and 4, $p^t_{3,4}$, have been fixed to the results of a fit to *flat* Monte Carlo background events in these categories, as explained in §5.3.2 and shown in figure 6.6.
- The core fraction, bias and scale factor parameters are left to float, as well as the scale factor of the tail component. The rest of the parameters have been fixed to the values found in step 2a and summarized in tables 6.12 and 6.13. The outliers bias parameters for both $K_s\pi^+\pi^-$ and $K_sK^+K^-$ have been fixed to zero, as explained in §6.2.1.2.

- The parameterization of the decay model is described in §2.4.8. The parameters $f^{pr}_{\pi\pi,j}$ of the production vector, all the parameters of the generalized LASS function, described in 2.4.6, and the mass and width of the $K^{\star\pm}(892)$ are fixed to the results found in step 2b, described in §6.2.2. The mass and width of the $\phi(1020)$ and the base residue function $g^0_{K\bar{K}}$ have also been fixed to the values obtained in step 2b.

- The decay model PDF for events in categories 3 and 4 is non-parametric and has been determined from the data in the m_D sidebands, as explained in §6.2.2.2.

- The right tag fractions are fixed to 1 in category 1 and to 0.5 in category 2.

The fits are performed for $K_s\pi^+\pi^-$ and $K_sK^+K^-$, both together and separately. The values of δ_x and δ_y are based on the same string in these three fits, so their results can be compared without need to unblind.

6.4.1 No CP violation allowed

The fit results for the $\tilde{D}^0$ average lifetime and the blind mixing parameters are shown in table 6.29. The results for the three fits are consistent. The statistical resolution on the mixing parameters is about $0.23 \cdot 10^{-2}$ for x and $0.20 \cdot 10^{-2}$ for y, which represents an improvement with respect to the result from the Belle collaboration [70], performed on 540 fb^{-1} with $K_s\pi^+\pi^-$ events only.

The complete list of fit results to the combined $K_s\pi^+\pi^-$ and $K_sK^+K^-$ sample is shown in tables 6.30, 6.31, 6.32 and 6.33. A toy Monte Carlo study, reported in §6.5.3, has been done to check if the errors reported by the fit are a good estimate of the resolution of the mixing parameters.

Magnitude	$K_s\pi^+\pi^-$ only	$K_sK^+K^-$ only	Combined
τ (ps)	0.4086 ± 0.0009	0.4058 ± 0.0033	0.4084 ± 0.0009
x_b	-0.0089 ± 0.0024	-0.0250 ± 0.0093	-0.0098 ± 0.0023
y_b	-0.0050 ± 0.0021	-0.0065 ± 0.0057	-0.0052 ± 0.0020

Table 6.29: Results of the $\tilde{D}^0$ average lifetime and blind mixing parameters from the step 3 fit to all combined $K_s\pi^+\pi^-$ and $K_sK^+K^-$ data events.

The correlation matrices of the parameters of the $\tilde{D}^0$ lifetime resolution function, $\tilde{D}^0$ lifetime

Parameter	Re $\left(a_r e^{i\phi_r}\right)$	Im $\left(a_r e^{i\phi_r}\right)$	Limits
$K_0^{\star-}(1430)$	$0.196 \pm 1.8 \cdot 10^{-2}$	$2.643 \pm 1.5 \cdot 10^{-2}$	$(-10, 10)$
$K_0^{\star+}(1430)$	$-0.030 \pm 1.5 \cdot 10^{-2}$	$0.142 \pm 1.4 \cdot 10^{-2}$	$(-10, 10)$
$K^{\star-}(892)$	$-1.1961 \pm 5.8 \cdot 10^{-3}$	$1.2569 \pm 6.3 \cdot 10^{-3}$	$(-5, 5)$
$K^{\star+}(892)$	$0.1181 \pm 3.3 \cdot 10^{-3}$	$-0.1141 \pm 3.0 \cdot 10^{-3}$	$(-5, 5)$
ω	$-0.01924 \pm 6.7 \cdot 10^{-4}$	$0.03738 \pm 5.3 \cdot 10^{-4}$	$(-5, 5)$
$K^{\star-}(1680)$	$-0.889 \pm 3.3 \cdot 10^{-2}$	$-0.151 \pm 3.8 \cdot 10^{-2}$	$(-5, 5)$
$K_2^{\star-}(1430)$	$-1.042 \pm 1.3 \cdot 10^{-2}$	$0.782 \pm 1.6 \cdot 10^{-2}$	$(-5, 5)$
$K_2^{\star+}(1430)$	$-0.103 \pm 1.3 \cdot 10^{-2}$	$0.051 \pm 1.3 \cdot 10^{-2}$	$(-5, 5)$
$f_2(1270)$	$-0.396 \pm 1.2 \cdot 10^{-2}$	$0.106 \pm 1.3 \cdot 10^{-2}$	$(-5, 5)$

Table 6.30: Results of the isobar component parameters from the step 3 fit to all combined $K_s\pi^+\pi^-$ and $K_sK^+K^-$ data events.

Parameter	Re	Im	Limits
β_1	5.533 ± 0.047	-0.298 ± 0.043	$(-50, 50)$
β_2	-15.634 ± 0.057	-0.264 ± 0.068	$(-50, 50)$
β_3	-40.87 ± 0.86	17.78 ± 0.78	$(-50, 50)$
β_4	-6.14 ± 0.21	6.93 ± 0.18	$(-50, 50)$

Table 6.31: Results of the P-vector parameters from the step 3 fit to all combined $K_s\pi^+\pi^-$ and $K_sK^+K^-$ data events.

and mixing parameters for the combined $K_s\pi^+\pi^-$ and $K_sK^+K^-$ fit are

$$\rho_{K_s\pi^+\pi^-} = \begin{array}{c} \begin{array}{cccccc} \tau & b_c & k_c & k_t & x & y \end{array} \\ \begin{pmatrix} 1 & -0.636 & -0.291 & -0.125 & 0.0006 & 0.054 \\ -0.636 & 1 & 0.054 & -0.183 & 0.0013 & 0.005 \\ -0.291 & 0.054 & 1 & 0.771 & 0.0006 & 0.0004 \\ -0.125 & -0.183 & 0.771 & 1 & 0.0003 & 0.0015 \\ 0.0006 & 0.0013 & 0.0006 & 0.0003 & 1 & 0.0353 \\ 0.054 & 0.005 & 0.0004 & 0.0015 & 0.0353 & 1 \end{pmatrix} \end{array}, \tag{6.6}$$

$$\rho_{K_sK^+K^-} = \begin{array}{c} \begin{array}{cccccc} \tau & b_c & k_c & k_t & x & y \end{array} \\ \begin{pmatrix} 1 & -0.302 & -0.054 & 0.006 & 0.0006 & 0.054 \\ -0.302 & 1 & 0.177 & 0.073 & 0.0011 & -0.0053 \\ -0.054 & 0.177 & 1 & 0.794 & 0.0026 & -0.0009 \\ 0.006 & 0.073 & 0.794 & 1 & 0.0030 & 0.0009 \\ 0.0006 & 0.0011 & 0.0026 & 0.0030 & 1 & 0.0353 \\ 0.054 & -0.0053 & -0.0009 & 0.0009 & 0.0353 & 1 \end{pmatrix} \end{array}. \tag{6.7}$$

Parameter	$\mathrm{Re}\left(a_r e^{i\phi_r}\right)$	$\mathrm{Im}\left(a_r e^{i\phi_r}\right)$	Limits
$a_0^+(980)$	-0.6184 ± 0.0048	-0.1419 ± 0.0079	$(-5, 5)$
$a_0^-(980)$	-0.0975 ± 0.0063	0.0775 ± 0.0052	$(-5, 5)$
ϕ	0.1295 ± 0.0017	-0.1916 ± 0.0014	$(-5, 5)$
$f_2(1270)$	0.384 ± 0.015	0.024 ± 0.013	$(-1, 1)$

Table 6.32: Results of the $K_sK^+K^-$ decay model parameters from the step 3 fit to all combined $K_s\pi^+\pi^-$ and $K_sK^+K^-$ data events.

$\tilde{D}^0$ decay mode	Parameter	Value	Limits	Units
$K_s\pi^+\pi^-$	b_c	$5.11 \cdot 10^{-3} \pm 8.4 \cdot 10^{-4}$	$(-1, 1)$	ps
	f_c	$0.9309 \pm 8.8 \cdot 10^{-3}$	$(0, 1)$	
	k_c	$1.00315 \pm 5.2 \cdot 10^{-3}$	$(10^{-3}, 2)$	
	k_t	$1.753 \pm 4.9 \cdot 10^{-2}$	$(10^{-3}, 5)$	
$K_sK^+K^-$	b_c	$5.1 \cdot 10^{-3} \pm 2.2 \cdot 10^{-3}$	$(-1, 1)$	ps
	f_c	$0.919 \pm 1.5 \cdot 10^{-2}$	$(0, 1)$	
	k_c	$1.032 \pm 1.0 \cdot 10^{-2}$	$(10^{-3}, 2)$	
	k_t	$1.964 \pm 8.9 \cdot 10^{-2}$	$(10^{-3}, 5)$	
	τ	$0.40837 \pm 9.1 \cdot 10^{-4}$	$(0.1, 1)$	ps
	x_b	$-9.8 \cdot 10^{-3} \pm 2.3 \cdot 10^{-3}$	$(-0.2, 0.2)$	
	y_b	$-5.2 \cdot 10^{-3} \pm 2.0 \cdot 10^{-3}$	$(-0.2, 0.2)$	

Table 6.33: Results of the resolution function, $\tilde{D}^0$ average lifetime and mixing parameters from the step 3 fit to all combined $K_s\pi^+\pi^-$ and $K_sK^+K^-$ data events.

The statistical covariance matrix is found to be

$$V_{\mathrm{stat}} = \begin{array}{c} \begin{array}{cc} \quad x \quad\quad\quad & \quad\quad y \end{array} \\ \begin{pmatrix} 5.43 \cdot 10^{-6} & 1.64 \cdot 10^{-7} \\ 1.64 \cdot 10^{-7} & 4.00 \cdot 10^{-6} \end{pmatrix} \end{array}. \tag{6.8}$$

As discussed in §6.2.1.2, there is a large correlation between the $\tilde{D}^0$ average lifetime and the bias parameter of the core component of the resolution function. The correlation between the parameters of the resolution function and the mixing parameters is negligible, so there is a very small sensitivity of x and y to the details of the resolution function.

The $\tilde{D}^0$ lifetime and Dalitz plot projections of the fit to combined $K_s\pi^+\pi^-$ and $K_sK^+K^-$ data events are shown in figure 6.22 for $K_s\pi^+\pi^-$ and in figure 6.23 for $K_sK^+K^-$.

6.4.2 CP violation allowed

With the data available for this analysis, it is possible to test for the three kinds of CP violation presented in §1.3. However, this analysis is not intended to measure CP violation, but to test for

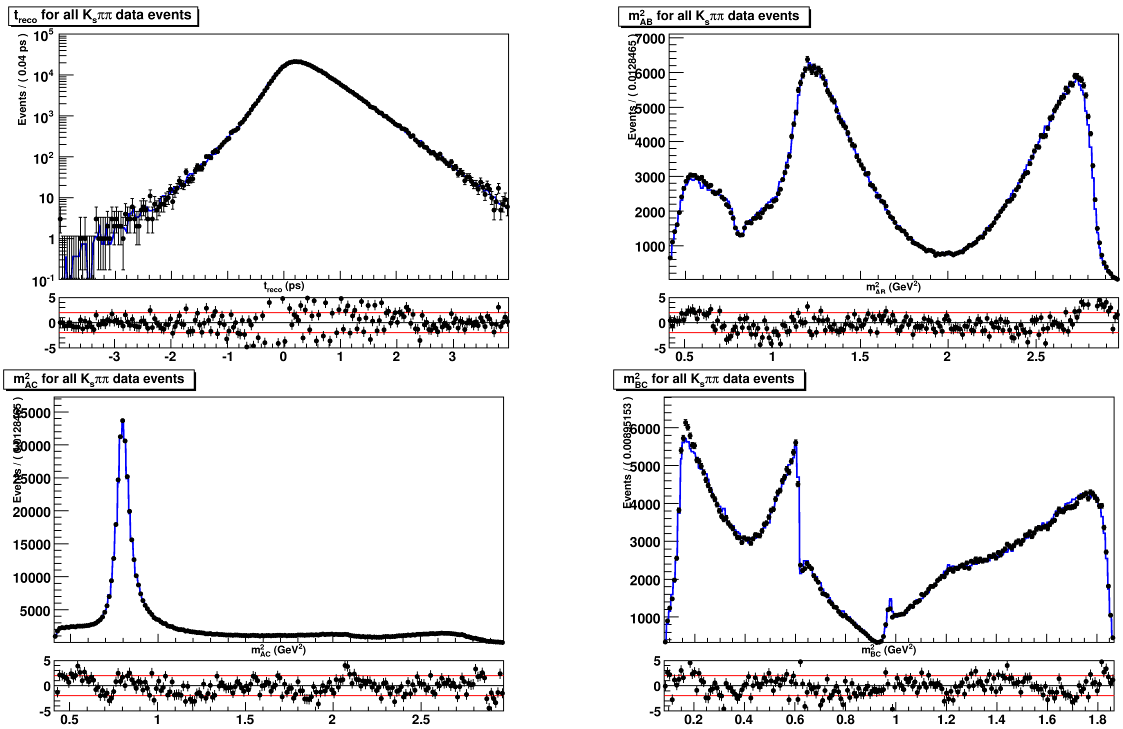

Figure 6.22: Reconstructed $K_s\pi^+\pi^-$ $\tilde{D}^0$ lifetime and Dalitz plot projections of the step 3 fit to all combined **data** events.

possible CP violation effects on the measurement of the mixing parameters.

Two tests of CP violation are performed: on one hand, a test for CP violation in the mixing, on the other hand, a test for CP violation in the decay. Both tests consist of a measurement of x and y separately on D^0 and $\bar{D}^0$ events, namely (x_D, y_D) and $(x_{\bar{D}}, y_{\bar{D}})$. The two tests are performed on the combined $K_s\pi^+\pi^-$ and $K_sK^+K^-$ data sample.

In the test for CP violation in the mixing, q/p has been fixed in the fit to $q/p = 1$, so any effects of this kind of CP violation are absorbed in the decay rate and the mixing parameters measured separately, Γx_D, $\Gamma x_{\bar{D}}$, Γy_D, $\Gamma y_{\bar{D}}$. To enforce no CP violation in the decay, the fit has been done on the combined D^0 and $\bar{D}^0$ samples, with the additional condition that $A_f = \bar{A}_{\bar{f}}$. It is important to notice that, since both the decay rate and the mixing parameters are real, they cannot absorb an eventual phase of q/p, so any effects from CP violation in the interference between decays with and without mixing are limited to CP violation effects in the mixing. The covariance and correlation

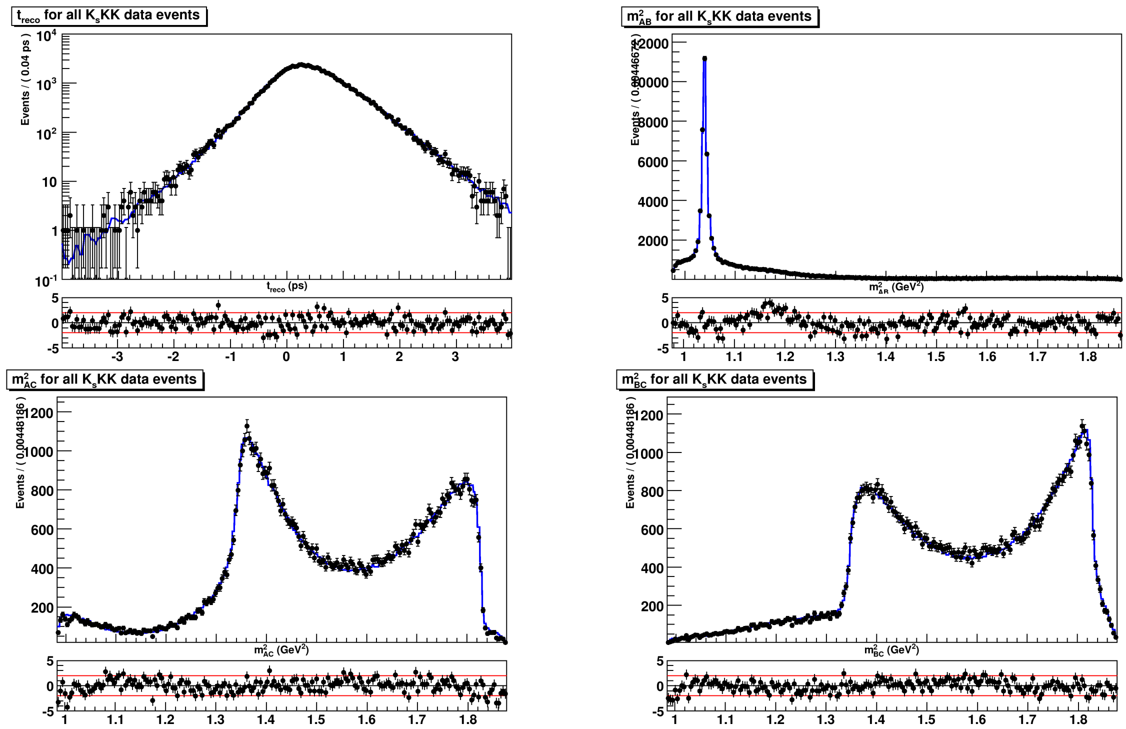

Figure 6.23: Reconstructed $K_s\pi^+\pi^-$ $\tilde{D}^0$ lifetime and Dalitz plot projections of the step 3 fit to all combined $K_sK^+K^-$ **data** events.

matrices obtained from this fit are, respectively,

$$
V_{\text{mix}}^{\text{CPV}} = \begin{array}{c} \begin{array}{cccc} x_D & y_D & x_{\bar{D}} & y_{\bar{D}} \end{array} \\ \begin{pmatrix} 7.62 \cdot 10^{-6} & 2.69 \cdot 10^{-7} & 2.94 \cdot 10^{-6} & 4.84 \cdot 10^{-8} \\ 2.69 \cdot 10^{-7} & 5.69 \cdot 10^{-6} & 3.8 \cdot 10^{-8} & 2.31 \cdot 10^{-6} \\ 2.94 \cdot 10^{-6} & 3.8 \cdot 10^{-8} & 7.79 \cdot 10^{-6} & 8.69 \cdot 10^{-8} \\ 4.84 \cdot 10^{-8} & 2.31 \cdot 10^{-6} & 8.69 \cdot 10^{-8} & 5.57 \cdot 10^{-6} \end{pmatrix} \end{array}, \tag{6.9}
$$

$$
\rho_{\text{mix}}^{\text{CPV}} = \begin{array}{c} \begin{array}{cccc} x_D & y_D & x_{\bar{D}} & y_{\bar{D}} \end{array} \\ \begin{pmatrix} 1 & 0.0408 & 0.382 & 0.00743 \\ 0.0408 & 1 & 0.00571 & 0.411 \\ 0.382 & 0.00571 & 1 & 0.0132 \\ 0.00743 & 0.411 & 0.0132 & 1 \end{pmatrix} \end{array}, \tag{6.10}
$$

$$
\tag{6.11}
$$

In the test for CP violation in the decay, the complex coefficients of the linear combination of resonances of the decay model are allowed to take different values for the D^0 and $\bar{D}^0$ samples. The effects of CP violation in the mixing are also absorbed in the separate mixing parameters for the D^0 and $\bar{D}^0$ samples, which are fit separately in this test. It is important to remark, however, that for the magnitude χ, defined in equation (1.21), it has been assumed that $A_f = \bar{A}_{\bar{f}}$. This is the most important reason why this test must be considered just a consistency check for mixing against possible CP violation effects, and not a measurement of CP violation. The covariance and correlation matrices obtained from these two fits are, respectively,

$$V_D^{\text{CPV}} = \begin{array}{cc} x_D & y_D \\ \end{array} \begin{pmatrix} 1.05 \cdot 10^{-5} & 3.62 \cdot 10^{-7} \\ 3.62 \cdot 10^{-7} & 8.01 \cdot 10^{-6} \end{pmatrix}, \quad \rho_D^{\text{CPV}} = \begin{array}{cc} x_D & y_D \\ \end{array} \begin{pmatrix} 1 & 0.0395 \\ 0.0395 & 1 \end{pmatrix}, \tag{6.12}$$

$$V_{\bar{D}}^{\text{CPV}} = \begin{array}{cc} x_{\bar{D}} & y_{\bar{D}} \\ \end{array} \begin{pmatrix} 1.08 \cdot 10^{-5} & 1.14 \cdot 10^{-7} \\ 1.14 \cdot 10^{-7} & 7.89 \cdot 10^{-6} \end{pmatrix}, \quad \rho_{\bar{D}}^{\text{CPV}} = \begin{array}{cc} x_{\bar{D}} & y_{\bar{D}} \\ \end{array} \begin{pmatrix} 1 & 0.0123 \\ 0.0123 & 1 \end{pmatrix}. \tag{6.13}$$

The blind results of the mixing parameters obtained from the nominal fit and from the two tests for CP violation are shown in table 6.34.

Magnitude	Sample	No CP violation	CPV test in mixing	CPV test in decay
x_b	D^0	-0.0098 ± 0.0023	-0.0138 ± 0.0028	-0.0115 ± 0.0033
	$\bar{D}^0$		-0.0056 ± 0.0028	-0.0081 ± 0.0033
y_b	D^0	-0.0052 ± 0.0020	-0.0051 ± 0.0024	-0.0055 ± 0.0029
	$\bar{D}^0$		-0.0054 ± 0.0024	-0.0051 ± 0.0028

Table 6.34: Blind results of the mixing parameters obtained from the nominal fit and from the two tests for CP violation.

The complete list of differences between the fit results to the D^0 and $\bar{D}^0$ events separately is shown in tables 6.35, 6.36, 6.37 and 6.38.

Parameter	Re $\left(a_r e^{i\phi_r}\right)$	Im $\left(a_r e^{i\phi_r}\right)$
$K_0^{\star -}(1430)$	-0.035 ± 0.036	-0.002 ± 0.031
$K_0^{\star +}(1430)$	0.004 ± 0.030	-0.038 ± 0.028
$K^{\star -}(892)$	-0.009 ± 0.012	0.005 ± 0.013
$K^{\star +}(892)$	-0.0078 ± 0.0065	-0.0021 ± 0.0060
ω	0.0011 ± 0.0013	0.0001 ± 0.0011
$K^{\star -}(1680)$	0.048 ± 0.066	0.062 ± 0.079
$K_2^{\star -}(1430)$	-0.037 ± 0.025	0.062 ± 0.033
$K_2^{\star +}(1430)$	0.028 ± 0.026	-0.004 ± 0.026
$f_2(1270)$	-0.0095 ± 0.024	-0.026 ± 0.026

Table 6.35: Differences between the results of the isobar component parameters from the step 3 fit to the D^0 and $\bar{D}^0$ events separately.

Parameter	Re	Im
β_1	0.09 ± 0.11	-0.078 ± 0.083
β_2	-0.13 ± 0.11	0.27 ± 0.14
β_3	-0.95 ± 2.04	1.01 ± 1.52
β_4	0.31 ± 0.47	-0.50 ± 0.35

Table 6.36: Differences between the results of the P-vector parameters from the step 3 fit to the D^0 and $\bar{D}^0$ events separately.

Parameter	Re $\left(a_r e^{i\phi_r}\right)$	Im $\left(a_r e^{i\phi_r}\right)$
$a_0^+(980)$	-0.001 ± 0.010	0.022 ± 0.022
$a_0^-(980)$	0.001 ± 0.013	-0.0002 ± 0.013
ϕ	-0.0055 ± 0.0035	-0.0017 ± 0.0028
$f_2(1270)$	-0.036 ± 0.029	0.018 ± 0.028

Table 6.37: Differences between the results of the $K_sK^+K^-$ decay model parameters from the step 3 fit to the D^0 and $\bar{D}^0$ events separately.

$\tilde{D}^0$ decay mode	Parameter	Value	Units
$K_s\pi^+\pi^-$	b_c	0.0005 ± 0.0017	ps
	f_c	-0.021 ± 0.022	
	k_c	-0.011 ± 0.012	
	k_t	-0.15 ± 0.11	
$K_sK^+K^-$	b_c	-0.0068 ± 0.0045	ps
	f_c	-0.059 ± 0.046	
	k_c	-0.025 ± 0.026	
	k_t	-0.32 ± 0.18	
	τ	0.0040 ± 0.0018	ps
	x	-0.0034 ± 0.0046	
	y	-0.0004 ± 0.0040	

Table 6.38: Differences between the results of the resolution function, $\tilde{D}^0$ average lifetime and mixing parameters from the step 3 fit to the D^0 and $\bar{D}^0$ events separately.

6.5 Mixing fit validation

6.5.1 Fits to signal truth matched Monte Carlo events

Fits to Monte Carlo truth matched events are a test to ensure that the fitter retrieves the generated values of the $\tilde{D}^0$ lifetime dependent amplitude parameters. These Monte Carlo events are fitted with the PDF described by equation (5.30), except that no $\tilde{D}^0$ lifetime resolution effects need to be taken into account. Efficiency non-uniformities across the phase space, however, have been taken into account because the true Monte Carlo events have been found by obtaining the associated true particle of candidates that have passed the reconstruction and selection criteria, described in §4. The efficiency non-uniformities across the phase space have been reevaluated with true Dalitz variables.

The fit results of the mixing parameters and $\tilde{D}^0$ average lifetime are shown in table 6.39. No significant bias in either the $\tilde{D}^0$ average lifetime or mixing parameters is observed.

The fit projections of the Dalitz plot for events in the *nomix* sample, described in §4.1, are shown in figure 6.24 for $K_s\pi^+\pi^-$ and in figure 6.25 for $K_sK^+K^-$. The residuals in these figures show that the largest deviations of the model from the sample arise in some edges of the Dalitz kinematically allowed region. These effects are caused by the imperfections in the parameterization of the efficiency non-uniformities across the phase space with a two-variable polynomial, and has also been observed in §5.2.3, where fits to *flat* Monte Carlo events are performed. An additional crosscheck to confirm that these effects are really due to the parameterization of the efficiency non-uniformities has been done by performing the same fit to generated true Monte Carlo events, without requiring any reconstruction and selection criteria. The deviations observed in truth matched Monte Carlo events disappear in generated true Monte Carlo events.

$\tilde{D}^0$ decay mode	Magnitude	*mix* sample	*nomix* sample
$K_s\pi^+\pi^-$	τ (ps)	0.41226 ± 0.00039	0.41218 ± 0.00039
	x	0.0120 ± 0.0014	0.0001 ± 0.0014
	y	0.0080 ± 0.0013	-0.0030 ± 0.0013
$K_sK^+K^-$	τ (ps)	0.41179 ± 0.00078	0.41061 ± 0.00077
	x	0.0074 ± 0.0036	-0.0004 ± 0.0036
	y	0.0093 ± 0.0022	0.0007 ± 0.0022

Table 6.39: Results of the $\tilde{D}^0$ average lifetime and mixing parameters from the step 3 fit to all true $K_s\pi^+\pi^-$ and $K_sK^+K^-$ Monte Carlo events.

6.5.2 Fits to reconstructed Monte Carlo events

Fits to reconstructed Monte Carlo events are sensitive to possible biases caused by the presence of background events and detector effects, mostly $\tilde{D}^0$ mass and lifetime resolution. Some correlations between the fit variables have not been taken into account and can also introduce biases. Reconstructed Monte Carlo events have passed the reconstruction and selection criteria, described in §4, and fitted with the PDF described by equation (5.30).

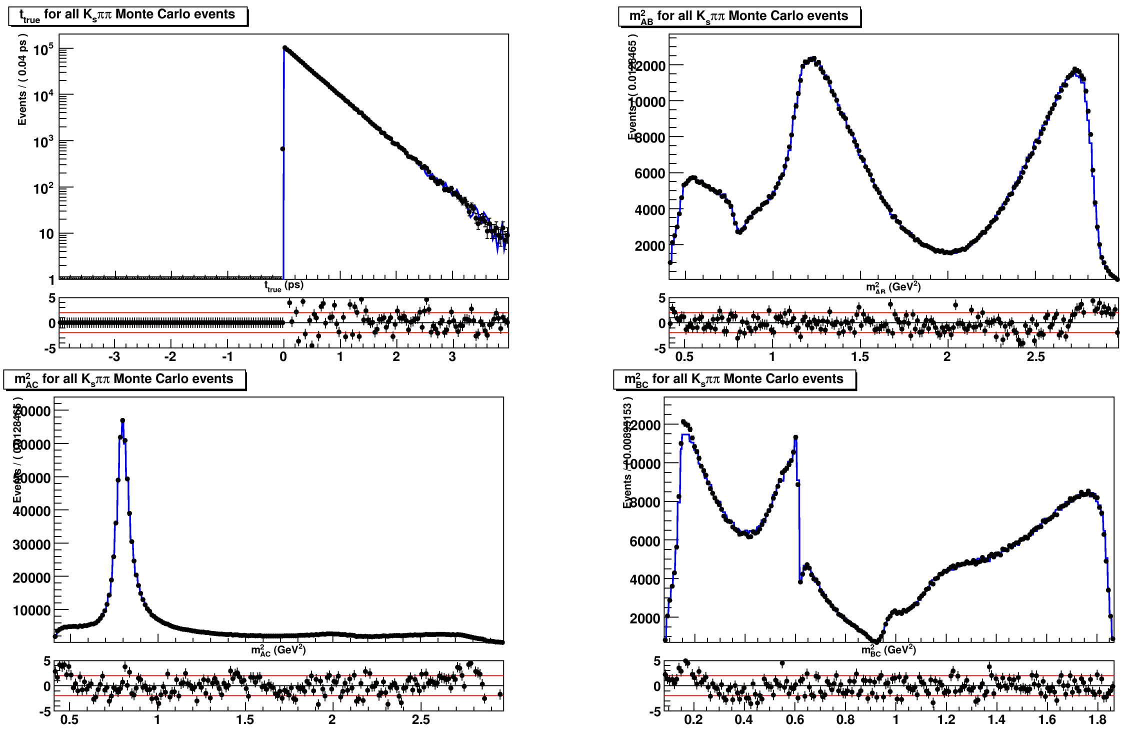

Figure 6.24: True $\tilde{D}^0$ lifetime and Dalitz plot projections of the step 3 fit to truth matched *nomix* $K_s\pi^+\pi^-$ **Monte Carlo** events.

The Monte Carlo sample considered here includes both signal and background events, with the different background channels, presented in table 4.2, appropriately weighted to reproduce the luminosity of the data. The contribution of the background channels is expected to be small, since the purity of the data sample in the signal box region exceeds 99 %.

The fit results of the mixing parameters and $\tilde{D}^0$ average lifetime are shown in table 6.40. No significant bias is observed in either the $\tilde{D}^0$ average lifetime or the mixing parameters.

The $\tilde{D}^0$ lifetime and Dalitz plot projections for events in the *nomix* sample are shown in figure 6.26 for $K_s\pi^+\pi^-$ and in figure 6.27 for $K_sK^+K^-$. The residuals in these figures show the previously observed deviations in some edges of the Dalitz kinematically allowed region, induced by the efficiency non-uniformities across the phase space. In addition to these deviations, there are also clear structures around the $K^{\star -}(892)$ mass peak for $K_s\pi^+\pi^-$ and around the $\phi(1020)$ mass peak for $K_sK^+K^-$. These deviations are associated to mass resolution effects.

Additionally, only for the $K_s\pi^+\pi^-$ $\tilde{D}^0$ decay mode, the fit has been done on reconstructed signal Monte Carlo events. This fit is not sensitive to possible biases caused by the presence of background, but isolates the detector effects, as well as possible effects due to correlations not taken into account, from the background effects. The results of this fit are shown in table 6.41.

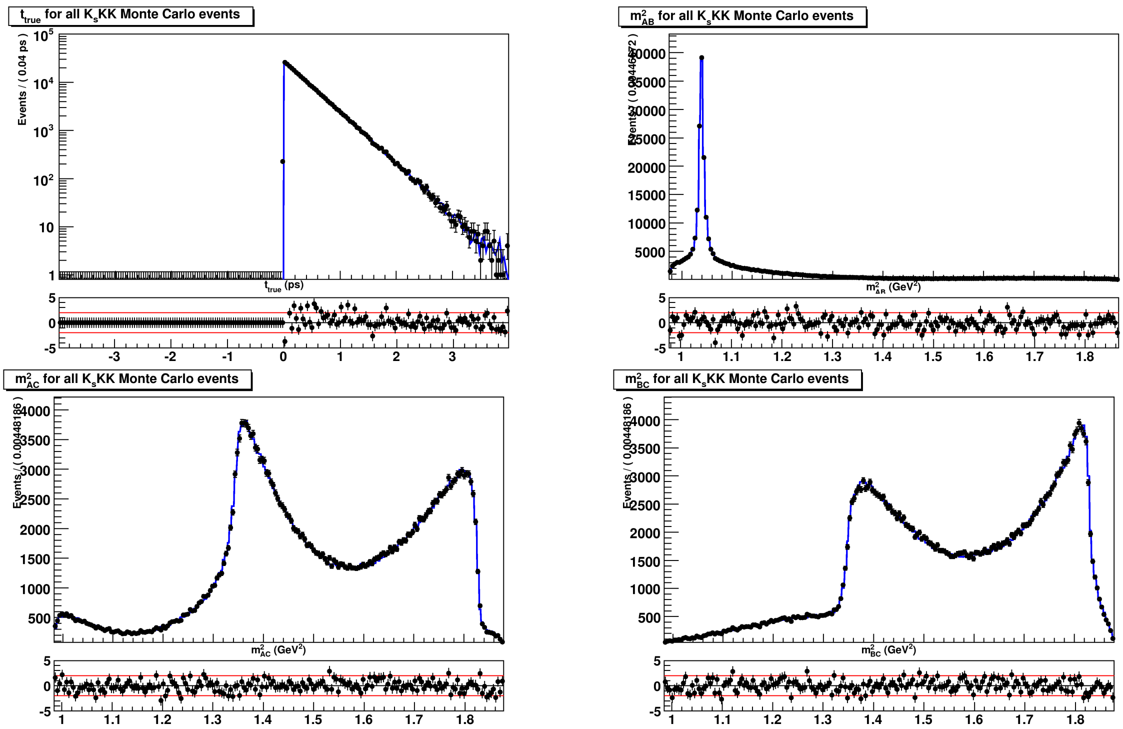

Figure 6.25: True $\tilde{D}^0$ lifetime and Dalitz plot projections of the step 3 fit to truth matched *nomix* $K_sK^+K^-$ **Monte Carlo** events.

6.5.3 Toy Monte Carlo validation

A fit to 105 toy Monte Carlo experiments, tuned to the results on data, has been performed with a double purpose: on one hand, to verify that no biases exist in the mixing parameters obtained from the nominal fit on the combined $K_s\pi^+\pi^-$ and $K_sK^+K^-$ data sample and, on the other hand, to verify that the fit error reproduces correctly the resolution of the fit parameters, specifically x and y. Since the results on the mixing parameters are blind, both x and y have been tuned to $x = y = 10^{-2}$ to generate these toy Monte Carlo experiments.

The residual[1], error and normalized[2] distributions of x, y and τ obtained from these toy Monte Carlo experiments tuned to the results of the nominal mixing fit to the combined $K_s\pi^+\pi^-$ and $K_sK^+K^-$ data sample are shown in figure 6.28. There is good agreement between the errors from the nominal fit and the errors obtained from the toy Monte Carlo experiments. The values of the parameters from a Gaussian fit to the residuals on x, y and τ, namely d_x, d_y, and d_τ, respectively, are shown in table 6.42.

With the amount of toy Monte Carlo experiments, small biases on the mixing parameters are observed. These biases are taken into account as a source of systematic uncertainty and are explained in detail in §7.1.1.

[1]The residual of a magnitude is the difference between the fitted and generated values of that magnitude. Therefore, $d_x = x_{\rm fit} - x_{\rm gen}$, and $d_y = y_{\rm fit} - y_{\rm gen}$.

[2]The normalized distribution is the distribution of the residuals divided by their errors.

$\tilde{D}^0$ decay mode	Magnitude	*mix* sample	*nomix* sample
$K_s\pi^+\pi^-$	τ (ps)	0.41212 ± 0.00067	0.41166 ± 0.00067
	x	0.0128 ± 0.0017	-0.00009 ± 0.00177
	y	0.0098 ± 0.0015	-0.0027 ± 0.0015
$K_sK^+K^-$	τ (ps)	0.41395 ± 0.00175	0.40997 ± 0.00173
	x	0.0060 ± 0.0050	-0.0007 ± 0.0050
	y	0.0106 ± 0.0031	0.0041 ± 0.0032

Table 6.40: Results of the $\tilde{D}^0$ average lifetime and mixing parameters from the step 3 fit to all reconstructed $K_s\pi^+\pi^-$ and $K_sK^+K^-$ Monte Carlo events.

$\tilde{D}^0$ decay mode	Magnitude	*mix* sample	*nomix* sample
$K_s\pi^+\pi^-$	τ (ps)	0.40909 ± 0.000945	0.41011 ± 0.00066
	x	0.0106 ± 0.0014	0.00315 ± 0.00093
	y	0.0094 ± 0.0013	0.0014 ± 0.0010

Table 6.41: Results of the $\tilde{D}^0$ average lifetime and mixing parameters from the step 3 fit to signal reconstructed $K_s\pi^+\pi^-$ Monte Carlo events.

In addition, a fit to 100 toy Monte Carlo experiments, tuned to the results of the nominal fit on the $K_sK^+K^-$ data sample only, has been performed. No bias in the mixing parameters has been found in this fit, and the resolution in the mixing parameters is found to be 0.0098 for x and 0.0060 for y, which is in agreement with the nominal fit errors on data. The residual, error and normalized distributions of x, y and τ obtained from these toy Monte Carlo experiments are shown in figure 6.29.

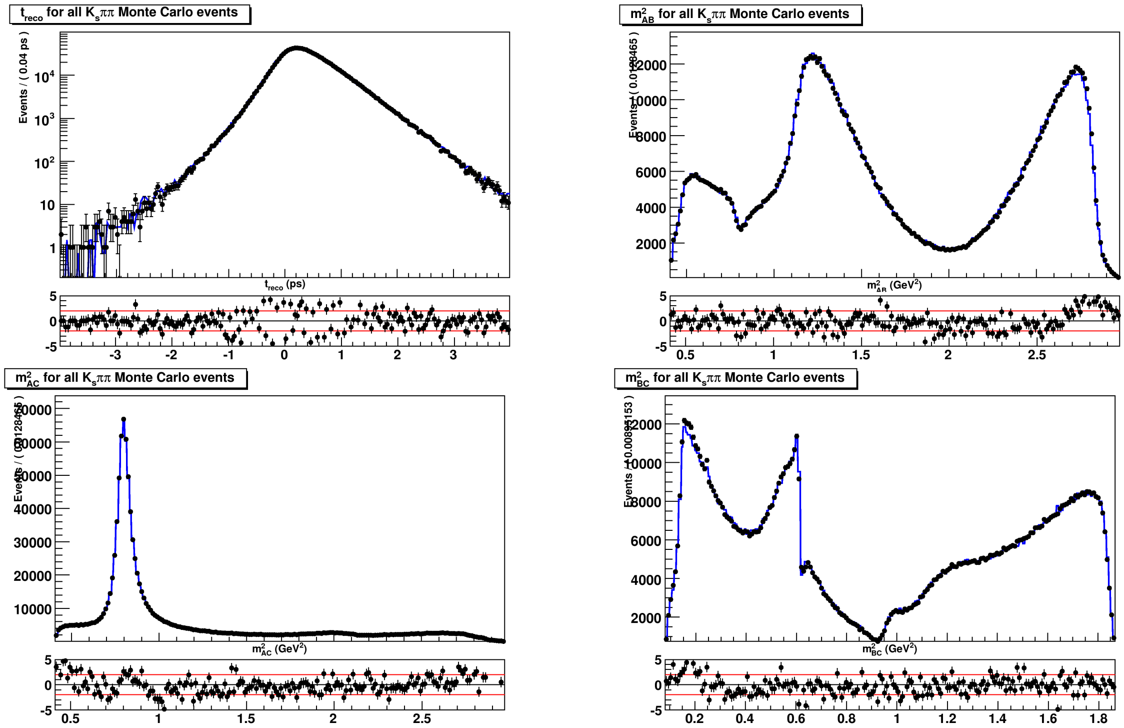

Figure 6.26: Reconstructed $\tilde{D}^0$ lifetime and Dalitz plot projections of the step 3 fit to *nomix* $K_s\pi^+\pi^-$ **Monte Carlo** events.

Magnitude	μ	σ
d_x	$5.56 \cdot 10^{-4} \pm 2.2 \cdot 10^{-4}$	$2.20 \cdot 10^{-3} \pm 1.8 \cdot 10^{-4}$
d_y	$-8.0 \cdot 10^{-4} \pm 2.1 \cdot 10^{-4}$	$2.10 \cdot 10^{-3} \pm 1.7 \cdot 10^{-4}$
d_τ (fs)	-0.574 ± 0.099	1.033 ± 0.074

Table 6.42: Mean μ and width σ from a Gaussian fit to the distribution of the residuals on x, y and τ obtained from the toy Monte Carlo experiments.

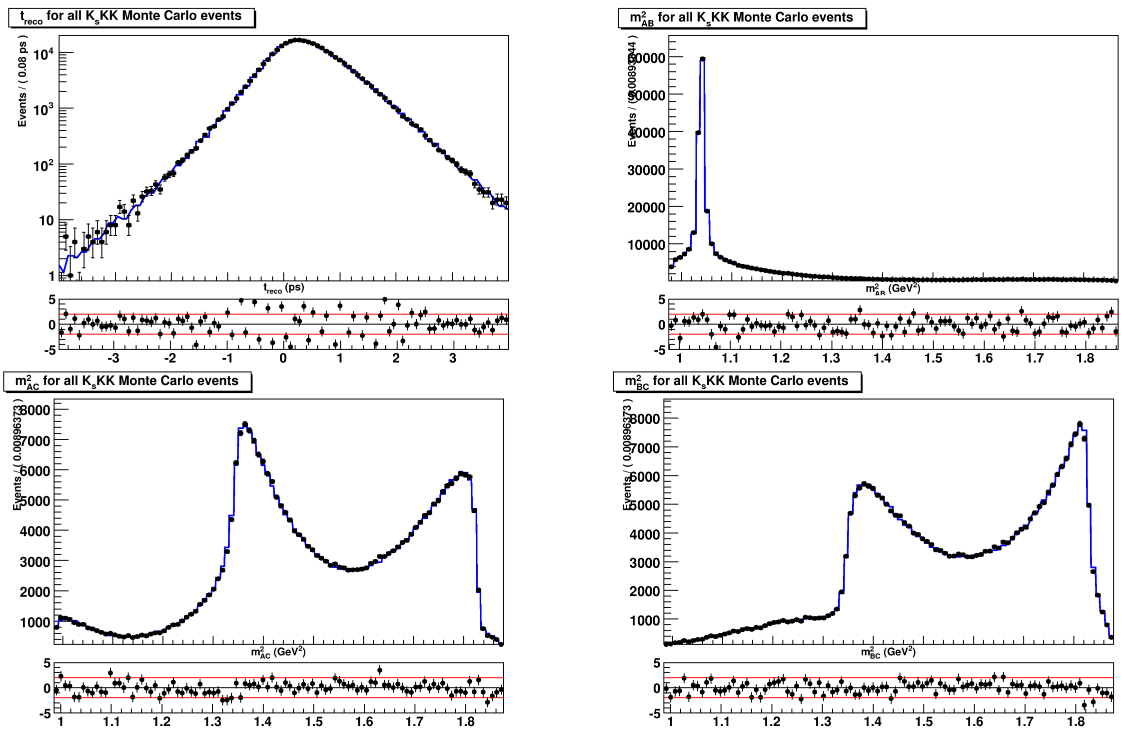

Figure 6.27: Reconstructed $\tilde{D}^0$ lifetime and Dalitz plot projections of the step 3 fit to *nomix* $K_sK^+K^-$ **Monte Carlo** events.

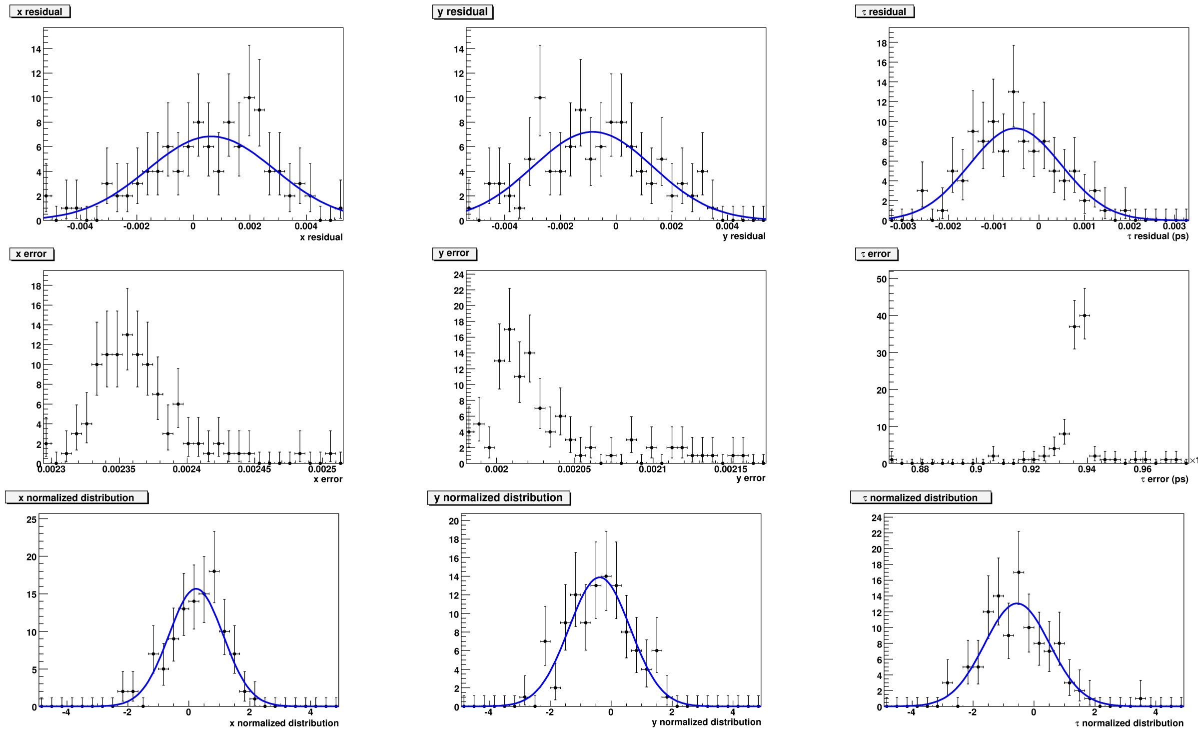

Figure 6.28: Residual (top row), error (middle row) and normalized (bottom row) distributions of x (left column), y (middle column) and τ (right column) of the fits to toy Monte Carlo events tuned to the results of the nominal mixing fit to the combined $K_s\pi^+\pi^-$ and $K_sK^+K^-$ data sample.

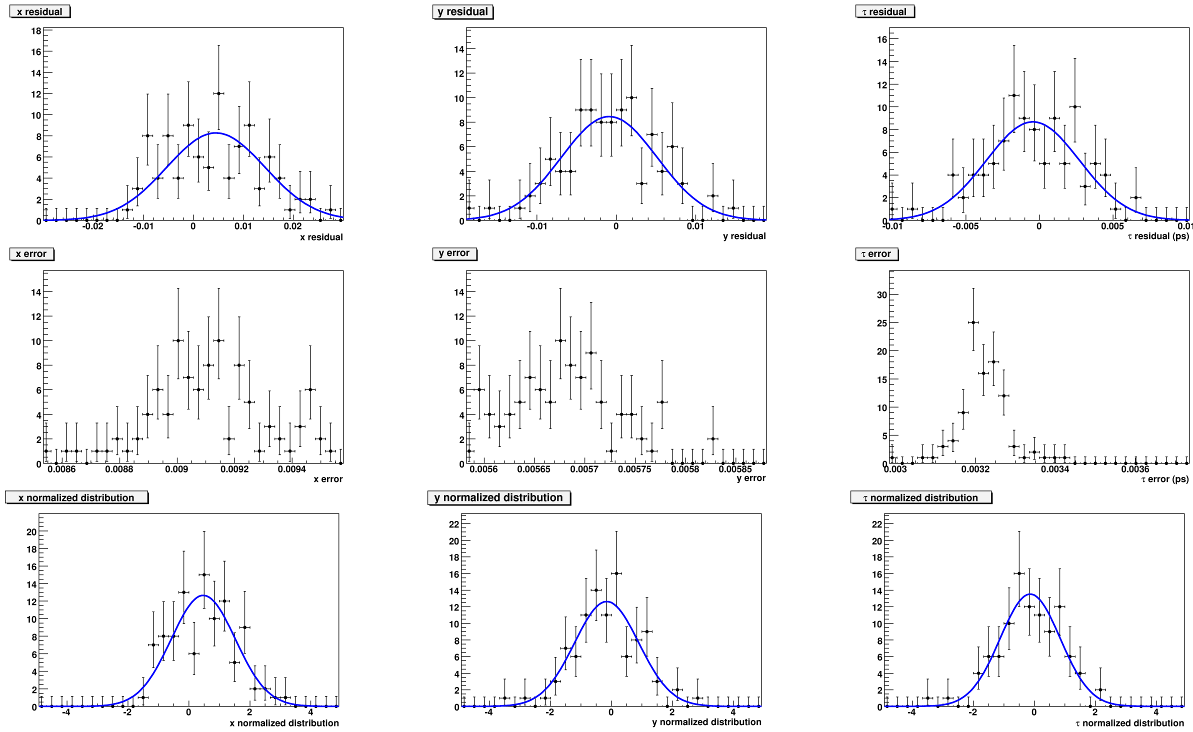

Figure 6.29: Residual (top row), error (middle row) and normalized (bottom row) distributions of x (left column), y (middle column) and τ (right column) of the fits to toy Monte Carlo events tuned to the results of the nominal mixing fit to the $K_sK^+K^-$ data sample.

6.6 Experimental crosschecks

The mixing fit has been repeated for different regions of $\tilde{D}^0$ momentum, $\tilde{D}^0$ cosine of polar angle $\cos\theta$, $\tilde{D}^0$ azimuthal angle ϕ, all of them seen from the laboratory rest frame, and run period, with the purpose to check that the mixing fit results are stable within these different regions. Since this test mainly checks for resolution function effects, the decay model has been fixed to the nominal one, and only the parameters of the resolution function, the $\tilde{D}^0$ lifetime and the mixing parameters have been floated.

Ten regions of $\tilde{D}^0$ momentum and $\tilde{D}^0$ cosine of polar angle have been chosen in such a way that the different regions contain approximately the same number of events. The ten regions of the axial angle ϕ have been chosen to cover the same arc $(2\pi/10)$. Small differences in number of events in different bins in ϕ arise because some regions of the SVT have more damaged modules than others. The blind results on x and y in each of these regions are shown in figure 6.30. No significant systematic effects are observed.

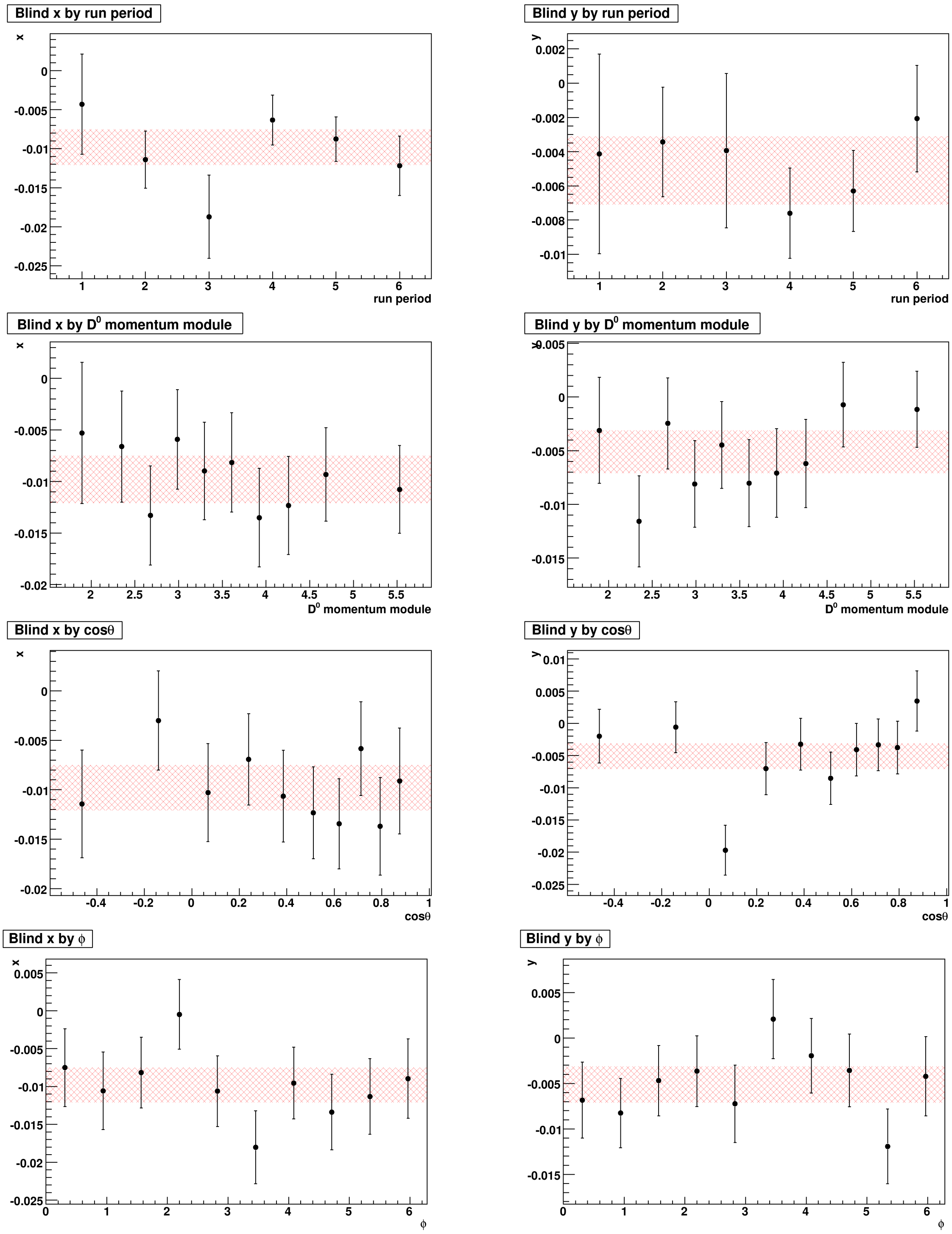

Figure 6.30: Blind results for the mixing parameters x (left column) and y (right column) for different run periods (top row), $\tilde{D}^0$ momentum magnitude (second row), cosine of $\tilde{D}^0$ polar angle $\cos\theta$ (third row) and $\tilde{D}^0$ azimuthal angle ϕ (bottom row). The red band shows the $1\,\sigma$ statistical uncertainty of the blind nominal measurement.

Chapter 7

Systematic uncertainties

The following sections describe how each contribution to the systematic uncertainty has been evaluated. Two different classes of systematic uncertainties have been distinguished: on one hand, experimental systematic uncertainties, that arise from the selection criteria or from imperfections either in the detector or in the characterization of the fit variables, are described in §7.1. On the other hand, theoretical uncertainties, related to the choice of the nominal decay model, are described in §7.2. When other selection criteria are studied, the complete chain of fit steps has to be redone, while in other cases, only step 3 needs to be repeated.

The forward-backward production asymmetry of $c\bar{c}$ events, due to γ/Z^0 interference and to high order QED diagrams, leads to different observed rates for $D^{\star +}$ and $D^{\star -}$ events and, therefore, also for D^0 and $\bar{D}^0$ events. Any tests for CP violation in the mixing or decay have not been based in the comparison of the overall number of D^0 and $\bar{D}^0$ events, but on the differences in the time dependent distributions of these events in the phase space. In addition, the $\tilde{D}^0$ decay products, $K_s\pi^+\pi^-$ or $K_sK^+K^-$, are identical for D^0 and $\bar{D}^0$ events, and equal reconstruction efficiency is assumed for both flavor states, as verified on Monte Carlo events. Reconstruction efficiency non-uniformities are accounted for as described in §5.2.3. For these reasons, the systematic uncertainties in the mixing parameters obtained from the tests allowing for CP violation, (x_D, y_D) and $(x_{\bar{D}}, y_{\bar{D}})$, are assumed to have the same systematic uncertainties as the nominal mixing parameters x and y, with CP conservation imposed.

The contribution of a source k of systematic uncertainty to x or y is named $\sigma_{x,k}$ or $\sigma_{y,k}$, respectively. In almost all cases, except otherwise specified, each contribution to the systematic uncertainties is taken as the difference between the alternative and nominal mixing fit results, and is therefore signed. In the specific cases where quadratic differences of fit errors are used, the contribution is unsigned. All the contributions from the different sources of systematic uncertainty are added in quadrature to obtain the total systematic error for each parameter.

The use of signed contributions allows for an estimation of the systematic correlation between x and y. To obtain this correlation, each signed contribution is assigned a correlation coefficient of

$+1$ if $\sigma_{x,k}$ and $\sigma_{y,k}$ have the same sign, or -1 otherwise,

$$\rho_{xy,k} = \frac{\sigma_{x,k}\sigma_{y,k}}{|\sigma_{x,k}\sigma_{y,k}|}. \tag{7.1}$$

The unsigned contributions are assigned a zero correlation coefficient.

The total systematic covariance matrix is calculated as

$$V = \sum_k \begin{array}{c} \begin{array}{cc} x & y \end{array} \\ \begin{pmatrix} \sigma_{x,k}^2 & \sigma_{x,k}\sigma_{y,k} \\ \sigma_{x,k}\sigma_{y,k} & \sigma_{y,k}^2 \end{pmatrix} \end{array}. \tag{7.2}$$

7.1 Experimental systematic uncertainties

Table 7.1 summarizes the main experimental contributions to the systematic uncertainty on the mixing parameters. Details on how each contribution has been estimated are given in the following sections.

From the values reported in table 7.1, the experimental systematic covariance matrix is found to be

$$V_{\text{exp}} = \begin{array}{c} \begin{array}{cc} x & y \end{array} \\ \begin{pmatrix} 1.38 \cdot 10^{-6} & 2.45 \cdot 10^{-7} \\ 2.45 \cdot 10^{-7} & 1.695 \cdot 10^{-6} \end{pmatrix} \end{array}, \tag{7.3}$$

and the correlation coefficient due to this contribution is $\rho_{\text{exp}} = 0.16$.

7.1.1 Fit bias

It has been confirmed in §6.5.1 that the decay amplitude implemented in the event generator is consistent with the decay amplitude used in the fitter. It has also been shown, in §6.5.2, that there are no significant biases due to background or detector effects, and it has been verified with toy Monte Carlo experiments that there are no significant biases due to limited statistics, as explained in §6.5.3. However, these statements on the absence of fit biases on x and y rely on either toy or full Monte Carlo simulations, which are based on a limited number of events.

This section describes the systematic uncertainty due to the statistical precision implied by the limited size of the Monte Carlo samples used to check for fit biases.

Two different sources are considered:

- The effects caused by the limited statistics are estimated from the error on the mean of the residual distributions of the mixing parameters obtained from the fit to toy Monte Carlo experiments tuned to the results on data, described in §6.5.3 and shown in table 6.42. These mean residuals are $d_x^{\text{toy}} = (5.56 \pm 2.2) \cdot 10^{-4}$ and $d_y^{\text{toy}} = (-8.0 \pm 2.1) \cdot 10^{-4}$. Though the central value of the mean could be used to apply a small correction to the x and y central values from the nominal mixing fit to data, it has been preferred to assign a systematic uncertainty to them.

- The background and detector effects that may have not been accounted for in the nominal mixing fit (mass resolution, residual correlations between fit variables, ...), are reasonably well reproduced by the full simulation. These effects are evaluated as the quadratic difference of statistical errors on the mixing parameters, obtained from a fit to the full signal Monte Carlo reconstructed events, on one hand, and their truth matched events on the other hand, $\sigma^2_{\text{det}} = \sigma^2_{\text{reco}} - \sigma^2_{\text{true}}$. Here, σ_{true} is affected by limited statistics effects, taken into account as explained in the previous paragraph, and also effects due to the selection criteria, detailed in §7.1.2. The magnitude σ_{det}, therefore, contains any reconstruction effects that are not due to the limited statistics or selection criteria, and represents the detector and background effects. For this calculation, it is assumed that the detector and background effects are independent from the effects due to limited statistics and selection criteria and, therefore, σ_{det} and σ_{true} can be added in quadrature as sources of σ_{reco}. The values of σ_{true} and σ_{reco} are reported in tables 6.39 and 6.40, respectively, and their differences (central values and statistical differences) are reported in table 7.2. As in the previous paragraph, the differences in central values between the reconstructed and true fit results could be used to apply a small correction to the nominal mixing fit results, but it has been preferred to assign a systematic uncertainty to them.

The fits to Monte Carlo reconstructed and true events are performed on the $K_s\pi^+\pi^-$ and $K_sK^+K^-$ signal Monte Carlo samples separately, and for the *mix* and *nomix* samples. The fit deviations from the *mix* and *nomix* samples are averaged, and their inverse errors are added in quadrature. The $K_s\pi^+\pi^-$ and $K_sK^+K^-$ results and their uncertainties are combined taking into account their relative statistical weights, obtained from the nominal mixing fit to data and reported in table 6.29,

$$d^{\text{det}} = \frac{\sum_h \omega_h d_h^{\text{det}}}{\sum_h \omega_h}, \tag{7.4}$$

$$\frac{1}{\sigma^2_{\text{det}}} = \frac{\sum_h \omega_h \frac{1}{\sigma^2_{h,\text{det}}}}{\sum_h \omega_h}, \tag{7.5}$$

where the sum is over the $\tilde{D}^0$ decay modes $K_s\pi^+\pi^-$ and $K_sK^+K^-$, and the weights are

$$\omega_h = \frac{1}{\sigma^2_{h,\text{stat}}}. \tag{7.6}$$

This yields $d_x^{\text{det}} = (2.53 \pm 7.12) \cdot 10^{-4}$ and $d_y^{\text{det}} = (12.10 \pm 6.28) \cdot 10^{-4}$.

The contributions from the two effects reported in this section are averaged, and their uncertainties are added in quadrature. The overall fit biases are $d_x = (5.33 \pm 7.45) \cdot 10^{-4}$ and $d_y = (-5.98 \pm 6.62) \cdot 10^{-4}$. With the assigned systematic uncertainties, these biases are consistent with zero at less than one standard deviation, thus no correction is applied to the central values obtained from the nominal mixing fit.

7.1.2 Selection criteria

This section describes a check for stability of the mixing fit results against changes in the selection ranges of the four variables involved in the fit: m_D, Δm, t, and σ_t. Since the contributions to the mixing fit results of the cuts on each of these variables are strongly correlated, the variation giving the largest change on each mixing parameter is used to assign a global systematic uncertainty component to the selection criteria.

This component of the systematic uncertainty has been calculated from the result of a fit to data, but with alternative selection criteria, different from those reported in §4.3. In all the cases, the differences in central values of the alternative and nominal fits are consistent with the difference of their statistical uncertainties, so these latter have been taken as the component of the selection criteria to the systematic uncertainty, $\sigma^2_{\text{sel}} = \sigma^2_{\text{alt}} - \sigma^2_{\text{nom}}$.

The alternative selection criteria are a redefinition of the signal box region, and a redefinition of the cuts on the $\tilde{D}^0$ lifetime and lifetime error. These redefinitions require a reevaluation of the signal and background yields (step 1b, in the case of the redefinition of the signal box region, or the whole step 1, in the case of the redefinition of the $\tilde{D}^0$ lifetime and lifetime error cuts), as well as a reevaluation of the parameters of the resolution function that are fixed to the values found in the step 2a fit to signal Monte Carlo events (b_t, f_o and σ_o), the parameters of the $\tilde{D}^0$ lifetime distribution (categories 3 and 4), the decay model background distribution (in the case of the redefinition of the $\tilde{D}^0$ lifetime and lifetime error cuts), the $\tilde{D}^0$ lifetime error distribution for signal and background, and the mixing fit (step 3).

- **m_D and Δm signal box region cut.** To estimate the level of understanding of the background and the robustness of the mixing fit against it, the nominal mixing fit has been redone with an alternative definition of the signal box region, defined in §6, from $\pm 2\sigma$ to $\pm 3\sigma$ in both m_D and Δm. This alternative definition increases significantly the amount of background, as reported in table 7.3. With this extended window, the overall purity of the sample changes from 98.5 % to 97.4 % for $K_s\pi^+\pi^-$ and from 99.2 % to 98.7 % for $K_sK^+K^-$. The observed variation of the mixing parameters with respect to the values found in the nominal fit are $d_x^{\text{box}} = (8.49 \pm 3.95)\cdot 10^{-4}$ and $d_y^{\text{box}} = (8.21 \pm 5.09)\cdot 10^{-4}$.
- **$\tilde{D}^0$ lifetime cut.** The nominal cut on $\tilde{D}^0$ lifetime is $t \in (-6, 6)$ ps. This cut has been restricted to the alternative range $t \in (-2, 4)$ ps, as used in other BaBar analyses [2], which provides a check of the level of understanding of events with large lifetime. These events may potentially affect the mixing parameters, since a significant component of events with poorly reconstructed long lived $\tilde{D}^0$ candidates may not be correctly accounted for in the PDF. The observed variation of the mixing parameters with respect to the values found in the nominal fit are $d_x^t = (1.37 \pm 2.15)\cdot 10^{-4}$ and $d_y^t = (-0.92 \pm 1.59)\cdot 10^{-4}$.
- **$\tilde{D}^0$ lifetime error cut.** The nominal cut on $\tilde{D}^0$ lifetime error is $\sigma_t < 1$ ps. This cut has been restricted to the alternative $\sigma_t < 0.8$ ps, which, as in the case of the $\tilde{D}^0$ lifetime, provides a

check of the level of understanding of events with a poor $\tilde{D}^0$ lifetime resolution. The observed variation of the mixing parameters with respect to the values found in the nominal fit are $d_x^{\sigma_t} = (3.62 \pm 3.44) \cdot 10^{-4}$ and $d_y^{\sigma_t} = (-0.75 \pm 1.86) \cdot 10^{-4}$.

7.1.3 Signal and background yields

Signal and background yields are not allowed to float in step 3 of the fit. They are fixed to the values obtained from step 1, which also provides covariance and correlation matrices for the yields in the different categories, reported in equations (6.2) and (6.3). Since the nominal mixing fit does not use the m_D and Δm distributions, any systematic uncertainty in the determination of the yields in step 1, including effects from the m_D and Δm parameterization described in §5, propagates to step 3 exclusively through the values of the yields.

For the evaluation of this component to the systematic uncertainty on the mixing parameters, the systematic contribution to the yields covariance matrix has been estimated. Several sources of uncertainties have been considered:

- The parameters of the signal (category 1) PDF that have been fixed in the nominal fit are allowed to float, for both $K_s\pi^+\pi^-$ and $K_sK^+K^-$ modes. In addition, the third Gaussian in $p_{nc}^{m_D}$ and the second Gaussian with width correlation in $p_c^{m_D,\Delta m}$ are removed for the $K_sK^+K^-$ mode only. No components have been removed from the $K_s\pi^+\pi^-$ PDF, since they are clearly needed, or otherwise the residual distributions would be dramatically worse (and the fit would have difficulties to converge). With these changes, the contribution of the events from category 2 to this systematic uncertainty is implicitly taken into account, since, on one hand, the m_D PDF is obtained as the m_D projection of the signal PDF and, on the other hand, uncertainties due to the parameterization of the Δm distribution of events in category 2 are negligible because its parameter $\xi^{\Delta m,2}$ is extracted from the fit to the data, which have a purely combinatorial distribution with no complex structures.

- In the nominal fit, the yield for category 3 events has been fixed to the one obtained by counting on Monte Carlo, as explained in §6.1.1. To account for the effect of the differences in cross sections, branching fractions, and reconstruction efficiency between the data and Monte Carlo samples, this yield has been varied $\pm 10\,\%$.

- The nominal m_D and Δm PDF for events in category 3 is a non-parametric two-variable function. An alternative parameterization is considered,

$$\begin{aligned} p_3^{m_D,\Delta m} = \; & f_1^{m_D,\Delta m,3} \cdot p_1^{m_D,\Delta m} + \\ & (1 - f_1^{m_D,\Delta m,3}) \cdot \Big\{ f_B^{\Delta m,3} \cdot P_1(m_D; a_0, a_1) \cdot B\left(\Delta m; m_\pi, \xi^{\Delta m,3}\right) + \\ & \quad (1 - f_B^{\Delta m,3}) \cdot G_b\left(m_D; \mu^{m_D,3}, \sigma_l^{m_D,3}, \sigma_r^{m_D,3}\right) \cdot \\ & \quad \left[f_{G1}^{\Delta m,3} \cdot G\left(\Delta m; \mu_1^{\Delta m,3}, \sigma_1^{\Delta m,3}\right) + (1 - f_{G1}^{\Delta m,3}) \cdot G\left(\Delta m; \mu_1^{\Delta m,3}, \sigma_2^{\Delta m,3}\right) \right] \Big\}, \end{aligned} \tag{7.7}$$

where the first term is a signal component that accounts for the observed correlation between m_D and Δm in category 3 events, and the third term introduces an additional peaking component in both m_D and Δm. Notice that the two Gaussians that parameterize this additional Δm peaking component share the same central value $\mu_1^{\Delta m,3}$. The fit projections of this alternative parameterization are shown in figure 7.1.

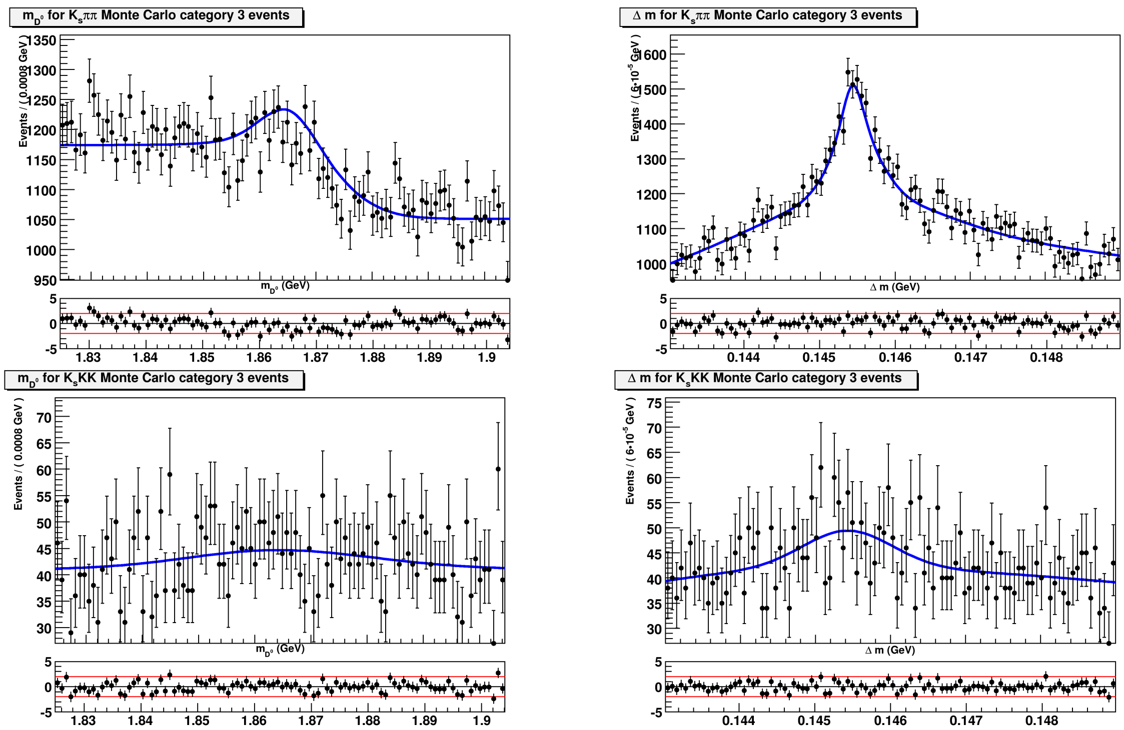

Figure 7.1: m_D (left column) and Δm (right column) projections of the fit to *flat* Monte Carlo background events in category 3 for $K_s\pi^+\pi^-$ (top row) and $K_sK^+K^-$ (bottom row).

- In addition, differences between data and Monte Carlo are accounted for by fixing the fraction of correlated component, $f_1^{m_D,\Delta m,3}$, to 0 and to 0.02, and also by floating the parameter of the Δm modified Argus function, $\xi^{\Delta m,3}$. The maximum difference in the mixing fit results with respect to the nominal values is taken as this component to the systematic uncertainty.

- In the nominal mixing fit, the fraction of peaking component in the m_D distribution for events in category 4, parameterized according to expression (5.35), is fixed to zero. To account for a small peaking component, this value has been fixed to 0.1, as discussed in §5.3.1 and shown in figure 5.12. As has been discussed above for events in category 2, uncertainties in the parameterization of the Δm distribution of events in category 4 are considered to be negligible because its parameter $\xi^{\Delta m,2}$ is extracted from the fit to data, which present a purely combinatorial distribution with no complex structures.

- For background events in category 6 (K_sK_s), the $\tilde{D}^0 \to K_sK_s$ branching fraction has been fixed to zero and to twice its nominal value [55]. This variation accounts for uncertainties in the branching fraction itself and also for discrepancies in K_s reconstruction efficiency between data and Monte Carlo events.

- To account for biases in the yields fitting method, the yields obtained from the nominal fit to Monte Carlo events have been compared to those obtained by counting on Monte Carlo, both summarized in table 6.3. Their differences have been rescaled to data luminosity and used to correct the yields on data.

For each of these sources, a component to the yields covariance matrix is evaluated. These components are summed together to form the total yields systematic covariance matrix.

To estimate each contribution to the covariance matrix, the yields have been reevaluated for each of the sources that have been considered. The signed differences in the yields with respect to their values from the nominal fit are rescaled to the signal box region by means of the ratio of the PDF integrals in the large and signal box regions, and taken as the uncertainty due to each source. Full correlation or anti-correlation is assumed to estimate the off-diagonal elements of each component of the covariance matrix, according to the signs of these differences,

$$V_{\text{syst}}^{\text{yields}} = \sum_k \begin{array}{c} \begin{array}{ccc} \quad n_1 \quad & \quad n_2 \quad & \quad n_4 \quad \end{array} \\ \begin{pmatrix} \sigma_{n_1,k}^2 & \sigma_{n_1,k}\,\sigma_{n_2,k} & \sigma_{n_1,k}\,\sigma_{n_4,k} \\ \sigma_{n_2,k}\,\sigma_{n_1,k} & \sigma_{n_2,k}^2 & \sigma_{n_2,k}\,\sigma_{n_4,k} \\ \sigma_{n_4,k}\,\sigma_{n_1,k} & \sigma_{n_4,k}\,\sigma_{n_2,k} & \sigma_{n_4,k}^2 \end{pmatrix} \end{array}. \tag{7.8}$$

The total yields covariance matrices is the sum of the statistical contribution obtained in §6.1.2 and reported in equations (6.2) and (6.3), and the systematic contributions obtained from the procedure described here. This total covariance matrix is found to be

$$V_{K_s\pi^+\pi^-}^{\text{yields}} = \begin{array}{c} \begin{array}{ccc} \quad n_1 \quad & \quad n_2 \quad & \quad n_4 \quad \end{array} \\ \begin{pmatrix} 3024510 & -242391 & -250950 \\ -242391 & 411314 & -381462 \\ -250950 & -381462 & 676213 \end{pmatrix} \end{array}, \tag{7.9}$$

$$V_{K_sK^+K^-}^{\text{yields}} = \begin{array}{c} \begin{array}{ccc} \quad n_1 \quad & \quad n_2 \quad & \quad n_4 \quad \end{array} \\ \begin{pmatrix} 261739 & -37276.1 & -13398 \\ -37276.1 & 31502.1 & 1699.29 \\ -13398 & 1699.29 & 10363.5 \end{pmatrix} \end{array}. \tag{7.10}$$

Using these covariance matrices, for each $1\,\sigma$ variation of a given yield, the variation on all the other yields is obtained by taking into account their correlations. For example, for a $1\,\sigma$ variation of n_1, $n_1 + \sigma_{n_1}$, the variation on n_2 is $n_2 + \rho_{n_1,n_2}\sigma_{n_2}$, and on n_4 is $n_4 + \rho_{n_1,n_4}\sigma_{n_4}$.

For the evaluation of this component to the systematic uncertainty, each yield has been varied $1\,\sigma$ above and below with respect to its nominal value, and the mixing fit is redone. For each yield, the maximum effect on the mixing parameters from these upper and lower variations is taken as its contribution to the systematic uncertainty, and then, the contributions from all the yields are added in quadrature.

As a crosscheck, step 3 of the mixing fit has been performed explicitly including the m_D and Δm PDFs. Since the mixing fit is performed in the signal box region, with a very high purity, no significant effects are expected from the inclusion of these PDFs due to additional signal to background discrimination or residual correlations between the $\tilde{D}^0$ mass and the $\tilde{D}^0$ lifetime, lifetime error or Dalitz variables. This effect is found to be negligible, $-4 \cdot 10^{-7}$ for x and $2.5 \cdot 10^{-5}$ for y.

7.1.4 $\tilde{D}^0$ lifetime PDF

The signal $\tilde{D}^0$ lifetime resolution function is a linear combination of Gaussian distributions, with two components taking the per-event error and one taking a global error. Some of these components (b_t, f_o and σ_o) have been fixed in the nominal mixing fit to the values obtained from a fit to signal *nomix* Monte Carlo events, and b_o is fixed to zero, as described in §6.2.1. Background events use an effective parameterization of the $\tilde{D}^0$ lifetime distribution, described in §5.3.2.

This section describes the effect on the measurement of the mixing parameters due to assumptions on the model of the signal resolution function or the background effective parameterization, as well as due to fixing some of the parameters of the resolution function.

- **Signal resolution function.** To evaluate the component of the systematic uncertainty due to the parameterization of the $\tilde{D}^0$ lifetime resolution function and the way that some parameters have been fixed in the nominal mixing fit, six alternative setups of the resolution function parameters have been defined. These setups are summarized in table 7.4. In setup A, the parameters b_t, f_o and b_o are allowed to float, and σ_o is fixed to its nominal value. Setup B is identical to setup A, except that σ_o is fixed to twice its nominal value. In setup C, the core and tail components of the resolution function are assumed to have a common bias parameter, $b_{ct} \equiv b_c = b_t$, while all the other parameters are floated or fixed in the same way as in the nominal mixing fit. Setup D is identical to setup C, except that all the bias parameters are assumed to be common, $b_{cto} \equiv b_c = b_t = b_o$. Setup E is identical to setup D, except that the outliers component takes the per-event error, as the core and tail components do. Finally, in setup F, the bias parameter of the tail component if fixed to zero, $b_t = 0$, while the rest of the parameters are kept as in the nominal mixing fit. In all the setups, the variations are of order 10^{-5}, two orders of magnitude lower than the statistical uncertainty. The largest variation observed on x and y is taken as the component from these effects to the systematic uncertainty, namely $d_x = -4.3 \cdot 10^{-5}$, $d_y = -3.2 \cdot 10^{-5}$.

- **Background $\tilde{D}^0$ lifetime PDF. Differences between data and Monte Carlo.** The $\tilde{D}^0$ lifetime distribution for events with a fake $\tilde{D}^0$ (categories 3 and 4) is parameterized using an effective function, described in §5.3.2. The parameters of this function are determined from separate fits to fake Monte Carlo $\tilde{D}^0$ events in the signal box region, as described in §6.2.1.3. To account for differences between data and Monte Carlo, the parameters of this PDF are alternatively determined from fits to data and Monte Carlo m_D sidebands. Their $\tilde{D}^0$ lifetime projections are shown in figure 7.2. The largest variation of the mixing parameters obtained from the fits to the two alternative sources of background used to determine the background $\tilde{D}^0$ lifetime PDF is used as this contribution to the systematic uncertainty.

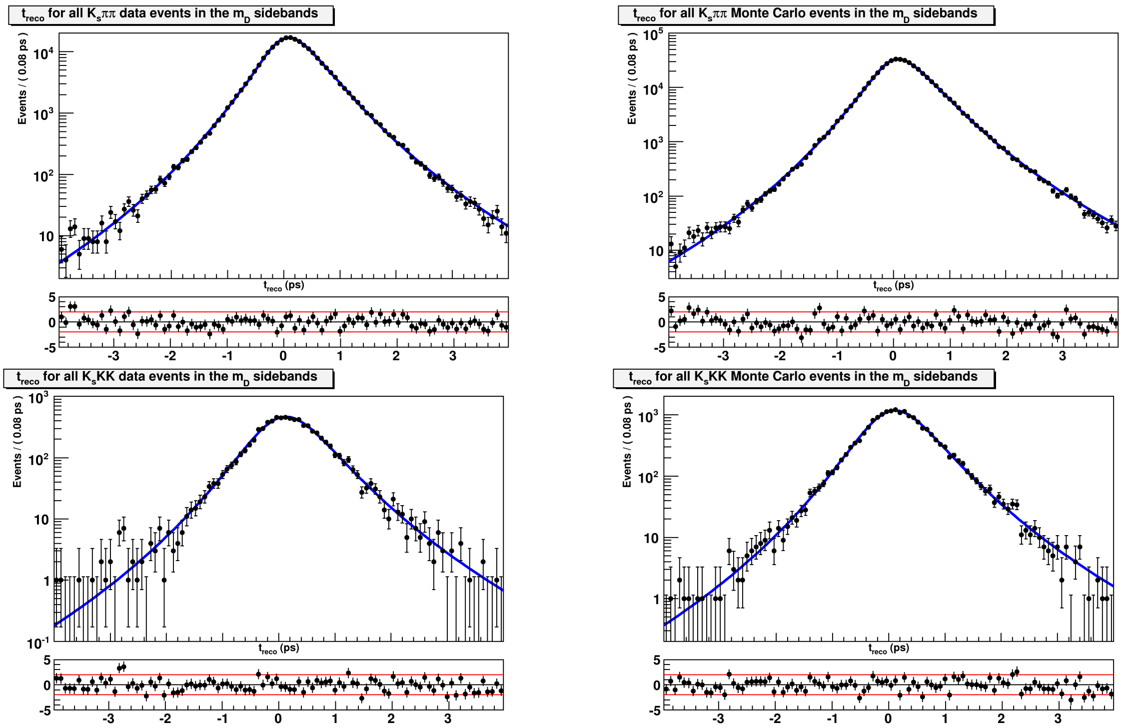

Figure 7.2: $\tilde{D}^0$ lifetime projections of the fit to data (left column) and Monte Carlo (right column) background events in the m_D sidebands in categories 3 and 4 for $K_s\pi^+\pi^-$ (top row) and $K_sK^+K^-$ (bottom row).

- **Background $\tilde{D}^0$ lifetime PDF. Parameterization.** To evaluate the effect of the parameterization of the $\tilde{D}^0$ lifetime PDF for background events in categories 3 and 4, an alternative parameterization has been introduced, consisting of a linear combination of Gaussian functions convoluted with a negative exponential decay law with an effective lifetime for background events. This effective lifetime accounts for wrongly reconstructed $\tilde{D}^0$ events where one or more particles are missing or wrongly reconstructed. The parameters of the effective parameterization are determined from two sources: on one hand, from a sample of fake $\tilde{D}^0$ events in the signal box region, and on the other hand, from a sample of data in the m_D sidebands. These parameters are fixed and the mixing fit is redone with them. The results of the mixing parameters obtained using these two sources are compared with the results from the nominal parameterization using the same sources. The largest observed variation in the mixing parameters is taken as this contribution to the systematic uncertainty.

- **Background $\tilde{D}^0$ lifetime PDF for category 6.** The parameters of the $\tilde{D}^0$ lifetime PDF for K_sK_s background events (category 6), described in §5.3.2, have been determined from a fit to background category 6 Monte Carlo events in the signal box region, as explained in §6.2.1.3. This component may potentially be relevant since not only it has a characteristic dynamics that may interfere with the nominal decay model, described in §2.4.8, but it also has a longer reconstructed lifetime as a result of a possible distortion of the incorrectly reconstructed decay vertex, which can induce biases on the average $\tilde{D}^0$ lifetime fit and, therefore, on the mixing parameters. Since the contamination from events in this category is small, the effect from the level of understanding of its lifetime distribution is estimated conservatively by changing by 100 % the amount of these events, i.e., changing its yield to zero and to twice its value in the nominal mixing fit.

7.1.5 $\tilde{D}^0$ lifetime error PDF

- **Signal $\tilde{D}^0$ lifetime error PDF.** To account for the correlation between σ_t and the event Dalitz variables, the Dalitz plot has been divided in 16×16 boxes for $K_s\pi^+\pi^-$ and 16 slices for $K_sK^+K^-$, and the σ_t PDF has been fit to data events in the signal box region, separately on each box or slice, as described in §5.2.2. Two different sources of systematic uncertainty have been considered: on one hand, the contribution of the binning in boxes or slices has been conservatively accounted for by using a single box or slice (i.e., ignoring the correlation between σ_t and the Dalitz variables). On the other hand, the σ_t PDF has been fit to Monte Carlo events in the signal box region, instead of data, to obtain the parameters in each box or slice. These two contributions have been added in quadrature.

- **Background $\tilde{D}^0$ lifetime error PDF.** The parameters of the nominal σ_t PDF are fixed from a fit to Monte Carlo fake $\tilde{D}^0$ events (categories 3 and 4) in the signal box region. Alternatively, these parameters are determined from a fit to m_D sideband data events and to Monte Carlo fake $\tilde{D}^0$ events in the large box region. The largest variation of the mixing parameters from these two alternatives is taken as this contribution to the systematic uncertainty.

7.1.6 Reconstruction efficiency non-uniformities over the phase space

The reconstruction efficiency non-uniformities across the phase space have been taken into account with two-variable polynomials, different for $K_s\pi^+\pi^-$ and $K_sK^+K^-$ events, as described in §5.2.3. The coefficients of these polynomials have been obtained from a fit to *flat* Monte Carlo signal events. It has been observed that this parameterization has evident flaws in some borders of the $K_s\pi^+\pi^-$ Dalitz plot, which can be observed in figures 5.8, 6.18, and 6.19. To estimate the contribution of the efficiency parameterization to the systematic uncertainty, the nominal fit to Monte Carlo events has been redone with a flat efficiency parameterization (i.e., ignoring any reconstruction non-uniformities). This effect is estimated from differences in the central values of the fit results with respect to the values obtained with the nominal parameterization, independently from the $K_s\pi^+\pi^-$ and $K_sK^+K^-$ $\tilde{D}^0$ decay modes, and for the *nomix* and *mix* Monte Carlo samples. The fit deviations from the *nomix* and *mix* samples are averaged, and the $K_s\pi^+\pi^-$ and $K_sK^+K^-$ results are combined taking into account their relative statistical weights, obtained from the nominal mixing fit to data, reported in table 6.29.

As a crosscheck, the nominal mixing fit to data is also performed with a flat efficiency parameterization. The deviation of the mixing parameters with respect to those obtained with the nominal parameterization is in agreement with the effect obtained from Monte Carlo events, but is affected by larger statistical uncertainties.

Differences in the efficiency parameterization between D^0 and $\bar{D}^0$ events are not explicitly accounted for, since they are not statistically significant (tables 5.2 and 5.3) and the flat efficiency parameterization represents an alternative with significantly larger differences.

7.1.7 Mistagged events

Mistagged events are those events where the flavor of the $\tilde{D}^0$ is not correctly tagged. A Dalitz plot showing these events has the axes reversed with respect to the Dalitz plot of correctly tagged events, which can dilute sensitivity to mixing.

For signal (category 1) events, the fraction of mistagged events is fixed to zero in the nominal mixing fit. However, events in this category may contain a small fraction of events where the $\tilde{D}^0$ and the soft pion are not sisters and, therefore, the charge of the soft pion may incorrectly tag the $\tilde{D}^0$. To account for this effect, the fraction of wrong tagged events is fixed to 0.12 % in this category, obtained from direct counting on Monte Carlo events.

For events in category 2, the flavor of a correctly reconstructed $\tilde{D}^0$ is tagged with a soft pion that is not the decay product of a $D^{\star\pm}$. In the nominal mixing fit, it is assumed that the mistag fraction of these events is 50 %, since this is the probability for a random pion to have the charge that correctly tags the $\tilde{D}^0$ flavor. However, asymmetries in the detector response produce a small deviation from this 50 %, as has been shown in table 6.21 for Monte Carlo events. To account for this effect, the mixing fit has been redone with the values in table 6.21.

The contributions from both categories 1 and 2 have been added in quadrature to produce the contribution of the mistagged events to the systematic uncertainty.

7.1.8 Mixing in the background

Background events in category 2 contain true $\tilde{D}^0$ mesons that undergo mixing. However, the PDF for events in category 2, described in §5.3.3, is not sensitive to mixing, which can bias the nominal mixing fit results.

To account for possible biases due to mixing effects in events in category 2, an independent set of mixing parameters, specific for category 2, namely x_2 and y_2, has been introduced. The nominal mixing fit has been redone fixing one of these parameters to zero and the other to ± 0.02. The mixing fit results obtained fixing $(x_2, y_2) = (0, \pm 0.1)$ are compared to the nominal mixing fit results, and the largest differences are added in quadrature with the largest differences obtained fixing $(x_2, y_2) = (\pm 0.1, 0)$, to obtain the contribution of this effect to the systematic uncertainty.

This source of systematic uncertainty is not considered for categories 3 and 4, since they only contain events with a fake $\tilde{D}^0$.

7.1.9 Invariant mass resolution

The structures observed in the residual plots in figure 6.18 around the $K^{\star -}(892)$ peak for $K_s\pi^+\pi^-$ and in figure 6.20 around the $\phi(1020)$ peak for $K_sK^+K^-$, are caused by invariant mass resolution effects not explicitly accounted for in the nominal model.

The resolution on the Dalitz plot variables has been evaluated by means of Monte Carlo truth matched signal events. The squared invariant masses are evaluated using the reconstructed momenta of the particles but applying m_{K_s} and m_D mass constraints. Besides improving the resolution, the m_D mass constraint assures that the reconstructed Dalitz variables lie within the kinematic boundaries. The residual distribution of the invariant masses of truth matched signal events is shown in figure 7.3 for $K_s\pi^+\pi^-$ and figure 7.4 for $K_sK^+K^-$ events. The estimated mass resolution is $\sim 2\,\mathrm{MeV}$ for $K_s\pi^+\pi^-$ and $\sim 1.2\,\mathrm{MeV}$ for $K_sK^+K^-$, on average over the whole phase space. Since most of the resonances that the decay model takes into account are quite wider compared with this resolution, this effect is expected to be small or negligible.

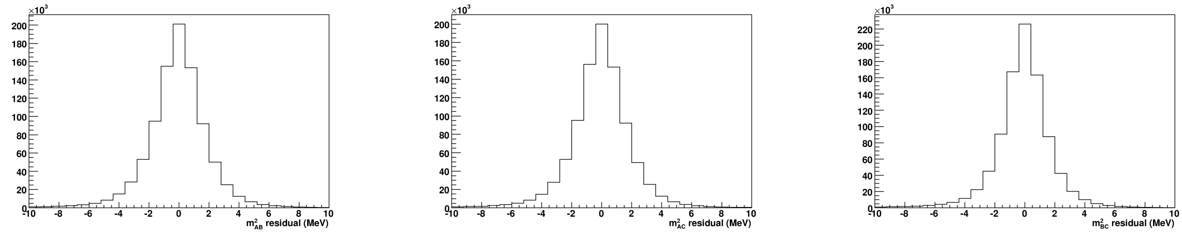

Figure 7.3: Residual distributions of the invariant masses of truth matched signal $K_s\pi^+\pi^-$ events.

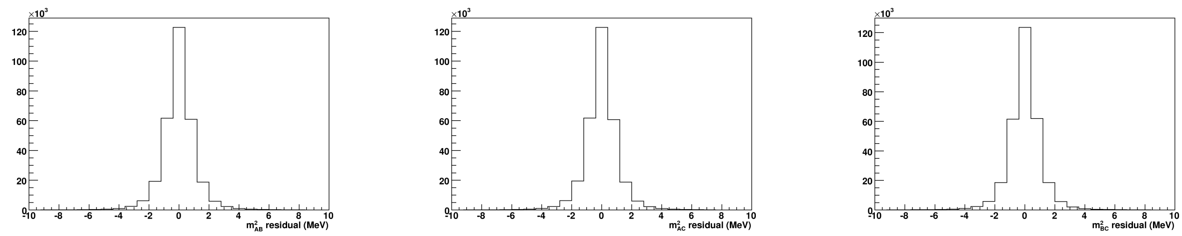

Figure 7.4: Residual distributions of the invariant masses of truth matched signal $K_sK^+K^-$ events.

Only the $\omega(782)$ resonance in the $K_s\pi^+\pi^-$ model and the $\phi(1020)$ resonance in the $K_sK^+K^-$ model have intrinsic widths comparable to the mass resolution. The $\omega(782)$ component has a small fit fraction, as reported in table 6.22 and, therefore, mass resolution effects in the $\omega(782)$ region are expected to be suppressed. For the $\phi(1020)$ component of the $K_sK^+K^-$ decay model, though it has a large fit fraction, its mass and width have been left to float in step 2b of the fit, which partially accounts for mass resolution effects (not completely, since width changes affect the resonance pattern, while a real mass resolution does not).

To evaluate the residual effects of limited mass resolution, the nominal mixing fit has been performed on both reconstructed and truth matched *nomix* and *mix* Monte Carlo events. Reconstructed events are affected by mass resolution effects, while truth matched events are not. These fits are performed separately on $K_s\pi^+\pi^-$ and $K_sK^+K^-$ events. Since this procedure is identical to the calculation of the fit bias contribution to the systematic uncertainty, described in §7.1.1, no additional contribution is assigned to mass resolution effects, to avoid double counting the same source of systematic uncertainty.

7.1.10 Phase space background profile

The background amplitude PDFs for events in categories 3 and 4, with fake $\tilde{D}^0$ mesons, are non-parametric, and the different sources considered to extract these PDFs are described in 6.2.2.2. The nominal fit uses data in the m_D sidebands. However, comparisons between Monte Carlo and data events in the upper and lower sidebands, shown in figures 6.13 and 6.14, as well as comparisons between Monte Carlo and data events in both sidebands, shown in figure 6.15, reveal differences in both the combinatorial and resonant structures.

To account for the effect of the choice of data in the m_D sidebands, rather than other sources, the mixing fit has been redone with the background profiles determined from four alternative sources:

- Lower data m_D sideband.
- Upper data m_D sideband.
- Monte Carlo m_D sidebands (both upper and lower together).
- Monte Carlo fake $\tilde{D}^0$ events in the signal box region.

The largest deviation of the results of the mixing parameters obtained with these four alternative parameterizations, with respect to the nominal mixing fit result, is assigned as this contribution to the systematic uncertainty.

7.1.11 Normalization of the decay model

The normalization of the decay model uses a numerical integration technique based on a grid with 400×400 cells, for both $K_s\pi^+\pi^-$ and $K_sK^+K^-$. The effect of this choice of binning has been estimated redoing the nominal mixing fit with a tighter binning of 4000×4000 cells. The deviation of the mixing parameters obtained from this fit with respect to the nominal mixing fit results is assigned as the component of the binning to the systematic uncertainty.

7.1.12 $\tilde{D}^0$ mass cut

The measured $\tilde{D}^0$ decay time t is correlated with the measured $\tilde{D}^0$ mass m_D, as shown in figure 7.5. Since the mixing parameters modify the $\tilde{D}^0$ decay time distribution, an uncertainty in the $\tilde{D}^0$ mass may imply a systematic uncertainty in the mixing parameters.

The average mean of the reconstructed $\tilde{D}^0$ mass for *flat* Monte Carlo events, differs in $-0.6\,\mathrm{MeV}$ from the generated value. To account for the effect of the $\tilde{D}^0$ mass cut, the nominal mixing fit has

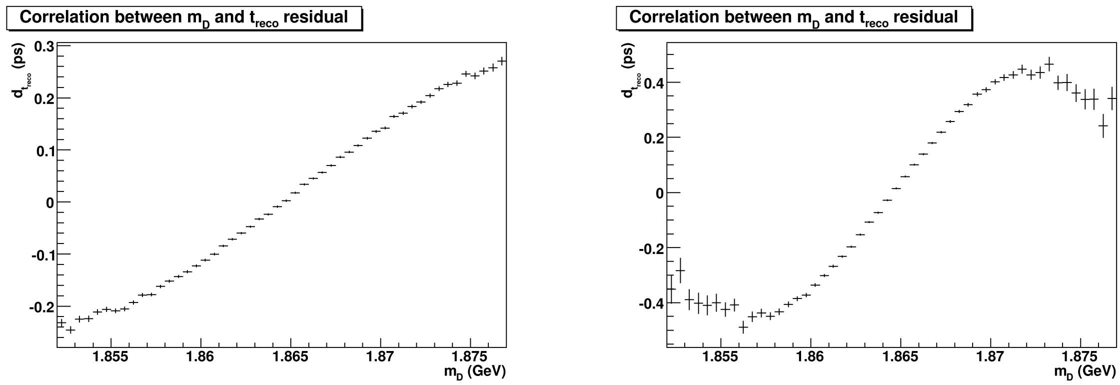

Figure 7.5: Average difference between the reconstructed and generated $\tilde{D}^0$ decay times with respect to the reconstructed $\tilde{D}^0$ mass for signal Monte Carlo $K_s\pi^+\pi^-$ (left) and $K_sK^+K^-$ (right) events.

been redone with the signal box region shifted 0.5 MeV up and down in m_D. The largest difference between the results of the fits in these two regions with respect to the nominal mixing fit, in the default signal box region, is considered as the contribution of the $\tilde{D}^0$ mass cut to the systematic uncertainty.

7.1.13 SVT misalignment

The position of the 340 wafers of the SVT are not perfectly constant over time, at the level of micrometers. The procedure used to measure deviations of the actual wafer positions with respect to the nominal values is described in [71].

Since the measurement of the $\tilde{D}^0$ lifetime is sensitive to SVT wafer misalignments, the mixing parameters may also be affected by these misalignments. To account for this effect, Monte Carlo events are generated with $x = y = 10^{-2}$ and with the SVT wafers deliberately misaligned. Five different misalignment configurations are used. Each wafer in these configurations contains a displacement and a rotation with respect to the nominal design position. Four of these configurations are obtained from differences between successive measurements of the wafer alignments, and thus represent the time dependence of the wafer positions. They are referred to as *time-like* configurations. The fifth configuration is generated by shifting each layer of wafers in the z direction of the BaBar axis system by an amount proportional to the wafer radial position with respect to the z axis. This is intended to test the effect of systematic shifts in wafer positions, and is referred to as *boost-like* configuration. Additionally, a sample with no misalignment is also generated. This sample and the five samples with the different misalignment configurations use a common generated true Monte Carlo sample, so the same exact reconstructed events can be compared.

It is important to notice that the systematic effect of the SVT misalignment should be checked with a virtually infinite sample of events with misalignment, to avoid including a statistical effect in this systematic component. As a compromise between the practical and ideal situations, 8 million events have been generated for each of the five misalignment configurations. The contribution of the SVT misalignment to the systematic uncertainty is therefore understood to be overestimated, since it contains a statistical contribution.

The difference of the mixing fit results obtained from the fits to the misalignment samples with respect to the mixing parameters obtained from the configuration with no misalignment is shown in table 7.5. These differences are shown in figure 7.6, as well as the differences in reconstructed average lifetime τ and bias parameter of the core component of the resolution function, b_c.

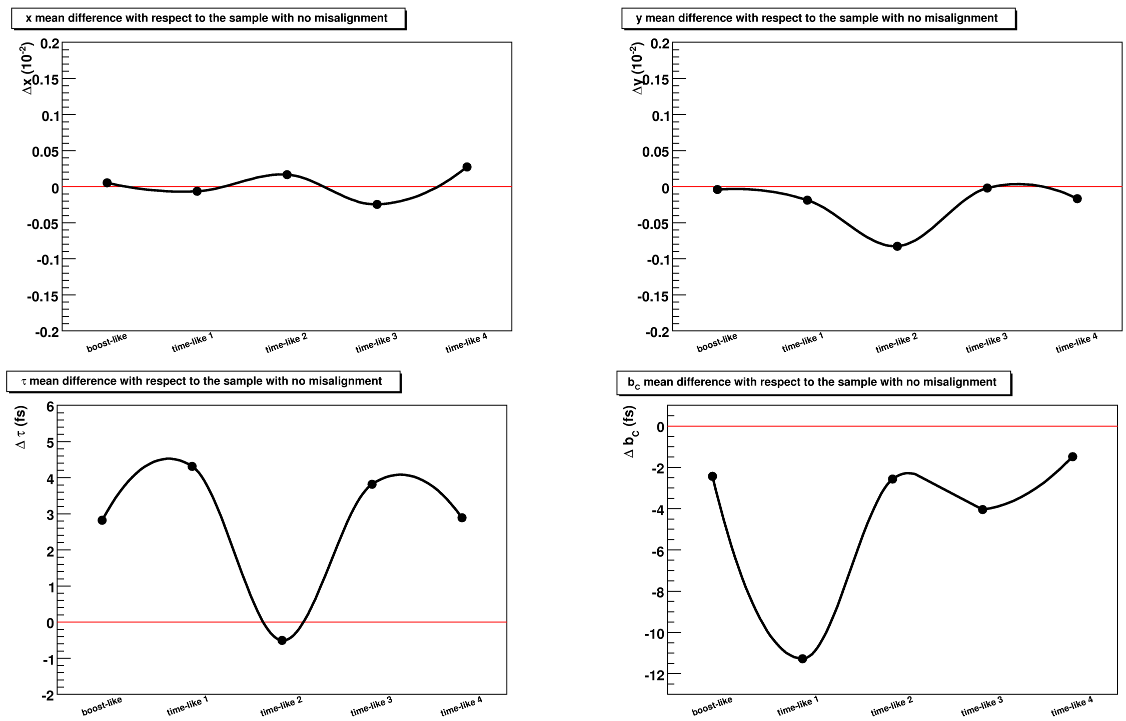

Figure 7.6: Differences in the fit results to signal Monte Carlo samples with misaligned SVT wafers with respect to the values obtained from the fit to the sample with no misalignment.

Following the prescription of the tracking group [72, 73], the contribution of the SVT misalignment to the systematic uncertainty is taken as the quadratic sum of two components. The first component is the maximum deviation of the mixing parameters from all the *time-like* configurations with respect to the sample with no misalignment. The second component is the deviation of the mixing parameters from the *boost-like* configuration with respect to the sample with no misalignment. These values are highlighted in bold in table 7.5. Following this procedure, the SVT misalignment contribution to the systematic uncertainty is $2.79 \cdot 10^{-4}$ for x and $8.26 \cdot 10^{-4}$ for y.

Source	$x\,(10^{-2})$	$y\,(10^{-2})$	Section
Fit bias	0.0745	0.0662	7.1.1
Limited statistics	0.0220	0.0210	
Background and detector effects	0.0712	0.0628	
Selection criteria	0.0395	0.0508	7.1.2
m_D and Δm signal box region cut	0.0395	0.0508	
$\tilde{D}^0$ lifetime cut	0.0215	0.0159	
$\tilde{D}^0$ lifetime error cut	0.0344	0.0186	
Signal and background yields	0.0109	0.0069	7.1.3
Category 1 yield for $K_s\pi^+\pi^-$	0.0043	−0.0029	
Category 1 yield for $K_sK^+K^-$	−0.0041	0.0028	
Category 2 yield for $K_s\pi^+\pi^-$	0.0045	0.0027	
Category 2 yield for $K_sK^+K^-$	0.0045	0.0029	
Category 4 yield for $K_s\pi^+\pi^-$	−0.0051	−0.0024	
Category 4 yield for $K_sK^+K^-$	−0.0042	−0.0032	
$\tilde{D}^0$ lifetime PDF	0.0134	0.0128	7.1.4
Signal resolution function	−0.0043	−0.0032	
Background $\tilde{D}^0$ lifetime: data vs Monte Carlo	−0.0037	−0.0080	
Background $\tilde{D}^0$ lifetime: parameterization	0.0085	−0.0058	
Background $\tilde{D}^0$ lifetime for category 6	0.0088	0.0077	
$\tilde{D}^0$ lifetime error PDF	0.0058	0.0087	7.1.5
Signal $\tilde{D}^0$ lifetime error	−0.0043	0.0080	
Background $\tilde{D}^0$ lifetime error	−0.0039	−0.0034	
Reconstruction efficiency non-uniformities	0.0367	0.0175	7.1.6
Mistagged events	0.0487	0.0398	7.1.7
Category 1 events	0.0378	0.0322	
Category 2 events	0.0307	0.0234	
Mixing in background	0.0103	0.0082	7.1.8
Mixing in category 2 events: x_{bkg}	−0.0099	0.0010	
Mixing in category 2 events: y_{bkg}	−0.0028	−0.0081	
Phase space background profile	0.0331	0.0142	7.1.10
Normalization of the decay model	−0.0106	0.0053	7.1.11
$\tilde{D}^0$ mass cut	0.0250	0.0250	7.1.12
SVT misalignment	0.0279	0.0826	7.1.13
Total experimental systematics	0.1177	0.1302	

Table 7.1: Experimental systematic uncertainties on the mixing parameters x and y. Contributions to some subtotals are also indicated. The sign of each contribution indicates the sign of the variation of the corresponding parameter with respect to the result from the nominal mixing fit.

Sample	Magnitude	$K_s\pi^+\pi^-$	$K_sK^+K^-$
mix	$d_x^{\rm det}$	$(0.0842 \pm 0.0947) \cdot 10^{-2}$	$(-0.1381 \pm 0.3425) \cdot 10^{-2}$
	$d_y^{\rm det}$	$(0.1803 \pm 0.0855) \cdot 10^{-2}$	$(0.1291 \pm 0.2150) \cdot 10^{-2}$
nomix	$d_x^{\rm det}$	$(-0.0192 \pm 0.1011) \cdot 10^{-2}$	$(-0.0250 \pm 0.3485) \cdot 10^{-2}$
	$d_y^{\rm det}$	$(0.0303 \pm 0.0827) \cdot 10^{-2}$	$(0.3403 \pm 0.2237) \cdot 10^{-2}$

Table 7.2: Differences between fits in full Monte Carlo reconstructed and truth variables. The errors are obtained as quadratic differences of the errors on the reconstructed and true fit results.

$\tilde{D}^0$ decay mode	Category	Yield increase in the signal box region (%)
$K_s\pi^+\pi^-$	1	9.7
	2	57.3
	3	98.9
	4	124.0
	6	12.1
$K_sK^+K^-$	1	6.4
	2	52.3
	3	102.7
	4	124.0

Table 7.3: Relative increase of signal and background yields in the mixing fit on data with the alternative definition of the signal box region from $\pm 2\sigma$ to $\pm 3\sigma$ in both m_D and Δm.

Setup	Description	d_x	d_y	d_τ (fs)
A	Float b_t, f_o and b_o. Fix σ_o to nominal value.	$-2.7 \cdot 10^{-5}$	$6.0 \cdot 10^{-6}$	-2.61
B	Float b_t, f_o and b_o. Fix σ_o to twice its nominal value.	$1.0 \cdot 10^{-6}$	$-1.4 \cdot 10^{-5}$	-2.60
C	$b_{ct} \equiv b_c = b_t$.	$2.4 \cdot 10^{-5}$	$-9.0 \cdot 10^{-6}$	-1.16
D	$b_{cto} \equiv b_c = b_t = b_o$.	$2.4 \cdot 10^{-5}$	$-6.0 \cdot 10^{-6}$	-1.16
E	$b_{cto} \equiv b_c = b_t = b_o$. Per-event error in all components.	$2.0 \cdot 10^{-5}$	$-3.2 \cdot 10^{-5}$	-1.05
F	$b_t = 0$.	$-4.3 \cdot 10^{-5}$	$-1.0 \cdot 10^{-6}$	-0.81

Table 7.4: Summary of the six different setups that have been defined to obtain the component to the systematic uncertainty due to the parameterization of the $\tilde{D}^0$ lifetime resolution function and the way that some of its parameters have been fixed.

Configuration	$x\,(10^{-2})$	$y\,(10^{-2})$	d_x	d_y
No misalignment	1.1299 ± 0.3280	0.8418 ± 0.2923		
boost-like	1.1353 ± 0.3301	0.8377 ± 0.2947	**0.0054**	**-0.0041**
time-like 1	1.1236 ± 0.3309	0.8232 ± 0.2947	-0.0063	-0.0186
time-like 2	1.1467 ± 0.3315	0.7593 ± 0.2961	0.0168	**-0.0825**
time-like 3	1.1054 ± 0.3293	0.8397 ± 0.2948	-0.0245	-0.0020
time-like 4	1.1573 ± 0.3296	0.8253 ± 0.2954	**0.0274**	-0.0165

Table 7.5: Results of the fits to signal Monte Carlo samples with misaligned SVT wafers, with the difference in the mixing fit results for each configuration with respect to the sample with no misalignment.

7.2 Decay model systematic uncertainties

It has been remarked in §2 that the fundamental description of a $\tilde{D}^0$ decay involves difficult calculations with strong interactions and, for this reason, this analysis uses a formulation that describes the decay in an effective way. This formulation has been explained in detail in §2. The contribution of the effective description of the decay model to the systematic uncertainty is important enough to quote it separately from the rest purely experimental systematic effects.

To estimate the systematic uncertainty from using a model rather than another, several steps are followed:

- Ten signal only toy Monte Carlo experiments are generated, each with the same signal yield as measured in the data sample. Generating ten times the available statistics in data helps to reduce statistical effects in the estimation of the component of the model to the systematic uncertainty. Since the purpose of these experiments is to study the component of the systematic uncertainty due to the choice of decay model, these events are generated with true resolution, i.e., are free from experimental systematic effects, which are accounted for as described in §7.1. The decay model used in the generation of these events is the nominal decay model, with parameters extracted from the nominal mixing fit. Since the mixing parameters obtained from the nominal mixing fit are still blind in this stage of the analysis, values of $x = y = 10^{-2}$ have been used. Alternatively, a single sample with 10 times the available statistics in data could be generated, but splitting it in 10 data-sized samples allows to estimate statistical differences between models while it overcomes the increase in the computing power needed to fit a much larger data sample.

- The mixing fit is performed on each of the 10 Monte Carlo samples, and the decay model and mixing parameters are extracted, yielding $(x_{0,i}, y_{0,i})$, with i indexing the toy Monte Carlo samples. Some parameters of the decay model, that are fixed in step 3 to the values obtained in step 2b of the nominal fit, are also allowed to float here, in order to account for possible correlations of these parameters with other model or mixing parameters. These parameters are the $\pi\pi$ S-wave P-vector parameters $f^{pr}_{\pi\pi,j}$, the $K\pi$ S-wave generalized LASS parameters B, a, r, ϕ_B, ϕ_R, $m_{K^{\star 0}(1430)}$ and $\Gamma_{K^{\star 0}(1430)}$, and the mass and width of the $K^{\star\pm}(892)$. The effect of fixing these parameters in the nominal mixing fit is evaluated below.

- N alternative models have been used to estimate how much the mixing parameters depend on the choice of the nominal decay model. It is understood that models with the same parameterization but with different values of the parameters, or with parameters fixed or left to float differently from the nominal model, are considered to be part of this set of alternative models. The fits to the mixing parameters have been repeated for each of these alternative models, yielding $(x_{m,i}, y_{m,i})$, with m indexing the alternative model and i indexing the toy Monte Carlo samples. The same parameters that have been allowed to float in the fit to the nominal decay model, are also allowed to float in the fits to these alternative models. The contribution of each alternative model to the decay model systematic uncertainty is taken as the difference of the fit results obtained with the alternative model with respect to the fit results obtained with the nominal model, averaged over the 10 toy Monte Carlo samples,

$$\sigma_{x,m} = \langle x_m \rangle - \langle x_0 \rangle = \frac{1}{10} \sum_{i=1}^{10} (x_{m,i} - x_{0,i}) \,, \tag{7.11}$$

$$\sigma_{x,m} = \langle x_m \rangle - \langle x_0 \rangle = \frac{1}{10} \sum_{i=1}^{10} (x_{m,i} - x_{0,i}) \,. \tag{7.12}$$

This contribution is signed, and allows to assign a correlation coefficient and construct a covariance matrix, as explained at the beginning of this chapter and expressed in equations (7.1) and (7.2).

- Similarly, the change in statistical uncertainty with respect to the reference model can be estimated from the root mean squared of the per-experiment differences,

$$\Delta\sigma_{x,m} = \sqrt{\frac{1}{10-1} \sum_{i=1}^{10} (x_{m,i} - x_{0,i} - \sigma_{x,m})^2}, \tag{7.13}$$

$$\Delta\sigma_{y,m} = \sqrt{\frac{1}{10-1} \sum_{i=1}^{10} (y_{m,i} - y_{0,i} - \sigma_{y,m})^2}, \tag{7.14}$$

which provide an estimate of the difference in statistical sensitivity between the alternative and nominal models.

A few of the alternative models introduce changes that may be affected by resolution effects. Since the toy Monte Carlo experiments described above are generated with true resolution, fitting these models to these experiments may underestimate their contribution to the systematic uncertainty. For this reason, this contribution has been evaluated from fits to data or to toy Monte Carlo experiments generated with resolution effects, instead. In these cases, it is explicitly stated in the description of these alternative models.

Three approaches have been considered to combine the contribution to systematic uncertainties from each alternative model:

1. Adding the contributions from each alternative model in quadrature,

$$\sigma_x^{\text{mod}} = \sqrt{\sum_{m=1}^{N} \sigma_{x,m}^2}, \tag{7.15}$$

$$\sigma_y^{\text{mod}} = \sqrt{\sum_{m=1}^{N} \sigma_{y,m}^2}. \tag{7.16}$$

2. Taking the root mean squared of all the contributions from each alternative model,

$$\sigma_x^{\text{mod}} = \text{rms}(\sigma_{x,m}) \tag{7.17}$$

$$\sigma_y^{\text{mod}} = \text{rms}(\sigma_{y,m}). \tag{7.18}$$

3. Taking the contribution with the maximum absolute value,

$$\sigma_x^{\text{mod}} = \text{maxabs}(\sigma_{x,m}) \tag{7.19}$$
$$\sigma_y^{\text{mod}} = \text{maxabs}(\sigma_{y,m}). \tag{7.20}$$

These three approaches have some degree of arbitrariness:

- It is not obvious that the differences between the alternative and nominal fit results can be considered independent and added in quadrature, as in approach 1. Besides, the total uncertainty obtained from this approach depends on the number of proposed alternatives.
- Taking the root mean squared of all the contributions, as in approach 2, also makes the assigned contribution to the uncertainty depend on the number of proposed alternatives. For example, if many of the alternative models have very small differences with respect to the nominal model, the differences in the measured mixing parameters will be expected to be also small, thus reducing the root mean squared and yielding to a small underestimated systematic uncertainty.
- Taking the contribution with the maximum absolute value, as in approach 3, lies between the overestimation of approach 1 and the eventual underestimation of approach 2, but is also not supported by a strong physics motivation.

Approach 1 has been adopted, since it is clearly the most conservative.

7.2.1 Alternative $K_s\pi^+\pi^-$ decay models

The alternative $K_s\pi^+\pi^-$ decay models are built either with different parameterizations for some of the resonances, or by adding or removing resonances from the model:

- $\pi\pi$ **S-wave.** The nominal decay models uses the K-matrix parameters obtained from fits to scattering data [49, 50]. The effect of the uncertainty due to the parameterization of the K-matrix is evaluated using different solutions of the K-matrix, described in [49]. In addition, the $\pi\pi$ invariant mass dependence on the non-resonant term of the production vector (f_{ij}^{pr}) has been removed [74]. As a crosscheck of the robustness of the mixing result against the $\pi\pi$ S-wave, a relativistic Breit-Wigner propagator has been used, replacing the K-matrix parameterization, as described in §7.2.2.
- $\pi\pi$ **P-wave.** The mass and width parameters of the Gounaris-Sakurai propagator that describes the $\rho(770)$ resonance and of the Breit-Wigner propagator that describes the $\omega(782)$ resonance are allowed to float simultaneously with the mass and width parameters of the $K^{\star\pm}(892)$ resonance. These resonances represent regions of the Dalitz plot that present sensitivity to mixing, and allowing their parameters to float produces the uncertainties in the mixing parameters in a properly correlated way. In addition, the Gounaris-Sakurai propagator used to describe the $\rho(770)$ resonance has been replaced with a Breit-Wigner propagator. Since the toy Monte Carlo experiments described above are generated with true resolution

(no detector effects), and the $\omega(782)$ region is affected by mass resolution effects, using these toy Monte Carlo experiments may underestimate this contribution to the systematic uncertainty. For this reason, in this case, the mixing fit with the alternative model is done to the data sample, instead of to the toy Monte Carlo generated samples, and the quoted systematic uncertainty is the observed change in the mixing parameters.

- $K\pi$ **P-wave.** This wave is dominated by the $K^\star(892)$ in both the Cabibbo allowed and doubly Cabibbo suppressed amplitudes. The mass and width of this resonance is obtained in step 2b of the fit and fixed in step 3.

- **Allowing extra parameters to float.** The effect of fixing the parameters of the decay model in step 3 of the fit to the values obtained in step 2b (the $\pi\pi$ S-wave P-vector parameters $f^{pr}_{\pi\pi,j}$, the $K\pi$ S-wave generalized LASS parameters B, a, r, ϕ_B, ϕ_R, $m_{K^{\star 0}(1430)}$ and $\Gamma_{K^{\star 0}(1430)}$, and the mass and width of the $K^{\star\pm}(892)$) has been evaluated with a set of 30 toy Monte Carlo experiments, generated with the nominal model with resolution effects, as those in §6.5.3. Again, since the results of the mixing parameters are still blind in this stage, values of $x = y = 10^{-2}$ have been used. The nominal mixing fit has been redone for these 30 toy Monte Carlo samples, but with these parameters left to float. The root mean squared of the per-experiment residuals gives an estimate of the loss of statistical power on x and y when these parameters are floated, and is quoted as an additional contribution to the systematic uncertainty. As a crosscheck of the correlation of these parameters with the mixing parameters, the nominal mixing fit on data (the combined $K_s\pi^+\pi^-$ and $K_sK^+K^-$ dataset) has been redone also allowing these parameters to float. The differences in central values of the mixing results of this fit with respect to the mixing results of the nominal mixing fit are consistent within one standard deviation, obtained as the squared difference of the statistical uncertainties in the mixing results obtained from both fits, $\Delta x = (4.83\pm6.78)\cdot10^{-4}$, $\Delta y = (4.74 \pm 5.32) \cdot 10^{-4}$.

- $\pi\pi$ **D-wave.** The values of the mass and width of the $f_2(1270)$ have been shifted above and below the nominal values by their quoted uncertainties [55]. The largest difference in the mixing parameters with respect to the fit results obtained with the nominal model is taken as this contribution to the systematic uncertainty.

- $K\pi$ **D-wave.** The values of the mass and width of the $K_2^\star(1430)$ have been shifted above and below the nominal values by their quoted uncertainties [55]. The largest difference in the mixing parameters with respect to the fit results obtained with the nominal model is taken as this contribution to the systematic uncertainty.

- **More resonances.** The $K^\star(1410)$ and $\rho(1450)$ have been added to the model.

- **Blatt-Weisskopf barrier factors.** The effective radius of the Blatt-Weisskopf centrifugal barrier factors is fixed to $1.5\,\mathrm{GeV}^{-1}$ in the nominal fit. The effect from fixing this parameter is accounted for by changing this value from 0 to $3\,\mathrm{GeV}^{-1}$.

- **Helicity formalism.** The helicity formalism [40, 41, 42, 43] is used as an alternative to the Zemach formalism [38, 39, 40] for the description of the angular distribution of the $\tilde{D}^0$ decay products. This has a small effect on the P-wave, but larger on the D-wave.

- **Reference frame.** As described in §2, the Blatt-Weisskopf centrifugal barrier factor at the $\tilde{D}^0$ decay vertex is computed using the momentum of the non-resonant daughter c in the rest frame of its mother $\tilde{D}^0$ [37, 75]. Alternatively, this momentum has been evaluated using the momentum of the non-resonant particle c in the rest frame of the resonant pair ab [55].

The different contributions to the decay model systematic uncertainty are summarized in table 7.6 for fits to only $K_s\pi^+\pi^-$ events.

Source	$x\,(10^{-2})$	$y\,(10^{-2})$
$\pi\pi$ S-wave: K-matrix solution-I	0.0129 ± 0.0124	-0.0087 ± 0.0088
$\pi\pi$ S-wave: K-matrix solution-IIa	-0.0036 ± 0.0021	0.0023 ± 0.0013
$\pi\pi$ S-wave: Alternative NR term production vector	-0.0042 ± 0.0034	-0.0198 ± 0.0059
$\pi\pi$ P-wave: $\rho(770)$ and $\omega(782)$ float mass and width	0.0298 ± 0.0303	-0.0091 ± 0.0258
$\pi\pi$ P-wave: $\rho(770)$ BW line shape	-0.0011 ± 0.0067	0.0059 ± 0.0059
$K\pi$ P-wave: $K^*(1680)$ mass variation	-0.0134 ± 0.0025	0.0023 ± 0.0036
$K\pi$ P-wave: $K^*(1680)$ width variation	-0.0035 ± 0.0018	0.0028 ± 0.0017
$K\pi$ P-wave: $K^*(1680)$ mass and width from PDG [55]	-0.0183 ± 0.0045	0.0042 ± 0.0052
P-vector, LASS and $K^*(892)$ parameters left to float	0.0723	0.0606
$\pi\pi$ D-wave: $f_2(1270)$ mass variation	-0.0007 ± 0.0009	-0.0008 ± 0.0008
$\pi\pi$ D-wave: $f_2(1270)$ width variation	0.0005 ± 0.0012	0.0008 ± 0.0011
$K\pi$ D-wave: $K_2^*(1430)$ mass variation	0.0014 ± 0.0015	-0.0008 ± 0.0015
$K\pi$ D-wave: $K_2^*(1430)$ width variation	-0.0006 ± 0.0014	0.0013 ± 0.0010
More $K_s\pi^+\pi^-$ resonances: $K^*(1410)$ and $\rho(1450)$	-0.0001 ± 0.0038	-0.0011 ± 0.0028
P,D-waves: Blatt-Weisskopf penetration factors	0.0023 ± 0.0061	0.0044 ± 0.0087
P,D-waves: Helicity formalism	0.0042 ± 0.0260	-0.0203 ± 0.0193
P,D-waves: Reference frame	-0.0251 ± 0.0264	-0.0326 ± 0.0197
Total $K_s\pi^+\pi^-$ only decay model systematics	0.0866	0.0762

Table 7.6: Summary of the $K_s\pi^+\pi^-$ only contributions to the decay model systematic uncertainty on the mixing parameters x and y. The sign of each contribution indicates the sign of the variation of the corresponding parameter with respect to the result from the nominal mixing fit. The error of each contribution is the root mean squared of the toy Monte Carlo per-experiment differences between each alternative model and the nominal mixing fit result.

The overall model systematics correlation coefficient between x and y in $K_s\pi^+\pi^-$ only events has been estimated to be 0.0478.

In general, all the alternative decay models that have been considered as sources of systematic uncertainty have either a slightly larger χ^2/ndof[1] or a rather marginal difference. Models with a significantly larger χ^2/ndof are not supported by the analyzed data and are, therefore, rejected. This is the case, for example, of an alternative model where the generalized LASS parameterization is replaced with a Breit-Wigner propagator, which yields $\chi^2/\text{ndof} = 12183.5/(8626-34) = 1.4180$,

[1]Obtained using an adaptive binning that produces uniformly populated bins across the phase space, as described in §6.2.2.4.

significantly larger than the χ^2/ndof obtained with the nominal model, $\chi^2/\text{ndof} = 10429.2/(8626-41) = 1.2148$.

Interestingly, an alternative model with a Breit-Wigner parameterization for both the $\pi\pi$ and $K\pi$ S-waves yields $\chi^2/\text{ndof} = 12107.1/(8626-34) = 1.4091$, which is similar to the χ^2/ndof obtained with the model that describes the $K\pi$ S-wave with a Breit-Wigner propagator. This indicates that the largest loss in fit quality comes from replacing the generalized LASS parameterization with a Breit-Wigner propagator to describe the $K\pi$ S-wave, rather than from the details in the description of the sophisticated $\pi\pi$ S-wave.

7.2.2 $\pi\pi$ and $K\pi$ S-wave crosschecks

As a crosscheck, the effect of using a Breit-Wigner model to describe the $\pi\pi$ S-wave has been evaluated using the toy Monte Carlo experiments described in 7.2, while keeping the generalized LASS model for the $K\pi$ S-wave. The difference in the mixing parameters obtained from the fit to this model with respect to those obtained from the fit to the nominal model is $(-2.10 \pm 5.46)\cdot 10^{-4}$ for x and $(-2.14 \pm 4.09)\cdot 10^{-4}$ for y. This result is comparable to the contribution of the $\pi\pi$ S-wave to the systematic uncertainty, that is based on the alternative K-matrix solutions reported in [49] and on removing the non-resonant contribution from the P-vector [74], which provides a crosscheck of the robustness of the mixing fit result against the details of the description of the $\pi\pi$ S-wave. It is interesting to notice that this result has a larger root mean squared than any other result from all the alternative decay models. This indicates that there are significant statistical differences between the K-matrix and Breit-Wigner descriptions of the $\pi\pi$ S-wave.

If, additionally to the $\pi\pi$ S-wave, also the $K\pi$ S-wave is described by the Breit-Wigner model, instead of the nominal generalized LASS parameterization, the observed difference with respect to the nominal model is also consistent with the systematics assigned to the $\pi\pi$ and $K\pi$ S-waves.

7.2.3 Alternative $K_sK^+K^-$ models

Similarly to the $K_s\pi^+\pi^-$ models, several alternative $K_sK^+K^-$ decay models are considered:

- The parameters of the $a_0^0(980)$ resonance, expressed as a coupled channel formulation, as described in §2.4.8.2, and taken from a Crystal Barrel measurement [52], are shifted above and below the nominal values by their quoted uncertainties. The largest difference in the mixing parameters with respect to the fit results obtained with the nominal model is taken as this contribution to the systematic uncertainty. No contribution is associated to $g^0_{K\bar{K}}$, since this parameter is allowed to float in the nominal mixing fit.

- The parameters of the $f_0(1370)$ resonance, taken from a BES measurement [53], with mass $1350 \pm 50\,\text{MeV}$ and width $265 \pm 40\,\text{MeV}$, are shifted above and below their nominal values by their quoted uncertainties. The largest difference in the mixing parameters with respect to the fit results obtained with the nominal model is taken as this contribution to the systematic uncertainty.

- Alternatively, the values of the parameters of the $f_0(1370)$ are fixed to the values obtained from an E791 measurement [54], with mass $1434 \pm 18\,\mathrm{MeV}$ and width $173 \pm 32\,\mathrm{MeV}$.
- Similarly to $a_0^0(980)$ and $f_0(1370)$, the parameters of the $f_2(1270)$ and $a_0(1450)$ resonances are shifted above and below by their quoted uncertainties [55].
- **More resonances.** The doubly Cabibbo suppressed $a_0^-(1450)$ and $f_0(980)$ resonances have been added to the model. The $f_0(980)$ has been parameterized using the coupled channel formalism, described in §2.4.3, with the parameters taken from a BES measurement [53], with mass $965 \pm 10\,\mathrm{MeV}$ and base residue functions $g^0_{\pi\pi} = 165 \pm 18\,\mathrm{MeV}$ and ${g^0}^2_{K\bar{K}}/{g^0}^2_{\pi\pi} = 4.21 \pm 0.32$, which yields $g^0_{K\bar{K}} = 695 \pm 94\,\mathrm{MeV}$.
- **Less resonances.** The $f_0^0(1370)$ and $f_2^0(1270)$ resonances, which do not couple strongly to K^+K^-, as discussed in §2.4.8.2, are removed from the model.
- **Blatt-Weisskopf barrier factors.** The effective radius of the Blatt-Weisskopf centrifugal barrier factors is fixed to $1.5\,\mathrm{GeV}^{-1}$ in the nominal fit. The effect from fixing this parameter is accounted for by changing this value from 0 to $3\,\mathrm{GeV}^{-1}$.
- **Helicity formalism.** The helicity formalism [40, 41, 42, 43] is used as an alternative to the Zemach formalism [38, 39, 40] for the description of the angular distribution of the $\tilde{D}^0$ decay products.
- **Reference frame.** As described in §2, the Blatt-Weisskopf centrifugal barrier factor at the $\tilde{D}^0$ decay vertex is computed using the momentum of the non-resonant daughter c in the rest frame of its mother $\tilde{D}^0$ [37, 75]. Alternatively, this momentum has been evaluated using the momentum of the non-resonant particle c in the rest frame of the resonant pair ab [55].

The different contributions to the decay model systematic uncertainty are summarized in table 7.7 for fits to only $K_sK^+K^-$ events. It can be observed that the largest contribution to the systematic uncertainty in both x and y comes from the removal of the $f_0^0(1370)$ and $f_2^0(1270)$ resonances. These resonances do not couple strongly to $K\bar{K}$, as their fit fractions indicate in table 6.25. The data show a larger agreement on the nominal decay model used in this analysis, rather than any alternative models, although the inclusion of the $f_0^0(1370)$ and $f_2^0(1270)$ resonances, as well as the doubly Cabibbo suppressed $a_0(1450)$ and $f_0(980)$ resonances, is accompanied with significant increases on the global fit fraction, as a consequence of the difficulties of the model to isolate the contribution of many scalar resonances. While the nominal model yields $\chi^2/\mathrm{ndof} = 1511.2/(1195-17) = 1.2829$ and a fit fraction of 163.4 %, the alternative model without the $f_0^0(1370)$ and $f_2^0(1270)$ resonances yields $\chi^2/\mathrm{ndof} = 2055.0/(1195-13) = 1.7386$ and a total fit fraction of 142.7 %.

The overall model systematics correlation coefficient between x and y in $K_sK^+K^-$ only events has been estimated to be -0.9492.

7.2.4 Combined $K_s\pi^+\pi^-$ and $K_sK^+K^-$ decay model uncertainties

The procedure followed to estimate the systematic uncertainty associated to the decay model, described in §7.2, has been applied separately for the $K_s\pi^+\pi^-$ and $K_sK^+K^-$ $\tilde{D}^0$ decay modes, and

Source	$x\,(10^{-2})$	$y\,(10^{-2})$
KK S-wave: $a_0(980)$ mass variation	0.0017 ± 0.0061	0.0085 ± 0.0020
KK S-wave: $g_{\eta\pi}$ variation	0.0056 ± 0.0143	0.0263 ± 0.0050
KK S-wave: $f_0(1370)$ mass variation	-0.0056 ± 0.0069	-0.0100 ± 0.0048
KK S-wave: $f_0(1370)$ width variation	-0.0018 ± 0.0037	-0.0038 ± 0.0031
KK S-wave: $f_0(1370)$ from E791 [54]	-0.0063 ± 0.0060	-0.0075 ± 0.0059
KK S-wave: $a_0(1450)$ mass variation	-0.0036 ± 0.0065	0.0057 ± 0.0023
KK S-wave: $a_0(1450)$ width variation	0.0021 ± 0.0041	0.0028 ± 0.0020
KK D-wave: $f_2(1270)$ mass variation	-0.0011 ± 0.0014	-0.0005 ± 0.0021
KK D-wave: $f_2(1270)$ width variation	0.0007 ± 0.0012	-0.0005 ± 0.0006
More $K_sK^+K^-$ resonances: $a_0(1450)$ DCS and $f_0(980)$	-0.0110 ± 0.0207	-0.0024 ± 0.0210
Less $K_sK^+K^-$ resonances: $f_0(1370)$ and $f_2(1270)$	-0.2640 ± 0.1735	0.1861 ± 0.0750
P,D-waves: Blatt-Weisskopf factors	0.0045 ± 0.0094	-0.0100 ± 0.0020
P,D-waves: Helicity formalism	-0.0545 ± 0.0319	0.0056 ± 0.0091
P,D-waves: Reference frame	-0.0142 ± 0.0242	0.0438 ± 0.0074
Total $K_sK^+K^-$ only decay model systematics	0.2704	0.1941

Table 7.7: Summary of the $K_sK^+K^-$ only contributions to the decay model systematic uncertainty on the mixing parameters x and y. The sign of each contribution indicates the sign of the variation of the corresponding parameter with respect to the result from the nominal mixing fit. The error of each contribution is the root mean squared of the toy Monte Carlo per-experiment differences between each alternative model and the nominal mixing fit result.

has been detailed in §7.2.1 and §7.2.3. The contributions from each alternative model m for the two $\tilde{D}^0$ decay modes are combined taking into account their relative statistical weights, obtained from the nominal mixing fit to data and reported in table 6.29,

$$\sigma_m = \frac{\sum\limits_h \omega_h \sigma_{h,m}}{\sum\limits_h \omega_h}, \tag{7.21}$$

where the sum is over the $\tilde{D}^0$ decay modes $K_s\pi^+\pi^-$ and $K_sK^+K^-$, and the weights are

$$\omega_h = \frac{1}{\sigma^2_{h,stat}}. \tag{7.22}$$

The combined $K_s\pi^+\pi^-$ and $K_sK^+K^-$ contributions to the systematic uncertainty are reported in table 7.8.

From the values reported in table 7.8, the model-related systematic covariance matrix is found to be

$$V_{\rm mod} = \begin{array}{c} \begin{array}{cc} \quad x & \qquad\qquad y \end{array} \\ \begin{pmatrix} 6.89\cdot 10^{-7} & -1.56\cdot 10^{-8} \\ -1.56\cdot 10^{-8} & 4.69\cdot 10^{-7} \end{pmatrix} \end{array}, \tag{7.23}$$

and the correlation coefficient due to this contribution is $\rho_{\mathrm{mod}} = -0.0274$.

Source	$x\,(10^{-2})$	$y\,(10^{-2})$
$\pi\pi$ S-wave: K-matrix solution-I	0.0121 ± 0.0116	-0.0077 ± 0.0077
$\pi\pi$ S-wave: K-matrix solution-IIa	-0.0033 ± 0.0020	0.0020 ± 0.0012
$\pi\pi$ S-wave: Alternative NR term production vector	-0.0040 ± 0.0032	-0.0174 ± 0.0052
$\pi\pi$ P-wave: $\rho(770)$ and $\omega(782)$ float mass and width	0.0279 ± 0.0284	-0.0080 ± 0.0227
$\pi\pi$ P-wave: $\rho(770)$ BW line shape	-0.0010 ± 0.0063	0.0052 ± 0.0052
$K\pi$ P-wave: $K^*(1680)$ mass variation	-0.0125 ± 0.0023	0.0020 ± 0.0031
$K\pi$ P-wave: $K^*(1680)$ width variation	-0.0033 ± 0.0017	0.0025 ± 0.0015
$K\pi$ P-wave: $K^*(1680)$ mass and width from PDG [55]	-0.0172 ± 0.0042	0.0037 ± 0.0046
P-vector, LASS, $K^*(892)$, $\phi(1020)$, and $g_{K\bar{K}}$ left to float	0.0678	0.0532
$K\pi$ D-wave: $K_2^*(1430)$ mass variation	0.0013 ± 0.0014	-0.0007 ± 0.0014
$K\pi$ D-wave: $K_2^*(1430)$ width variation	-0.0005 ± 0.0013	0.0012 ± 0.0009
More $K_s\pi^+\pi^-$ resonances: $K^*(1410)$ and $\rho(1450)$	-0.0001 ± 0.0036	-0.0010 ± 0.0025
KK S-wave: $a_0(980)$ mass variation	0.0001 ± 0.0004	0.0010 ± 0.0002
KK S-wave: $g_{\eta\pi}$ variation	0.0003 ± 0.0009	0.0032 ± 0.0006
KK S-wave: $f_0(1370)$ mass variation	-0.0003 ± 0.0004	-0.0012 ± 0.0006
KK S-wave: $f_0(1370)$ width variation	-0.0001 ± 0.0002	-0.0005 ± 0.0004
KK S-wave: $f_0(1370)$ from E791 [54]	-0.0004 ± 0.0004	-0.0009 ± 0.0007
KK S-wave: $a_0(1450)$ mass variation	-0.0002 ± 0.0004	0.0007 ± 0.0003
KK S-wave: $a_0(1450)$ width variation	0.0001 ± 0.0003	0.0003 ± 0.0002
More $K_sK^+K^-$ resonances: $a_0(1450)$ DCS and $f_0(980)$	-0.0007 ± 0.0013	-0.0003 ± 0.0026
Less $K_sK^+K^-$ resonances: $f_0(1370)$ and $f_2(1270)$	-0.0165 ± 0.0109	0.0226 ± 0.0091
$\pi\pi, KK$ D-waves: $f_2(1270)$ mass variation	-0.0007 ± 0.0009	-0.0008 ± 0.0008
$\pi\pi, KK$ D-waves: $f_2(1270)$ width variation	0.0006 ± 0.0012	0.0006 ± 0.0010
$\pi\pi, KK$ P,D-waves: Blatt-Weisskopf factors	0.0025 ± 0.0058	0.0026 ± 0.0077
$\pi\pi, KK$ P,D-waves: Helicity formalism	0.0005 ± 0.0245	-0.0172 ± 0.0170
$\pi\pi, KK$ P,D-waves: Reference frame	-0.0244 ± 0.0248	-0.0233 ± 0.0173
Total decay model systematics	0.0830	0.0685

Table 7.8: Summary of the combined $K_s\pi^+\pi^-$ and $K_sK^+K^-$ contributions to the decay model systematic uncertainty on the mixing parameters x and y. The sign of each contribution indicates the sign of the variation of the corresponding parameter with respect to the result from the nominal mixing fit. The error of each contribution is the root mean squared of the toy Monte Carlo per-experiment differences between each alternative model and the nominal mixing fit result.

Chapter 8

Results and conclusions

The final unblind results of this analysis are

$$x = (0.16 \pm 0.23(\text{stat}) \pm 0.12(\text{exp}) \pm 0.08(\text{mod})) \cdot 10^{-2}, \tag{8.1}$$
$$y = (0.57 \pm 0.20(\text{stat}) \pm 0.13(\text{exp}) \pm 0.07(\text{mod})) \cdot 10^{-2}, \tag{8.2}$$

where the first quoted error is statistical, the second is experimental systematic and the third is model-related systematic. These systematic components are described in detail in §7.

The covariance matrices of each component of the uncertainty are

$$V_{\text{stat}} = \begin{array}{c} \begin{array}{cc} \quad x \quad & \quad\quad y \quad \end{array} \\ \begin{pmatrix} 5.43 \cdot 10^{-6} & 1.64 \cdot 10^{-7} \\ 1.64 \cdot 10^{-7} & 4.00 \cdot 10^{-6} \end{pmatrix} \end{array}, \tag{8.3}$$

$$V_{\text{exp}} = \begin{array}{c} \begin{array}{cc} \quad x \quad & \quad\quad y \quad \end{array} \\ \begin{pmatrix} 1.38 \cdot 10^{-6} & 2.45 \cdot 10^{-7} \\ 2.45 \cdot 10^{-7} & 1.695 \cdot 10^{-6} \end{pmatrix} \end{array}, \tag{8.4}$$

$$V_{\text{mod}} = \begin{array}{c} \begin{array}{cc} \quad x \quad & \quad\quad y \quad \end{array} \\ \begin{pmatrix} 6.89 \cdot 10^{-7} & -1.56 \cdot 10^{-8} \\ -1.56 \cdot 10^{-8} & 4.69 \cdot 10^{-7} \end{pmatrix} \end{array}. \tag{8.5}$$

The result for $K_s\pi^+\pi^-$ only is

$$x_{K_s\pi^+\pi^-} = (0.26 \pm 0.24(\text{stat})) \cdot 10^{-2}, \tag{8.6}$$
$$y_{K_s\pi^+\pi^-} = (0.60 \pm 0.21(\text{stat})) \cdot 10^{-2}, \tag{8.7}$$

and for $K_sK^+K^-$ only is

$$x_{K_sK^+K^-} = (-1.36 \pm 0.92(\text{stat})) \cdot 10^{-2}, \tag{8.8}$$
$$y_{K_sK^+K^-} = (\ \ 0.44 \pm 0.57(\text{stat})) \cdot 10^{-2}. \tag{8.9}$$

Regions of confidence level in the two-variable (x, y) parameter subspace are defined according to the one-variable Gaussian coverage from 1 to 5 σ: $0.6827\,(1\,\sigma)$, $0.9545\,(2\,\sigma)$, $0.9973\,(3\,\sigma)$, $1 - 6.334 \cdot 10^{-5}\,(4\,\sigma)$ and $1 - 5.733 \cdot 10^{-7}\,(5\,\sigma)$. Several techniques exist to evaluate the two-variable confidence level contours of the measured mixing parameters:

1. A toy Monte Carlo based approach would allow the evaluation of the confidence level contours of the measured mixing parameters without any assumption about the sampling distribution, by measuring the fraction of toy Monte Carlo experiments with fit results inside that region. A point α in the parameter space is determined by $(x_\alpha, y_\alpha, \vec{p}_\alpha)$, where (x_α, y_α) are the mixing parameters and $\vec{p}_\alpha$ are the rest of the parameters. To determine the confidence level at point (x_α, y_α) a few steps are followed:

   - Do a fit to the data sample $\vec{v}_{\text{data}}$, fixing the mixing parameters to (x_α, y_α), to extract $\vec{p}_\alpha$.
   - Generate N data-sized toy Monte Carlo samples $\vec{v}_{\alpha n}$, with $(x_\alpha, y_\alpha, \vec{p}_\alpha)$.
   - For each of the N samples $\vec{v}_{\alpha n}$, do a maximum likelihood fit to obtain the parameters $(x_{\alpha n}, y_{\alpha n}, \vec{p}_{\alpha n})$, such that

   $$\ln \mathcal{L}(\vec{v}_{\alpha n}; x_{\alpha n}, y_{\alpha n}, \vec{p}_{\alpha n}) = \ln \mathcal{L}^{\max}_{\alpha n}. \tag{8.10}$$

   - Take the maximum value of the likelihood, obtained from the nominal mixing fit,

   $$\ln \mathcal{L}(\vec{v}_{\text{data}}; x, y, \vec{p}) = \ln \mathcal{L}^{\max}_{\text{data}}. \tag{8.11}$$

   - Evaluate

   $$\chi^2_{\alpha n} = -2\Delta \ln \mathcal{L}_{\alpha n} = 2 \ln \mathcal{L}^{\max}_{\alpha n} - 2 \ln \mathcal{L}(\vec{v}_{\alpha n}\ ; x_\alpha, y_\alpha, \vec{p}_\alpha), \tag{8.12}$$
   $$\chi^{2\,\text{data}}_{\alpha} = -2\Delta \ln \mathcal{L}_{\alpha} = 2 \ln \mathcal{L}^{\max}_{\text{data}} - 2 \ln \mathcal{L}(\vec{v}_{\text{data}}; x_\alpha, y_\alpha, \vec{p}_\alpha). \tag{8.13}$$

   - Evaluate how often

   $$\chi^2_{\alpha n} > \chi^{2\,\text{data}}_{\alpha}, \tag{8.14}$$

     and this is the confidence level. For example, if this inequality is satisfied more than 68.27 % of the times, then α is in the interior of the $1\,\sigma$ confidence level contour. If it is less, then it is in the exterior, and if it is 68.27 % of the times, it is a point of the contour.

   This technique is very computer intensive, and is not feasible in this analysis.

2. Alternatively to the toy Monte Carlo technique, the confidence level at a point (x_α, y_α) is usually found following these steps:

- Do a fit to the data sample, fixing the mixing parameters to (x_α, y_α), to extract $\vec{p}_\alpha$.
- Take the maximum value of the likelihood, obtained from the nominal mixing fit,

$$\ln \mathcal{L}(\vec{v}_{\text{data}}; x, y, \vec{p}) = \ln \mathcal{L}^{\text{max}}_{\text{data}}. \tag{8.15}$$

- Find the locus of points α where $\chi^{2\,\text{data}}_\alpha$, evaluated using expression (8.13), takes a given value, specific for each required confidence level. With a large data sample, one expects χ^2_α to be distributed according to a χ^2 distribution with 2 degrees of freedom, described in §A. Therefore, regions at a confidence level β can be chosen as

$$\left\{(x_\alpha, y_\alpha) \middle| P_{\chi^2}\left(\chi^{2\,\text{data}}_\alpha, 2\right) \leq \beta\right\}. \tag{8.16}$$

  The contours of the confidence levels can be obtained by means of a likelihood scan of points that verify this condition. Though not as computer intensive as the toy Monte Carlo technique, expression (8.13) requires to fit for $\vec{p}_\alpha$ at every scanned point, which is also somewhat computer demanding.

3. Finally, it can be assumed for large data samples that the likelihood is a bivariate Gaussian distribution on (x_α, y_α), with a correlation coefficient ρ,

$$G(x_\alpha, y_\alpha; x, \sigma_x, y, \sigma_y, \rho) = \frac{1}{2\pi\sigma_x\sigma_y\sqrt{1-\rho^2}} \exp\left\{-\frac{1}{2(1-\rho^2)}\left[\left(\frac{x_\alpha - x}{\sigma_x}\right)^2 + \left(\frac{y_\alpha - y}{\sigma_y}\right)^2 - 2\rho\left(\frac{x_\alpha - x}{\sigma_x}\right)\left(\frac{y_\alpha - y}{\sigma_y}\right)\right]\right\}, \tag{8.17}$$

   where the values of x, σ_x, y, σ_y and ρ are taken from the nominal mixing fit to data. In this case, the contours of confidence level are ellipses on (x, y) that can be computed analytically, since

$$\ln \mathcal{L}_G(x_\alpha, y_\alpha) = \ln G(x_\alpha, y_\alpha; x, \sigma_x, y, \sigma_y, \rho). \tag{8.18}$$

   However, this is a strong assumption and it is necessary to validate it before drawing any conclusion that relies on it.

8.1 Gaussian approach

The Gaussian approach has been validated by means of a likelihood scan of combined $K_s\pi^+\pi^-$ and $K_sK^+K^-$ data, in points that satisfy the condition expressed in equation (8.16). To reduce computing time, 5 points are evaluated for each contour. This validation is done with statistical errors only, with the parameters of the Gaussian function taken from the nominal fit result, and from the statistical covariance matrix, quoted in equation (6.8).

Figure 8.1 shows the statistical contours at the confidence level of the first five standard deviations, computed with both the Gaussian approach and the five-point likelihood scan per contour.

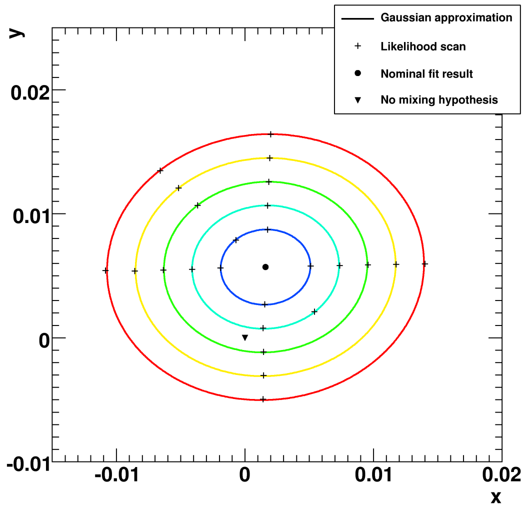

Figure 8.1: Statistical contours at the first five standard deviations for the combined $K_s\pi^+\pi^-$ and $K_sK^+K^-$ data sample. The crosses identify the points obtained from a likelihood scan, while the solid lines are the result of the Gaussian approximation with parameters taken from data.

Once the Gaussian approach is validated with the statistical uncertainties, the confidence regions, including systematic effects, can be calculated assuming a Gaussian behavior with a total covariance matrix equal to the sum of the statistical and systematic contributions, quoted in equations (6.8), (7.3) and (7.23), respectively,

$$V_{\rm tot} = V_{\rm stat} + V_{\rm exp} + V_{\rm mod}. \tag{8.19}$$

Figure 8.2 shows the confidence level contours including the experimental and decay model systematic uncertainties, and figure 8.3 shows these contours separately for $K_s\pi^+\pi^-$ and $K_sK^+K^-$.

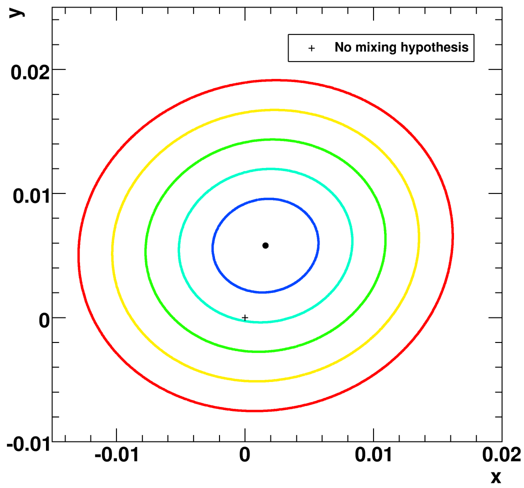

Figure 8.2: Contours at the first five standard deviations for the combined $K_s\pi^+\pi^-$ and $K_sK^+K^-$ result, with both statistical and systematic uncertainties included.

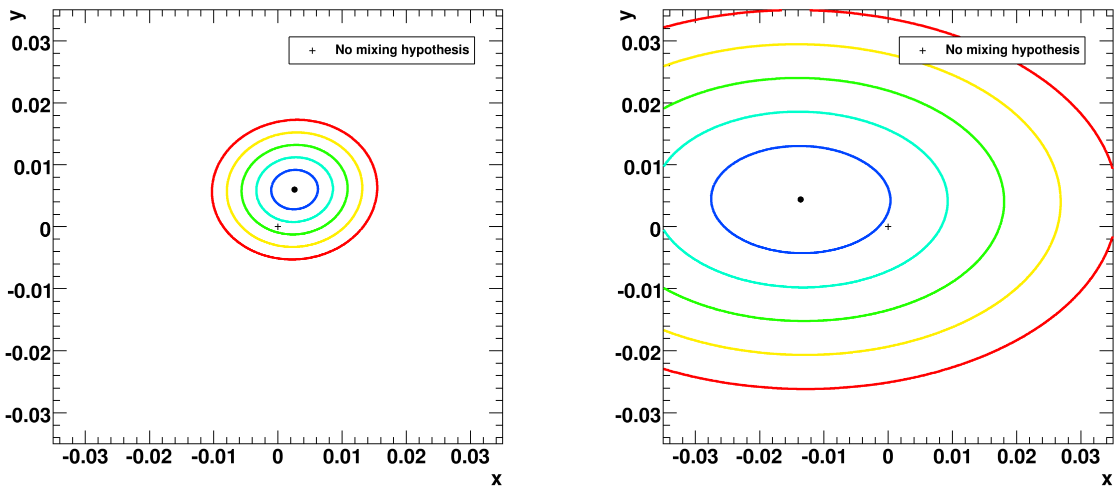

Figure 8.3: Contours at the first five standard deviations for the $K_s\pi^+\pi^-$ (left) and $K_sK^+K^-$ (right) results, with both statistical and systematic uncertainties included.

8.2 Mixing results and significance

The significance of the mixing result with respect to the hypothesis of no mixing has been evaluated by measuring the difference of negative double logarithms of the likelihoods for the two hypotheses with the Gaussian assumption, expressed in equation (8.18), taking the total covariance matrix, i.e. including both statistical and systematic uncertainties,

$$\chi^2 = -2\Delta \ln \mathcal{L}_G = 2\ln \mathcal{L}_G(x,y) - 2\ln \mathcal{L}_G(0,0). \tag{8.20}$$

Since the likelihood has been assumed to be Gaussian, this χ^2 is expected to follow a χ^2 distribution with 2 degrees of freedom, described in §A, and, therefore, the hypothesis of no mixing is excluded with a confidence level equal to $P_{\chi^2}(\chi^2, 2)$.

The value found, $\chi^2 = 5.56$, excludes the hypothesis of no mixing at a confidence level of 93.79 %, which is equivalent to $1.87\,\sigma$.

8.3 Tests of CP violation

A test for CP violation in the mixing or in the decay has been described in §6.4.2. The parameters obtained in that fit have been unblinded and are shown in table 8.1. Figure 8.4 shows the contour plot of the results of the test of CP violation in the decay, where the complex coefficients of the linear combination of resonances of the decay model are allowed to take different values for the D^0 and $\bar{D}^0$ samples. A significant separation between the two solutions on the (x, y) plane would be sign of CP violation in the decay. However, the two results are compatible within less than one standard deviation, which rules out any CP violation effects on the mixing results.

Magnitude	Sample	No CP violation	CPV test in mixing	CPV test in decay
x	D^0	0.0016 ± 0.0023	-0.0024 ± 0.0028	-0.0001 ± 0.0033
	$\bar{D}^0$		0.0059 ± 0.0028	0.0033 ± 0.0033
y	D^0	0.0057 ± 0.0020	0.0059 ± 0.0024	0.0055 ± 0.0029
	$\bar{D}^0$		0.0055 ± 0.0024	0.0059 ± 0.0028

Table 8.1: Unblind results of the mixing parameters obtained from the nominal fit and from the two tests for CP violation.

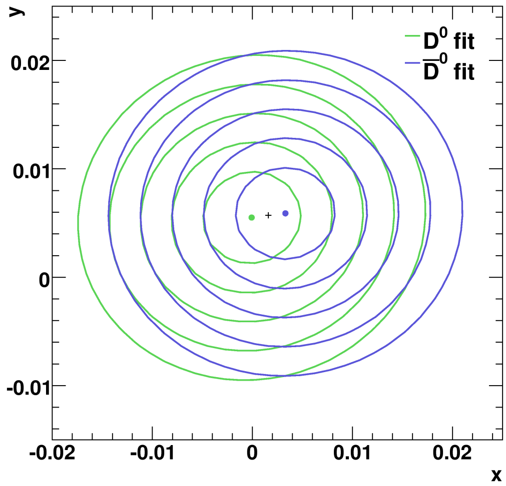

Figure 8.4: Contours at the first five standard deviations of statistical error only for the D^0 and $\bar{D}^0$ samples from a combined fit of $K_s\pi^+\pi^-$ and $K_sK^+K^-$ data samples. The marked point shows the value that maximizes the likelihood for both D^0 and $\bar{D}^0$ samples, and corresponds to the nominal mixing fit result.

8.4 Comparison with the result from Belle

The result by Belle [70], performed on 540 fb^{-1} with $K_s\pi^+\pi^-$ events only, yields

$$x = (0.80 \pm 0.29 \,^{+0.09}_{-0.07} \,^{+0.10}_{-0.14}) \cdot 10^{-2}, \tag{8.21}$$

$$y = (0.33 \pm 0.24 \,^{+0.08}_{-0.12} \,^{+0.06}_{-0.08}) \cdot 10^{-2}. \tag{8.22}$$

To compare BaBar and Belle's measurements, it has been assumed that in Belle's result there is no correlation between x and y, and the reported uncertainties have been symmetrized and added in quadrature, yielding

$$x = (0.80 \pm 0.32) \cdot 10^{-2}, \tag{8.23}$$

$$y = (0.33 \pm 0.27) \cdot 10^{-2}. \tag{8.24}$$

Figure 8.5 shows the contour plots of both BaBar and Belle results, where it can be seen that both measurements are compatible at less than one standard deviation.

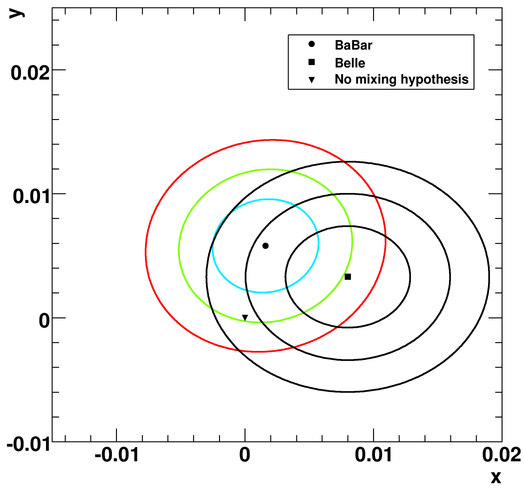

Figure 8.5: Contours at the first three standard deviations for the BaBar combined $K_s\pi^+\pi^-$ and $K_sK^+K^-$ result (colored) and Belle $K_s\pi^+\pi^-$ result (black), with both statistical and systematic uncertainties included.

8.5 Conclusions

This document has presented a measurement of the mixing parameters x and y by means of a time-dependent amplitude analysis of $\tilde{D}^0$ decays to $K_s\pi^+\pi^-$ and $K_sK^+K^-$. This measurement has used 468.5 fb^{-1} of data, taken with the BaBar experiment at the SLAC National Accelerator Laboratory.

After passing the selection criteria, 540789 ± 782 $K_s\pi^+\pi^-$ and 79908 ± 297 $K_sK^+K^-$ signal events are retained in the signal box region.

The mixing parameters x and y have been measured directly, yielding

$$x = (0.16 \pm 0.23(\text{stat}) \pm 0.12(\text{exp}) \pm 0.08(\text{mod})) \cdot 10^{-2}, \tag{8.25}$$

$$y = (0.57 \pm 0.20(\text{stat}) \pm 0.13(\text{exp}) \pm 0.07(\text{mod})) \cdot 10^{-2}, \tag{8.26}$$

and using, for the first time, a combined analysis of $\tilde{D}^0 \to K_s\pi^+\pi^-$ and $\tilde{D}^0 \to K_sK^+K^-$ events. These results are consistent with the previous similar measurements in $K_s\pi^+\pi^-$ events only [8,70], and have improved precision, thus representing a significant addition to the current knowledge of the mixing parameters.

These results exclude the no-mixing hypothesis with a confidence level equivalent to 1.9 standard deviations, and are in agreement with the range of predictions of the standard model [10,32,33,34, 11,12].

This measurement favors a lower value for x than for y, and also lower x and y values, which makes the central values move toward the standard model prediction. These measurements are still consistent with those obtained when combining results from other $\tilde{D}^0$ decay channels [2,3,5,4,6,7,

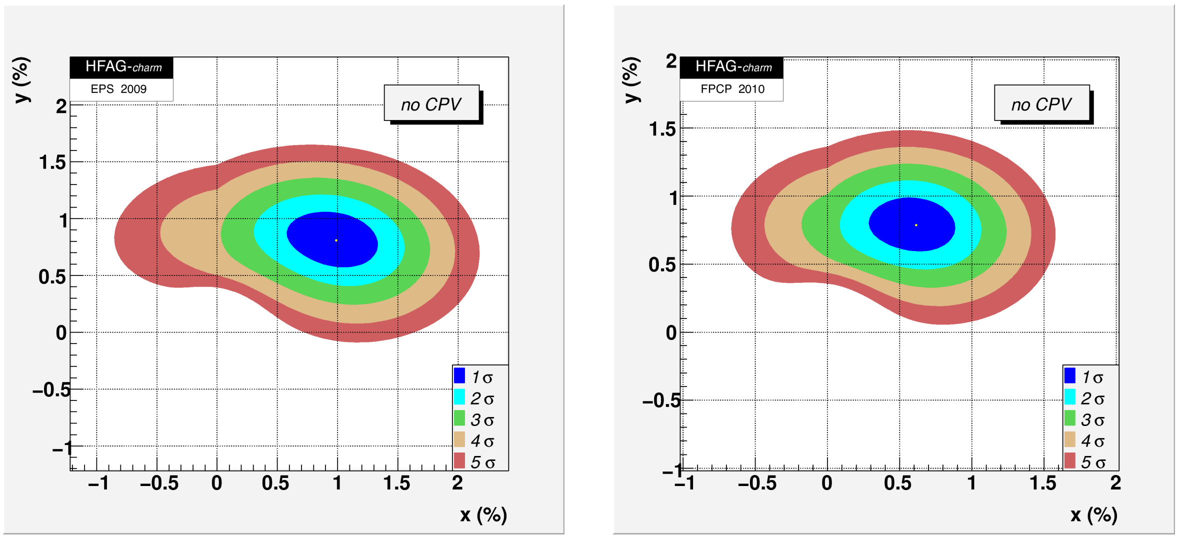

Figure 8.6: Heavy Flavor Averaging Group averages for x and y, before (left) and after (right) the measurement from BaBar.

76]. This can be seen in figure 8.6, which shows the Heavy Flavor Averaging Group contour levels at the first five standard deviations [22], obtained from all the available measurements before and after the last measurement from BaBar. A significant improvement in the current knowledge of the mixing parameters is also observed in these plots.

The measurement of the mixing parameters has been tested against possible effects of CP violation, but no hints of CP violation have been found.

Bibliography

[1] A. Pais and S. B. Treiman, Physical Review D **12**, 2744 (1975). [Erratum-ibid. D **16**, 2390 (1977)].

[2] B. Aubert et al., BaBar collaboration, Physical Review Letters **98**, 211802 (2007).

[3] T. Aaltonen et al., CDF Collaboration, Physical Review Letters **100**, 121802 (2008).

[4] M. Starič et al., Belle Collaboration, Physical Review Letters **98**, 211803 (2007).

[5] B. Aubert et al., BaBar Collaboration, Physical Review D **78**, 011105(R) (2008).

[6] B. Aubert et al., BaBar Collaboration, Physical Review D **80**, 071103 (2009).

[7] B. Aubert et al., BaBar Collaboration, Physical Review Letters **103**, 211801 (2009).

[8] D. M. Asner et al., CLEO Collaboration, Physical Review D **72**, 012001 (2005).

[9] L. M. Zhang et al., Belle Collaboration, Physical Review Letters **99**, 131803 (2007).

[10] A. Falk, Y. Grossman, Z. Ligeti, Y. Nir and A.A. Petrov, Physical Review D **69**, 114021 (2004).

[11] E. Golowich et al., Physical Review D **76**, 095009 (2007).

[12] Y. Grossman et al., Physical Review D **75**, 036008 (2007).

[13] L. M. Zhang et al., Belle Collaboration, Physical Review Letters **96**, 151801 (2006).

[14] B. Aubert et al., BaBar Collaboration, Physical Review D **76**, 014018 (2007).

[15] U. Bitenc et al., Belle Collaboration, Physical Review D **72**, 071101(R) (2005).

[16] U. Bitenc et al., Belle Collaboration, Physical Review D **77**, 112003 (2008).

[17] B. Aubert et al., BaBar Collaboration, Physical Review Letters **100**, 061803 (2008).

[18] M. Starič et al., Belle Collaboration, Physics Letters B **670**, 190-195 (2008).

[19] B. Aubert et al., BaBar Collaboration, Physical Review D **78**, 051102 (2008).

[20] K. Arinstein et al., Belle Collaboration, Physics Letters B **662**, 102-110 (2008).

[21] X. C. Tian et al., Belle Collaboration, Physical Review Letters **95**, 231801 (2005).

[22] www.slac.stanford.edu/xorg/hfag/charm/index.html

[23] B. Aubert et al., BaBar collaboration, Physical Review D **78**, 034023 (2008).

[24] J.M. Blatt and V.F. Weisskopf, Theoretical nuclear physics. John Wiley & Sons, Inc.

[25] G.J. Gounaris and J.J. Sakurai, Physical Review Letters **21**, 244 (1968).

[26] D. Aston et al., Nuclear Physics **B296**, 493-526 (1988).

[27] P.K. Kabir, The CP puzzle, appendix A. Academic press, 1968.

[28] BaBar Analysis Document, BAD188.

[29] I.I. Bigi and A.I. Sanda, CP violation. Cambridge University Press (2000)

[30] N. Cabibbo, Physical Review Letters **10**, 531 (1963).

[31] M. Kobayashi and T. Maskawa, Progress of Theoretical Physics **49**, 652 (1973).

[32] A.A. Petrov, International Journal of Modern Physics A **21**, 5685 (2006).

[33] I.I.Y. Bigi and N.G. Uraltsev, Nuclear Physics B **592**, 92 (2001).

[34] L. Wolfenstein, Physics Letters B **164**, 170 (1985).

[35] R.H. Dalitz, Philosophical Magazine Series 7 **44**, 1068 (1953).

[36] E. Fabri, Nuovo Cimento **11**, 479 (1954).

[37] S. Kopp et al., CLEO Collaboration, Physical Review D **63**, 092001 (2001).

[38] C. Zemach, Physical Review **133**, B1201-B1220 (1964).

[39] C. Zemach, Physical Review **140**, B97-B108 (1965).

[40] V. Filippini, A. Fontana and A. Rotondi, Physical Review D **51**, 2247 (1995).

[41] M. Jacob and G.C. Wick, Annals of Physics **7**, 404 (1959).

[42] M. Jacob and G.C. Wick, Annals of Physics **281**, 774 (2000).

[43] S.U. Chung, Physical Review D **48**, 1225 (1993). [Erratum-ibid. D, **56** 4419 (1997)].

[44] M. Peskin and D. Schroeder, An introduction to quantum field theory. Collæge Press Ltd., 1995.

[45] C. Itzykson and J. Zuber, Quantum field theory. McGraw-Hill, Inc., 1980.

[46] F. von Hippel and C. Quigg, Physical Review D **5**, 624 (1972).

[47] I.J.R. Aitchison, Nuclear Physics **A189**, 417-423 (1972).

[48] S.L. Adler, Physical Review **137**, B1022 (1965).

[49] V.V. Anisovich and A.V. Sarantsev, European Physical Journal A **16**, 229 (2003).

[50] V.V. Anisovich and A.V. Sarantsev, private communication.

[51] H.A. Bethe, Physical Review **76**, 38-50 (1949).

[52] A. Abele et al., Crystal Barrel Collaboration, Physical Review D **57**, 3860 (1998).

[53] M. Ablikim et al., BES Collaboration, Physics Letters B **607**, 243 (2005).

[54] E.M. Aitala et al., E791 Collaboration, Physical Review Letters **89**, 121801 (2002).

[55] W.M. Yaho et al., Particle Data Group, Journal of Physics G **33**, 1 (2006).

[56] B. Aubert et al., BaBar Collaboration, Nuclear Instruments and Methods in Physics Research **A 479**, 1-116 (2002).

[57] I. Adam et al., Nuclear Instruments and Methods in Physics Research **A 538**, 281 (2005).

[58] D. Piccolo et al., Nuclear Instruments and Methods in Physics Research **A 477**, 435-439 (2002).

[59] F. Anulli et al., Nuclear Instruments and Methods in Physics Research **A 508**, 128-132 (2003).

[60] D.J. Lange, Nuclear Instruments and Methods in Physics Research **A 462**, 152 (2001).

[61] V.N. Ivanchenko et al., Nuclear Instruments and Methods in Physics Research **A 494**, 514 (2002).

[62] BaBar Analysis Document, BAD1291.

[63] N.L. Johnson, Biometrika **36**(3/4), 297-304 (1949).

[64] H. Albrecht et al., ARGUS Collaboration, Physics Letters B **241**, 278 (1990).

[65] S. Baker and R.D. Cousins, Nuclear Instruments and Methods in Physics Research **221**, 437 (1984).

[66] G. Punzi, In the Proceedings of PHYSTAT2003: Statistical Problems in Particle Physics, Astrophysics and Cosmology, Menlo Park, California, 8-11 September 2003, pp WELT002 [arXiv:physics/0401045].

[67] B. Aubert et al., BaBar Collaboration, Physical Review D **72**, 052008 (2005).

[68] Z.Z. Xing, Physics Letters B **353** 313 (1995) [Erratum-ibid. B, **363** 266 (1995)]

[69] D.M. Asner et al., CLEO Collaboration, Physical Review D **70**, 091101 (2004).

[70] K. Abe et al., Belle Collaboration, Physical Review Letters **99**, 131803 (2007).

[71] D.N. Brown, A.V. Gritsan, Z.J. Guo, D. Roberts, Nuclear Instruments and Methods in Physics Research **A 603**, 467-484 (2009).

[72] http://www.slac.stanford.edu/BFROOT/www/Detector/SVT/LocalAlignment/systematics-14/

[73] BaBar Analysis Document, BAD1876.

[74] I.J.R. Aitchison, private communication.

[75] H. Muramatsu et al., CLEO Collaboration, Physical Review Letters **89**, 251802 (2002). [Erratum-ibid. **90** 059901 (2003)]

[76] J.L. Rosner et al., CLEO Collaboration, Physical Review Letters **100**, 221801 (2008).

Appendix A

χ^2 distribution

The χ^2 distribution with n degrees of freedom is given by

$$p_{\chi^2}(x;n) = \frac{1}{2^{\frac{n}{2}}\Gamma\left(\frac{n}{2}\right)}\, x^{\frac{n}{2}-1}e^{-\frac{x}{2}}. \tag{A.1}$$

The cumulative distribution function is

$$P_{\chi^2}(x;n) = \frac{\gamma\left(\frac{n}{2},\frac{x}{2}\right)}{\Gamma\left(\frac{n}{2}\right)}, \tag{A.2}$$

where $\gamma(s,x)$ is the lower incomplete gamma function,

$$\gamma(s,x) = \int_0^x t^{s-1}\, e^{-t}\, dt. \tag{A.3}$$

In the special case where $n = 2$,

$$P_{\chi^2}(x;n=2) = 1 - e^{-\frac{x}{2}}. \tag{A.4}$$

Appendix B

Integration over the phase space

B.1 Split integral

To simplify the calculation of the integrals in (2.101-2.103), the total amplitude can be split in a sum of resonances:

$$A_f = \sum_i a_i A^i, \tag{B.1}$$

which allows to write

$$\int \epsilon A_f^2 \, d\mathcal{P} = \sum_{ij} a_i^\star a_j \epsilon \int A^{i\star} A^j \, d\mathcal{P} = \sum_{ij} a_i^\star a_j I_D^{ij} = a^\dagger I_D a, \tag{B.2}$$

$$\int \epsilon A_f^\star \bar{A}_f \, d\mathcal{P} = \sum_{ij} a_i^\star a_j \int \epsilon A^{i\star} \bar{A}^j \, d\mathcal{P} = \sum_{ij} a_i^\star a_j I_X^{ij} = a^\dagger I_X a, \tag{B.3}$$

$$\int \epsilon \bar{A}_f^2 \, d\mathcal{P} = \sum_{ij} a_i^\star a_j \int \epsilon \bar{A}^{i\star} \bar{A}^j \, d\mathcal{P} = \sum_{ij} a_i^\star a_j I_C^{ij} = a^\dagger I_C a, \tag{B.4}$$

The subindices D, X and C in these equations mean *direct*, *crossed* and *conjugate*, respectively.

CP violation in the decay or in the interference between decays with and without mixing, can be implied by either considering different partial amplitudes $\bar{A}^i$ and A^i, or different a_i terms for them. In the specific case where CP violating effects are restricted to the second case, as well as in the limit of no CP violation, the integrals I_D, I_X and I_C do not depend on these CP violating effects.

Notice that the evaluation of each matrix element in I_D, I_X and I_C involves the evaluation of two amplitudes at every numerical sampling point, as opposed to evaluating all the amplitudes directly, as written in (2.101-2.103).

Some properties of the matrices I_D, I_X and I_C are useful to reduce the number of operations to do. It is useful to take into account that, for each resonance, there is a resonant pair AB for the decay of the particle, and AC for that of the antiparticle. This property holds whenever there's a pair BC with particles of equal mass. If the reconstruction efficiency over the phase space ϵ is symmetric over the exchange of the charged particles, $\epsilon(m_{ab}^2, m_{ac}^2)\bar{A}^i(m_{ab}^2, m_{ac}^2) = \epsilon(m_{ac}^2, m_{ab}^2)A^i(m_{ac}^2, m_{ab}^2)$. This property, together with $d\mathcal{P} = dm_{ab}^2 dm_{ac}^2$, is very powerful, since it can be used to infer the following properties:

$$I_C = I_D \tag{B.5}$$

$$I_D = I_D^\dagger \tag{B.6}$$

$$I_X = I_X^\dagger \tag{B.7}$$

This result is independent of having direct CP violation or not, since direct under the previous considerations, CPV would affect the coefficients a_i, but not the propagators. Moreover, if there is no direct CPV, $I_{\chi^2} = |q/p|^2$.

Another consequence of this is that the integrals (B.2-B.4) must be real, since the right part of the equality is Hermitian.

Since these matrices are Hermitian, they have $N(N+1)/2$ independent elements, instead of N^2. So now only the upper triangle of the matrices I_D and I_X is needed. Of course, only the terms that may have been varied in a minimization step need to be calculated. If N is the total number of amplitudes in the model and n is the number of amplitudes that may have varied in a minuit iteration, the number of pairs of integrals (I_D and I_X) to be computed is

$$\frac{(2N+1-n)n}{2} \tag{B.8}$$

So a good strategy could be the following:

```
for ( int i = 0; i < N; i++ )
  for ( int j = i; j < N; j++ )
    if ( changed[ i ] || changed[ j ] )
      {
        I[ i ][ j ] = integrate( i, j );
        if ( i != j )
          I[ j ][ i ] = I[ i ][ j ].conj();
      }
```

Moreover, if a grid numerical integration technique is used, it's possible to use the property $\bar{A}^i(m_{ab}^2, m_{ac}^2) = A^i(m_{ac}^2, m_{ab}^2)$ to reduce to one half the number of points to integrate over.

```
for ( int binX = 0; binX < nBins; binX++ )
  for ( int binY = binX; binY < nBins; binY++ )
    {
      m2AB = m2( binX );
      m2AC = m2( binY );

      if ( ( m2AC > m2ACmin( m2AB ) ) && ( m2AC < m2ACmax( m2AB ) ) )
```

```
        {
          AiStar    = evaluateReso( i, m2AB, m2AC ).conj();
          AiStarBar = evaluateReso( i, m2AC, m2AB ).conj();
          Aj        = evaluateReso( j, m2AB, m2AC );
          AjBar     = evaluateReso( j, m2AC, m2AB );

          if ( binX == binY )
            {
              Id += ( AiStar * Aj    + AiStarBar * AjBar ) / 2.;
              Ix += ( AiStar * AjBar + AiStarBar * Aj    ) / 2.;
            }
          else
            {
              Id += AiStar * Aj    + AiStarBar * AjBar;
              Ix += AiStar * AjBar + AiStarBar * Aj;
            }
        }
    }

  Id *= pow( step, 2 );
  Ix *= pow( step, 2 );
```

So if N_s is the number of nodes in the grid, this integral can be done using $N_s/2$ steps. At each step, 4 amplitudes, 4 products and 4 sums need to be evaluated.

If t_A is the average time needed to compute an amplitude and t_O that to compute an operation (sum or product), the time needed to compute the norm using this technique is

$$t = (2N + 1 - n)nN_s(t_A + 2t_O) \approx (2N + 1 - n)nN_s t_A \tag{B.9}$$

B.2 Unsplit integral

The integrals in (B.2-B.3) can also be computed as a single integral in N_s steps. Using this method, if direct CPV may be considered, there are 3 integrals to compute. They can be done at the same time. At each step, N amplitudes are needed to compute A_f, and N more to compute $\bar{A}_f$. At each step, these amplitudes must be multiplied in pairs and accumulated to the result of the previous step, and once for each integral. This means there are 3 products and 3 sums to compute at each step.

So the total time needed to compute the integral using this method is

$$t = 2N_s(Nt_A + 6t_O) \approx 2NN_s t_A \tag{B.10}$$

B.3 All split integrals at a time

The split integral takes much longer than the unsplit one because the amplitudes are computed in pairs, which translates into evaluating amplitudes more times, which is computationally expensive. An amplitude may be evaluated as many as N times at the same point using that method. These extra unnecessary calculations may be reduced if all the amplitudes that may have varied are computed only once at each step, and then multiplied and added to the matrix elements that require recomputation.

With this technique it's enough to compute $N_s/2$ steps. At each step, $2N$ amplitudes must be evaluated With these $2N$ amplitudes, the number of pairs of integrals (I_D and I_X) that have to be evaluated are

$$\frac{(2N+1-n)n}{2} \tag{B.11}$$

At each step, 4 products and 4 sums must be done for each pair of integrals.

So the total time needed to compute the integral using this method is

$$t = N_s\left[Nt_A + 2(2N+1-n)nt_O\right] = NN_s\left[t_A + \frac{2(2N+1-n)n}{N}t_O\right] \leq NN_s[t_A + 2(N+1)t_O] \tag{B.12}$$

The computation of an amplitude needs at least about 35 operations (about 35 for RBW, more for GS, coupled RBW and K-matrix). For $N \gtrsim 15$, it may be that $2(N+1)t_O \sim t_A$

A reasonable approximation may be

$$t \lesssim 2NN_st_A \tag{B.13}$$

B.4 Another little improvement

Some of the resonances in the model are the conjugate of others. For example, $A_{K^{\star+}} = \bar{A}_{K^{\star-}}$. It's not necessary to compute the amplitude for $A_{K^{\star+}}$, once $\bar{A}_{K^{\star-}}$ is computed.

B.5 Error estimation

It has been noticed that the integrals (B.2-B.3) must be real. However, complex numbers must be used to compute them. The deviation from zero in the imaginary part of the results is a first order estimation of the error in their real part.

Appendix C

Model implementation in EvtGen

This appendix documents the D0MIXDALITZ model recently implemented in EvtGen.

C.1 Description of the model

The model implements the three body $\tilde{D}^0$ decays $\tilde{D}^0 \rightarrow K_s\pi^+\pi^-$ and $\tilde{D}^0 \rightarrow K_sK^+K^-$.

So far, the decay of the D^0 meson through these models has been generated by means of the D_DALITZ model, where only $K^{\star+}(892)\pi^-$ and $K^0\rho^0(770)$ resonances and no mixing are implemented.

Some correlations have been observed between the different variables of this analysis, which have arised the question of what the impact of these correlations could be on the measurement of the x and y mixing parameters. To answer this question, a full Monte Carlo simulation with a more realistic model is necessary.

The new model implements the resonances described in [23], as well as the mixing effects described by the parameters x and y that the time dependent amplitude depends on.

For the $K_s\pi^+\pi^-$ mode, a relativistic Breit-Wigner model and a K-matrix model can be chosen. It's possible to choose which one to use by means of a parameter in the dec file.

C.1.1 Time dependent amplitude

To simplify the process of generating the value of the $\tilde{D}^0$ lifetime the dimensionless quantity $\beta = \Gamma t$ has been defined, and the functions $h_{1,2}(t)$ that describe the evolution of the Hamiltonian eigenstates, defined in §1.17, are

$$h_{1,2}(t) = g_{1,2}(\beta) = e^{\mp\frac{(y+ix)\beta}{2}}. \tag{C.1}$$

The squared amplitude is the (unnormalized) PDF, which depends on the point on the Dalitz plot and the time,

$$\left|\langle f|\mathcal{H}|\tilde{D}^0(\beta)\rangle\right|^2 = \left|\tilde{A}_f\right|^2 e^{-\beta}\left|\frac{1+\chi^{\pm1}}{2}g_1(\beta)+\frac{1-\chi^{\pm1}}{2}g_2(\beta)\right|^2 \tag{C.2}$$

$$= \left|\tilde{A}_f\right|^2 e^{-\beta}\left[\frac{1+|\chi|^{\pm2}}{2}\cosh(y\beta)+\frac{1-|\chi|^{\pm2}}{2}\cos(x\beta)- \mathrm{Re}\left(\chi^{\pm1}\right)\sinh(y\beta)+\mathrm{Im}\left(\chi^{\pm1}\right)\sin(x\beta)\right], \tag{C.3}$$

To avoid any problem with the accept-reject method on the PDF, β can be generated based on importance, i.e., generate more low values of β, which must be the majority, and modify the function that accept-reject must run on.

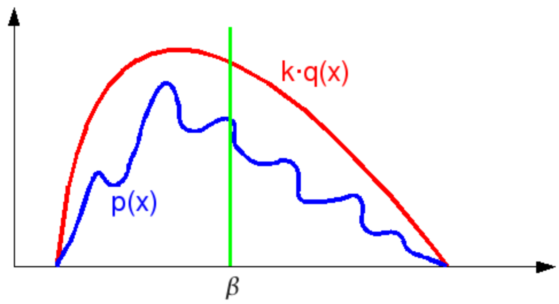

The steps of this technique are:

- Generate β according to $q(x)$, preferably some PDF that is easy to generate.
- Throw a flat random number $U(0,k)$. The value k must verify that $k > h(x) = \frac{p(x)}{q(x)}\ \forall x$. It is important to notice that $h(x)$ cannot be, for example, a function growing *ad infinitum*. The function $q(x)$ must be chosen in order to make $h(x)$ finite $\forall x$. This is specially important in our case, since the term between brackets in equation (C.3) does not verify this condition, thus it's not right to take $q(\beta) = e^{-\beta}$. $q(\beta) = e^{-(1-y)\beta}$ is a much better choice.
- If $U(0,k) < h(\beta)$ accept the value of β. Otherwise reject it.

C.1.2 Usage

The amplitudes, phases, masses and widths of each resonance have been hard coded, as well as the radius of the Blatt-Weisskopf factors. The mixing parameters x and y are zero by default, but can be easily changed in the `dec` file.

The format of the decay specification is

```
BrFr [anti-]K0 [pi+|K+] [pi-|K-] DOMIXDALITZ [x y] [reqp imqp] [doKm];
```

Here, `x` and `y` are the mixing parameters, `reqp` and `imqp` are the real and imaginary part, respectively, of the parameter q/p of CPV in the mixing, and `doKm` is 1 to select K-matrix or 0 to select a relativistic Breit-Wigner model.

All the parameters between brackets are optional, but if they are specified, both elements of a bracketed pair must be given. `x` and `y` default to $x = y = 0$, `reqp` and `imqp` default to $q/p = 1$, and the default model is the relativistic Breit-Wigner.

Example:

To generate the decay $D^0 \to \bar{K}^0\pi^+\pi^-$ described by a relativistic Breit-Wigner model, with mixing parameters $x = y = 0.1$ and no CPV, the following entry in the decay table should be used:

```
Decay my-D0
1.000    my-anti-K0  pi+  pi-    D0MIXDALITZ 0.1 0.1 1.0 0 0;
Enddecay
```

C.2 Validation of the model

Data samples of $25k$ D^0 and $25k$ $\bar{D}^0$ with the relativistic Breit-Wigner and K-matrix models with different values of x and y have been generated. The obtained datasets have been used as the input of a fit of the model to the data. The $\tilde{D}^0$ lifetime and the mixing parameters have been floated in the fit, but not the parameters of the decay models. For all the data sets, the obtained values are consistent with the generated ones.

Model	D^0 mode	Generated x/y	Fitted x	Fitted y
RBW	$K_s\pi^+\pi^-$	0.0	$(2.5 \pm 5.0) \cdot 10^{-3}$	$(-2.5 \pm 4.2) \cdot 10^{-3}$
RBW	$K_s\pi^+\pi^-$	0.1	0.1008 ± 0.0051	0.1006 ± 0.0041
RBW	$K_s\pi^+\pi^-$	0.5	0.5046 ± 0.0084	0.5014 ± 0.0036
K-matrix	$K_s\pi^+\pi^-$	0.0	$(4.2 \pm 5.1) \cdot 10^{-3}$	$(-3.8 \pm 4.1) \cdot 10^{-3}$
K-matrix	$K_s\pi^+\pi^-$	0.1	0.0995 ± 0.0049	0.0997 ± 0.0042
K-matrix	$K_s\pi^+\pi^-$	0.5	0.5071 ± 0.0081	0.5016 ± 0.0037
RBW	$K_sK^+K^-$	0.0	$(-1.46 \pm 0.60) \cdot 10^{-3}$	$(8.3 \pm 3.7) \cdot 10^{-3}$
RBW	$K_sK^+K^-$	0.1	0.1004 ± 0.0064	0.1076 ± 0.0036
RBW	$K_sK^+K^-$	0.5	0.4941 ± 0.0091	0.5022 ± 0.0031

As an example, the plots of the projections of the K-matrix model with $x = y = 0.0$ and $x = y = 0.5$ are shown below.

Similarly, the models have also been verified by fitting the same generated datasets allowing the model parameters to float.

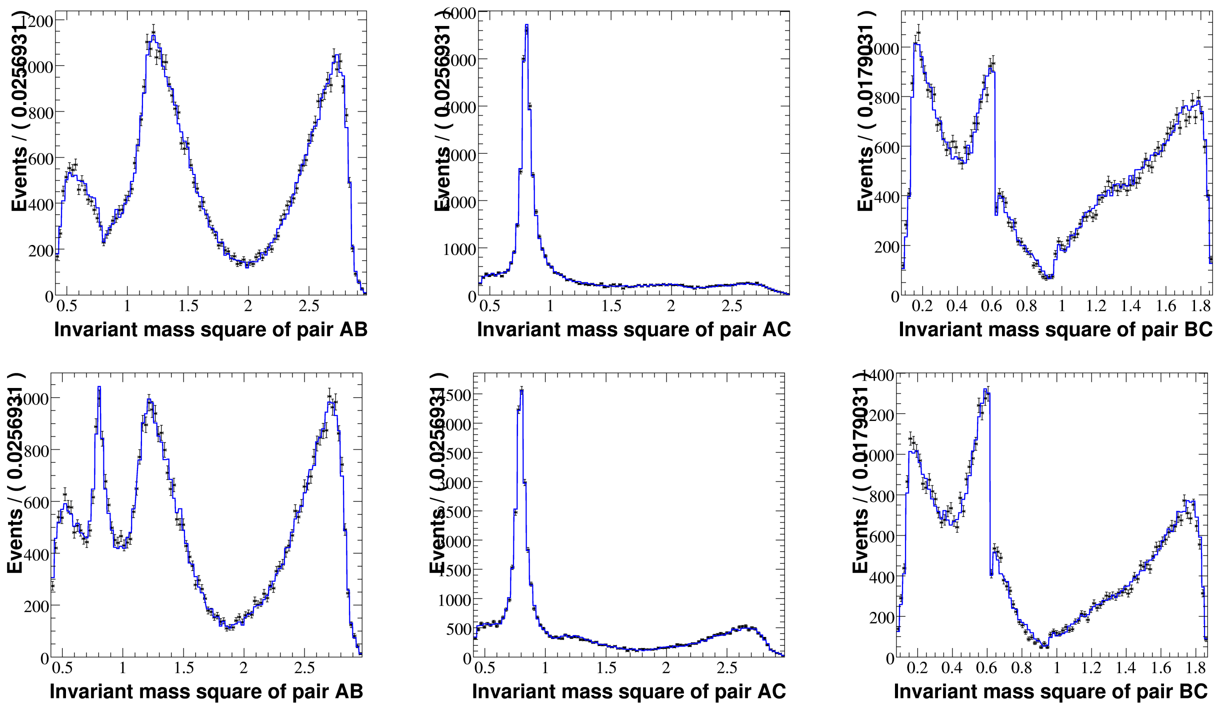

Figure C.1: Dalitz projections of the complete K-matrix model for $x = y = 0.0$ (upper plots) and $x = y = 0.5$ (lower plots). The points are the MC data, and the blue curve is the model.